Final Report
Design Synthesis Exercise

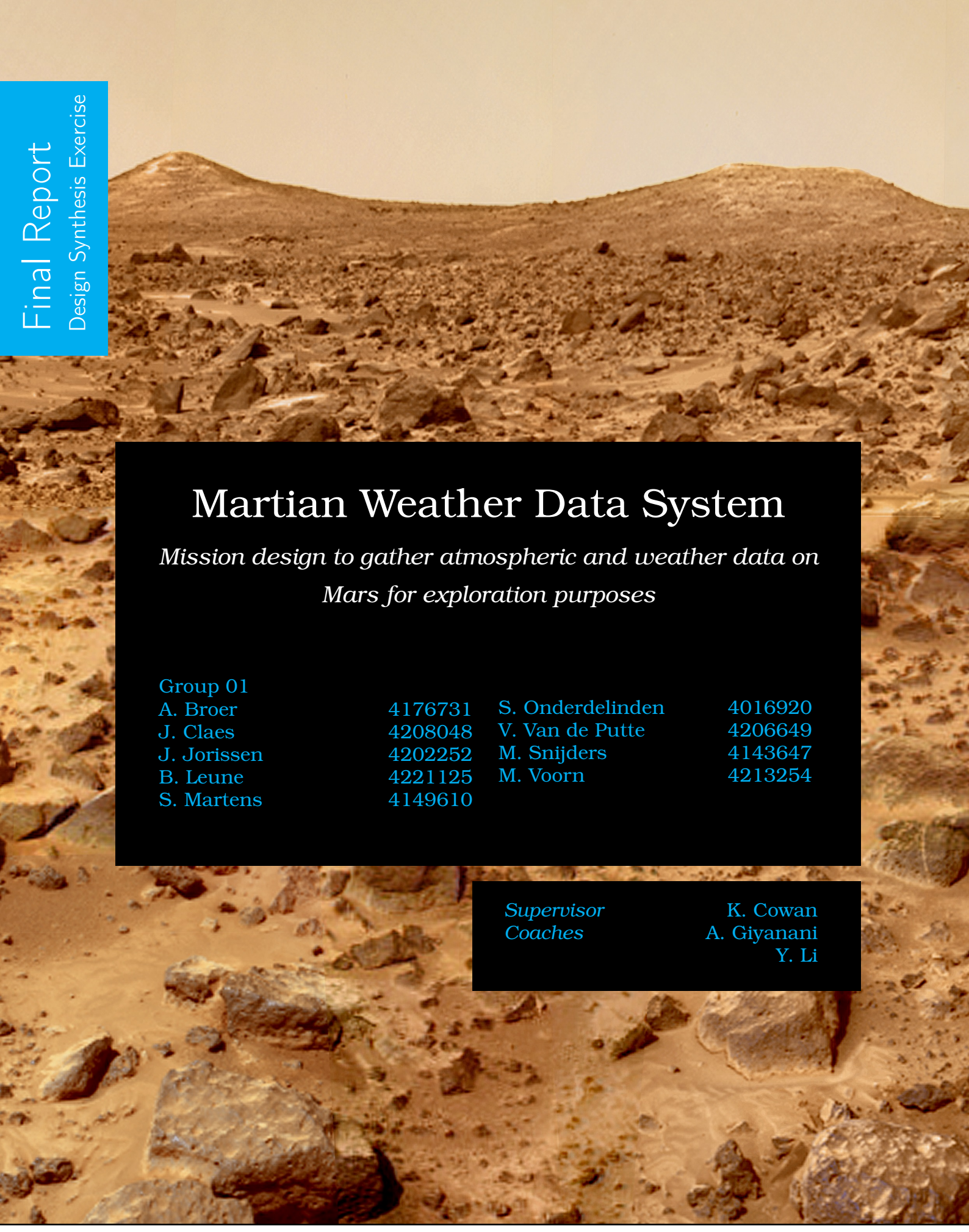

Martian Weather Data System

Mission design to gather atmospheric and weather data on Mars for exploration purposes

Group 01

A. Broer	4176731	S. Onderdelinden	4016920
J. Claes	4208048	V. Van de Putte	4206649
J. Jorissen	4202252	M. Snijders	4143647
B. Leune	4221125	M. Voorn	4213254
S. Martens	4149610		

Supervisor	K. Cowan
Coaches	A. Giyanani
	Y. Li

TU Delft Delft University of Technology

Aerospace Engineering

30 June 2015

Frontpage figure source: Parker, T., "Super Resolution Stereo Pairs of "Twin Peaks"," *JPL Planetary Photojournal* [online database], URL: `http://mars.nasa.gov/MPF/parker/highres-stereo.html` [cited 17 May 2015]

Preface

Over the course of 11 weeks, our Design Synthesis Exercise group made a detailed concept to explore and investigate the environment of Mars. To do so, we developed the Martian Weather Data System, or MUUDS. This system is capable of collecting atmospheric data on temperature, pressure, wind speeds, radiation, dust content and atmospheric composition, both on ground as well as throughout the entire Martian atmosphere. This data is of absolute importance towards the future, when human landing on Mars will become reality. The combination of orbiter measurement and local, on-ground, measurements, will lead to a clearer image on the environment humans can expect when arriving at Mars. Detailed information on the Martian climate is scarce, and we do not wish to send the first humans to ever set foot on Mars into the unknown.

This final report is built up such that the development of MUUDS is presented per phase of the mission. We start with the launch of the space probe on Earth and continue to design the spacecraft for its transfer orbit to Mars. The spacecraft is delivered to a circular orbit around Mars and will release 10 ground stations that have been designed in such a way that they can perform an entry, descent and landing on Mars. These stations will execute the on-ground measurements. The part of the spacecraft left in orbit around Mars, the orbiter, will collect the atmospheric data throughout the entire thickness of the atmosphere. The end-of-life disposal concludes the life of MUUDS and is the last step in the per-phase design of the Martian Weather Data System. The design steps in all these phases fuse together towards a final design concept.

Apart from the design process, the technical work breakdown of the design is highlighted. Besides, a risk and contingency approach is described together with a sustainability approach. In addition, a market analysis is executed and the budget breakdown of mass and power for the design is outlined. Finally, we looked into the next step after the design process and came up with a development logic and production plan.

We would like to express our sincere gratitude to our supervisor, Kevin Cowan, and our coaches, Yalin Li and Ashim Giyanani, for their valuable technical support and guidance. We also would like to thank Svenja Woicke, Jasper Bouwmeester, Max Mulder, Julien Chimot, Koen Groot, Jacco Geul, Daphne Stam, Marcel Schouwenburg, Paul Boef, Mark van Bourgondiën, Barry Zandbergen, Angelo Cervone, Eelco Doornbos, Pieter Visser and Eddy van den Bos, who provided us the opportunity to further enhance the quality and content of this MUUDS mission.

DSE Group 01 - MUUDS
Delft University of Technology
Delft, 30 June 2015

Summary

Ever since the first manned space mission, humankind has never stopped expanding the borders of what is possible. Plans for a manned mission to Mars get more serious every day: Mars One aims to populate Mars by 2025 and NASA plans to land people on Mars in the mid 2030's. However, very little is known about the environmental circumstances these pioneers will face once they have arrived and it is essential that a better image of the Martian climate and radiation environment exists before such a mission can be successful.

For this purpose, the MUUDS group was assigned to design a Martian weather data system which will map the ground and atmospheric climate for two consecutive Martian years. In this time frame, data is collected on atmospheric properties (temperature, pressure, wind velocity, dust content, atmospheric composition) and the radiation environment on the Martian surface, as well as vertical profiles of said atmospheric properties. The measurements on ground are taken at maximally variable locations which are selected as feasible human landing sites. The design covers the launch; interplanetary travel; entry, descent and landing; ground and orbit operations and the end-of-life phase.

A space probe is designed consisting of ten landers, an orbiter and the fuel required to travel to Mars. It has a total mass of 5,365.09 kg. For the launch, the Falcon Heavy will be used: it can bring the entire space probe straight to the Mars transfer orbit. Moreover, the boosters of this launcher are reusable, which adds to the sustainability of the project. The transfer vehicle is brought into a Hohmann transfer orbit to Mars, to which the probe travels in 278 days. Once at Mars, the probe delivers a ΔV of 1.885 km/s to bring the spacecraft in a circular orbit of 220 km altitude. From this orbit, the landers are released. A ballistic entry was chosen, using an inflatable aeroshell, parachute and reverse thrusters (in this order) to decelerate the pods and ensure a safe landing on a crushable honeycomb cone. Although this approach is risky, due to the considerable weight savings and the redundancy of ten pods, the requirement of placing eight ground stations can still be met. Also, the inflatable aeroshell provides an excellent opportunity to test this kind of entry, since this method will most likely be used on a manned lander.
Each lander has a mass of 89.63 kg and after the release of the deceleration mechanisms, the remaining mass of the ground stations is 43.65 kg. The ground stations are all equipped with 2.55 m^2 solar cells: the systems require 200 Wh during the day and 1,000 Wh during the night for operations of all instruments and subsystems. To provide this power during daytime, a lithium ion battery pack is used, and passive thermal control is applied to ensure proper operation temperatures for all systems.
To gather the mission data, a number of instruments are installed on the ground stations. For temperature and wind velocity measurements, three booms are installed. Temperature is measured in the tip of these booms using a platinum RTD. Wind velocity is measured using hot film anemometry. Three of such booms are installed spaced at 120° from each other such that two booms face the wind at all times: this way, both wind speed and direction can be determined and the system is sufficiently redundant. A fibre optic sensor is used for atmospheric pressure measurements: these are measured on opposite sides of the ground station. An emission spectrometer is installed as well to measure atmospheric composition. Finally, on the top, a laser optic measurement device is mounted for dust content measuring and an opening provides room to measure radiation intensity through a semiconductor. These instruments all take measurements during one minute, once per hour, day and night. Each ground station transfers data to the orbiter once per day.
The orbiter makes vertical profiles of the atmosphere throughout the day. For this, three instruments are used: the SPICAM UV spectrometer (for pressure, temperature and composition measurements), the SPEX spectropolarimeter (for atmospheric composition and dust content measurements) and the Coherent Doppler Lidar (for wind measurements). These all measure multiple times per day (depending on the instrument) and once per day the orbiter transfers data to Earth. For operations of the orbiter, a total power of 409 W is required and a total solar array of 5.44 m^2 is installed to provide this.

Despite that fact that the MUUDS team has done everything possible to ensure a satisfactory result of the design process, further research is required for the actual execution of the project. This includes many tests and simulation to make sure the mission is successful.

Contents

List of Figures

List of Tables

List of Abbreviations

Abbreviation	Description
A(D)CS	Attitude Determination and Control System
AGE	Aerospace Ground Equipment
AU	Astronomical Unit
BC	Boundary condition
BER	Bit Error Rate
BPSK	Binary phase-shift keying
BOL	Beginning-of-life
BWG	Beam-Wave Guide
CCAFS	Cape Canaveral Air Force Station
C&DH	Command and Data Handling
CFD	Computational Fluid Dynamics
CG	Centre of Gravity
CIRUS	Compact Inertial Reference Unit for Space
CMG	Control moment gyro
CNSA	Chine National Space Administration
COSPAR	Committee on Space Research
COTS	Commercial off-the-shelf
CSS	Coarse Sun Sensor
Delta-DOR	Delta Differential One-way Range
DGB	Disk-Gap-Band
DL	Downlink
DoD	Dept of Discharge
DOR	Differential One-way Range
DSE	Design Synthesis Exercise
DSN	Deep Space Network
DNS	Direct Numerical Simulation
DPU	Data Processing Unit
EDL	Entry, Descent, Landing
EEPROM	Electrically Erasable Programmable Read-Only Memory
EIS	Environmental Impact Statement
EOL	End-of-life
EPS	Electrical Power System
ESA	European Space Agency
ESTO	Earth Science Technology Office
FAA	Federal Aviation Administration
FPGA	Field-programmable Gate Array
FOG	Fiber Optic Gyro
FOV	Field Of View
FTS	Flight Termination System
FY	Fiscal Year
GEO	Geostationary Earth Orbit
GN	Guidance and Navigation
GPS	Global Positioning System
GRMS	Root-Mean-Square Acceleration
GTO	Geostationary Transfer Orbit
HGA	High Gain Antenna
HIAD	Hypersonic Inflatable Aerodynamic Decelerator
IMU	Inertial Measurement Unit
I/O	Input/Output
IR	Infrared
IRU	Inertial Reference Unit
ISS	International Space Station
JPL	Jet Propulsion Laboratory
JUICE	Jupiter Icy Moon Explorer
KSC	Kennedy Space Center
LaRC	Langley Research Center
LEO	Low Earth Orbit
LGA	Low Gain Antenna
LIDAR	Laser Imaging Detection And Ranging
LLRP	Laser Risk Reduction Program
Mars-GRAM	Mars Global Reference Atmospheric Model
MER	Mars Exploration Rover
MIPS	Million Instructions Per Second
MFSS	Mini Fine Sun Sensors
MGS	Mars Global Surveyor
MOI	Mars Orbit Insertion
MRO	Mars Reconnaissance Orbiter
MSL	Mars Science Laboratory
MSU	Microwave Sounding Units
MUUDS	Martian Weather Data System
NASA	National Aeronautics and Space Administration
OBC	On-Board Computer
Ops	Operations
PRF	Pulse Repetition Frequency
QPSK	Quadrature Phase-Shift Keying
SRAM	Static Random-Access Memory
RAMS	Reliability, Availability, Maintainability and Safety
RF	Radio Frequency
RGA	Residual Gas Analyzer
RSR	Range Safety Responsibility
RST	Range Safety Tracking
RTD	Resistance Temperature Device
RTS	Range Tracking Systems
RWA	Reaction Wheel Assembly
SAD	Solar Array Drive
s/c	Spacecraft
SDST	Small Deep-Space Transponders
SF	Scale/Safety Factor
SNR	Signal to Noise Ratio
SoI	Sphere of Influence
SPEX	Spectropolarimeter for Planetary Exploration
SPICAM	Spectroscopy for Investigation of Characteristics of the Atmosphere of Mars
SRAM	Static Random Access Memory
SSPA	Solid-State Power Amplifier
SSR	Solid State Recorder
SWA	Simpson Weather Associates
TC	Temperature condition
TPS	Thermal Protective Systems
TRL	Technology Readiness Level
TT&C	Telemetry, Tracking & Control
TWTA	Travelling Wave Tube Amplifier
UD	Unidirectional
UHF	Ultra High Frequency
UL	Uplink
UV	Ultraviolet
VAFB	Vandenberg Air Force Base
VDC	Voltage Direct Current
WDE	Wheel Drive Electronics Box

List of Symbols

Symbol	Description	Unit
Greek		
β	Atmospheric scale height	[m]
γ	Flight path angle	[deg]
Δ	Increment	[-]
η	Efficiency ratio	[-]
θ	Angle local vertical and principal axis	[rad]
γ	Correlation factor to account for differences between theory and predicted instability loads	[-]
λ	Wavelength	[m]
μ	Gravitational parameter	[km^3/s^2]
ν	Poisson ratio	[-]
φ	Angle of incidence sun	[rad]
ϕ	Solar constant	[W/m^2]
ρ	Density	[kg/m^3]
σ	Stress	[MPa]
τ_{core}	Shear stress in core	[Pa]
$\tau_{max,core}$	Maximum allowed shear stress in core	[Pa]
θ	Half power beamwidth antenna	[deg]
ω	Angular velocity	[rad/s]
Roman		
A	Area	[m^2]
a	Acceleration	[m/s^2]
a	Length of beam part a	[m]
a	Semi-major axis	[km]
B	Magnetic field strength	[T]
b	Length of beam part b	[m]
BC	Ballistic coefficient	[kg/m^2]
c	Speed of light	[m/s]
C_D	Drag coefficient	[-]
CF	Circumference	[m]
cg	Centre of gravity	[m]
D	Bending stiffness	[Nm^2]
D	Data rate	[bit/s]
D	Diameter	[m]
D	Spacecraft residual dipole moment	[A$\cdot$ m^2]
D_o	Outer diameter	[m]
D_q	Transverse shear stiffness	[Pa$\cdot$t]
E	Energy	[J]
E	Young's modulus	[GPa]
e	Euler's constant	[-]
e	Off-point angle antenna	[deg]
E_R	Reduced modulus	[Pa]
F	Force	[N]
$f_{n,lat}$	Natural frequency in lateral direction	[Hz]
$f_{n,long}$	Natural frequency in longitudinal direction	[Hz]
G	Gain factor	[dBi]
g	Gravitational acceleration	[m/s^2]
G_W	Core shear modulus in transverse direction	[Pa]
H	Angular momentum	[$(kg \cdot m^2)/s^2$]
H	Height	[km]
h	Angular momentum	[Nm]
h	Height	[m]
I	Area moment of inertia	[m^4]
I	Mass moment of inertia	[$kg \cdot m^2$]
I_{sp}	Specific impulse	[s]
k	Vibrational stiffness	[N/m]
L	Length	[m]
L	Loss factor	[dB]
V	Momentum arm	[m]
L_{spring}	Length of spring	[m]
M	Margin	[m]
M	Moment	[Nm]
m	Mass	[kg]
N_0	Noise spectral density	[J]
N_X	Axial load per unit width of circumference for cylinder	[N]
P	Force	[N]
P	Power	[W]
q	Reflectivity index	[-]
R	Reaction force	[N]
r	Radius	[m]
R_A	Reaction force in A	[N]
R_B	Radius of adapter	[m]
R_B	Reaction force in B	[N]
R_L	Radius of lander	[m]
R_{LC}	Curved diameter of landers	[m]
R_M	Radius Mars	[km]
S	Transmitter-receiver distance	[m]
SF	Safety Factor	[-]
S_L	Distance between landers	[m]
T	Disturbance torque	[N]
T	Noise temperature	[K]
T	Temperature	[K]
t	Burn time	[s]
t	Thickness	[mm]
t	Time	[s]
t_{core}	Thickness of core material	[m]
t_{sheet}	Thickness of sheet material	[m]

V	Velocity	[m/s]
V	Volume	[m^3]
v_e	Effective exhaust velocity	[m/s]
Z	Sectional modulus	[m^3]
z	Distance in z-direction from origin	[m]

List of Constants

Symbol	Description	Value [1]	Unit
Greek			
γ	Isentropic expansion factor	1.2941	[-]
π	Pi	3.14159265359	[-]
σ	Stefan–Boltzmann constant	$5.67 \cdot 10^{-8}$	[$W/(m^2 \cdot K^4)$]
Roman			
AU	Astronomical unit	$149{,}597{,}871 \cdot 10^3$	[m]
c	Speed of light	299,792,458	[m/s]
G	Gravitational constant	$6.67428 \cdot 10^{-11}$	[$m^3/(kg \cdot s^2)$]
g_{Earth}	Gravitational acceleration constant Earth	9.81	[m/s^2]
g_{Mars}	Gravitational acceleration constant Mars	3.75	[m/s^2]
k	Boltzmann constant	$1.3866488 \cdot 10^{-23}$	[J/K]
M_{Earth}	Mass of the Earth	$5.9726 \cdot 10^{24}$	[kg]
M_{Mars}	Mass of the Mars	$0.64174 \cdot 10^{24}$	[kg]
M_{Sun}	Mass of the Sun	$1{,}988{,}500 \cdot 10^{24}$	[kg]
a_{Earth}	Semimajor axis of Earth	$149.60 \cdot 10^9$	[m]
a_{Mars}	Semimajor axis of Mars	$227.92 \cdot 10^9$	[m]
e_{Earth}	Eccentricity of Earth	0.0167	[-]
e_{Mars}	Eccentricity of Mars	0.0935	[-]
$r_{a,Earth}$	Aphelion Earth	$152.1 \cdot 10^9$	[m]
$r_{a,Mars}$	Aphelion Mars	$249.23 \cdot 10^9$	[m]
$v_{a,Earth}$	Minimum orbital velocity Earth	$29.29 \cdot 10^3$	[m/s]
$v_{a,Mars}$	Minimum orbital velocity Mars	$31.97 \cdot 10^3$	[m/s]
$r_{p,Earth}$	Perihelion Earth	$147.09 \cdot 10^9$	[m]
$r_{p,Mars}$	Perihelion Mars	$206.62 \cdot 10^9$	[m]
$v_{p,Earth}$	Maximum orbital velocity Earth	$30.29 \cdot 10^3$	[m/s]
$v_{p,Mars}$	Maximum orbital velocity Mars	$26.50 \cdot 10^3$	[m/s]
P_{Sun}	Power of the Sun	$3.852 \cdot 10^{26}$	[W]
R	Gas constant	188.92	[J/K/mol]
R_{Earth}	Volumetric mean radius of Earth	$6{,}371 \cdot 10^3$	[m]
R_{Mars}	Volumetric mean radius of Mars	$3{,}389.5 \cdot 10^3$	[m]
R_{Sun}	Volumetric mean radius of Sun	$696{,}000 \cdot 10^3$	[m]
$T_{SunEarth}$	Orbital period of Earth around the Sun	365.256	[days]
$T_{SunMars}$	Orbital period of Mars around the Sun	686.980	[days]

1 | Introduction

A human mission to Mars has been out of reach for years. However, the proposals to send people to Mars are getting more serious by the day. Mars One is one of many organisations that are aiming to start a population on Mars by 2025 [2], and NASA has the ambition to land people on Mars in the mid 2030s [3]. In other words: the human race is getting ready for the 'Next Giant Leap'. To make this mission successful, more knowledge is required on the habitability of Mars. The Martian environment is vastly unknown up to this point. The current knowledge describes the Martian environment as rather hostile for human life after all.

The purpose of this project is to map these dangers, by designing a mission that will investigate the Martian atmosphere and ground climate. The mission will collect data for two consecutive Martian years. This data contains the variables temperature, pressure, dust content, atmospheric composition, wind-speed, and radiation on possible landing sites on Mars. In addition the same parameters, except for radiation, will be analysed throughout the Martian atmosphere. The results of this mission aim to provide a clearer picture on the feasibility of manned missions to Mars. The final product of this 11 week project is presented in this Final Report. In this report, the technical facets of the design, in as much detail as possible, are presented and justified.

The structure of the report is as follows. The mission profile, mission timeline and mission requirements and constraints will be discussed in Chapter 2. The following chapters relate to different mission phases: Chapter 3 describes the launch phase, in which the launch vehicle, launch operations and control is discussed. The interplanetary trajectory, involving the timeline, departure and arrival procedures, navigation, ADCS and propulsion system, is described in Chapter 4. Chapter 5 describes the entry, descent and landing; the decoupling of the ground stations from the orbiter and the deceleration mechanisms used. Chapter 6 discusses the Martian orbit, the maintenance, ADCS and tracking. This is followed by the in-orbit operations in Chapter 7, which has the sections remote sensing, tracking and ADCS. The ground operations are discussed in Chapter 8. It consists of the general methods, instrument selection, the ground station architecture and the instruments overview. The proposal for the end-of-life strategy, divided in the launcher, de de-orbiting at Mars and the passivation of the ground stations, is described in Chapter 9. The final design, including the power system, thermal system, the command and data handling system, the telecommunication system and the structural analysis is presented in Chapter 10. In Chapter 11 all the coding and calculations are verified and validated. Furthermore, remaining issues are addressed. Chapter 12 discusses the market and stakeholder analysis. The risk and contingency management is described in Chapter 13. The budgeting; link-, mass-, power-, propellant, ΔV-budgets and the sensitivity analysis are summarised in Chapter 14. The sustainability approach is discussed in Chapter 15. Lastly, the development strategies will be presented in Chapter 16.

2 | Mission Description

This chapter provides an overview of the Martian Weather Data System mission. The mission profile includes the mission statement, mission objective and mission scope (Section 2.1). A timeline of the mission is given in Section 2.2, where the mission is described in a number of phases and subphases. These phases are used to structure the design process. Finally, some insights on the requirements and constraints of the mission are provided in Section 2.3.

2.1 Mission Profile

The mission is characterised by the mission profile. The mission profile consists of the mission statement, the mission objective and the mission scope.

The mission statement answers the questions "what will be done" and "why will this be done". It provides a direct insight for external parties and includes a common goal for all team members.

Mission Statement

The purpose of this mission is to collect data on the atmosphere and the radiation environment at the surface of Mars, as well as to provide a vertical profile of the Martian atmospheric properties. The mission was designed by a group of 9 people over a period 11 weeks. The mission is to be performed with the purpose of providing an image of the climate on Mars, in order to prepare for future human exploration. The mission has to deliver a minimum of two Martian years of atmospheric data before 2025.

The mission objective explains the goals of the mission: a number of levels the project outlines to accomplish the mission.

Mission Objective

The mission objective is to gather data on the Martian climate in order to contribute to the greater challenge of human exploration on Mars.

Finally, the mission scope describes the rough boundaries of the design: what will be designed and what not?

Mission Scope

- The project entails the design of a mission to Mars including the launch, the interplanetary transfer orbit, the landing and operative phase, in order to analyse the Martian climate according to the given requirements.
- The end-of-life mission termination is designed in such a way that the environment is minimally harmed.
- The design of the Earth's ground operations to receive mission data is not included in the project.
- Detailed execution plans, such as exact dates, are not part of the design project (although reliable estimates are made later in the report).

2.2 Mission Timeline

The MUUDS mission is divided in five consecutive phases as shown in Figure 2.1. An explanation of each phase is given below.

- **Launch**
  The system is launched from Earth using a readily available launcher. This launcher will bring the MUUDS space probe to the interplanetary orbit from which the probe starts its journey to Mars.
- **Interplanetary trajectory**
  After the launcher brings the MUUDS space probe into a Hohmann transfer orbit to Mars, the space probe will complete its interplanetary space travel once it reaches its parking orbit around Mars. From this parking orbit around Mars, the landers, also called ground pods, will be released from an orbiter, into entry, descent and landing.

- **Entry, descent, landing (EDL)**
  This phase can be divided in three subphases, all serving to guide the ground stations from the orbiter to touchdown on the Martian surface.
  - Entry of the Martian atmosphere
  - Descent to the surface
  - Landing on the surface
- **Operations**
  In the operative phase, the mission measurements are performed, both on ground and in orbit. This phase continues for at least two Martian years.
- **End-of-life (EOL)**
  At the end of the mission, it is essential that the orbiter and ground systems shut down properly and are disposed of in a sustainable way.

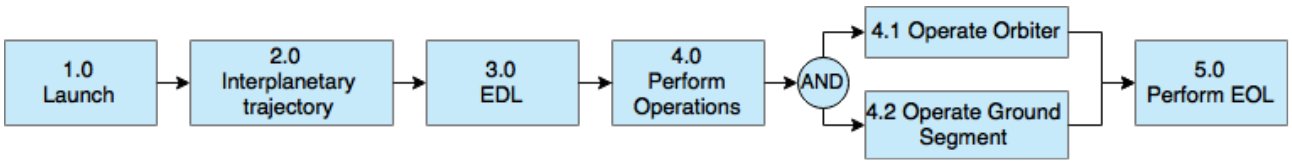

Figure 2.1: *Functional flow block diagram representing the phases in their chronological order.*

2.3 Mission Requirements and Constraints

A set of requirements was established according to the mission requirements and the requirements created throughout the initial phases of the design. These can be divided in two categories, the first set consists of requirements on how to perform the mission *technically* and the second set consists of requirements on how to perform the mission within its *non-technical* constraints.
Within the top-level requirements on how to perform the mission *technically*, the following high-level categories can be distinguished:

- **Mission control**: these requirements include those for propulsion, ADCS, and more.
- **Data handling**: this category mainly concerns the operative phase of the mission. It can be divided in the subcategories communication (throughout the mission), data retrieval and data processing.
- **General technical requirements**: in this category, the requirements concerning payload, structures and materials are situated.

The second set of requirements on how to perform the mission within its *non-technical* constraints, concern the boundaries of the design and are divided in the following categories:

- **Cost:** in this category, requirements are developed for the maximum cost of the total mission.
- **Sustainability:** in order to design a mission that is minimally harmful to the Earth and Martian environment, sustainability requirements are implied.
- **RAMS:** this category summarises the reliability, availability, maintainability and safety aspects of the system.
- **Regulations:** requirements based on space mission regulations set by international space authorities are included in this category.
- **Schedule:** this set of requirements concerns the possible launch windows.

A full list of requirements can be found in Appendix B, this list of requirements is accompanied by its status of compliance.

2.4 Preliminary layout MUUDS Spacecraft

The MUUDS spacecraft will consist of three major stages: a disposable propulsion stage, an orbiter stage for in-atmospheric measurements and communication relay, and a top fairing in which the ten landers are stacked in two levels around a central beam. The proposed preliminary design will be elaborated upon in this report.

3 | Launch

The first phase of the MUUDS mission will be elaborated upon in this chapter. After having discussed the launch vehicle which will kick-off the space journey to Mars in Section 3.1, the location and possible launch window will be examined in Section 3.2. The control techniques which will make sure that this phase is executed successfully, are scrutinised in Section 3.3.

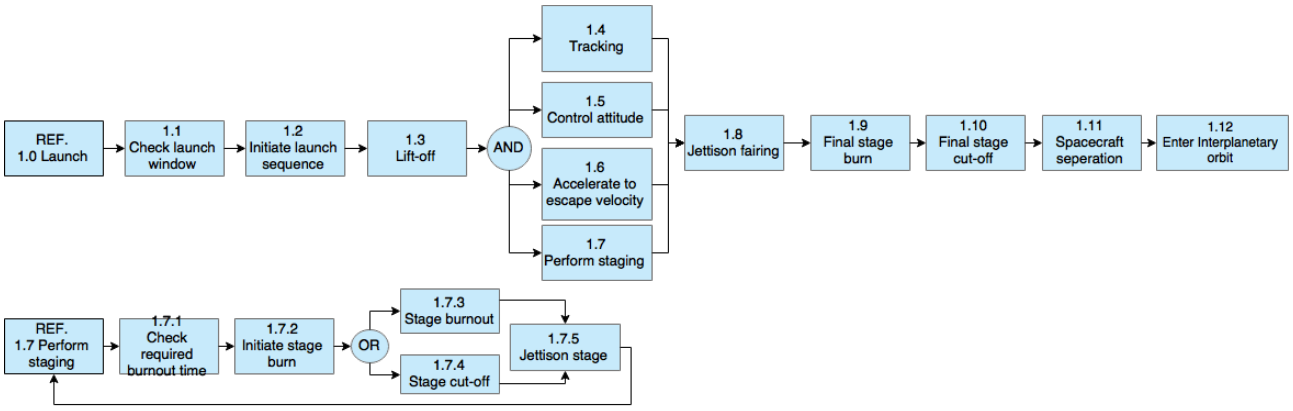

Figure 3.1: *Functional flow block diagram representing the steps undertaken during launch phase.*

3.1 Launch Vehicle Falcon Heavy

To launch the MUUDS probe into an interplanetary trajectory, a trustworthy and sustainable launcher must be chosen while still taking care of the driving requirements on fairing size, maximum launch mass and ΔV delivery. Due to the conceptual character of this mission, which needs to be placed in the context of a possible mission in the future, the availability of current launch vehicles needs to be taken into account. Trading-off these criteria for possible launchers resulted in the selection of the most feasible option: the super-heavy lift space launch system developed and maintained by Space Exploration Technologies, SpaceX. In this mission, the launch will be executed by SpaceX and the mission will rely on this service.

In Table 3.1 the most relevant and driving parameters when opting for the Falcon Heavy are shown. The allowable boundaries concerning the mass budget (mass budget of this mission can be found in Chapter 14) are now defined by a total of 13,200 kg devoted to payload mass which can be sent to Mars.

Table 3.1: *Relevant characteristics of the Falcon Heavy.*

Falcon Heavy	
Payload to Mars	13,200 kg
Standard payment plan (2016)	€ 80.1 million
Final orbit	Interplanetary transfer orbit

Extra elements in which the Falcon Heavy outshines the other competitors are its sustainability, reliability and its payload mass to launch cost ratio. The launcher scores positive points on sustainability, since current testing and progress promises the success of developing partially re-usable core boosters which have the ability to return to their designated launch pad. The Falcon 9 v1.1 boosters, used as core boosters, have already proven their reliability during previous operations. SpaceX states that this launcher will only have one-third of the operational cost of the Delta IV Heavy[1], an important factor in an industry where cutting costs is a driving parameter.

Propulsion system during launch

The Falcon Heavy relies on the design of the Falcon 9 v1.1, as shortly mentioned above. The first stage of the launcher is a liquid bi-propellant propulsion system consisting of three core boosters that are identical to the Falcon 9 v1.1 boosters. These boosters, each containing 9 Merlin 1D Engines, deliver a combined thrust

[1] Falcon Heavy: `http://www.spacex.com/falcon-heavy`

of 17,615 kN at lift-off and 20,017 kN in vacuum conditions. The 27 Merlin 1D Engines ensure that the Falcon Heavy has an excellent engine-out capability. It is able to sustain more than one unplanned engine out at any point in flight, where it will adjust to a new trajectory due to this loss accordingly and can realise that the nominal flight path is reinstated. This will be discussed in Section 3.3.

The second stage uses one Merlin 1D Vacuum Engine, which delivers a specific impulse of 340 s in vacuum conditions. The engine delivers 801 kN of vacuum thrust and can restart multiple times to bring the payload to its intended orbit (LEO, GEO, GTO and Trans-Martian orbit) [4].

Structural layout

The general layout of the Falcon Heavy can be found below in Figure 3.2[2]. Since the MUUDS design will need to fit into the launcher, the fairing volume and spacing is detrimental for consecutive design choices. The structural facet of this configuration will be discussed in more detail in Chapter 10.5.

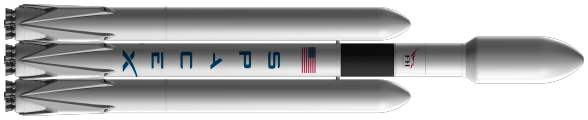

Figure 3.2: *Structural layout of the Falcon Heavy launch vehicle.*

3.2 Launch Operations

With the to be used launcher chosen, a launch location (Subsection 3.2.1) and optimal launch window (Subsection 3.2.2) is identified. The launch location will largely depend on the services SpaceX will and can provide in the near future, while the optimal launch windows form an output of the interplanetary trajectory. This will be more elaborated on in Chapter 4. It is important to note that the procedures and launch performances are not elaborated upon in this report, since the launch will be conducted by SpaceX itself. Due to the fairly new launch site, current launch schedules are not readily available yet.

3.2.1 Launch Site

Choosing the most favourable launch site for the MUUDS mission primarily depends on two factors: 1) the launch sites available to SpaceX; 2) the parameters favourable for launching interplanetary space missions. Weighing these two factors against each other resulted in selection of the following launch site: Boca Chica area of South Texas. The precise location can be found in Figure 3.3 and will remain distanced from populated areas. Operational launches using the Falcon Heavy will be expected from the year 2016 onwards.

This launch site will be the first future commercial launch site owned and built by SpaceX itself. Since the launch platform will support launches for the Falcon Heavy[3] and the company's industry will be centred in the area, costs can be reduced (this will be discussed more thoroughly in the production plan, Chapter 16). Sustainability of the launch site can be guaranteed by referring to the EIS (Environmental Impact Statement) prepared by the FAA (Federal Aviation Administration) and agreed upon by SpaceX [5]. The EIS states that no negative impact will be expected towards natural, biological, as well as human, resources.

The launch site, with coordinates [26° N , 97° W], earns its operational benefits from its location close to the equator (closer than the other operational launch sites of SpaceX), where it can profit from the higher Earth's rotational speed. A comparison with locations of other operational launch sites can be found in Figure 3.4, which represents the Earth's rotational velocity as function of latitude.

3.2.2 Launch Window

The launch window describes the time span in which the launcher can lift-off while still complying with the constraints on safety and mission objectives as stated in Chapter 2. The chosen launch window is a result of the high dependency on the most favourable trans-Martian trajectory orbit. The input and model used for the generation of the plots is further explained in Chapter 4, Section 4.1.

[2] Falcon Heavy: `http://www.spacex.com/falcon-heavy`
[3] Boca Chica: `http://www.spacex.com/about/capabilities`

Figure 3.3: *Location of the Boca Chica launch site [5].*

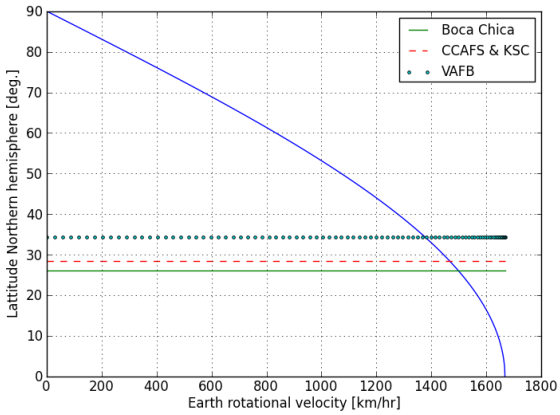

Figure 3.4: *Earth's rotational velocity as a function of latitude.*

Due to the relative motion of Mars and Earth around the Sun and the chosen Hohmann transfer for interplanetary travel, the most optimal launch window repeats itself after a specific period of time. This period is the synodic period. Assuming the planetary orbits are 2D, circular (valid assumption due to low eccentricity) and coincide with the plane in which Earth moves around the Sun (coplanar), this period can be calculated using Equation 3.1 [6]. Inserting the orbital period of Earth (τ_{p1}) and Mars (τ_{p2}) into the equation, a synodic period of 2.135 Earth years was found.

$$\tau_s = \frac{360}{(\frac{360}{\tau_{p1}} - \frac{360}{\tau_{p2}})} = \frac{360}{\omega_{p1} - \omega_{p2}} = \frac{360}{0.986 - 0.524} = 779.934\text{days} \tag{3.1}$$

Assuming the most ideal Hohmann transfer between Mars and Earth while taking into account the relative orbital velocity and the transfer time, resulted in a phase angle of 0.7109 rad between Earth and Mars at launch. This value can be computed using Equation 3.2 and filling in the parameters of Chapter 4 (θ = true anomaly ([0,2=π]), n = angular motion). This value is shown as a horizontal line in Figure 3.5. Using these results, the launch date can be computed.

$$\Psi = (\theta_{Mars} - \theta_{Earth}) - n_{Mars} \cdot t_{transfer} \tag{3.2}$$

From Figure 3.5 it can be concluded that a favourable launch window is available each 2.135 Earth years, which is the synodic period. Figure 3.5 was made using the method described in Chapter 4, in which the assumption of a circular orbit was removed and an elliptical orbit was used. The variable in Figure 3.5 is the number of years after the J2000 epoch (1 January 2000, 12:00 AM). Launching in 2018 is not a realistic goal due to development and operational constraints and a launching in 2018 can thus not be achieved in this short time interval. When opting for the launch date of 24 August 2020, a check should be done with the requirements in Appendix B. The requirement "MUUDS-Constraints-RAMS-Avail.02", which says that a minimum of two Martian years of data needs to be available before 2025, will not be met when a launch date of 24 August 2020 is selected. However, enough data will have been collected by 2025 to realise a good image of the Martian atmosphere. The exact timing and expected mission termination will be discussed more thoroughly in Chapter 16.
If one wants to meet this requirement of data availability, the design elaborated upon in this report will need to be modified. For this, systems with a high TRL combined with already operational orbiters around Mars could be used as a plausible solution.
Concluding, the MUUDS mission has shown confidence in picking 24 August 2020 as the most optimal launch date. The fuel capability of the MUUDS mission is designed to execute the nominal transfer plus extra margins (1.1 times the ΔV at arrival) that were accounted for due to non-optimal transfers executed at earlier or later epochs. The duration of an optimal launch opportunity can be found by means of Lambert targeting methods, which forms a recommendation for further investigation since it provides more accurate results when using a more sophisticated planetary ephemeris. This will result in a launch window of around 20-30 days [6]. Adding a margin of 10 days at both ends, results in a launch window ranging from 14 August 2020 till 3 September 2020.

It is important to mention that this launch window is even more restricted by the hourly constraints in which the launch can take place. The EIS states that the majority of launches are conducted between the hours of 7:00 AM and 7:00 PM. However, it is possible to have one nighttime launch per year [5].

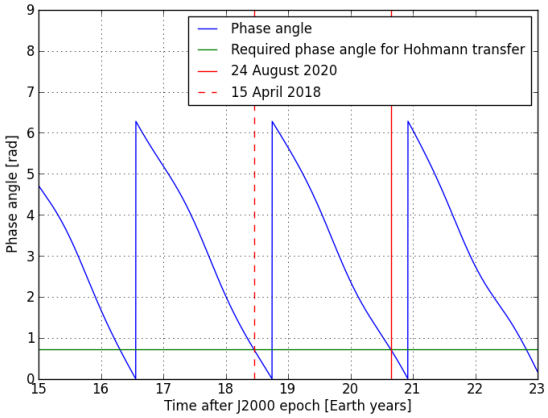

Figure 3.5: *Variation in the phase angle in years after the J2000 epoch.*

3.3 Control Systems and Tracking during Launch

As mentioned, the Falcon Heavy has proven in delivering a reliable service by conducting numerous tests as stated by SpaceX. Nevertheless, multiple factors can cause the launcher to behave differently than anticipated, e.g. thruster failure, environmental factors, etc. Thus, there is a need for tracking the launch vehicle's trajectory until it has left for interplanetary transfer (Subsection 3.3.1), for control of the vehicle in case of any abnormalities (Subsection 3.3.2), and for a safety protocol in case the launch would fail (Subsection 3.3.3).

3.3.1 Tracking Devices during Launch

In order to assess the "quality" of the launch, its path should be tracked and evaluated as being accurate and safe. This is done using Range Safety Tracking (RST).
"*The Range Safety policy is defined in the test management process and policies as a function of the specific Range, vehicle under test, mission scenario, and other safety constraints.*" [7].
This responsibility is stated in the Range Safety Responsibility (RSR), which is the range over which the path should be tracked by the three range tracking systems (RTS). In the range of RSR, the public should be protected while tyring to guarantee the success of the mission. The RSR range ends after the payload fairings are jettisoned safely [8].

Range Safety policies aim at the protection of life and property along with the assurance of mission success . The Range Safety is mission- and launcher-specific and ranges may vary due to geographical or other limitations of the particular range. Tracking is necessary to determine whether the launch vehicle complies to the preset safety range. The Falcon Heavy uses, similar to its little brother the Falcon 9, a C-band transponder for RST. For redundancy reasons, GPS receivers and inertial measurement units (IMUs) are utilised to provide position and velocity data on the launcher [4]. These three tracking systems are called the RTS. The three RTS comply with the Range Safety Group Standards, more specifically: "*a minimum of two independent tracking sources is required to assure public safety. However, additional tracking sources may provide flexibility and increase the probability of mission success.*" [7].

3.3.2 Control Devices during Launch

The flight computers on board of the launcher will process the tracking data and give inputs to the different controllers when deviations from the nominal flight path are recorded. These controllers entail the propulsion system, the valves, the pressurisation system, the separation system and the payload interfaces, which is similar to the Falcon 9.

The interactions between the tracking system and control group work are clearly visible in actions such as booster release at a predefined position in time. Mostly ground control, which determines the separation position and timing, uses the standard-issued C-band transponder after which the command is forwarded to the on-board computer. Furthermore, the corrective function of the control systems during launch is given by a deviation of the launcher from its nominal trajectory. The tracking data processed by the vehicle's computer can provide real-time analysis on whether the launcher is still following its nominal trajectory (within the allowed accuracies

[9]). If there are deviations, the computer can give a command to the propulsion system to adjust its thrusting force and direction in order to readjust the flight path to the nominal trajectory.

3.3.3 Safety Protocol in Case of a Launch Failure

If anything goes catastrophically wrong in the Safety Responsibility Range, a safety protocol should be adhered to in order to guarantee the public safety and the success of the mission. However, public safety prevails over mission success. When the launcher is still on ground level, it can be opted to shut down the launcher. When the launcher has already been launched, it should be disposed of when an irreversible deviation from the nominal path and the inability to adjust to its predetermined safe trajectory occurs.
"*The Falcon 9 launch vehicle is equipped with a standard flight termination system. This system includes two redundant strings of command receiver and encoder, batteries, safe and arm devices, and ordnance in the event of an anomaly in flight.*" [4]

In each of the abort-mission situations, one person is responsible for making a decision: the Safety Commander. This individual, supported by a team of specialists, will decide to shut down the launch or interrupt it prematurely before reaching interplanetary orbit if the safety of the mission or the public safety is endangered. Generally, a successful flight termination system (FTS) is determined by the Flight Termination Systems Commonality Standard. According to this standard, the goal of a FTS is:
"*In addition to disabling thrust, the goal of the FTS is to result in a termination action that minimizes the debris footprint. The FTS shall minimize significant lateral or longitudinal deviation in the impact point.*" [10].

The tracking data recorded by the transponders, GPS receivers and IMUs are of utmost importance in the decision making process of aborting the launch. The three RTS can provide one profile of the trajectory or provide different profiles. If all three RTS data sets converge to the same path and this path deviates from the nominal trajectory, it is almost certain that the vehicle is indeed loosing control over its path.
In case one of the RTS disagrees with the other RTS, information from the worst-case data source may be used to determine whether an action should be taken to terminate or constrain the launch flight. The extreme case of only one RTS remaining, together with the risk of producing undetectable false position data, a well thought-out decision should be taken based on general mission rules of range safety and based on the judgement of the team of Range Safety experts [10].

4 | Interplanetary Trajectory

After having left the gravity field of planet Earth, the space probe will start its long journey through outer space. The trajectory it will follow is discussed in Section 4.1 and is calculated against the background of travel duration and ΔV delivery. Next, the departure and arrival phases are discussed in Section 4.2. Interplanetary tracking, manoeuvring and propulsion are covered in Section 4.3, Section 4.4 and Section 4.5, respectively.

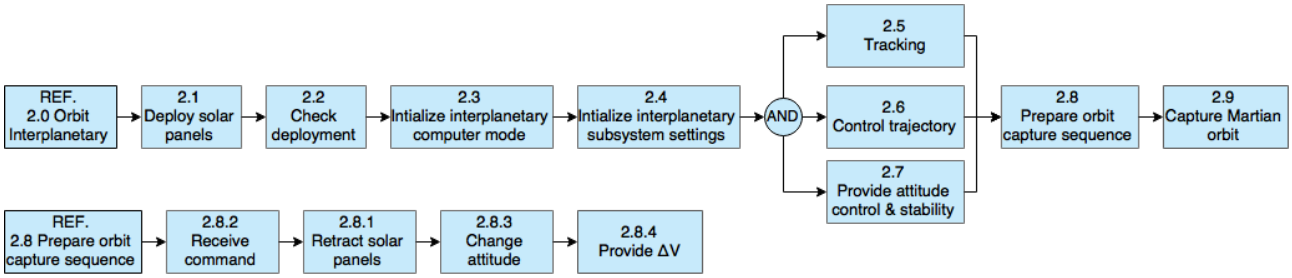

Figure 4.1: *Functional flow block diagram representing the steps undertaken during the interplanetary phase.*

4.1 Trajectory Timeline

Throughout this section the interplanetary journey of the space probe will be examined and determined. The used model is self-built and adapted to the context of this design phase, of which all the steps can be found in Subsection 4.1.1. Using this tool the transfer orbit can be designed (Subsection 4.1.2), and mission characteristics can be derived (Subsection 4.1.3).

4.1.1 Model Implementation

The model which serves as a basis for the calculations of the interplanetary trajectory and the launch window, is a tool valid for making first order calculations, which is valid in the scope of this research. It provides a help in iterating and relating parameters such as orbital radius, velocity and true anomaly in time.

Model input

In order to be able to simulate the orbits of Mars and Earth around the Sun and to be able to perform calculations which are influenced by planetary characteristics. Data on planetary characteristics is retrieved from the NASA Fact Sheet Database[1]. This database forms a reliable, up-to-date source when considering the accuracies required.

To initialise the model in time, a starting point needs to be defined where the exact position at that instant of time is noted. The planetary orbital elements of Reference [11] are used, which refer to the mean ecliptic and equinox of J2000 at the J2000 epoch, starting on 1 January 2000, 12:00 AM. The main characteristics of the planet Mars and Earth are stated in Table 4.1.

Table 4.1: *Orbital characteristics at J2000 epoch.*

Orbital element	Earth	Mars
Ω, Right ascension of ascending node	348.739°	49.559°
ω, Argument of pericentre	114.208°	286.497°
M, Mean anomaly	357.517°	19.390°

Simplifications and assumptions

Since the program forms a first order approximation, it is paramount to know which deviation could occur and what the possible origin is for this offset. The assumptions on which this model is built are stated below.

1. **Coplanar movement of planets around the Sun.**
   The planetary orbits coincide with the plane of the ecliptic. The inclination of both the Earth orbit and Mars orbit will be set to zero ($i = 0°$). This results in a slightly different relative motion and position, since this inclination is considered small.

[1] NASA Planetary Fact Sheet: `http://nssdc.gsfc.nasa.gov/planetary/factsheet/`

2. **Perihelion and aphelion location of planets around the Sun coincide.** ($\mathbf{\Omega = 0°}$, $\omega = \mathbf{0°}$)
   Due to the low eccentricity values of both Mars and Earth, assuming a circular orbit is a valid simplification. To keep the elliptical orbit and order to let the perigee and apogee points coincide, the right ascension of the ascending node and the argument of pericentre are set to zero. This has proven to be helpful, since Kepler equations can now be applied to both in similar fashion. The impact of this assumption will again result in a small offset when considering the exact relative location of Mars and Earth in time.

3. **A hybrid model is used to compute the interplanetary trajectory [12].**
   This is achieved by converting the n-body problem to multiple two-body problems, of which the solution can be determined using the standard Kepler orbits. The interplanetary trajectory will be handled with a heliocentric conic section, while planetary trajectories will be solved using a patched-conic model. The justification for making this assumption is that the radius of influence of the planets is small compared to scale of the solar system.

4. **Acceleration and deceleration will be achieved by performing an impulsive shot.**
   The ΔV delivered will be assumed to be significantly smaller than the time the spacecraft remains in the sphere of influence of the planet under consideration. Since the burn time of the rocket will be longer than a small instant, the position and velocity profile will vary in time causing a deviation of this more ideal model.

It is important to note that all planets will move in the same direction around the Sun, as given by the true anomaly direction convention. However, this is not implemented in the model.

Model layout

In Figure 4.2 the structure and functionality of the model used to simulate the interplanetary trajectory is shown, followed by an overview of the methods used to link the different boxes.

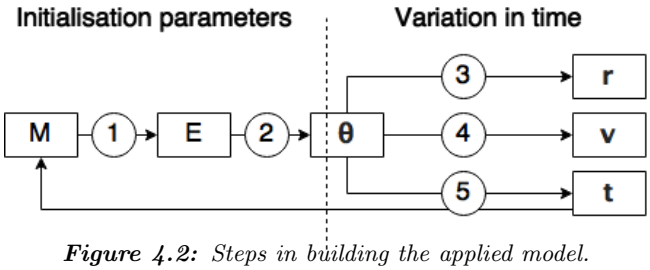

Figure 4.2: *Steps in building the applied model.*

- **Step 1:** Mean anomaly (M) → Eccentric anomaly (E):
  To compute the true anomaly (θ) with the mean anomaly as an input, the eccentric anomaly is needed. This value can be found by applying the Newton-Raphson method which is shown in Equation 4.1 [11]. In this equation $E_k = M$ is chosen as first approximation for both values.

$$E_{k+1} = E_k - \frac{E_k - e \cdot sin(E_k) - M}{1 - e \cdot cos(E_k)} \tag{4.1}$$

- **Step 2:** Eccentric anomaly (E) → True anomaly (θ) :
  In order to compute the true anomaly (θ) when the eccentric anomaly is known, Equation 4.2 can be used by solving for θ. To implement the second assumption, the true anomaly in the 3D case (obtained from Table 4.1 and Equation 4.1) needs to be transformed into the true anomaly in 2D ($i = 0°$), for which the pericentres of the orbit of Mars and Earth coincide. The steps which show these simplifications are presented in Figure 4.3a to Figure 4.3c. This is done by taking the result from Equation 4.2 and plugging it in Equation 4.3.

$$tan\left(\frac{\theta}{2}\right) = \left(\frac{1+e}{1-e}\right) \cdot tan\left(\frac{E}{2}\right) \tag{4.2}$$

$$\theta_{model} = \theta_{2D,uncorrected} - \omega - \Omega \tag{4.3}$$

- **Step 3:** True anomaly (θ) → position ($\vec{r}$) :
  Using the Kepler equation (Equation 4.4), the distance from the focal point (Sun) can be calculated. The inputs in the equation are the standard Keplerian orbital elements which pertain to the heliocentric orbit of the planets and the satellite around the Sun [11].

$$r = \frac{a \cdot (1 - e^2)}{1 + e \cdot cos(\theta)} \tag{4.4}$$

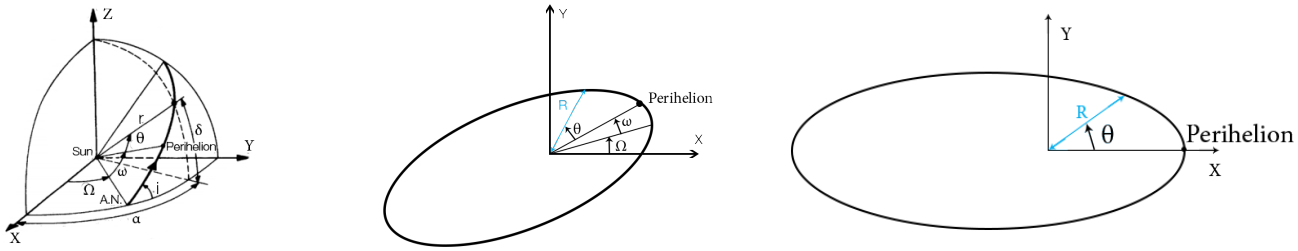

(a) $i \neq 0°$, $\Omega \neq 0°$, $\omega \neq 0°$. *(b)* $i = 0°$, $\Omega \neq 0°$, $\omega \neq 0°$. *(c)* $i = 0°$, $\Omega = 0°$, $\omega = 0°$.

Figure 4.3: *3D, coplanar, and corrected coplanar axis systems used for the trajectory model.*

- **Step 4:** True anomaly (θ) → velocity ($\vec{v}$) :
  Using the vis-viva equation (Equation 4.5), the velocity vector in each point of its orbit around the focal point (Sun) can be calculated. The inputs are similar to those in Step 3. In order to be able to decompose the velocity vector into Cartesian coordinates, the flight path angle γ needs to be calculated using Equation 4.6 [11].

$$V^2 = \mu \cdot \left(\frac{2}{r} - \frac{1}{a}\right) \tag{4.5}$$

$$\gamma = \frac{e \cdot sin(\theta)}{1 + e \cdot cos(\theta)} \tag{4.6}$$

- **Step 5:** True anomaly (θ) ↔ time (t) :
  To solve for time when the true anomaly is known, the eccentric anomaly first has to be obtained from Equation 4.2. Afterwards the time can be extracted from Equation 4.7, in which τ is the time of last pericentre passage. Knowing the time and orbital parameters, the mean anomaly can be computed using Equation 4.7, after which this value can be used as an input for Step 1 and Step 2 in order to obtain the true anomaly.

$$E - e \cdot sin(E) = \sqrt{\frac{\mu}{a^3}} \cdot (t - \tau) = n \cdot (t - \tau) = M \tag{4.7}$$

4.1.2 Interplanetary Transfer Orbit

As discussed in assumption three, the problem will be tackled by splitting up the n-body problem into multiple two-body problems. In order to do so, the sphere of influence (SoI) of the celestial bodies under consideration needs to be determined by implementing Equation 4.8. Where the Sun is assumed to be the 3rd-body perturbation body when considering the planet-spacecraft system. This results in a SoI for Earth and Mars of $5.8{\cdot}10^5$ km and $9.3{\cdot}10^5$ km, respectively.

$$r_{SoI,planet} = r_{3rd} \cdot \left(\frac{M_{planet}}{M_{3rd}}\right)^{0.4} \tag{4.8}$$

In Figure 4.4 the effective acceleration of Mars, Earth and Sun are represented as a function in time. The intersection points of the effective accelerations of the Sun with Mars and Earth, represents the area where a spacecraft would enter the sphere of influences of Mars and Earth. The operations executed in the SoI of Earth will not be treated in the scope of this report, since the MUUDS mission will rely on the service provided of SpaceX for this. The mission in the SoI of Mars will be dealt with in more detail in Chapter 6.
From Figure 4.4 it can be concluded that the Sun will be the main perturbing body for interplanetary trajectory. While trading-off the most feasible interplanetary trajectory, the urge of complying to top-level requirements and design options played a significant role during the process. A compromise needed to be made between transfer time and ΔV delivery. Choosing for low-thrust propulsion, results in not meeting the requirements of providing measurement data for at least two Martian years before 2025. Choosing fast trajectories will require a higher ΔV delivery, resulting in a too heavy space probe, which does not comply with the sustainability approach of the mission. As golden mean, the Hohmann transfer turned out to be the most feasible outcome.

The characteristics of a Hohmann transfer using the described model can be found in Table 4.2. In Figure 4.5, the Hohmann transfer is visually represented together with the departure and arrival positions of Mars and Earth. This is a first order estimation made using the model which is based on assumptions and simplifications. Therefore, extra margins are implemented during the propulsion sizing.

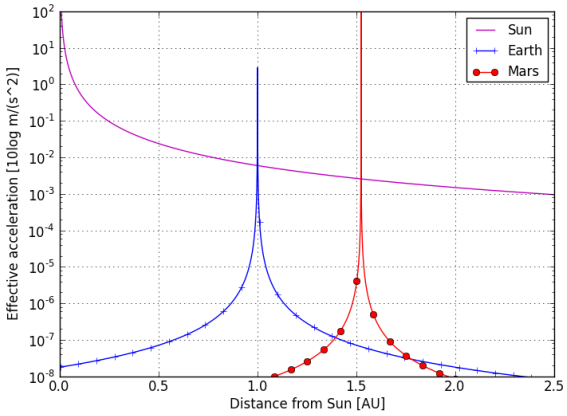

Figure 4.4: *Effective accelerations of planets in solar system.*

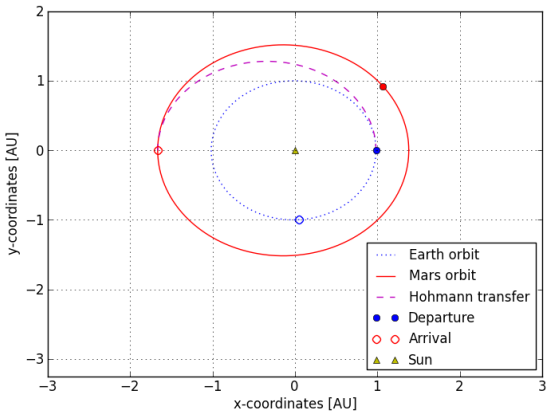

Figure 4.5: *Ideal Hohmann transfer from Mars to Earth.*

Table 4.2: *Transfer orbit characteristics of Hohmann transfer from Earth to Mars.*

Optimal Hohmann transfer orbit characteristics		
i	Inclination	0°
e	Eccentricity	0.258
a_{trans}	Semi-major axis	$198.16 \cdot 10^6$ km
$r_{trans,p}$	Distance perihelion in transfer	$147.09 \cdot 10^6$ km
$r_{trans,a}$	Distance aphelion in transfer	$249.23 \cdot 10^6$ km
$V_{trans,p}$	Heliocentric velocity at departure position	30.29 km/s
$V_{trans,a}$	Heliocentric velocity at arrival position	21.97 km/s
T	Transfer time	278.42 days

4.1.3 Mission Characteristics

With the shape of the interplanetary trajectory set, several properties can be determined which could lead to significant design consequences of the subsystems, e.g. solar panel and battery sizing, as well as communication subsytem design. Based on the trajectory shown in Figure 4.5, the properties related to the relative position of the planets will be discussed. It is important to note that the relations below do not take into account the relative motion of the space probe around Mars. Therefore, extra limitations are implemented in Chapter 6.

Figure 4.7 provides a good overview of the distance of the space probe from the Sun when assuming that Mars does not lie in its line of sight. The power flux is presented in the same graph, which becomes important when sizing the power subsystem. In order to simulate the disturbances that are acting on the MUUDS space vehicle, Figure 4.6 is plotted. With the help of this plot, the ADCS can be sized. The sudden shift in solar radiation acceleration can be explained due to the separation of the landers from the probe causing a loss in surface area. This will be explained later on.

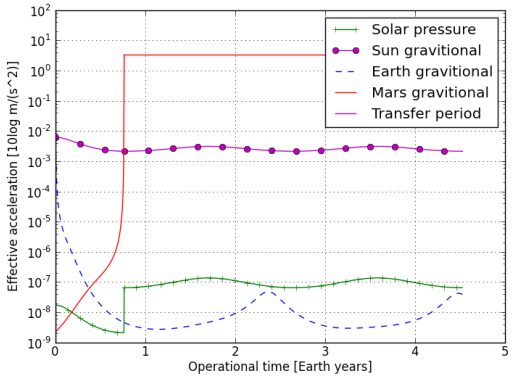

Figure 4.6: *Disturbance accelerations in function of in service operations.*

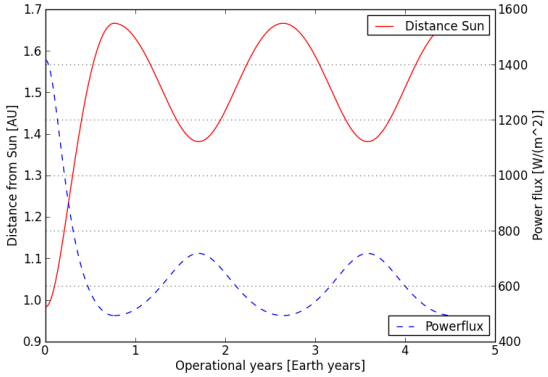

Figure 4.7: *Distance of Sun-space probe and its variations in power flux.*

To be able to size for, among others, the communication systems and data handling components, the absolute distance between Earth and Mars needs to be determined. Deriving the communication time is possible by combining the speed of light c and the Earth-Mars distance. A solar conjunction will take place each 2.14 Earth years (the synodic period), in which the Sun will line-up with Earth and Mars with the consequence of no communication means. Figure 4.8 shows the section of the Martian orbit in which no communication is possible. Reference [13] states that an angle of 5° needs to be accounted for on both sides, although basic geometry will suffice as well. From Figure 4.9 it can be concluded that the period of solar conjunction will result in a no communication time interval of about 10 Earth days.

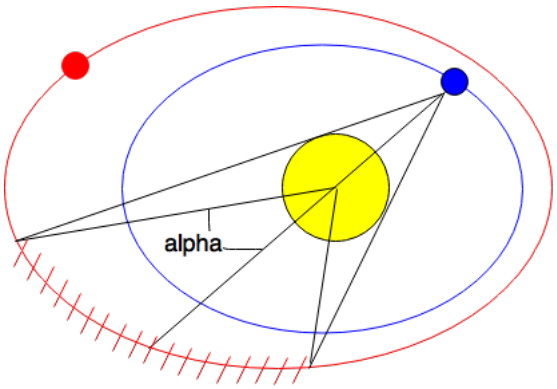

Figure 4.8: *Solar conjunction angle.*

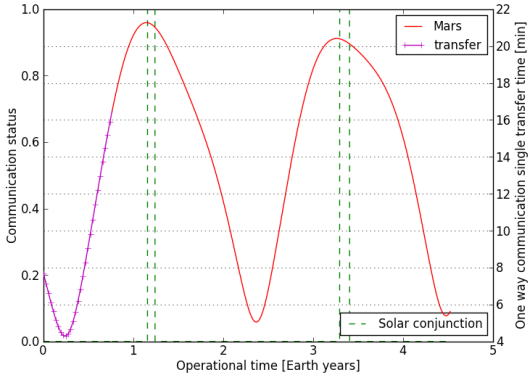

Figure 4.9: *Communication time Earth-Mars with solar conjunction periods.*

4.2 Departure and Arrival Procedures

Operations in the SoI of Mars (planetocentric approach) will be discussed in Chapter 6, but the connection between the interplanetary trajectory and Mars orbit first needs to be clarified. Only the arrival procedure will be discussed in this subsection, since 1) the operational steps from launch till the insertion into Martian transfer orbit will be issued by SpaceX, 2) computations are analogue to the arrival computations. Using parameters from Table 4.2 in combination with the schematic diagrams described in Figure 4.10 and 4.11, the ΔV required to inject into a Martian orbit will be calculated.

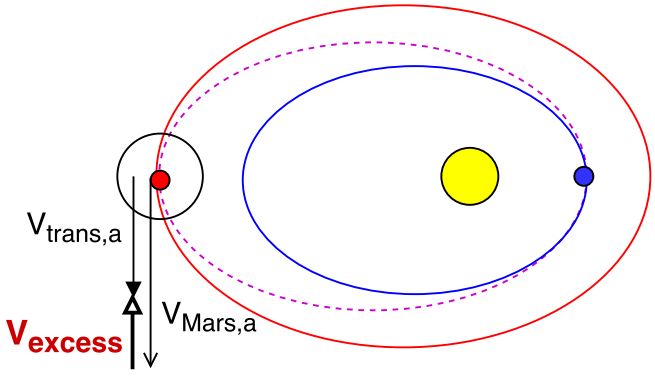

Figure 4.10: *ΔV component for insertion circular orbit Mars.*

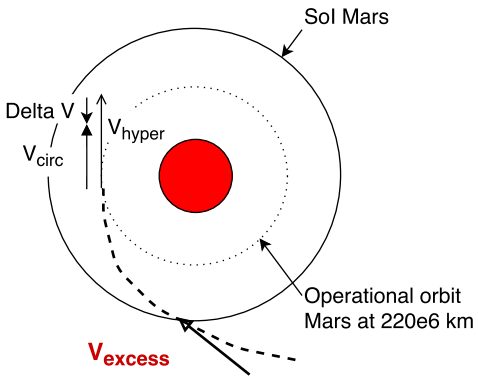

Figure 4.11: *Velocity components at arrival Mars from heliocentric orbit.*

The variables which determine the range of orbits around the arrival planet are the excess hyperbolic velocity, the right ascension and the declination of the approaching relative velocity vector [6]. Due to the scope of this project only the effect of the excess hyperbolic velocity, V_∞, will be examined. The ΔV delivery mechanisms will be sized in Section 4.5, while for this computation it will be examined as an impulsive shot.

In Figure 4.10, the heliocentric model is considered from which the excess velocity can be calculated, which is the velocity needed to escape the gravity field of Earth. In order to capture the Martian gravity field a deceleration is needed by providing a ΔV tangential to its orbit in opposite direction of flight; this results in a ΔV of 1.86 km/s which can be computed using the equations mentioned in Table 4.3.

Table 4.3: *ΔV computation during arrival steps of in-orbit insertion around Mars.*

Parameter		Expression	Velocity
$V_{Mars,a}$	Heliocentric velocity Mars at arrival	$\sqrt{\mu_{Sun} \cdot \left(\frac{2}{r_{Mars,a}} - \frac{1}{a_{Mars}}\right)}$	21.971 km/s
V_{circ}	Planetocentric velocity circular target orbit Mars	$\sqrt{\frac{\mu_{Mars}}{r_{Mars,orbit}}}$	3.444 km/s
$V_{trans,a}$	Heliocentric velocity transfer orbit at arrival	$\sqrt{\mu_{Sun} \cdot \left(\frac{2}{r_{Mars,a}} - \frac{1}{a_{transfer}}\right)}$	19.882 km/s
V_{∞}	Excess velocity at Mars arrival	$\lvert V_{trans,a} - V_{Mars,a} \rvert$	2.089 km/s
V_{hyper}	Velocity in pericentre of hyperbola at Mars	$\sqrt{\frac{2 \cdot \mu_{Mars}}{r_{Mars,orbit}} + V_{\infty}^2}$	5.301 km/s
ΔV	**Manoeuvre velocity in pericentre around Mars**	$\lvert V_{hyper}$ **-** $V_{circ} \rvert$	**1.856 km/s**

4.3 Navigation and Tracking

When navigating through deep space towards Mars, knowledge on the position and velocity of the space vehicle should be available. This knowledge can be used to assess whether the transfer probe still pursues its designed interplanetary trajectory.

Two main types of systems are used to follow the path of the spacecraft: on-board sensors and tracking/surveillance sensors. The on-board sensors provide information on the spacecraft's navigation by performing measurements within the vehicle itself. The tracking and surveillance sensors interact with Earth-based ground systems. Only active tracking sensors in combination with on-board sensors will be used to obtain navigation data on the space vehicle through its interplanetary orbit, since passive Earth-based surveillance sensors are restricted to a GEO orbit to accurately track a space probe.

4.3.1 On-board Sensors

Sensors on board of the spacecraft should be able to acquire data on the vehicle's position and its trajectory velocity. To this purpose, accelerometers are positioned inside the craft's structure. This way, an indication of the accelerations the vehicle is experiencing in all directions can be provided. Based on these accelerations and the velocities coupled to these accelerations, the position of the space probe can be determined based on the designed trajectory.
A total of four 3-axis accelerometers will be taken on board the space probe. The four accelerometers are positioned in pairs. The first pair is used "*to provide for self-aligning, enduring and sophisticated navigational capability. A second pair of accelerometers is added for redundancy and added sensitivity. Each pair of accelerometers are disposed at diametrically opposed positions and respective axes are co-aligned*" [14]. They will be positioned in that part of the vehicle that will remain in orbit around Mars as the orbiter satellite.

The accelerometers are made by Analog Devices Inc. and the specific accelerometer used on the space vehicle is the ADXL377. These sensors are small, consume few power, and can measure accelerations up to ± 200 g. In addition, they have a shock resistance of 10,000 g. Important technical specifications are listed in Table 4.4[2].

Table 4.4: *Technical specification of the ADXL377 accelerometers used on the space probe [15].*

Accelerometer ADXL377	
Size	3 mm × 3 mm × 1.45 mm
Mass	41 mg
Measurement range	± 200 g
Shock resistance	± 10,000 g
Operating voltage range	1.8 V - 3.6 V
Supply current	300 μA
Turn-on time	1 ms
Power	0.54 mW - 1.08 mW
Operating temperature range	-40 °C - +85 °C
Storage temperature range	-65 °C - +150 °C

The accelerometers will thus consume at most 4.32 mW of the power budget and 164 mg of the mass budget. These budgets can be consulted in Chapter 14.

[2] ADXL377: `http://uk.farnell.com/analog-devices/adxl377bcpz-rl7/accelerometer-3axis--200g-16lfcsp/dp/2250677`

4.3.2 Active Tracking Sensors

Active tracking sensors, Earth-based, are used to track whether the space probe is still following its predetermined trajectory. These sensors will interact with the spacecraft that is being tracked. The active tracking sensors that will track the MUUDS space probe are the antennas of the Deep Space Network.

This network is selected for deep-space communication, navigation and tracking of the space vehicle since it provides the possibility of constant observation and communication between Earth and deep-space probes. This is achieved by the strategic position of the three ground stations, which are positioned at approx. 120° longitude of each other. The ground stations are located in Canberra (AU), Robledo de Chavela (ES) and Barstow (CA, USA). Each of the DSN sites has multiple large antennas, to be more specific at least four. "*Each [site is] equipped with large, parabolic dish antennas and ultra-sensitive receiving systems capable of detecting incredibly faint radio signals from distant spacecraft*"[3].
In addition to providing constant observation possibilities, the DSN can determine the position of a deep-space vehicle with an accuracy of 1 nrad at a certainty level of $3\,\sigma$. This corresponds to an accuracy of 150 m at a distance of 1 AU.
A last asset of the Deep Space Network is that it can track deep-space missions to the edges of the solar system, up to 16 billion km. The DSN is thus a tool to track, navigate and telecommand the MUUDS spacecraft [1].

To achieve an interaction between the DSN and the MUUDS space probe, the space probe should be equipped with transponders. A transponder has several functions [16]:

- "*transmit/receive function: translates digital electrical signals (ones and zeros used by the computer) into radio signals for sending data to Earth, and translates radio signals to digital electrical signals for receiving commands from Earth*",
- "*transponding function: listens for and detects a signal coming in from Earth, to which it automatically responds*",
- "*navigation function: transmits several types of signals that provide critical navigation clues, enabling navigators on the ground to make precise calculations of the spacecraft speed and distance from Earth*".

For the space probe tracking in interplanetary transfer phase, the focus will lie on the two latter functions: transponding and navigation.

Two Small Deep-Space Transponders (SDST) are incorporated in the spacecraft structure. One transponder would suffice for telecommand, telecommunication and tracking during interplanetary space travel. However, a second unit is installed as a redundancy.
The SDST chosen for the MUUDS space probe are the Small Deep-Space Transponders developed by General Dynamics and NASA's Jet Propulsion Laboratory. These transponders have been used in the past on the Mars Reconnaissance Orbiter (MRO) for interplanetary cruise navigation and proved to be reliable systems when using the X-band for telecommunications (the Ka-band link failed). These SDST of General Dynamics are compatible with the Deep Space Network [17] [18].
The SDST transponders have two possible configurations: X/X configuration and X/X/Ka configuration. Since the Ka-band proved to be not fully reliable in the MRO mission, the X/X configuration is selected. Detailed technical specifications of the SDST are listed in Table 4.5 [18].

Table 4.5: *Small Deep-Space Transponder used during interplanetary space travel for tracking, telecommunications, and telecommand [18].*

Small Deep-Space Transponder X/X configuration	
Size	118.1 mm × 166.37 mm × 114.3 mm
Mass	3.2 kg
Operating voltage range	22 VDC - 36 VDC
Power	15.8 W
Operating temperature range	-40 °C - +60 °C
X-Band uplink	7.145 GHz - 7.235 GHz
X-Band downlink	8.400 GHz - 8.500 GHz
Noise figure	$<$ 3.2 dB
Minimum tracking range	$\pm$ 200 kHz
Command data rates	7.8125 bp - 4,000 bps
Modulation modes	subcarrier, BPSK, QPSK
Telecommunications data rates	15 Mbps (BPSK) - 100 Mbps (QPSK)
Differential One-way Ranging tones	19.2 MHz

[3] DSN: `http://deepspace.jpl.nasa.gov/about/DSNComplexes/`

Only one transponder will be in use at a time, the second transponder will only be turned on if the first transponder fails. The nominal power usage of the transponder system is 15.8 W, taking up a significant part of the communications and command & data handling power budget discussed in Chapter 14. Their mass will accumulate up to 6.4 kg.

With the transponders selected as a means to acquire position and velocity data during interplanetary transfer, the way they acquire this data should be highlighted as well.
The method used by the transponders to gather three-dimensional position and velocity data is called "Delta-DOR", or Delta Differential One-way Range. Two widely-spaced[4] antennas on Earth, more specifically the antennas of the DSN, simultaneously track the MUUDS space probe on its interplanetary journey. The MUUDS probe is transmitting a signal, which is a sequence of frequency-spaced tones. The signal transmitted by the MUUDS SDST transponders are dedicated X-band DOR tones, specially transmitted with the purpose of Delta-DOR ranging. The name "One-way Range" thus is about the one-way signal being transmitted by the transponder, there is no Earth-transmitted and transponded signal [19].

Because two widely-spaced antennas receive the signal, it is possible to determine the delay time of the signal. The delay time is the time difference between signals arriving at the two stations. In theory, "*the delay depends only on the positions of the two antennas and the spacecraft*" [19]. In reality, there are numerous sources of error that affect the delay: the Earth atmosphere interferes with the radio signal transmitted by the transponder and clock instabilities at the ground station can also be a source of error.

To mitigate this error, a "quasar" close to the space vehicle is tracked for calibration (see Figure 4.12). The location of this quasar is known to a high degree of accuracy, typically 50 nrad. The quasar is chosen within 10° from the spacecraft such that their signal paths through the Earth atmosphere are similar and thus comparable. When the quasar is tracked, a noise signal from this quasar is received by the widely-spaced Earth antennas. Since all three positions - of the two antennas and the quasar - are accurately known, the delay time of the quasar can be calculated with a high degree of accuracy. Once the delay time of the quasar is determined, the antennas reposition themselves to track the spacecraft once again. The uncalibrated delay time of the spacecraft is determined after which the delay time of the quasar is subtracted from the spacecraft's delay time. This results in the Delta-DOR measurement [19].

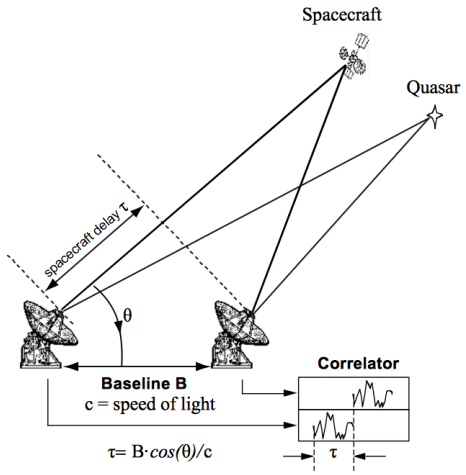

Figure 4.12: *Delta-DOR observation geometry between the Deep Space Network and the Small Deep-Space Transponders of the MUUDS spacecraft [20].*

An important remark is that the quasar and the spacecraft cannot be tracked at the same time. The time that the space vehicle is in view of the antennas thus has to be divided between tracking the craft and tracking the quasar, resulting in a sequence of spacecraft-quasar-spacecraft scans. To obtain delays at the same moment in time, an interpolation needs to be performed: an interpolation between the first and third scan converts them to the same time as the second measurement from which the Delta-DOR data point is calculated [19].
From the delays and Delta-DOR data, the distance between Earth and the space probe can be calculated by multiplying the delay by the speed of light. Since the space vehicle is tracked under an angular view by two antennas, a three-dimensional position of the spacecraft on that distance can be computed, this 3D position being relative to the Earth. The velocity of the craft can be determined based on the profile sketched by the sequence of distances determined during one tracking period and the duration of that period [19].

[4]The antennas should be widely-spaced in order to reduce the angular error on the delay measurements [19]. They are thus spaced at a 120° longitude angle, thereby covering the full 360° with three DSN bases.

4.3.3 Navigation and Tracking Actuators

The sensors support the function of the actuators in the sense that the sensors gather data on the trajectory which can be processed and analysed by the Earth ground control stations. After analysis, the decision can be made to intervene and correct the path using actuators.

If the sensors record a small deviation from the nominal path and ground control assesses this deviation as an endangerment for the mission success, a command can be given to the small ADCS thrusters of which 12 are positioned on the body of the space probe. These small thrusters can provide small trajectory control forces. The thrusters are discussed more in-depth in Subsection 4.4.2. Their propellant mass and control thrust are slightly oversized in order to accommodate for these path changes in the mass and power budget, see Table 4.13.

Larger path deviations can be corrected by using the main propulsion system. These thrusters can provide larger thrust forces for trajectory control. More information on the main thrusters will be provided in Section 4.5. The ΔV budget and thus propellant mass should again be slightly oversized to incorporate sudden major trajectory changes in the mass and power budget.

4.3.4 Overview of Sensors and Actuators for Navigation and Tracking

To conclude this section, an overview of all the necessary sensors and actuators for tracking, navigation and trajectory control are given in Table 4.6.

Table 4.6: *Sensors and actuators for navigation and tracking during interplanetary transfer orbit.*

ADCS System for Interplanetary Transfer Orbit		
Sensor	**Mass per system**	**Power per system**
3-axis accelerometers (4x)	$0.164 \cdot 10^{-3}$ kg	$4.32 \cdot 10^{-3}$ W
Small Deep-Space Transponders (2x)	6.4 kg	15.8 W
Actuators	**Mass**	**Power**
MR-111C thrusters (12x)	9.92 kg	13.64 W
Total	16.32 kg	29.44 W

4.4 ADCS during Interplanetary Space Travel

During interplanetary transfer, the space probe should maintain a certain attitude to a certain degree of accuracy. Different *actuators* can be used for *attitude control* of the MUUDS spacecraft. The methods and systems most commonly used are: spin stabilisation, reaction wheels, momentum wheels, control moment gyros (CMG), magnetic torquers and thrusters. Often, reaction wheels and momentum wheels are combined systems, called momentum and reaction wheels assemblies.

For an actuator to perform its stabilising function, a sensor should first record whether the craft is drifting away from its desired attitude. *Sensors* commonly used in space missions for *attitude determination* are: Sun sensors, star sensors, horizon sensors, magnetometers, GPS receivers and gyroscopes [21].

Key is to identify the most suitable sensor(s) and actuator(s), and size them, for attitude determination and control (ADCS) during interplanetary space travel to counteract the external and internal disturbance torques and achieve a 3-axis stabilised spacecraft.

External disturbance torques encountered during interplanetary space travel are solar radiation pressure disturbances, and to a negligible amount gravity gradient and magnetic field disturbances. Atmospheric disturbances can be fully neglected, since there is no atmosphere present during transfer orbit [21]. The only external disturbance torques thus considered are solar radiation pressure torques.
Internal disturbance torques that should be accounted for are an uncertainty in the centre of gravity, thruster misalignment, rotating machinery, thermal shocks and liquid sloshing [21].

Key will be to identify which external and internal disturbance torques will be driving for the sizing of the actuators.

4.4.1 Sensors for Attitude Determination

To perform attitude control over a space vehicle, it is required to know its attitude. *Attitude determination* is the process of determining the space probe's attitude with respect to a certain reference. If the *sensors* record that the attitude of the space probe is diverging from its nominal attitude, outside its accuracy boundaries, then the *attitude controllers* or *actuators* should interfere.

The space probe is already equipped with accelerometers for trajectory tracking and navigation. If these four ADXL377 accelerometers are used in combination with three gyroscopes, an inertial measurement unit (IMU) is created. This IMU is able to measure the speed or angle of rotation from an inertial reference, together with position and velocity data, but without any knowledge on the absolute reference frame. When gyros are used in combination with external sensors such as a star tracker or Sun sensor, precision attitude determination becomes possible and an external, absolute reference frame can be decided upon [21].
Thus, it is necessary to take on board at least three gyroscopes and one star/Sun sensor.

Three gyroscopes will suffice to determine the spacecraft's attitude. However, a fourth gyro is added for the sake of redundancy. If three to four gyroscopes are grouped together, they form an *inertial reference unit* (IRU). The inertial reference unit that will be included on the MUUDS spacecraft is the Compact Inertial Reference Unit for Space (CIRUS) IRU manufactured by L-3 Space and Navigation. CIRUS features four Fiber Optic Gyro (FOG) sensors in a fully redundant configuration for spacecraft attitude control. This small size and low cost IRU enables mission-critical precision pointing. CIRUS is used in numerous space missions of today in which it has proven its performance and reliability, since L-3 Space and Navigation has been the premier supplier of this type of systems. The most important technical specifications of the CIRUS IRU are listed in Table 4.7 [22].

Table 4.7: *Compact Inertial Reference Unit for Space (CIRUS), inclu. 4 Fiber Optic Gyros [22].*

Compact Inertial Reference Unit for Space (CIRUS)	
Size	Ø 396.2 mm × 203.2 mm
Mass	13.5 kg
Operating voltage range	28 V - 70 V
Power	25 W
Reliability	>0.98 Ps^5 for 15 y life, continuous operation
Operational temperature	-20°C - +60°C
Total radiation dose tolerance	>100 krad
Random vibration	14.7 GRMS lateral, 20.8 GRMS normal

The CIRUS IRU will thus occupy 13.5 kg in the mass budget, while taking up 25 W of the power budget. Using CIRUS will result in the spacecraft being 3-axis stabilised. In combination with the four ADXL377 accelerometers, full attitude, position and velocity determination is achieved.

On a 3-axis stabilised spacecraft, star trackers can be used to derive 2- or 3-axis attitude information. Star trackers are chosen over Sun sensors, since they excel in accuracy when used in combination with gyroscopes. The spacecraft should be stabilised before the star trackers can operate effectively. After initial stabilisation by CIRUS, the star trackers in their turn provide a high-accuracy external reference frame for the inertial reference of CIRUS, which it could never determine for itself. Two star trackers will be used, such that one star tracker remains operative if the other would fail. In addition, their measurements can be compared and combined to eliminate any errors or bias [21].

Four star trackers from three different manufacturers are traded-off against each other based on certain criteria. These criteria are assigned different weights according to their importance with the most important ones having a weight of 5. The criteria and their weights are:

- **Mass.** The lower the mass, the more favourable the system becomes in light of the mass budget. (5)
- **Sun exclusion.** The ability to shade out the Sun ensures that the star tracker will not be blinded. (3)
- **Accuracy.** The higher the accuracy, the more reliable the attitude data become. (4)
- **Maximum acceleration.** The higher the acceleration, the faster the spacecraft can turn to its desired direction. However, this rate should stay within the maximum acceleration limits of the space probe. (3)
- **Power consumption.** The lower the amount of power required to operate the system, the more beneficial it is for the power budget of the spacecraft. (5)

The four star trackers are:

- CT-602 star tracker from Ball Aerospace & Technologies Corp [23].
- Rigel-L star tracker from Surrey Satellite Technology Ltd. [24].
- Procyon star tracker from Surrey Satellite Technology Ltd. [25].
- HE-5AS star tracker from Terma Space [26].

Their mass, power, Sun exclusion capability, accuracy, and maximum deceleration are traded-off against each other in Table 4.8. The best performances are assigned a score of 5, the worst a score of 1. The weighted grades are summed up to a total weighted grade for each star tracker.

Table 4.8: *Trade-off between different star trackers [23][24][25][26].*

Star Trackers									
		CT-602		**Rigel-L**		**Procyon**		**HE-5AS**	
Criterion	**Weight**	Score	Grade	Score	Grade	Score	Grade	Score	Grade
Mass	5	1	5	3	15	5	25	3	15
Sun exclusion	3	1	3	5	15	5	15	5	15
Accuracy	4	1	4	4	16	3	12	5	20
Max acceleration	3	1	3	5	15	2	6	3	9
Power	5	3	15	4	20	5	25	1	5
		Total	30	**Total**	81	**Total**	83	**Total**	64

From the trade-off, the two star trackers from Surrey Satellite Technology Ltd. appear to be the most optimal star trackers for the MUUDS space mission. There is only a slight difference in favour of the Procyon star tracker. Since the mass of the star tracker is crucial for the mass budget, the lighter Procyon is preferred over the Rigel-L. Technical specifications of the Procyon star tracker can be found in Table 4.9.

Table 4.9: *Star trackers for the MUUDS mission: Procyon from Surrey Satellite Technology Ltd.[25].*

Procyon Star Tracker	
Size	155 mm × 210 mm × 56 mm
Mass	1.75 kg
Operating voltage range	15 V - 50 V
Power	6.5 W
Operational temperature	-20°C - +50°C
Total radiation dose tolerance	>5 krad
Lifetime	7.5 y in LEO
Attitude acquisition time	8 s
Accuracy	X/Y <5 arcsec (1σ)
	Z <30 arcsec (1σ)

Two Procyon star trackers will be taken on board of the MUUDS space probe, thereby taking up 3.5 kg of the mass budget and 13 W of the power budget (Chapter 14). However, only one star tracker is operational at a time, the second star tracker being a redundant system that is turned on when the first one fails. The nominal power usage of the star tracker system is thus 6.5 W.

The Procyon star trackers, the CIRUS inertial reference unit and the four ADXL377 accelerometers will work together to 3-axis stabilise the space probe and will provide attitude determination about all axes of the craft.

4.4.2 Actuators

When the attitude determination systems detect that the spacecraft is not maintaining its proper attitude, the *attitude control* or *actuators* should interfere and correct the position. A disturbance of its nominal attitude can be caused by solar pressure disturbance torques or by internal disturbance torques.

Another case can present itself, in which the Earth ground station commands the spacecraft to alter its attitude (and possibly change its interplanetary trajectory). After receiving the command, the spacecraft should be able to change the attitude as commanded by Earth. To achieve this, actuators are positioned on the spacecraft which *act* to alter the space probe's attitude. These can be divided into two main categories, being passive and active actuators.
Active actuators will actively change the spacecraft's attitude. These actuators are thrusters, momentum wheels, reaction wheels, control moment gyros (CMGs), spin stabilisation and magnetic torquers [21].
Passive actuators are changing the attitude of the spacecraft. Two passive control mechanisms are gravity-gradient and passive magnetic stabilisation [21].

Only active control systems will be used for the spacecraft. Passive control mechanisms are considered too unreliable since information on the interplanetary gravity-gradient and magnetic forces is scarce. In addition there is no need for passive stabilising actuators, since the spacecraft is 3-axis stabilised by the combination of accelerometers, IRU and star trackers.

Reaction wheels assembly

A system to control the attitude of the space probe about three axes is required. Therefore spin stabilisation is ruled out, since this type of attitude control can only stabilise the spacecraft about one axis. Control moment gyros are relatively expensive systems with a short lifetime compared to other attitude control systems. Since the magnitude of a magnetic field in deep space is unsure, magnetic torquers become unreliable systems since they only work if there is a magnetic field to react against [21].

With these actuators being ruled out, the choice is left between momentum and reaction wheels. The choice is made to use reaction wheels since they can spin in either direction and can actively cause the vehicle to rotate. By using at least three reaction wheels, attitude change and stability can be achieved about three axes. Momentum wheels are capable of providing stability about two axes, but can not make the vehicle actively rotate about one of its axes. Since it is requested that the space probe can actively rotate to adhere to a command given by Earth to change its attitude, momentum wheels are not considered [21].

Reaction wheels are often assembled together to provide 3-axis attitude control. Four reaction wheels from Rockwell Collins are compared to a reaction wheel assembly of Moog Bradford Engineering:

- W45E reaction wheel assembly developed by Moog Bradford Engineering [27].
- W45ES reaction wheel assembly developed by Moog Bradford Engineering [27].
- HT-RSI High Motor Torque Momentum and Reaction Wheels from Rockwell Collins [28].
- RDR 68 Momentum and Reaction Wheels from Rockwell Collins [29].

They are traded-off based on the following criteria, with each criterion attributed a different weight based on its relevance:

- **Mass.** The lower the mass, the more favourable the system becomes in light of the mass budget. (5)
- **Angular momentum.** The larger the angular momentum, the more likely it becomes that the reaction wheels will be able to rotate the space probe[6]. (3)
- **Reaction torque.** The higher the reaction torque of the reaction wheel, the more likely it becomes for the spacecraft to be able to resist external/internal disturbances in attitude. (3)
- **Power consumption.** The lower the amount of power required to operate the system, the more beneficial it is for the power budget of the spacecraft. (5)
- **Size.** The reaction wheels and assembly should fit in the space probe's inner structure. The smaller the wheels, the better. (4)
- **Temperature range.** The larger the temperature range in which the reaction wheels can operate, the less thermal isolation and control is needed thus the lighter the space probe. (3)

The reaction wheels of Rockwell Collins need to be tripled in mass and size since they need to be configured in a three-wheel assembly to achieve rotation and stiffness about three axes[7]. There is no need for a fourth redundant reaction wheel in the assembly. Hariharan Krishnan, Harris McClamroch and Mahmut Reyhanoglu proved that two reaction wheels "*can be used to control the attitude of a rigid spacecraft and that arbitrary reorientation manoeuvres of the spacecraft can be accomplished*" [30].

Table 4.10: *Trade-off between different reaction wheels and reaction wheel assemblies [27][28][29].*

Reaction Wheels and Reaction Wheel Assembly									
		W45E		**W45ES**		**HT-RSI**		**RDR 68**	
Criterion	**Weight**	Score	Grade	Score	Grade	Score	Grade	Score	Grade
Mass	5	5	25	4	20	1	5	2	10
Angular momentum	3	4	12	5	15	3	9	3	9
Reaction torque	3	5	15	5	15	3	9	1	3
Power	5	3	15	3	15	4	20	4	20
Size	4	5	20	5	20	3	12	2	8
Temperature range	3	4	12	4	12	4	12	2	6
		Total	99	**Total**	97	**Total**	67	**Total**	56

The reaction wheels of Rockwell Collins and the reaction wheel assemblies of Moog Bradford Engineering are traded-off based on the aforementioned criteria in Table 4.10. Each reaction wheel option is handed a score from 1 to 5 on their performance with respect to each criterion, with 1 being the worst and 5 the best. These scores are multiplied with the weight of each criterion, resulting in a total weighted grade.

[6] An angular momentum of at least 68 Nm is needed to be able to turn a space probe of ±6800 kg, as 6800 kg is the weight of the space probe during interplanetary transfer in a current mass estimation, see Chapter 10.

[7] It is not necessary to triple the power consumption, since it is assumed that only one wheel is spinning at a time.

From the trade-off it can be concluded that the compact, lightweight W45E reaction wheel assembly of Moog Bradford Engineering is the optimal solution for attitude control of the space probe during interplanetary transfer phase of the MUUDS mission. This reaction wheel assembly will perform three-dimensional rotation of the spacecraft and will provide the control torque to correct for any external and internal disturbances. The technical specifications of this reaction wheel assembly are listed in Table 4.11 [27].

Table 4.11: *Reaction wheel assembly used on the MUUDS space probe for attitude control [27].*

W45E Reaction Wheel Assembly	
Size RWA	Ø 365 mm × 123 mm
Size WDE	81 mm × 259 mm × 181 mm
Mass	7.9 kg
Operating voltage range	28 VDC - 50 VDC
Power at nominal wheel speed	29 W
Operational temperature	-30°C - +60°C
Shock resistance	400 g - 2,000 g

ADCS thrusters

The momentum storage in the reaction wheels is cleared every once and a while. Thrusters are used to de-spin the reaction wheels and by doing so, they dump the momentum stored in the wheels. Besides providing a de-spin function during interplanetary transfer orbit, thrusters can be used to actively change the spacecraft's attitude in case a fast change is requested (faster than can be accomplished by the reaction wheels assembly).

Different types of thrusting are available today, of which the most generally used ones are cold gas thrusting, mono- and bipropellant, and electric propulsion.
To determine which type of thrusting is the most feasible for attitude control during interplanetary phase, an initial estimation of the control force required to dump the stored momentum is made. In addition, the different propulsion systems will be compared on how precise they can deliver the torque impulse.

The accuracy to which the angular momentum should be delivered is determined by the reaction wheels and other subsystems on board the space probe. In general, the control torque should be large enough to meet the slew rates of the reaction wheels, while the force associated with that torque should be large enough to achieve momentum dumping and correct for external disturbances [21]. For the MUUDS space probe, the ADCS thrusters merely have to dump the momentum of the reaction wheels as can be seen in Table 4.12. The control torque for external and internal disturbances is delivered by the reaction wheels assembly. This assembly also delivers the torque required to perform any rotation about the three axes of the space probe.

Table 4.12: *Actuators used for ACS during interplanetary space travel, and their functions.*

Actuators during Interplanetary Transfer	
Actuator	**Function**
Reaction wheel assembly	- Control torque external disturbances (solar radiation pressure torques) - Control torque internal disturbances - Slow rotation space probe about 3 axes
Thrusters	- Momentum dumping reaction wheels - Fast attitude correction, quick rotation about 3 axes

The force required by the thrusters to dump the momentum stored in the RWA is given by Equation 4.9 [1].

$$F = \frac{h}{L \cdot t} \tag{4.9}$$

In Equation 4.9, F is the thrust force required for momentum dumping, h the momentum stored in the reaction wheel, L the momentum arm of the thruster with respect to the centre of mass of the space probe and t the burn time of the thrusters.

The momentum stored in the reaction wheels h at the instant that the momentum should be dumped, is assumed to be the maximum angular momentum storage capacity of the reaction wheel. When the maximum amount of momentum is reached, a command will be transmitted to the on-board computer which will forward a command to the ADCS thrusters to give the correct thrust force. This required force F is still unknown.

Besides needing to determine the control force for attitude control, the position of the thrusters should be selected. In order to achieve maximum torque authority, a maximum arm of the thruster with respect to the

space probe's centroid should be selected (L) to maximise the achievable torque, while remaining inside the physical boundaries of the space probe. Thus, thrust force may be large but the available torque is limited by the physical extent of the vehicle plus how the thrusters are mounted [21].

From the final design depicted in Chapter 10, the maximum moment arm is 1.5 m. This value is based on the cross-sectional length of the square orbiter surface of the space probe. On this square surface, which is 3 m by 3 m long, the landers are positioned. By assuming that the space probe's centroid lies exactly in the middle of the square cross-section, the moment arm L is equal to 1.5 m. This can be seen in Figure 4.13 [31] [8].

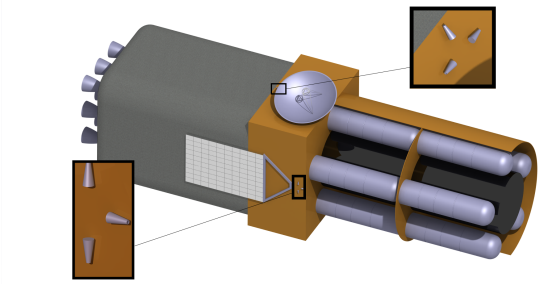

Figure 4.13: *Position of the ADCS thrusters on the MUUDS spacecraft.*

A last parameter that should be sized according to Equation 4.9 is the burn time of the thruster (t). It can be assumed that all the momentum should be dumped in a matter of seconds. For the sizing of the thruster systems for ADCS, a burn time of 2.83 s is assumed.

Using Equation 4.9, with a burn time t of 2.83 s, a moment arm L of 1.5 m and a maximum momentum storage of 68 Nm, the total thrust force required to dump the momentum is $\pm$ 16 N.

The ADCS thrusters are positioned in torque couples with the thrust force creating a torque about the three axes (see Figure 4.13). The total thrust required of 16 N to dump the stored momentum can thus be distributed over the thrusters that provide torque in the same direction. If the control thrusters are supposed to deliver the right amount of thrust in a rotation about the central beam to which the landers are attached, then four thrusters are used. Each thruster therefore has to deliver $\pm$ 4 N to achieve at least a torque force of 16 N.

Different propulsion systems exist that can be used for ADCS thrusting, with cold gas, electric, monopropellant, and bipropellant propulsion systems being the most frequently used. However, not every one of these aforementioned propulsion systems is a feasible ADCS thrusting system for the MUUDS space probe.

Electric propulsion systems will not be feasible to achieve the required torque force of 16 N in a 2.83 s burn time to desaturate the reaction wheels [21]. Electric propulsion systems can only achieve small thrust levels, in the order of 100 mN [9], which is below the thrust level required from each thruster (4 N).
Another reason that makes electric propulsion unfeasible is the large amount of power required by this type of propulsion (in the order to 2,000 W)[10]. The MUUDS space probe requires a higher amount of thrust and the power budget does not account for such a high power consumption by the propulsion system (Chapter 14).

Cold gas propulsion systems are also ruled out for attitude control. The same reason applies as for electric propulsion: a cold gas system is incapable of producing such a large control torque force in a burn time of a few seconds with few thrusters. For cold gas thrusters, a "*Maximum thrust level of 10 Newton is possible, but at the expense of a higher inlet pressure.*"[11]. More general, cold gas systems have a nominal thrust level of 50 to 100 mN [12], which is small in order to achieve a torque force of 16 N with a small thruster as depicted in Figure 4.13. The thrust level does not comply with the 4 N thrust level required from every single ADCS thruster.

[8] As few thrusters as possible are positioned on the space probe to reduce cost and complexity of the propulsion system. The minimum amount of thrusters is applied to achieve control about all axes.
[9] electric propulsion: `http://www.rocket.com/files/aerojet/documents/Capabilities/PDFs/Electric%20Propulsion%20Data%20Sheets.pdf`
[10] electric propulsion: `http://www.rocket.com/files/aerojet/documents/Capabilities/PDFs/Electric%20Propulsion%20Data%20Sheets.pdf`
[11] TU Delft Aerospace Engineering, Cold gas systems: `http://www.lr.tudelft.nl/nl/organisatie/afdelingen/space-engineering/space-systems-engineering/expertise-areas/space-propulsion/propulsion-options/chemical-rockets/cold-gas/`
[12] Cold gas systems Surrey Satellite Technology: `http://www.lr.tudelft.nl/nl/organisatie/afdelingen/space-engineering/space-systems-engineering/expertise-areas/space-propulsion/propulsion-options/chemical-rockets/cold-gas/`

Mono- and bipropellant propulsion systems are able to achieve thrust levels of 4 N for each thruster and 16 N in total. Thrust forces range from as small as 1 N up to 110 kN [1].

A trade-off should be performed between different mono- and bipropellant thrusters of different manufacturers in order to select the most optimal thruster system for the MUUDS space probe. This trade-off will be performed on the following criteria, each criterion having a certain weight:

- **Structural mass thruster.** The lower the structural mass of the thruster is, the better for the mass budget of the space probe. (3)
- **Propellant mass.** The less propellant a thruster needs to achieve a certain thrust level, the better. (5)
- **Propellant volume.** The less volume the propellant occupies in the internal structure of the space probe, the smaller the propellant tank can be. Consequently, the propellant system is lighter since a smaller propellant tank suffices. (3)
- **Thrust level.** The thrusters should be able to reach a thrust of at least 4 N each. It should not exceed this value too much since the burn time becomes too short in that case (it becomes shorter than the minimum firing bit of the thrusters). The closer the nominal thrust level of the thruster is to 4 N, the better. (5)

The criteria indicate that the propellant mass required for ADCS during transfer should be calculated. From this mass, the propellant volume can be sized. Propellant mass can be calculated with Equation 4.10 [21]:

$$m = \frac{F \cdot t}{g \cdot I_{sp}} \tag{4.10}$$

with F equal to 4 N, t equal to 2.83 s, g the gravitational acceleration constant on Earth being 9.81 m/s^2, and I_{sp} the specific impulse of the thruster.

The thrusters, for which the propellant mass and the propellant volume are calculated, are:

- MONARC-5 developed by Moog Bradford Engineering [32].
- MR-111C developed by Aerojet [33].
- MRE-1.0 developed by Northrop Grumman Space Technology [34].
- 4N Bipropellant Thruster developed by EADS Astrium [35].

These thrusters will also be compared in a trade-off later on in Table 4.14. In Table 4.13, the propellant mass is listed that every one of these thrusters needs to perform ADCS thrusting of 16 N on a daily basis. This propellant mass[13] is calculated using Equation 4.10.

It is thus assumed that the reaction wheels will become saturated every Earth day and therefore require momentum dumping on every Earth day of the interplanetary transfer time. This assumption is made in light of the high uncertainty on the magnitude of internal and external disturbances on the space probe. It is unknown how large these disturbances will be since the final layout of the MUUDS space probe is still a quite conceptual design (Chapter 10). Most details which determine the internal/external disturbances remain unknown.

The decision is made to assume this worst-case scenario where momentum dumping is required every day. Consequently, the propellant mass estimation for momentum dumping may be too high. However, excess propellant mass for ADCS thrusters can be used to correct a larger than foreseen internal/external disturbance, or can accommodate a quick attitude/trajectory change as requested by the Earth command centre by using pure ADCS thrusting. Table 4.13 gives an overview of the thrust level of each ADCS thruster, the total propellant mass needed to pulse 16 N of thrust every day in 2.83 s over the entire duration of the interplanetary transfer, the total structural mass of the 12 ADCS thrusters and the volume the required propellant occupies in the propellant tank of the space probe.
The different thrusters are compared and traded-off based on the aforementioned criteria. The trade-off is visualised in Table 4.14.

The monopropellant thruster manufactured by Aerojet has a slightly better overall grade compared to the bipropellant thruster developed by EADS Astrium. The MR-111C monopropellant thruster system of Aerojet has been especially developed for ADCS thrusting and has proven its performance in multiple space missions [33]. Therefore, these thrusters will be used for attitude control on the MUUDS spacecraft.
The technical specifications of the MR-111C thruster are given in Table 4.15.

[13] The propellant mass is calculated based on the 4 N thrust required from every ADCS thruster on a daily basis, times the number of Earth days the interplanetary transfer takes and times the number of ADCS thrusters on board the MUUDS space probe (12) as shown in Figure 4.13

Table 4.13: *Calculated propellant mass, propellant volume and thruster structural mass for the MUUDS space probe's ADCS thrusting, comprising 12 ADCS thrusters. The total propellant and structural thruster mass are listed for the 12 ADCS thrusters altogether [32] [33] [34] [35].*

	MONARC-5	**MR-111C**	**MRE-1.0**	**4N Bipropellant**
Thrust level one thruster	4.5 N	4 N	5 N	4 N
Total propellant mass	6.04 kg	5.96 kg	6.26 kg	4.71 kg
Total thruster structural mass	5.88 kg	3.96 kg	6.00 kg	4.20 kg
Propellant volume	5.87 l	5.79 l	6.09 l	4.31 l

Table 4.14: *Trade-off between different thrusters from Moog Bradford Engineering, Aerojet, Northrop Grumman Space Technology and EADS Astrium [32] [33] [34] [35].*

ADCS Thrusters								
		MONARC-5		**MR-111C**		**MRE-1.0**		**4N Bipropellant**	
Criterion	**Weight**	Score	Grade	Score	Grade	Score	Grade	Score	Grade
Structural mass thruster	3	3	9	5	15	2	6	4	12
Propellant mass	5	3	15	4	20	2	10	5	25
Propellant volume	3	2	6	3	9	1	3	5	15
Thrust level	5	3	15	4	20	2	10	4	20
		Total	45	**Total**	64	**Total**	29	**Total**	62

Table 4.15: *Technical specifications of the MR-111C thruster developed by Aerojet [33].*

MR-111C ADCS Thruster System					
Propellant	Hydrazine	Flow rate	0.6 g/s - 2.4 g/s	Total impulse	260,000 Ns
Nominal thrust	4 N	Maximum power	13.64 W	Total impulses	420,000
Feed pressure	5.5 bar - 27.6 bar	Mass	0.33 kg	Minimum impulse bit	0.08 Ns
Chamber pressure	3.4 bar - 12.1 bar	Specific impulse	215 s - 229 s	Minimum burn time	0.02 s
Expansion ratio	74:1				

Twelve of these monopropellant hydrazine thrusters will be mounted on the space probe body and provide active attitude control. Their configuration can be seen in Figure 4.13. The total structural mass of the ADCS thruster system will be 3.96 kg (excluding the propellant mass needed for momentum dumping). The system will consume approximately 13.64 W. The propellant mass required for momentum dumping is 5.96 kg.

4.4.3 Overview of Sensors and Actuators for Attitude Determination and Control

In Table 4.16, an overview of all the ADCS systems used during interplanetary transfer orbit is given. In addition, their mass and power consumption are listed. Finally, the total mass and power that the ADCS system will consume in interplanetary transfer is listed. Be aware that the total mass for the thruster system does not include the propellant mass (this mass is incorporated in the total propellant mass of the propulsion system, described in the propellant tank sizing in Section 4.5.3 Table 4.24).

Table 4.16: *Sensors and actuators for attitude determination and control during interplanetary transfer orbit.*

ADCS System for Interplanetary Transfer Orbit		
Sensor	**Mass**	**Power**
(4) 3-axis accelerometers	$0.164 \cdot 10^{-3}$ kg	$4.32 \cdot 10^{-3}$ W
(2) Small Deep-Space Transponders	6.4 kg	15.8 W
(1) CIRUS inertial reference unit	13.5 kg	25 W
(2) Procyon star trackers	3.5 kg	6.5 W
Actuators	**Mass**	**Power**
(1) W45E reaction wheel assembly	7.9 kg	29 W
(12) MR-111C thrusters	3.96 kg *ex. propellant*	13.64 W
Total	41.36 kg	89.94 W

4.5 Interplanetary Propulsion Mechanisms

When approaching Mars, the spacecraft will have to make a manoeuvre to insert itself in an orbit around Mars. This manoeuvre is called the Mars orbit insertion. To perform this manoeuvre, a propulsion system is required. This section discusses the propulsion system of the space probe in detail. Subsection 4.5.1 covers a selection

of the propulsion system type via a trade-off. Subsection 4.5.2 discusses the sizing process and the component selection of the system and also includes the storage system required for ADCS thrusting as was explained in Section 4.4. The final sizing and results are presented in Subsection 4.5.3.

4.5.1 Propulsion Method

There are different types of propulsion systems with each system characterised by its specific advantages and disadvantages. To determine the most suitable propulsion system for this mission, a trade-off is performed. First, the trade-off criteria are discussed and after that the trade-off will be executed.

Trade-off criteria

The trade-off criteria and their weights are used to determine the most suitable propulsion system are:

- **Thrust**: The amount of thrust the system type is able to deliver. The higher the amount of thrust, the higher the score of the system for this criterion. (5)
- **Specific Impulse**: The effective exhaust velocity and thereby the efficiency of the propulsion methods. The higher the specific impulse, the better this criterion is assessed. (4)
- **Controllability**: Includes the acceleration of the propulsion method, as well as the capability to throttle and to restart. The score on this criterion is higher when the propulsion method has a high acceleration possibility. Throttle and restart possibilities are useful for mission flexibility. (4)
- **Mass**: The lower the mass, the more favourable the system becomes in light of the mass budget. (5)
- **Complexity**: Estimates the complexity of the propulsion types. A more complex system translates in a lower value for this criterion. (3)
- **Sustainability**: This parameter assesses the impact the propulsion type has on the environment of both Earth and Mars. (4)
- **Power Consumption**: Assesses the power consumption of the propulsion system. The lower the power usage, the more favourable the system becomes in light of the power budget. (3)
- **Reliability**: The reliability of the propulsion method is crucial since maintenance is impossible after launch. A high reliability of the system is awarded a high score for this criterion. (4)
- **Technology Level of Readiness**: Assesses the state of technology for a product or method. A widely used propulsion system receives a high score for this criterion. (5)
- **Size**: Assesses the estimated volume of a certain method. A high volume corresponds to a low score. (3)
- **Safety**: The safety component is determined by the possible interference with humans on Earth but also with the consequences in case of collision in space or system failure. High safety risks translate into a low score of the system on this criterion. (5)

Trade-off propulsion system

With the criteria for the trade-off established, the different options for the propulsion system will be covered. The options that are considered are cold gas propulsion, solid propulsion, liquid propulsion (monopropellant, bipropellant and hybrid dual mode) and electric propulsion (electrothermal, electrostatic and electromagnetic). Each system type is first investigated for any major limitations that make it not suitable for this mission.

When looking at the cold-gas system, it is observed that cold-gas systems have a nominal thrust in the range of several Newtons [1]. This limitation is critical since the trajectory design, explained in section 4.1.2, relies on impulsive manoeuvres. Current electric propulsion systems have the same major limitation due to on board limited power generation [1]. Typical thrust levels range from millinewtons to several Newtons [1]. Besides that, the power consumption of electrical propulsion systems is considerably larger than that of chemical propulsion systems [36]. For the reasons stated above, the cold-gas and electrical propulsion systems are clearly unsuitable systems for this mission. Therefore, these system types are not taken into account during the trade-off.

The first parameter that is assessed is the thrust of the systems. Monopropellant systems are typically used for velocity increments up to 1,000 m/s [1]. Solid, bipropellant, dual mode and hybrid propulsion methods produce thrust forces in the range of kilonewtons and are used for missions with high ΔV requirements. Since the latter applies to the MUUDS mission, these methods are suitable for this mission and thus score well on this criterion.

Considering the specific impulse, bipropellant, hybrid and solid propulsion methods have similar specific impulses varying from 200 to 410 seconds [36]. Monopropellant systems score low on this criterion, with a specific impulse range varying from 180 to 223 seconds [1].

Regarding controllability, liquid propulsion methods are the best since these methods provide a high acceleration. Therefore, the desired change in velocity can be obtained in matters of second to minutes. Furthermore, these

systems have the option to restart and throttle. Cold gas is less favourable since the provided acceleration is small which means that impulsive manoeuvres with a high velocity increment are out of reach. Solid rocket propulsion scores low on this criterion, since this method does not have the ability to restart and once started, the predetermined thrust and duration cannot be changed [36]. This can cause problems, considering the possible necessity of trajectory correction manoeuvres or multiple burns during the Mars orbit insertion.

Looking at the mass, bipropellant and solid propulsion systems have the most favourable thrust-to-weight ratio, which varies from $10^{-2} - 100$ [36]. Monopropellant is also a solid option regarding its thrust-to-weight ratio, which varies from $10^{-2} - 10^{-1}$ [36]. Since dual mode consists of a combination of monopropellant and bipropellant propulsion, the system can attain both thrust-to-weight ratio.

Investigating the complexity of each system, it was found that solid propulsion systems score better than liquid propulsion systems due to their simple designs which require less parts. Liquid propulsion options score low on this criterion. Looking at the liquid propulsion systems, the bipropellant system is more complex than a monopropellant system and therefore bipropellant scores lowest on this criterion of all liquid propulsion systems. The dual mode system is also more complex than a monopropellant propulsion system, but is simpler than a bipropellant system [1].

Regarding sustainability, monopropellant and certain bipropellants are a good second option since combustion products of these options are acceptable and the exhaust is usually low in terms of plume, radiation and smoke, which are factors that may damage the spacecraft [1]. Hybrid and solid propellants score lower on this criterion, since these options require a lot of propellant and the exhaust products can cause damage to the measurement instruments [36].

Looking at the power consumption, the electric propulsion types are non-favourable options due to their high power needed to generate thrust. Liquid propulsion options need more power than solid propulsion options due to fuel regulation and possible restarts.

Inspecting the reliability, a disadvantage of solid propulsion is that the system cannot be tested before use [36]. This results in no correction of possible manufacturing errors. The mono- and bipropellant propulsion have a more complex design due to the need of tanks, valves, feed lines and other components. However, the system can be made fully redundant and tested at full thrust prior to launch [36]. Since the solid component of the hybrid method cannot be tested, the system scores the same value as solid propulsion.

The technology readiness level of the chemical propulsion is high since these options are widely used or have already been used on other Mars missions [1]. An exception is the hybrid propulsion, since the feasibility is not yet proven at large scale [1].

Judging the size of the systems, solid rocket propulsion is the best option since the solid fuel has an overall high density. Bipropellant, dual mode and monopropellant take up a larger volume due to the lower propellant density. Since hybrid uses both solid and liquid propellants, the method is placed between solid and liquid alternatives [36].

The last assessed criterion is the safety of the method. Compared to liquid, solid propulsion has a higher probability to explode and can even detonate under certain conditions [36]. Furthermore, solid propulsion cannot handle bullet impact, so impact from space debris can be fatal. Liquid propulsion systems have a risk of leakage, but in case of non-hypergolic propellants, it is unlikely that these will self-ignite spontaneously.

The trade-off of the cold gas, solid, liquid and electric propulsion methods is shown in Table 4.17.
From the table, it can be concluded that the chemical propulsion methods have an equal trade-off score. Although the trajectory is calculated and planned carefully, the spacecraft might deviate from its intended trajectory due to disturbances, leading to necessary trajectory correction manoeuvres. This requires the spacecraft to use a propulsion system with restart capabilities. Therefore, the solid propulsion system is not suitable for this mission.

High performance levels of the propulsion system are necessary for mission success. Therefore, reliability, complexity and experience with the system are key factors. Since the feasibility of a hybrid rocket propulsion is not proven at large scale, it is not a suitable propulsion system for the MUUDS mission [1].

Monopropellant, dual mode and bipropellant systems have the capability to be almost completely redundant systems. The high mass of the space probe and high ΔV needed to perform the Mars orbit insertion requires a

Table 4.17: *Trade-off between different types of propulsion systems.*

Propulsion Systems											
		Solid		**Hybrid**		**Bipropellant**		**Dual Mode**		**Monopropellant**	
Criterion	**Weight**	Score	Grade	Score	Grade	Score	Grade	Score	Grade	Score	Grade
Thrust	5	4	20	4	20	4	20	4	20	3	15
Specific Impulse	4	3	12	3	12	3	12	3	12	2	8
Controllability	4	2	8	4	16	4	16	4	16	4	16
Mass	5	4	20	3	15	3	15	3	15	4	20
Complexity	3	3	9	2	6	1	3	3	9	3	9
Sustainability	4	2	8	2	8	3	12	3	12	4	12
Power consumption	3	3	9	2	6	2	6	2	6	3	6
Reliability	4	2	8	2	8	3	12	3	12	4	12
TRL	5	4	20	3	15	4	20	4	20	4	20
Size	3	4	12	3	9	2	6	2	6	2	6
Safety	5	2	10	2	10	3	15	3	15	3	25
		Total	136	**Total**	125	**Total**	137	**Total**	143	**Total**	139

propulsion system which is able to deliver high thrust. Monopropellant is not the best option for this mission, since the thrust levels that can be delivered by monopropellant systems are inferior to the thrust delivered by dual mode and bipropellant systems.

Bipropellant and dual mode systems are the two best propulsion systems for the MUUDS mission. Dual mode is favourable regarding simplicity and mission flexibility, whereas bipropellant is preferred for its high efficiency. From all criteria assessed in the trade-off, a proper decision cannot be made. Since the MUUDS spacecraft will be launched in 2020, the system has to be built using the technology which is available today. A decision on the propulsion system will be made by looking at the available thrusters, which is done in the next subsection, Subsection 4.5.2.

4.5.2 System Sizing and Component Selection

This subsection discusses the sizing of the propulsion subsystem. First, a suitable thruster is selected, from which the propulsion system type is determined. Second, the system performance is determined. Third, decisions are made regarding the feed system and the cooling system. Furthermore, the storage system, which also includes the tanks for the ADCS thrusting into account, is sized and an overview of the propulsion system is given. In the final part, the remaining issues will be discussed.

Thruster selection

As discussed in Subsection 4.5.1, the decision of the propulsion system type is based on the technology available today. Therefore, a trade-off is made between different thrusters since these components determine the overall performance of the propulsion system. The possibility to design a new thruster has also been taken into account. The specifications of this self-designed thruster (the MUUDS thruster) is shown below in Table 4.18.

Table 4.18: *Technical specifications of the MUUDS Rocket Engine.*

MUUDS Rocket Engine			
Propellant	Hydrazine/N204	Flow rate	6.74 kg/s
Nominal thrust	20,012 N	Mass	79.52 kg
Chamber pressure	7 bar	Specific impulse	315 s
Expansion ratio	40:1	Engine length	1.9 m

For the trade-off, different thrusters have been selected. An itemisation of them is given below.

- Aerojet Rocketdyne R-42DM 890 N Dual Mode High Performance Rocket Engine [37].
- Aerojet Rocketdyne R-40B 4,000 N Bipropellant Rocket Engine [38].
- MUUDS Bipropellant Rocket Engine.
- Airbus Aestus Bipropellant Rocket Engine [39].

The selection of the most suitable thruster is based on the following criteria given below:

- **Mass**: Minimising mass is critical in space missions. The lower the mass, the better a thruster is.
- **Thrust**: The Mars orbit insertion manoeuvre requires a high thrust level. Higher thrust levels correspond to a higher score. The thrust level is based on one thruster.
- **Dimensions**: The whole spacecraft has to fit within the Falcon Heavy. Therefore, small dimensions of the thrusters are preferred. A small thruster receives a higher score on this subject
- **Cost**: A low cost is favourable. Expensive thrusters score lower on this criterion.

- **Propellants**: The propellants used by the thruster must be storable, lightweight and safe. If the propellant choice satisfies these criteria, this aspect scores higher.
- **Feed System**: A simple feed system is preferred. Therefore, pressure fed thrusters score higher on this criteria than turbo-pump systems.

The trade-off based on the criteria mentioned is visualised in Table 4.19.

Table 4.19: *Trade-off between main propulsion system thrusters from Aerojet, Airbus Space & Defense and MUUDS.*

Propulsion Thrusters									
		42DM Dual Mode		**R-40B Bipropelllant**		**MUUDS Bipropellant**		**Airbus Aestus 72**	
Criterion	**Weight**	Score	Grade	Score	Grade	Score	Grade	Score	Grade
Structural mass	5	4	20	5	25	2	10	2	10
Thrust level	4	1	4	2	8	4	16	5	20
Dimensions	4	4	16	5	20	2	8	2	8
Cost	3	4	12	4	12	1	3	3	9
Propellants	3	5	15	3	9	5	5	3	9
Feed System	3	5	15	5	15	5	15	5	15
		Total	82	**Total**	89	**Total**	67	**Total**	71

Looking at the mass, it can be observed that the Aerojet Rocketdyne R-40B thruster is the best option. With 6.8 kg it has the lowest structural mass of all options. The runner up is the Aerojet Rocket dyne R-42DM, with a structural mass of 7.3 kg. The MUUDS thruster and Airbus Aestus Engine are heavier with structural masses of 79.52 kg and 111 kg respectively.

Regarding thrust levels, the Airbus Aestus II 72 is the best option with 29.6 kN of thrust. Second best is the MUUDS thruster with a thrust level of 20 kN. The third option is the Aerojet Rocketdyne R-40B thruster with a nominal thrust of 4,000 N and the least favourable option in terms of thrust is the Aerojet Rocketdyne R-42DM, with a nominal thrust level 890 N.

Considering the dimensions of the thrusters, The Aerojet Rocketdyne R-40B and R-42DM are the best options with a total length of 0.711 m and 0.7112 m respectively. This is smaller than the 1.877 m and 1.9 m from the MUUDS thruster and Airbus Aestus engine respectively.

Investigating the costs, it can be said that smaller engines are in general cheaper than larger engines which provide more thrust. Therefore the two Aerojet Rocket Engines score similarly. The MUUDS thruster scores the lowest, since this is a new engine which still is designed in detail. This adds additional costs to process such as development and testing costs.

Looking at the type of propellants used, it can be observed that the Aerojet Rocket Dyne R-42DM and the MUUDS thruster score high since they uses hydrazine as fuel. This reduces the need for a separate propellant tank for the ADCS system during the trajectory phase. The other engines use monomethylhydrazine and therefore are given a lower score on this criterion.

The last criterion is the type of feed system. It is desirable to keep this system as simple as possible. All the thrusters use a pressure-feed system and score therefore similar on this criterion.

Although the Aerojet Rocketdyne R-40B thruster has a considerable lower thrust than the MUUDS and Aestus 72 thrusters, multiple R-40B thrusters can be used to achieve a similar thrust level while maintaining superiority in mass and dimensions. To obtain a similar thrust level with the Aerojet Rocket Dyne R-42DM, it would require more than 4 times as much thrusters which could lead to problems regarding dimensions and mass. Therefore, the Aerojet Rocketdyne R-40B thruster is the preferred choice for the MUUDS space probe. An overview of the techincal specifications of the chosen thruster is given Table 4.20 [38].

System performance

With the type of thruster set, a basic rocket analysis can be performed to get a grasp of the system performance. The propellant mass of the system required is calculated using Equation 4.11 [40].

$$m_{propellant} = m_0 - \frac{m_0}{e^{\frac{\Delta V}{g_0 \cdot I_{sp}}}} \tag{4.11}$$

Table 4.20: *Technical specifications of the R-40B Bipropellant Rocket Engine developed by Aerojet [38].*

R-40B Bipropellant Rocket Engine			
Propellant	MMH/NTO (MON-3)	Mass	6.8 kg
Nominal thrust	4,000 N	Specific impulse	293 s
Inlet pressure range	10.3 bar - 27.6 bar	Total impulse	92,073,600 Ns
Chamber pressure	10.34 bar	Total Pulses	50,000
Expansion ratio	60:1	Minimum impulse bit	111 Ns
Flow rate	1.4 kg/s	Minimum burn time	0.02775 s
Valve Power	70 W		

To account for unforeseen actions, a 10 % margin was incorporated in the ΔV budget. The mass flow of the system can be calculated with Equation 4.12 [40].

$$\dot{m}_{system} = \frac{F}{g_0 \cdot I_{sp}} \tag{4.12}$$

Next, the burn time of the system can be calculated using Equation 4.13 [40].

$$t_{burn} = \frac{m_{propellant}}{\dot{m}_{system}} \tag{4.13}$$

Propellant choice

The Aerojet Rocketdyne R-40B Engine uses monomethylhydrazine (MMH) as fuel and MON-3 as oxidiser. MMH is widely used in space rocket engines, mostly in combination with dinitrogentetraoxide as oxidiser. MON-3 is a mixture of 97 % dinitrogentetraoxide and 3 % nitrogenoxide. The combination of these fuels is a hypergolic mixture. This means that spontaneous combustion occurs when the chemicals mix. This reduces the need of a complex ignition system. However, attention is required during the risk analysis and mitigation that the tanks do not leak during the mission, since this could lead to explosion danger. Besides, careful policies for the handling of these fuels has to be set up in order to ensure the safety of the employees which have to work with these fuels. Proper guidance for such rules can be found in Occupational Safety & Health Administration Regulations Standards[14].
Before the sizing of the storage system can be done, the oxidiser/fuel ratio should be determined. For hydrazine/dinitrogentetraoxide combinations, the optimal ratio is near the condition for which the individual tanks have the same volume. This corresponds to a oxidiser/fuel ratio of 1.65 [40].

Cooling approach

The thrusters often operate at a temperature above the thermal limits of the materials. So, a cooling system is needed to avoid structural failure. Simplicity is the driving factor when designing the cooling system. The thrusters are partially placed outside the spacecraft, namely from the throat until the nozzle exit. This allows for the use of a method called radiation cooling. In this method, the heat from the combustion gasses transfers from the engine walls towards outer space by means of convection and radiation. For the thrust chamber, radiation cooling is not preferred since the combustion chamber is placed inside the spacecraft. To ensure that the engine stays under the thermal limits, ablative cooling is chosen. This method uses insulating material at the inside of the engine which vaporises during the combustion. This method is frequently used for small to mid-size engines with a burn time lower than 2,000 s. The advantages of his technique are the simplicity and flexible duty cycle. This means that it is possible to start and stop the engine at any time as long as the ablative material is left on the chamber walls. The simplicity comes at a price, namely that of increased weight. For hydrazine/dinitrogentetraoxide systems the ablative material mass can add an additional weight of 35.2 % to the engine structural mass [40].

Feed and storage system

Next, the feed and storage system is sized. First, the pressure levels throughout the system need to be calculated. The starting point is the combustion chamber pressure, which is known from the data sheet [38]. Next, the pressure level of the tank can be determined.
The largest drop in pressure occurs in the feed system. Typical values range from 35,000 to 50,000 Pa where te lower value is taken in case of an aggressive design strategy and the latter is used in case of a conservative design strategy [40]. Since a conservative design strategy is chosen, $\Delta_{p_{feed}}$ is chosen to be equal to 50,000 Pa.

[14] OSHA Regulations: `https://www.osha.gov/pls/oshaweb/owasrch.search_form?p_doc_type=STANDARDS`

To inject the fuel from the feed system into the combustion chamber, an injector is used. Typical values for the pressure drop in this part of the system range from 20 % up to 30 % of the feed system pressure loss, depending on the presence of a throttle capability [40]. Since a throttle system is not necessary for the Martian orbit insertion, $\Delta_{p_{injector}}$ is assumed to be equal to $0.2\Delta_{p_{feed}}$ Pa.

The last pressure drop is due to the dynamic pressure which occurs during the change in propellant velocity when the propellant leaves the tank. This last pressure drop is calculated using Equation 4.14 [40] where v is the flow velocity. A typical number for this flow velocity is 10 $\frac{m}{s}$.

$$\Delta p_{dynamic} = \frac{1}{2} \cdot \rho_{propellant} \cdot v^2 \tag{4.14}$$

Now the pressure changes are known, the tank pressure can be calculated using Equation 4.15 [40].

$$p_{tank} = p_{chamber} + \Delta_{p_{injector}} + \Delta_{p_{feed}} + \Delta_{p_{dynamic}} \tag{4.15}$$

Before the sizing can continue, it has to be determined whether a pressure-fed system or a pump-fed system will be used. Pressure-fed feed systems are preferred due to their simplicity whereas pump-fed systems allow lightweight tank masses. From historical data it can be seen that tank volume is a good indicator for the decision whether to use a pressure-fed or pump-fed system [40]. Since both tanks have a volume lower than 2 m^3, it is decided to select a pressure-fed feed system.
Using the oxidiser/fuel mixture ratio, the propellant mass of the fuel and oxidiser can be determined with Equations 4.16 and 4.17 [40], where $m_{p_{fuel}}$ is the required fuel needed for attitude control, orbit maintenance and orbital manoeuvres during the operations and end-of-life phase.

$$m_{p_{fuel}} = \frac{m_p}{1 + O/F} + m_{p_{monopropellant}} \tag{4.16}$$

$$m_{p_{oxidiser}} = \frac{m_p \cdot O/F}{1 + O/F} \tag{4.17}$$

With the propellant masses known, the volume for each propellant can be calculated using the propellant density. The required tank volume is larger than propellant volume since there is additional ullage volume. Ullage volume is needed to take propellant expansion and tank structure contraction into account. Typical ullage values are 3 % to 10 % of the fuel volume. Since a conservative design strategy is performed, 10 % ullage volume is assumed.
Using the volume, the actual dimensions can be calculated. To use the volume within the space probe efficiently, it has been decided to use cylindrical tanks with spherical caps. Using a predetermined height, the radius can be calculated using the Equations 4.18 and 4.19 [40].

$$V_{tank} = \frac{4}{3} \cdot \pi \cdot r^3 \cdot -2 \cdot \pi \cdot r^3 + h \cdot \pi \cdot r^2 \tag{4.18}$$

$$h = l_{cylinder} + 2 \cdot r \tag{4.19}$$

Finally, the tank masses are calculated using Equation 4.20 [40], better known as the pV/W method, in which ϕ is the tank mass factor which attains typical values of 2,500 m for metallic tanks.

$$m_{tank} = \frac{p_b \cdot V_{tot}}{g_0 \cdot \phi} \tag{4.20}$$

The valves, feedlines and other feed system components lead to a significant weight of the feed system and it therefore has to be taken into account. The mass of the feed system is estimated using emperical data and Equation 4.21 [40].

$$m_{engine_{system}} = \frac{F}{g_0 \cdot (0.0006098 \cdot F + 13.44)} \tag{4.21}$$

The mass of the total feed system is equal to the difference between the total engine mass estimated using Equation 4.21 and the real engine mass given by the manufacturer.

Pressurization system

In order to get the propellants from the tanks into the combustion chamber, the propellants must overcome the pressure drops throughout the system and be injected in the chamber at a target pressure. In order to do so, a pressurisation system is needed. Since a pressure-fed system is chosen, it is possible to use either a blow-down system or a regulated pressure system. A regulated pressure system will be used since this enables the delivery of a constant thrust level that is required to perform the Martian orbit insertion.
Next, a choice regarding the pressure gas has to be made. Different gasses like H_2, N_2 and He exists. After research, it turned out helium is the best choice due to its low weight and inert properties.

A regulated pressure system requires a separate tank which contains the pressuratization gass. This tank is sized using the following design process.
First, the final temperature at the end of the burn is calculated using Equation 4.22 [40], in which the initial tank pressure is equal a typical value of 21 MPa and the initial temperature is equal to the temperature vehicle. The final pressure is equal to the average pressure of the fuel and oxidiser tanks.

$$T_{final} = T_{initial} \cdot \frac{p_{final}}{p_{initial}}^{\frac{\gamma-1}{\gamma}} \tag{4.22}$$

Next, the volume of the pressurant gas is calculated using an iterative calculation scheme [40]:

1. Assume the pressurant tank volume is equal to zero.
2. Calculate the pressurant gass using the ideal gas law with the final conditions.
3. Calculate the pressurant gass volume needed to hold the pressurant gass mass using the perfect gas law with the initial conditions.
4. Go back to step 2 unless this algorithm is converged.

Using Equations 4.18 and 4.20, the tank dimensions and mass can be determined.

4.5.3 Design Results

In this subsection the design results are presented. Table 4.21 summarises the general system performance. The masses are summarised in Table 4.22 and an overview of the dimensions is given in Table 4.23. This subsection summarises the properties of both the interplanetary propulsion system and the ADCS storage system of the orbiter. After the Mars orbit insertion is performed, the propulsion system components used for trajectory are jettisoned. This is due to the fact that the inert mass of the trajectory propulsion system is high compared to the orbiter mass. If the system would not be jettisoned, the orbiter would lose altitude faster, leading to a higher required fuel mass. Expelling this system will thus save a significant amount of fuel. Details of the separation process can be found in Section 10.5.

Table 4.21: *System performance of the R-40B Bipropellant Rocket Engine developed by Aerojet [38].*

System Performance Propulsion System	
Nominal thrust	36,000 N
Propellant Mass	3,453.47 kg
Mass Flow	4.73 kg/s
Burn Time	275.73 s
Total Impulse	9,926,415 N·s

Table 4.22: *Mass distribution of the propulsion system.*

Mass distribution trajectory propulsion system.	
MMH	1,303.2 kg
MON-3	2,150.3 kg
Hydrazine (ADCS Propellant)	6 kg
Helium pressurant	31.2 kg
Engines	61.2 kg
MON-3 Tank	188.8 kg
Pressurant Tank	283.2 kg
Hydrazine Tank	0.715 kg
Feed System	41.8 kg

Table 4.23: *Dimensions of the propulsion system components.*

Dimensions of propulsion system components	
Engine length	0.711 m
Engine exit diameter	0.4 m
MMH Tank [radius x ID]	0.71 m x 0.0527 m
MON-3 Tank [radius x ID]	0.73 m x 0.017 m
Hydrazine Tank [radius x ID]	0.0932 m x 0.1137 m
Pressurant Tank [radius x ID]	0.48 m x 0.519 m

Table 4.24: *Mass distribution of the orbiter ADCS system.*

Mass distribution trajectory propulsion system	
Hydrazine	6 kg
Hydrazine Tank	0.715 kg
Helium Pressurant	0.061 kg
Pressurant Tank	0.55 kg

Table 4.25: *Dimensions of the propulsion system components.*

Dimensions of orbiter ADCS components	
Hydrazine Tank [radius x ID]	0.0932 m x 0.1137 m
Pressurant Tank [radius x ID]	0.04315 m x 0.5197 m

5 | Entry, Descent and Landing

The aim of this chapter is to present a more detailed description of the Entry, Descent and Landing phase of the MUUDS mission discussed in Section 5.1 till 5.3, respectively. The chapter will capture the sizing and qualitative analysis of the deceleration mechanisms and the velocity losses that will be realised. The functional flow diagram of this chapter is shown in Figure 5.1.

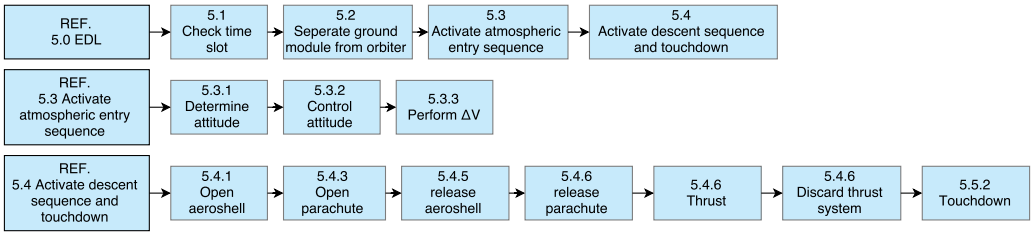

Figure 5.1: *Functional flow diagram for entry, descent and landing.*

5.1 Entry

Once the space probe is in an orbit around Mars, it will release the ground stations while the orbiter stays in orbit. This section will describe the release mechanism that decouples the ground pods. All ground stations need to be decoupled, which will be done within 2 sols. Once all ground stations are released and landed, the orbiter will make contact with the ground stations and check if the EDL was successful. This process will be discussed in this section. Furthermore, the ADCS of the orbiter during decoupling will be treated and the trajectory of the entry will be described.

5.1.1 Decoupling Mechanisms for the Landers

The landers should be released one-by-one, first clearing the upper part of the probe, followed by the bottom stage. To be able to do so, the spacecraft is excited to rotate about its longitudinal axis. In this way, each lander is pointed down towards the Martian surface once per rotation of the craft. When a lander is pointing down, the explosive bolts[1] connecting the lander to the rod, will be detonated and springs then push the lander away from the spacecraft's surface. Next, the EDL module can enter its trajectory towards the Martian surface.

Rotational spin of the orbiter for lander release

The propellant mass required for the ADCS thrusters to deliver a certain acceleration to the spacecraft and maintain a constant spin velocity needs to be sized. In addition, a decision should be made on how fast the craft is allowed to spin, thus sizing the spin velocity.

A first step in the sizing process is to calculate the rotational speed of the spacecraft V_{rot}. It is decided to let the spacecraft rotate over one full circle after every release. After this full rotation, another one-fifth rotation is required to place the next lander to be released in the release position. The process is visualised in Figure 5.2.

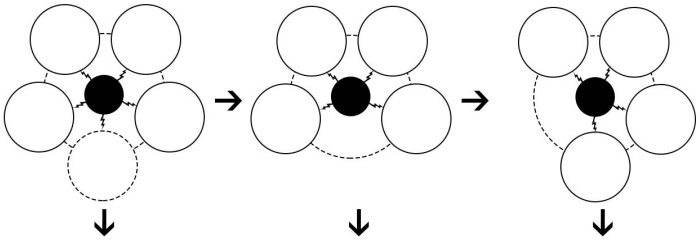

Figure 5.2: *Illustrative description of the rotation mechanism used to release the landers into an entry trajectory.*

Per Martian day, five landers are released. Releasing five landers a day thus requires five full rotations of the spacecraft plus five times one fifth of a turn to place a new lander at the release position. Therefore, during one Martian day, the spacecraft will perform six full rotations. One Martian day lasts approximately 24 h 40 min, or 88,800 s. Ergo, the rotational speed required to perform six full rotations per Martian day is the sextuple of the circumference of the circle described by the landers in rotation divided by the duration of one day.

[1] More on these bolts in Section 10.5.

The circumference CF of the inner circle can be determined when the radius of the centre beam R_B, the length of an explosive spring bolt L_{spring} and the radius of a lander R_L are known. These dimensions are sized in Subsection 10.5.1. R_B is determined to be 0.75 m, R_L is equal to 0.45 m and L_{spring} is equal to 0.15 m. The circumference CF of the inner describing circle C_i can be determined with Equation 5.1.

$$CF = 2 \cdot (R_B + R_L + L_S) \cdot \pi \tag{5.1}$$

Equation 5.2 is used to calculate the rotational speed V_{rot}.

$$V_{rot} = \frac{6 \cdot CF}{t} = \frac{6 \cdot 8.48\,m}{88,800\,s} = 0.00057\text{m/s} \tag{5.2}$$

The spacecraft should be accelerated from a zero spin velocity to a constant velocity of 0.57 mm/s. This is done by exerting a small acceleration force on the spacecraft, delivered by the ADCS thrusters. Four thrusters will have to work together to initiate the rotational movement of the craft (Figure 4.13). Four MR-111C thrusters deliver a combined nominal thrust force of 16 N. The spacecraft to be turned weighs ± 1,475 kg at the start of the first rotation[2]. The required acceleration is thus:

$$F = m \cdot a \iff a = \frac{F}{m} = \frac{16\,N}{1,475\,kg} = 0.0108\text{m/s}^2 \tag{5.3}$$

This acceleration should be applied over a certain time interval to achieve the V_{rot} of 0.57 mm/s. When this speed is achieved, the acceleration should stop. At that instant the thrusters have to be shut down. The time over which the acceleration is to be delivered is thus equal to the burn time of the thrusters. The kinematic Equation 5.4 gives the relation between the speed after the burn time which is V_{rot}, the initial speed V_i which is equal to zero, the acceleration a and the burn time t_{burn}. Next, the burn time can be determined.

$$V_{rot} = V_i + a \cdot t_{burn} \iff t_{burn} = \frac{V_{rot}}{a} \tag{5.4}$$

It should be noted that the burn time should be higher than the minimal burn time the MR-111C can achieve. t_{burn} is equal to 0.053 s which lies within the capabilities of the thrusters (their minimal burn time is 0.02 s, as shown in Table 4.15).

With the burn time, the thrust level F and the specific impulse I_{sp} of the four MR-111C thrusters known, the propellant mass required to initiate the rotation can be determined using Equation 5.5.

$$M_p = \frac{F \cdot t_{burn}}{I_{sp} \cdot g_0} \tag{5.5}$$

The propellant mass needed to initiate the rotation accumulates to $0.376 \cdot 10^{-3}$ kg.

Each time a lander is released, the mass of the rotating vehicle changes. This will cause the vehicle to accelerate. To maintain the same rotational speed V_{rot}, the spacecraft should be decelerated by active thrusting of the ADCS or by providing counter-torque from the reaction wheels assembly. The counter-force F_c required for the deceleration at each release instant can be computed with Equation 5.6.

$$F_c = \frac{d\,(m \cdot V_{rot})}{dt} = \frac{dm}{dt} \cdot V_{rot} \tag{5.6}$$

The rotational speed V_{rot} is constant. The change in mass is a decrease of ± 125 kg. The time instances over which the masses are released are spread over two Martian days, as this was the frequency of release that was requested, resulting in a time interval of 17,760 s. At those instances, the mass is dropped in a fraction of a second, resulting in dt assumed to be 0.1 s. The counter-force F_c at every release instant is thus equal to 0.72 N. Ten landers will be delivered for EDL over the course of 2 sols at equal time intervals of 17,760 s. The total force required for deceleration to retain the constant rotation speed when the mass is changing, is the tenfold of the counter-force F_c delivered at each time interval. The total force for corrections due to a changing mass therefore adds up to be equal to 7.2 N.
The burn time required from the MR-111C thrusters is determined by the maximum mass flow rate possible for that type of thruster, which is 0.0024 kg/s. It is assumed that the thrusters constantly fire at this maximum rate during a correction instance. Equation 5.7 gives the relationship between maximum mass flow rate $\dot{m}_{max}$, I_{sp}, g_0 and the thrust delivered. From this relationship, the minimum required burn time at each release instance can be calculated.

$$F_c = \dot{m}_{max} \cdot I_{sp} \cdot g_0 \iff t_{burn} = \frac{m_{max} \cdot I_{sp} \cdot g_0}{F_c} \tag{5.7}$$

[2]The weight of the spacecraft is slightly more than the eventual weight of the final design, see Chapter 10

The burn time t_{burn} at one release instance is then 7.53 s. The propellant mass released on that instance is:

$$M_p = \dot{m}_{max} \cdot t_{burn} = 0.01806\text{kg} \tag{5.8}$$

Ten landers are released, thus ten of these firing instances occur. The total propellant mass required for correction of the rotation due to a change in mass of the rotating vehicle is therefore 0.1806 kg.

At the end of the rotational phase of the satellite, when all the landers are released, the ADCS thrusters should halt the rotational motion by providing a counter-force and thereby annihilating the rotational velocity by a deceleration.
If the thrusters would fire at their maximum thrust level, accumulating to 16 N when four thrusters are operational, the deceleration would be 0.071 m/s^2 according to Equation 5.3. The speed in counter-direction should be equal in magnitude but opposite in sign to V_{rot}. Using the value of V_{rot} and Equation 5.4, the burn time can be calculated. t_{burn} will be 0.008 s when the thrusters are firing at full capacity, thereby violating the minimum firing bit of 0.02 s of the MR-111C thrusters (see Table 4.15).
The decision is made to let the thrusters fire at their lowest thrust level. The deceleration becomes 0.0231 m/s^2 causing the burn time to be 0.025 s, which is above the minimum firing bit of the thruster. The propellant mass required for this manoeuvre is then:

$$M_p = \frac{F_{min} \cdot t_{burn}}{I_{sp} \cdot g_0} = 5.74 \cdot 10^{-5}\text{kg} \tag{5.9}$$

An overview is provided in Table 5.1, showing the propellant masses required for the control of the satellite's rotational speed during the landers' release and for the initiation and termination of the rotation.

Table 5.1: *Propellant mass required for rotational movement initiation, maintenance and termination of the satellite during release of the landers.*

Propellant Mass	
To start rotation	$0.376 \cdot 10^{-3}$ kg
To maintain rotation	0.1806 kg
To end rotation	$5.74 \cdot 10^{-5}$ kg
Total	**0.204 kg**

5.1.2 ADCS during Decoupling of the Landers

After the bolts detonate, the springs elongate and thereby release a pushing force on the lander and push the lander away from the orbiter towards an entry trajectory. However, when a force is exerted on the lander and an equal but opposite force is applied to the beam of the orbiter on which the landers were attached, the force will create a moment about the centre of the orbiter. The five landers located in the first stage will cause the largest moment when they are released since the spring forces exerted have the longest moment arm.

If the moment created by the springs is not counteracted by a counter-rotating moment, the orbiter is left free to start spinning. This undesirable spin will cause the orbiter to rotate in such a way that the landers left to be released in orbit are no longer in a correct parallel position with respect to the orbiter's park orbit. Instead, the landers are tilted. This would result in a faulty release of the landers in their entry trajectory and will likely result in the landers not being able to reach the Martian surface correctly.

It is thus of major importance that the ADCS thrusters or reaction wheels or a combination of both, create a counter-rotating thrust for the release force of the landers. The counter-force should be large enough to annihilate the effect of the moment in order to let the orbiter and landers remain parallel to their park orbit. This will ensure a correct release of the landers in their entry trajectory and will make sure that the orbiter remains in its correct orbit.

The calculation of the exact counter-force and -moment is outside the scope of this DSE project, since the computation of the spring force is highly complex, see Subsection 5.1.1.

5.1.3 Entry Trajectory of the Landers

Once a lander has been decoupled from the space probe, it will need to descent to the surface of Mars. However, when the system would not provide any ΔV to decelerate, the pods would remain in orbit next to the orbiter. Therefore, a ΔV needs to be provided to descent. A transfer orbit has been designed to simulate a crash after approximately 5,000 seconds. In these calculations, a diameter of 5.4 m and a C_D of 0.8 have been assumed. To achieve this, a Hohmann transfer orbit is needed with its apogee at 220 km and its perigee at 120 km. Using Equation 6.12, a ΔV of 24.28 m/s is required to make this transfer. Once the EDL system has delivered this velocity difference, an aeroshell will open which has a diameter of 5.4 m. In Subsection 5.2.1, the aeroshell is designed in more detail. The trajectory of the lander has been visualised in Figure 5.3. In Figure 5.4a and Figure 5.4b the velocity profile and the height profile are shown respectively. In these figures, it has been assumed that the aeroshell will open and remain open until it will crash on Martian surface. However, as can be seen in Figure 5.4a, the velocity with which the system would crash, 70.43 m/s is too high for the structure of the landers. Therefore, other mechanisms will be used to decelerate the system. These systems will be explained further on in this chapter.

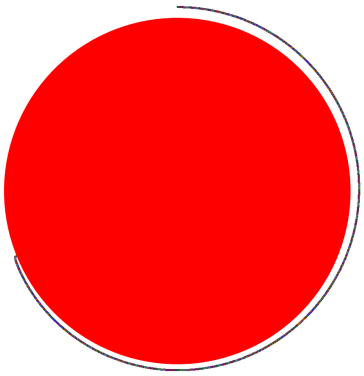

Figure 5.3: *Two-dimensional overview of the trajectory described by the EDL module during entry.*

5.2 Descent

In this section, the various deceleration mechanisms that will be used during the EDL phase are sized and discussed. The first deceleration mechanism is the heat shield that will be used. An inflatable heat shield will be used, as these type of heat shields have shown great opportunities in tests and analyses in an advanced state of testing [41]. The heat shield should have a reliability of at least 0.95. Next, the inflatable heat shield will be sized according to the requirement. Furthermore, the parachute and the thrusters will be discussed.

5.2.1 Sizing of the HIAD Aeroshell

In this subsection, the process of sizing the HIAD aeroshell is performed. First, the thickness of the isolation layer is approximated via a Monte Carlo approximation. Furthermore, the mass and diameter are estimated.

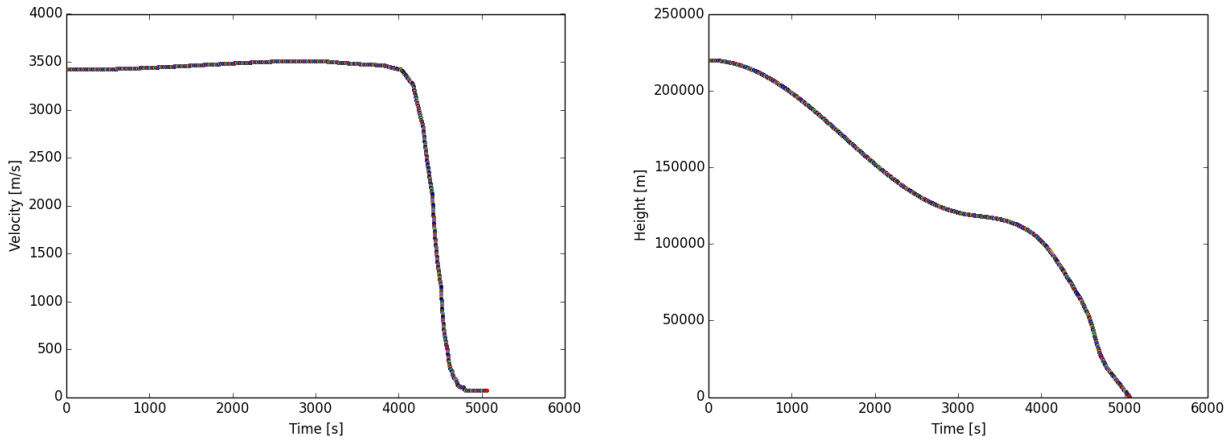

(a) *Velocity profile.* ***(b)*** *Height profile.*

Figure 5.4: *Profiles of the EDL module during entry.*

The isolation layer thickness

The hypersonic inflatable aerodynamic decelerator (HIAD) provides some great advantages over the more commonly used rigid aeroshells. Examples of advantages are very low costs and a reduced volume. However, the greatest benefit of using inflatable aeroshells, is that they have never been tested on Mars missions before. This may sound strange, however, if future manned missions to Mars are organised, inflatable aeroshells will probably be a necessity due to the high masses of the capsules. By then, having the experience of ten inflatable aeroshells used for EDL in the MUUDS mission, will be extremely valuable. The strength of an aeroshell lies in the fact that it is effective in distributing heat due to its blunt shape and its ability to protect the payload via thermal guidance and isolation. The HIAD that is currently developed is of a very low mass of about 10 kg and has a shield with a diameter of more than 20 m. The HIAD shield is constructed as a Thermal Protection System (TPS). TPS is a lay-up structure of a outer fabric, which consists of two layers, a number of 0.5 inch layers and a gas barrier. A schematic overview of the lay-up structure is shown in Figure 5.5.

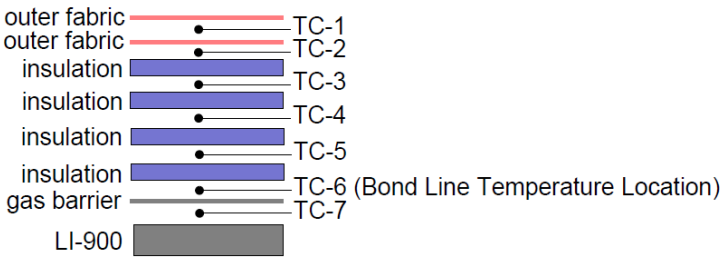

Figure 5.5: *Lay-up structure of the Thermal Protective System (TPS) of the HIADS aeroshell [42].*

The sizing of the heat shield is primarily done by determining the amount of insulators that resemble an acceptable performance of the heat shield. The situation can be viewed as a 2D thermal process, in which the temperature propagates through the outer fabric layers and the insulator layers to the gas barrier layer. This is schematically shown in Figure 5.6. Of specific interest is point TC 6 in the figure. The temperature in this region is called the bondline temperature and it determines whether the aeroshell will fail or succeed. For temperatures in these region above 400 °C, the aeroshell will fail. The thicker the isolation layers are, the lower the bondline temperature will be. A factor of interest will be the reliability of the heat shield, which will follow from simulation [42].

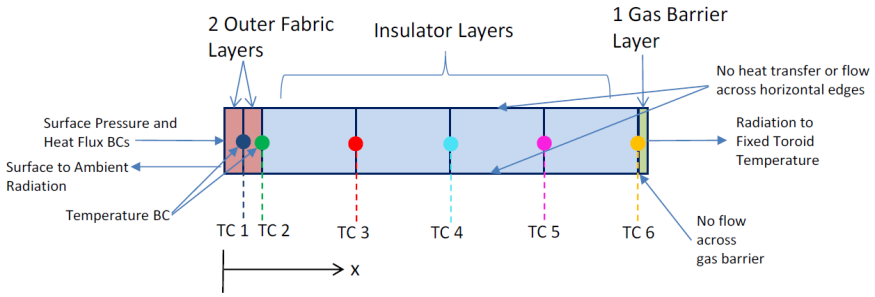

Figure 5.6: *Schematic overview of the heat propagation in the HIAD aeroshell [42].*

The bondline temperature depends on various different factors derived from the differential analysis of the thermal system. This mathematical approach is outside the scope of this project. However, probabilistic distributions were determined by NASA for the various parameters of influence and a Monte Carlo approach was executed to assess the bondline temperature (the expected value of the Monte Carlo analysis). This approach has shown to be much less conservative and more precise than more commonly used techniques. Therefore, this approach can result in serious mass and volume reductions. SF in the table stands for scale factor. The analysis was done for a Low Earth Orbit descent. The parameters investigated are:

- Insulator Virgin Conductivity (k_{vrg}) SF1.
- Insulator Virgin Conductivity (k_{vrg}) SF2.
- Insulator Specific Heat (Cps) SF.
- Latent Heat of Reaction 1 (H_{R1}) SF.
- Heat Flux (q_{cw}) SF.
- Bondline Temperature Bias.
- Insulator Thickness SF.
- Insulator Density SF.

These parameters combined determine the bondline temperature. They are analysed for a LEO orbit and a Monte Carlo analysis was executed for a 4, 4.5 and 5 inch isolation layer. From this analysis, it can be concluded that the isolation layer will have to be at least 5 inches thick in order to ensure a reliability of at least 97 %. The analysis for the Martian descent will be different from the LEO descent as the heat flux is about 20 % higher [43]. All characteristics of the probability distributions have been scaled in a sensitivity analysis to make sure that the summation of the distributions yields the correct temperature ranges.

A Monte Carlo analysis is executed using 2,000 samples. The parameters used are the same as in the NASA study, however the heat flux has been updated. The other factors are specific for the TPS and are therefore not adapted. From the Monte Carlo analysis, it is found that an additional 25 % TPS material should be added on the acceptable thickness, *in order to mitigate stochastic, parametric, and structural uncertainties* [42]. Furthermore, the same corrections for the increased layer thickness have been applied; a correction factor for the part of the TPS structure that is an isolation layer and a subtraction for the nominal shift in temperature.

The basis of Monte Carlo estimations depends on the characteristics of the various probability distributions and the fact that when a certain process with a certain probability is executed a large amount of times, the results will resemble this distribution. Important parameters in the Monte Carlo analysis are the expected value E and the standard deviation σ. The equations for this specific scenario of Monte Carlo simulation are described in Equations 5.10 to 5.12.

$$E = e^{\mu+\delta^2/2} \tag{5.10}$$

$$\sigma = \sqrt{e^{2\mu+\delta^2}(e^{\delta^2}-1)} \tag{5.11}$$

$$P(T_{BL} < 400) = \int_0^{400} \frac{1}{\sqrt{2\pi}\cdot\delta\cdot T_{BL}} e^{\frac{-(ln(T_{BL})-\mu)^2}{2\cdot\delta^2}} dT_{BL} \tag{5.12}$$

The characteristics of the earlier mentioned parameters are shown in Table 5.2. Furthermore, the only altered values are the nominal value and the standard deviation (1 σ) for the Heat Flux. The same factor is applied to the standard deviation as it is expected that the know-how of the Martian heat flux is limited in comparison to the Earth heat flux. To account for this, a higher value is allocated for the standard deviation.

Table 5.2: *Overview of the probabilistic distributions allocated to the heat shield parameters.*

Parameter	Distribution Type	Mean or Nominal Value	Standard Deviation or Range
Insulator Virgin Conductivity SF 1	Normal	0.885	0.106
Insulator Virgin Conductivity SF 2	Normal	1.09	0.106
Insulator Specific Heat SF	Normal	1.00	0.0738
Latent Heat of Reaction 1 SF	Uniform	1.00	0 to 2
Heat Flux SF	Normal	1.00 x factor	0.07 x factor
Bondline Temperature Bias	Uniform	0°	0 to 50
Insulator Thickness SF	Normal	1.00	0.084
Insulator Density SF	Normal	1.00	0.083

For the LEO analysis, a 5 inch heat isolation layer was found to be sufficient to have an acceptable reliability. However, the heat flux in the Martian descent will be higher, so the minimal thermal isolation layer is expected to be thicker. Therefore, the first Monte Carlo simulation is done for an isolation thickness of 5 inches, increasing it with 0.5 inches each simulation. The addition of 0.5 inches is the smallest contribution possible, due to manufacturing reasons [42]. The result of the first Monte Carlo estimation is shown in Figure 5.7a.
The mean value of the 2,000 samples is 330. The standard deviation is approximately 46. This implies that a rather large number of samples has exceeded the bondline temperature. Equation 5.12 shows the reliability of the isolation layer. The integral has been approximated by taking the number of succeeded samples (T<400) divided by the total number of samples. For this simulation the reliability was approximately 0.79. This is not acceptable as it would imply that two out of ten heat shields will likely fail. Therefore, a thicker layer is required. The next Monte Carlo simulation is using a 5.5 inch layer. The simulation results when using a 5.5 inch layer is shown in Figure 5.7b.
The mean value of this series of simulations is 277 en the standard deviation is around 45. The bondline temperature is thus smaller for the 5.5 inch layer than for the 5 inch layer, as was expected. The reliability will also be larger as more samples have lower temperatures than 400 °C. The reliability was found to be approximately 0.89 which is still too low to accept. A third Monte Carlo simulation has been executed using a thickness of 6 inches. This simulation is shown in Figure 5.7c.
Again, the expected value of the simulation is shifted towards the lower temperature regime. The mean is now approximately 231 and the standard deviation is approximately 47. The reliability is 0.95, which means that a 6 inch layer fulfils the requirement of the acceptable bondline temperature. The factor of 25 % is applied to this thickness, resulting a final thickness of 7.5 inches, or 19 cm.

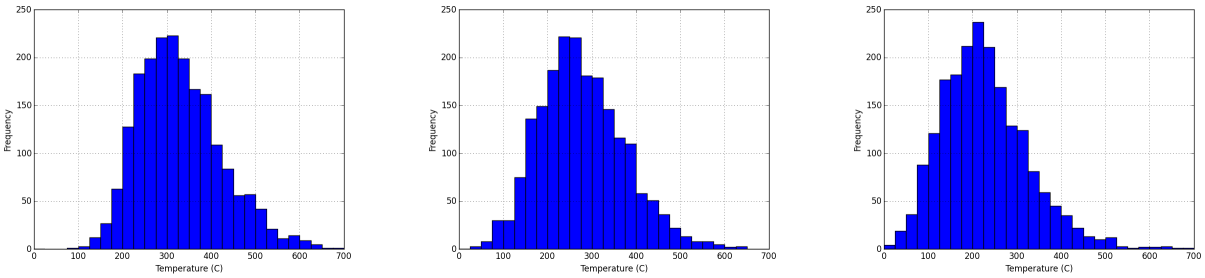

(a) 5 inch isolation layer. *(b) 5.5 inch isolation layer.* *(c) 6 inch isolation layer.*

Figure 5.7: *Monte Carlo simulation for the isolation layer on the HIADS aeroshell.*

Mass of the heat shield

The thickness of the TPS isolation layer is now known and an initial sizing can be executed. A first approximation will be made by adjusting NASA's mass estimation for a heat shield with a diameter of 9 m. This size was taken for a different type of lander. This lander had a larger mass, so for the MUUDS penetrator, the diameter of the heat shield will be smaller. A linearisation is used to calculate the corresponding mass and diameter for the MUUDS mission. After that, individual mass components, like the isolation layer will be estimated on the basis of their density and the heat shield geometry. This is used as a verification for the before mentioned linearisation.

The arrival mass of the lander that was used for the NASA HIAD sizing was 83.6 kg. The initial estimate of the arrival mass for the MUUDS project is 50 kg. The diameter can be scaled according to Equation 5.13.

$$D_{MUUDS} = D_{NASA} \cdot \frac{50}{83.6} = 5.4\text{m} \tag{5.13}$$

The mass can also be scaled according to this relation. However, the mass will not be completely evenly distributed, as the pressure and heat flux are the highest in the nose. Therefore, a scaling factor of 1.2 is applied. Furthermore, a scaling factor for the increase layer thickness has to be applied. The thickness is increased with 20 %, but as the contribution of the isolation to the total mass is only 38.5 %, the scaling factor is 1.077 [42]. The estimated mass of the heat shield will be 8.2 kg, according to Equation 5.14. The height of the EDL projectile that will be used by the HIAD aeroshell is at this point estimated to be 30 cm.

$$M_{MUUDS} = M_{NASA} \cdot \frac{50}{83.6} \cdot 1.2 \cdot 1.077 = 8.2\text{kg} \tag{5.14}$$

Deceleration of the HIAD

The deceleration of the HIAD aeroshell is from the initial Mach 16 to around Mach 1.8. This is the deceleration due to the aerodynamic drag of the heat shield and it resembles the deceleration from the speeds of approximately 3,500 m/s to 400 m/s. The height of this stage is from 220 km to approximately 11 km. The time is linearised for this phase and equals therefore 104.5 s. This was found by dividing the nominal height difference by the mean velocity.

5.2.2 Parachute

The aim of this section is to present the design of the parachute, which consists of the deployment system, the suspension lines and the canopy. The parachute decelerates the projectile from the supersonic (M=2) to the subsonic regime. Driving factors for the design of the parachute are for example its ability to resist the snatch force, which is the force on the suspension lines directly after deployment, and the ability to withstand the parachute opening force. It has to be noted that these calculations are extremely rough and should be handled with care. There are several reasons for the unreliability of the results of which the most important three are: parachutes are stochastic systems, they experience large scatter from time to time in their system performance, the atmosphere is of stochastic character, gusts, wind-shear, up- and down-winds change the kinematics of the trajectory and last there are almost never enough experiments to validate all the models that have been made[3].

It has been chosen to use the same type of parachute that was used for the MSL project, as it has proven to be successful in Mars descent, and is beneficial in both mass and volume. This type of parachute is called a Disk-Gap-Band (DGB) parachute. The canopy is made of nylon and the suspension lines are made of Technora.

[3]University of St. Louis: `http://www.mrc.uidaho.edu/~atkinson/IPPW/IPPW-3/Parachute`

The first step in the sizing process is to determine the required drag area, which is the product of the drag coefficient C_d and the canopy surface S. A schematic drawing of the dynamic situation is depicted in Figure 5.8. The derivation of an expression for the required drag area is shown in the following equations.

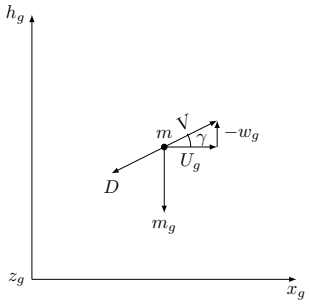

Figure 5.8: *Schematic overview of the dynamic situation of a point mass in flight with arbitrary flight angle.*

$$m\dot{u}_g = -D \cdot cos(\gamma) \quad (5.15) \qquad \dot{x}_g = u_g \quad (5.16)$$

$$m\dot{w}_g = D \cdot sin(\gamma) + m \cdot g \quad (5.17) \qquad \dot{z}_g = w_g \quad (5.18)$$

The initial conditions for this scenario are given by the following relations:

$$t = t_A; x_g = x_A; z_g = z_A; u_g = u_A; w_g = w_A \quad (5.19)$$

There are also some non-linear algebraic relations that need to be established:

$$C_D S(t) = (C_D S)_L + (C_D S)_P \quad (5.20) \qquad \rho = \rho(h) \quad (5.21)$$

For the vertical flight, as which the EDL trajectory is modelled, the following boundary conditions hold:

$$\gamma = -90°; u_g = 0; w_g = V \quad (5.22) \qquad m\dot{V} = m \cdot g - 0.5 \cdot \rho \cdot C_D \cdot S \cdot V^2 \quad (5.24)$$

$$m \cdot \dot{u}_g = 0 \quad (5.23)$$

Table 5.3 shows some basic parameters and their values that have been used as input for the equations.

The system decelerates until the drag equals the weight. The steady state velocity, known as the velocity of descent, can be determined via this principle and it will be used extensively in further calculations. The parameter is calculated via the following parameters.

$$D = m \cdot g \quad (5.25) \qquad mg = \frac{\rho}{2} \cdot V_e^2 \cdot C_D \cdot S \quad (5.26) \qquad V_e = \sqrt{\frac{2 \cdot m \cdot g}{\rho \cdot C_D \cdot S}} \quad (5.27)$$

Now, the drag is related to the weight in steady descent, which will reach an equilibrium. This equality is shown in Equation 5.28. The required drag area can be deduced from this.

$$(C_D \cdot S)_e \cdot \frac{\rho}{2} \cdot V_e^2 = m \cdot g \quad (5.28) \qquad (C_D \cdot S)_e = \frac{m_l \cdot g}{\frac{\rho}{2} \cdot V_e^2} \quad (5.29)$$

Table 5.3: *Input parameters for the load calculations on the parachute.*

Parameter	**Value**
Gravitational acceleration	3.75 m/s^2
Density	0.02 kg/m^3
Universal gas constant	188.92 J/K/mol
Mass projectile	115 kg
Mass parachute	15 kg
Isentropic expansion factor (gamma)	1.2941
Temperature	200 K
Initial Mach number	2.0
C_D parachute	0.65

Using the input variables as stated above, the required drag area is calculated to be 0.36. Using the drag coefficient that the Mars Science Laboratory parachute had, 0.65, the required surface area is calculated. This surface is 1.64 m^2 and relates to a diameter of 1.44 m. A safety factor is applied, increasing this diameter to 2 m^2. The nominal diameter of the canopy now becomes 2.17 m. The suspension lines are sized accordingly to

the Mars Science Laboratory suspension lines. The suspension lines were sized by applying a factor of 1.7 to the nominal diameter. For the case of the MUUDS EDL projectile this would result in a suspension length of 2.46 m. However, this is rather short after the rear of the projectile, so it is recommended to double this length, as the drag would be lower when the canopy would be deployed directly behind the projectile, in the wake rake and the unpredictable vorticity field. Later in this chapter, the control during landing will be discussed and these phenomena will be addressed further. The suspension length is determined to be 5 m instead.

Snatch force

A parameter of specific interest is the snatch force. This is the force that is subjected to the suspension lines during parachute deployment. The snatch force can be approximated by solving the force equilibrium schematically depicted in Figure 5.9.

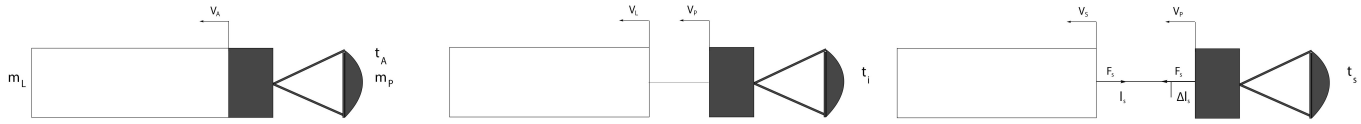

Figure 5.9: *Schematic overview of the dynamic situation on a point mass during parachute deployment.*

The basic principles that form the basis for calculating the snatch force are described in Equations 5.30 to 5.32.

$$\frac{m_L}{2} \cdot V_L^2 + \frac{m_P}{2} \cdot V_P^2 = \frac{m_L + m_P}{2} \cdot V_s^2 + \Delta E \tag{5.30}$$

$$m_L \cdot V_L + m_P \cdot V_P = (m_L + m_P) \cdot V_s \tag{5.31}$$

$$\Delta E = \frac{m_L \cdot m_P}{m_L + m_P} \cdot \frac{\Delta V^2}{2} \tag{5.32}$$

The following equations (Equations 5.36 to 5.39) are derived from Newtons laws of motions and describe the velocity difference at snatch, the distance between $t = 0$ and $t = t_s$. The boundary condition stating that at t_s the distance must equal l_s is applied. V_A is the initial velocity at the beginning of deployment and other parameters are stated in Equations 5.33 to 5.38[4].

$$s_L^* = \frac{2 \cdot m_L}{\rho \cdot (C_D \cdot S)_L} \tag{5.33}$$

$$s_P^* = \frac{2 \cdot m_P}{\rho \cdot (C_D \cdot S)_P} \tag{5.34}$$

$$\Delta s = s_L^* \cdot ln(1 + \frac{t}{t_L^*}) - s_P^* \cdot ln(1 + \frac{t}{t_P^*}) \tag{5.35}$$

$$\frac{\Delta V}{V_A} = \frac{1}{1 + \frac{t_s}{t_L^*}} - \frac{1}{1 + \frac{t_s}{t_P^*}} \tag{5.36}$$

$$t_L^* = \frac{s_L}{V_A} \tag{5.37}$$

$$t_P^* = \frac{s_P}{V_A} \tag{5.38}$$

$$\Delta s(t = t_s) = l_s \tag{5.39}$$

The time to snatch was linearised by taking the initial velocity, V_A as constant and taking the suspension line length as the length parameter. In this way, and using Equation 5.39 as boundary condition, the distance to snatch was determined to be 0.50 m. The energy relation can now be used to derive an expression for the snatch force. This derivation is shown in Equations 5.40 to 5.44.

$$\Delta E = n \cdot \int_0^{\epsilon_s} F_1 l_s d\epsilon \tag{5.40}$$

$$F_1 = k \cdot l_s \cdot \epsilon \tag{5.41}$$

$$k = \frac{F_{B1}}{\Delta l_B} = \frac{F_{B1}}{l_s \epsilon_B} \tag{5.42}$$

$$\Delta E = n \cdot k \cdot l_s^2 \int_0^{\epsilon_s} \epsilon d\epsilon = \frac{n}{2} \cdot k \cdot l_s^2 \cdot \epsilon_s^2 \tag{5.43}$$

$$F_s = n \cdot k \cdot l_s \cdot \epsilon_s = \sqrt{2 \cdot n \cdot k \cdot \Delta E} \tag{5.44}$$

The constant n is the number of suspension lines. This factor is scaled to the number of suspension lines for the MSL project. For this project the number of suspension lines should be 8.65, which was rounded up to the nearest integer, so 9 suspension lines [44]. The strain ϵ and the breaking force F_B are properties of the material and are found in the specifications of the producer[5]. The spring constant can now be determined via Equation 5.45.

$$k = \frac{F_B}{l_s \cdot \epsilon} \tag{5.45}$$

The spring constant equals 2,592 N/m. The breaking force is 3,400 N. The snatch force is calculated to be 6133 N. Last, the load factor can be calculated using Equation 5.46.

$$LF = \frac{F_s}{n \cdot F_B} \tag{5.46}$$

The load factor equals 0.143 for the Technora suspension lines. The last step is to determine the parachute inflation force F_x.

[4] University of St. Louis: `http://www.mrc.uidaho.edu/~atkinson/IPPW/IPPW-3/Parachute`
[5] Teijin Aramid: `http://www.teijinaramid.com/aramids/technora/`

Parachute inflation force

With the snatch force has been determined, there is one last important parameter to asses: the parachute inflation force or parachute opening shock. The parachute inflation force F(t) is captured by Equation 5.47.

$$F(t) = \frac{\rho}{2} \cdot V^2 \cdot (C_D \cdot S) \tag{5.47}$$

In a non-dimensional fashion, the force can be determined by the relative change in drag area. This is shown mathematically in Equation 5.48.

$$x(t) = \frac{\frac{\rho}{2} \cdot V^2 \cdot C_D \cdot S}{\frac{\rho}{2} \cdot V^2 \cdot (C_D \cdot S)_e} = (\frac{V}{V_s})^2 \frac{C_D \cdot S}{(C_D \cdot S)_e} \tag{5.48}$$

In the last equation, V_s is the velocity at snatch and $(C_D S)_e$ is the steady state drag area. The approach that will be used is to find a maximum of x(t), as in Equation 5.49, to determine the opening shock, F_x, which relation is stated in Equation 5.50.

$$C_K = x_{max}(t) \tag{5.49}$$

$$F_x = C_K \cdot \frac{\rho}{2} \cdot V_s^2 \cdot (C_D \cdot S)_e \tag{5.50}$$

Figure 5.10[6] shows the ratio of $C_D S$ over $(C_D S)_e$ for various canopy configurations. The category that fits best with the MUUDS parachute is the ringslot canopy. Its relation is simulated as a linear relation that starts at $t = 0.2$. Before this point in time, it is has a value of 0.1. (0 is not an option as singularities will occur in that case).

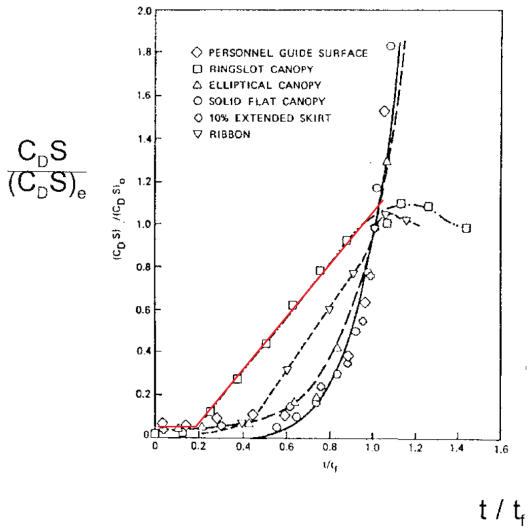

Figure 5.10: *The normalised drag areas versus the normalised time for various configurations of the parachute canopy.*

From Figure 5.10, the following relation, Equation 5.51, is determined, in which $\eta(t)$ is the non-dimensional drag area, t_f is the inflation time, j is an exponent and C_x is the opening force coefficient, or over-inflation factor.

$$\eta(t) = \frac{C_D \cdot S}{(C_D \cdot S)_e} = (\frac{t}{t_f})^j \tag{5.51}$$

The last equation has been subjected to the following boundary conditions:

$$\frac{t}{t_f} = 0 : \eta = 0; \frac{t}{t_f} = 1 : \eta = 1; \frac{t}{t_f} = C_x^{1/j} : \eta = C_x \tag{5.52}$$

The values for the important parameters, subjected to the time vector, are displayed in Table 5.4.
The parameters that have to be determined to find the opening shock, and for which the earlier mentioned parameters are needed, are stated in Equations 5.53 to 5.56.

$$C_K = C_{K0} + C1 + C2 \tag{5.53}$$

$$C1 = \sqrt{j} \cdot (\frac{V_e}{V_s})^2 e^{-B} \tag{5.54}$$

$$C2 = \sqrt{j} \cdot (\frac{V_e}{V_s})^2 (1 - e^{-B}) \cdot sin(-\gamma_0) \cdot e^{-\frac{A}{6} j^{0.25}} \tag{5.55}$$

[6] University of St. Louis: `http://www.mrc.uidaho.edu/~atkinson/IPPW/IPPW-3/Parachute`

Table 5.4: *Arrays that serve as inputs to calculate the opening shock of the parachute.*

t	η	j
0.0	0	0.01
0.2	0	0.01
0.4	0.3	1.314
0.6	0.55	1.170
0.8	0.85	0.728
1.0	1.0	1.0

Table 5.5: *Results of the opening force calculations via the polynomial C_K.*

Parameter	Value
C_{K0}	0.992
$C1$	0
$C2$	0
C_K	0.992
F_x	2071 N

The parameters A and B that emerge in these equations are ballistic parameters that are captured by Equations 5.56 and 5.57.

$$A = \frac{F_{re}}{n_f} = \frac{V_e^2}{g \cdot D_0 \cdot n_f} \tag{5.56}$$

$$B = \frac{F_{rs}}{n_f} = \frac{V_s^2}{g \cdot D_0 \cdot n_f} = A(\frac{V_s^2}{V_e^2}) \tag{5.57}$$

Factors that have not been determined so far are n_f, which is the non-dimensional inflation time, and V_e^2, the steady state velocity of descent. Besides, F_{re} and F_{rs} represent Froude numbers at snatch and at steady state.

$$n_f = t_f \cdot \frac{V_s}{D_0} \tag{5.58}$$

$$V_e^2 = \frac{2 \cdot m_t \cdot g}{\rho \cdot (C_D \cdot S)_e} \tag{5.59}$$

The results of the calculations are summarised in Table 5.5. The opening force is calculated to be 469 N, which is much lower compared to what it would be on Earth.

The mortar section of the Mars Science Laboratory was of dimensions 1.0 m height and 0.5 m in diameter. The canopy of the MUUDS project will be a lot smaller and less suspension lines will be used. To scale the dimensions accordingly to this would not be conservative enough, as the system of mortar firing and canopy deployment does not size according to the canopy surface. However, some reduction in volume is expected. Therefore it is assumed that 50 % of the dimensions are sufficient. This relates to a height of 0.5 m and a diameter of 0.2 m. The mass of this mortar than becomes 2 kg (volume is decreased by a factor 8 and a safety factor of 2 is included). The mass of the canopy and suspension lines can be estimated more precisely. It can be linearly scaled with the MSL mass with application of a safety factor to account for uncertainties. The mass will become approximately 10 % of the original MSL parachute mass, around 6 kg. The total parachute mass is now 8 kg.

Deceleration of the parachutes

The deceleration due to the parachutes starts at an altitude of 11 km and lasts until about 2 km. In this time the projectile decelerates from approximately 400 m/s to about 80 m/s. The time this takes is, using again a linearisation, equal to 37.5 s.

5.2.3 Reverse Thrusters

The last deceleration mechanism are the reverse thrusters. These thrusters will provide the last ΔV that is necessary to safely land and they can be used as guidance to direct the landing projectile. For the thrusters, a pressure feed mono-propellant engine will be used, with an on- and off-switch. Hydrazine will be used as a propellant. As inputs for the MATLAB script, that has been used for the other propulsion system designs, the following data was used (Table 5.6).

Table 5.6: *Input parameters for the EDL module's thruster sizing.*

Parameter	Value	Parameter	Value
ΔV	55 m/s	Nominal thrust	540 N
Burn duration	19.80 s	Total flow rate	0.23716 kg/s
Specific inpulse	232.1 s	Number of thrusters	6
Total inpulse	10,694 Ns		

The resulting masses of the script are detailed in Table 5.7. The last column provides some additional information. The total mass of the system is 12.2 kg. The dimensions are described in Table 5.8. The height of the EDL projectile that is taken by the thruster section is 0.4 m. The MONARC-90LT thruster was chosen to be used for the EDL phase[7].

[7] MOOG: `http://www.moog.com/literature/Space_Defense/Spacecraft/Propulsion/Monopropellant_Thrusters_Rev_0613.pdf`

Table 5.7: *Total mass of the thruster system for the EDL phase.*

Parameter	Value	Parameter	Value
Propellant mass 6 thrusters	4.697 kg	Fuel tank mass	0.39236 kg
Pressurant propellant mass 6 thrusters	0.0365 kg	Pressurant tank mass	0.3326 kg
Thruster mass 6 thrusters	6.72 kg	Total mass of the system	12.1786 kg

Table 5.8: *Dimensions of the thruster system for the EDL projectile.*

Parameter	Value	Parameter	Value
Radius pressurant tank	0.03275 m	Diameter fuel tank	0.162 m
Diameter pressurant tank	0.0655 m	Height fuel tank	0.3 m
Height pressurant tank	0.3 m	ID fuel tank	0.138 m
ID pressurant tank	0.2345 m	Total height EDL thruster stage	0.4 m
Radius fuel tank	0.081 m		

Deceleration of the reverse thrusters

The reverse thrusters are the last deceleration mechanism that is used to slow down the MUUDS projectile. The thrusters ignite shortly after the parachute is detached, at approximately 2 km of altitude. The ignition lasts until a velocity of approximately 25 m/s is reached, which will be at a very short distance to the Martian surface. The whole procedure lasts, estimated via linearisation, approximately 36 s.

5.3 Landing

By choosing the penetrator concept using impactors, there was the possibility to keep the mass and volume budgets within a feasible range. However, the landing phase is one of the critical phases of the mission, and has never been executed on Mars in this way. The purpose of this section is to present the landing phase of the EDL procedure.

5.3.1 Control during Landing

The aerodynamic behaviour of complex models in a hypersonic regime is extremely challenging to predict. The topic of the transition between laminar and turbulent boundary layers, including effects as shearing, warping and the emerging of perturbations, is still a relevant issue in aerodynamic studies. The aim of this subsection is to present a rough qualitative study on the behaviour of the penetrator concept after the thruster phase. Another subject that is addressed is the presence and effect of eventual control surfaces. Due to the very limited mass that is allocated to the EDL-procedure, the control surfaces will be rigid and straightforward.

The penetrator, with its current dimensions, was simulated in SolidWorks. The dimensions of the penetrator are a diameter of 0.9 m and length of 2.1 m for the cylindrical body and a 0.45 m semi-sphere for the blunt nose. The preliminary control surfaces configurations are simple rectangular fins, meant to guide the flow and make it more laminar. Their dimensions are 300 mm in length, 150 mm of height and 15 mm in width.

A number of steps is required for CFD analyses and for the MUUDS penetrator scenario that will now be addressed. Firstly, the geometry of the problem is defined, for the penetrator the earlier specified dimensions are modeled. Subsequently, the control volume that is used, is divided in a mesh. The mesh grid is established by SolidWorks. Then, the physical modelling is defined. This depends to a large extent on the Navier-Stokes equations and derivatives from it. The calculations and iterations are executed by SolidWorks [45]. The last step is defining the boundary conditions of the scenario. The dynamic characteristics have to be inserted. Naturally, the atmospheric conditions will differ for the various altitudes during descent. However, only a single value will be allocated to each of the parameters for simplicity reasons. The boundary conditions are specified in Table 5.9.

Table 5.9: *Input parameters and their relative importance for the CFD analysis of control during landing.*

Parameter	Value	Relative error due to changes
V_z	1,000 m/s	Significant
Pressure	600 Pa	Minimal
Temperature	200 K	Minimal
Gas composition	CO_2	Minimal

As can be seen in Table 5.9, the composition of the Martian atmosphere is assumed to be completely CO_2. In reality, the atmosphere only consists of about 96 % carbon dioxide, but at this stage of the design process, this assumption is assumed to be valid. The most important parameter with regard to potential errors is the speed. On one hand is the velocity direction modelled as a 2D-flow; wind speed is neglected, or alternatively, it is assumed for now that $V_{x,y} << V_z$. On the other hand is the deceleration of the penetrator left out of the equation. The projectile is only evaluated at a supersonic regime. Further studies should also include different velocities to model the projectile behaviour. For now it is assumed that the behaviour in hypersonic situations largely resembles the behaviour in subsonic flows.

First, the penetrator, without control surfaces, is put in the previously specified flow and conditions. The results can be found in Figure 5.11a. The graph displays the vorticity field around the model. The maximum vorticity occurs at the rear and is approximately 11,000 s^{-1} at its maximum.

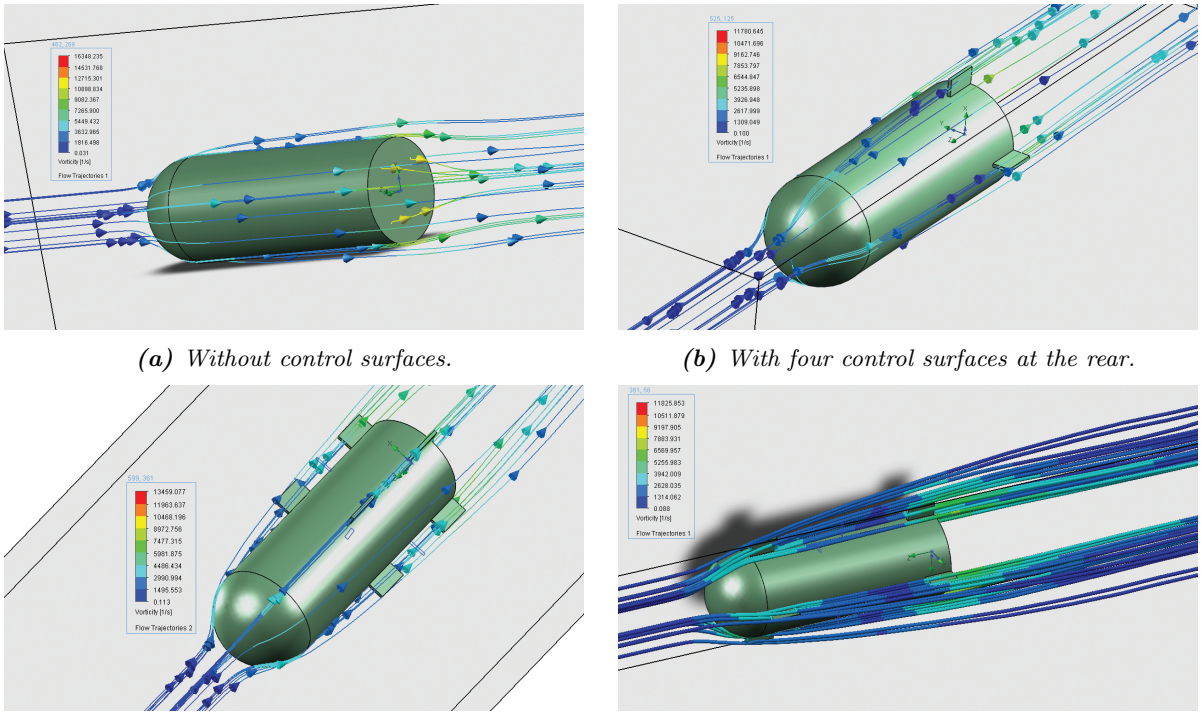

(a) *Without control surfaces.*

(b) *With four control surfaces at the rear.*

(c) *With eight control surfaces, with little spacing.*

(d) *With eight control surfaces, with large spacing.*

Figure 5.11: *CFD simulation of the vorticity field about the MUUDS landing module.*

The objective of this study is to reduce this value of the vorticity by means of adding control surfaces. The four control surfaces are situated on the rear. Again a flow simulation has been executed on the model to assess the change in vorticity due to the control surfaces. The results are depicted in Figure 5.11b. The maximum vorticity is about 7,800 s^{-1}, a decrease of about 30 % with regard to the situation without control surfaces.
Further studies have been done to assess the benefits of having an additional set of 4 control surfaces. Two situations have been evaluated; an extra ring of control surfaces with a little spacing and a ring situated right after the nose of the missile. The results are situated in Figures 5.11c and 5.11d. For the ring with minor spacing, the maximum vorticity level is about 7,500 s^{-1}, a small 4 % difference in comparison to a single ring of control surfaces. For the ring with a large spacing, the maximum vorticity level is also about 7,500 s^{-1}, and thus the same 4 % difference. Therefore, a single ring of four control surfaces will be added to the EDL design.

5.3.2 Inclination at Impact

Of particular interest for the project is the inclination with which the projectile will hit the ground. It is important that the deflection is not too large, as a great inclination will lead to less solar power in the best scenario and failure of the ground station in the worst scenario. Several factors are of influence for the angle, which are of stochastic character. Firstly, there is the velocity from the side. The average velocity is currently not known precisely. As a conservative estimate, it has been chosen to take 100 m/s as the average side wind velocity. The standard deviation has been estimated to be 20 m/s. The other parameters of influence are ground imperfections, thruster quality and the number of control surfaces. The probabilistic distributions of all factors are displayed in Table 5.10. The different thruster and control surface configurations are displayed in Table 5.11.

Table 5.10: *Probabilistic distributions for the parameters of influence on the inclination at impact.*

	Probability distribution	(μ,σ)
V_{side}	Normal	(1.0,0.2)
Ground imperfections	Normal	(0,1)
Thruster quality	Normal	(0,p)
Control surface quality	Normal	(0,q)

Table 5.11: *Standard deviations for different configurations of the thrusters and the control surfaces.*

Standard deviation thrusters, p	Low quality: 2	Medium quality: 0.8	High quality: 0.5
Standard deviation control surfaces, q	No control surfaces: 2	4 control surfaces: 0.8	8 control surfaces: 0.7

Again, it holds for these estimations, that they are rather unprecise. In further project phases the assumptions made should be extensively verified and validated. The approach however should lead to an estimation of the number of projectiles that would suffer great problems due to a too large inclination. In Figure 5.12 a 10,000 sample Monte Carlo simulation has been executed using the earlier mentioned parameters. The plot shows the absolute angle of deflection, measured from the normal. It is estimated at this point that up to an absolute angle of 20 °, the ground stations will not fail during landing. As the last section has shown that the difference between four and eight control surfaces is rather small, it has been chosen to model the angle for four control surfaces. The thruster quality has set to medium level.

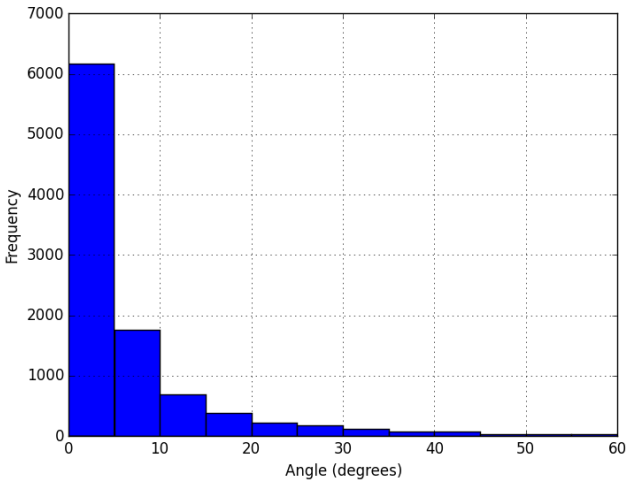

Figure 5.12: *Monte Carlo simulation for the inclination of the landing module with medium thrusters and four control surfaces.*

5.3.3 Impactor Sizing

For the landing of the MUUDS projectile, impactors will be used to absorb the energy from the collision with the Martian surface. This option has been chosen for many reasons, of which the most important is the fact that a lot less mass is needed for the deceleration mechanisms. Other pros in comparison with soft landings are the low costs and the possibility to investigate different terrains than would have been possible with soft landing.

For applications for which energy absorption is necessary, aluminium honeycomb structures often are the best solution for their beneficial strength-to-weight ratio and their capability of absorbing energy. Therefore, an aluminium honeycomb structure has been chosen as the crushable that will be used by the MUUDS projectile to land. The honeycomb that has been chosen is the HEXCEL $3/8 - 5052 - 0007$, which has proved to be a very good solution in both static and dynamic scenarios [46]. The nomenclature is explained in Table 5.12 [8].

Table 5.12: *Explanation for the aluminium honeycomb nomenclature.*

Number	**Explanation**
$\frac{3}{8}$	Cell size in fractions of an inch.
5052	The aluminium alloy.
0007	Nominal reference foil thickness in inches.

[8] Hexcel: `http://www.hexcel.com/Resources/DataSheets/Brochure-Data-Sheets/Honeycomb_Attributes_and_Properties.pdf`

A rough estimate for the total volume of crushables that is necessary will be made. The energy absorption of this honeycomb is 10 kJ/kg. For this stage of the project, the assumption is made that all the kinetic energy of the projectile is transferred to the crushables. This is mathematically shown in Equation 5.60. In this scenario, x is the total mass of the system at the moment of impact. The total mass without the crushables is approximately 50 kg.

$$\frac{1}{2} \cdot x \cdot V^2 = 10^4 \cdot (x - 50) \tag{5.60}$$

$$V = \frac{2}{3} \cdot \pi \cdot r^3 = 0.125 \tag{5.61}$$

From this equation it was deduced that the total mass at impact would be 51.61 kg. This would mean that 1.61 kg would be needed for the crushables. As this part of the mission is vastly critical, this number is rounded up to 2 kg. The mass density of the honeycomb is 16 kg/m^3 [46]. Therefore, 0.125 m^3 would be needed to store the 2 kg honeycomb. In Equation 5.61 it is calculated what radius a semi-sphere, like the one at the bottom of the EDL projectile, would need to have to store the crushables.

This equation yields a radius of 0.39 m and therefore would fit in the 0.45 m radius that it currently has. Therefore, the entire semi-sphere will be used for the crushables, on top of that 50 cm is allocated for all the payload.

5.3.4 Communications and Tracking

During the EDL phase no communication will take place between the orbiter and the EDL modules. In this phase, data is collected on the attitude and trajectory of the landers, but this information is only communicated after the ground stations have fully deployed. Therefore, there is no need to transmit data during EDL which eliminates the need for a transmitting antenna and thus communication on the EDL module.

In addition, Earth ground control is unable to interfere with the landing control since the time it takes to land a module is way shorter than the time it takes to transmit a signal from Earth to Mars, passing by the orbiter relay. There exists no possibility whatsoever to actively control the landers by means of Earth commands. Moreover, control during landing is decided to be merely passive as mentioned in Subsection 5.3.1, this in order to reduce the mass of the EDL module by eliminating the need for actual control by the thrusters and other active control devices. It is thus unnecessary for the orbiter to send commands to the modules during EDL, since this will not alter the passive control mechanisms.

By erasing the need to receive and transmit data for the EDL modules, they do not have an antenna. This highly reduces mass and cost. An antenna would add mass to the pods that would be to be jettisoned from the craft in a later stage of the landing (thus being an expendable, costly product).

The orbiter will start communicating with and tracking the ground station once they have completed their landing and have fully deployed to start their operational lives on the surface of Mars.

5.3.5 Overview of the EDL Module

Lastly, an exploded view of the EDL modules is depicted in Figure 5.13 [31]. In Table 5.13 the most important characters of the EDL module are stated. This mass includes anything except for the structural mass of the module.

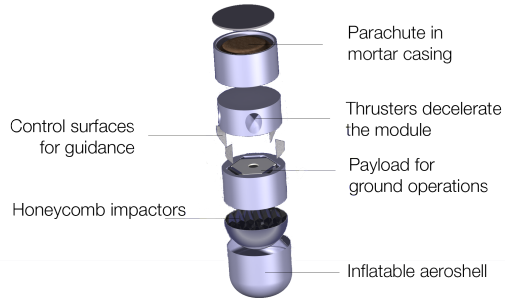

Figure 5.13: *Exploded view of an EDL module.*

Table 5.13: *EDL characteristics.*

Part	Height	Mass
HIAD aeroshell	30 cm	8.2 kg
Parachute	50 cm	8.0 kg
Thrusters	40 cm	12.2 kg
Payload	50 cm	43 kg
Impactors	40 cm	2 kg

6 | Mars Orbit

After the space probe has released the ground stations and its EDL system, the orbiter will be used to execute measurements and to provide communication possibilities with Earth and Mars. In this chapter the orbit in which the orbiter operates will be investigated. Although this chapter is not distinguished as a separate phase when looking back on Section 2.2, it forms the backbone for the orbiter's operational phase.

An overview of this chapter has been visualised in a functional flow diagram in Figure 6.1. First the orbit will be designed, this will be discussed in Section 6.1. A program has been written to simulate the orbit around Mars without any disturbances. However different external forces act on the orbiter, which disturb this motion. Multiple external forces will be treated and a selection of these forces will be implemented in the orbital motion. Other disturbances are left for the next design phase. Once the orbit is simulated, including the external forces, an overview will be made of the orbit. The main characteristics will be given in Section 6.1.1. When the characteristics are known the ΔV required to maintain in orbit will be discussed in Section 6.2. Once the ΔV for orbit maintenance is known the ADCS system will be designed. The last sections of this chapter elaborate on the attitude determination of the orbiter (Section 6.3) and the tracking mechanisms provided (Section 6.4).

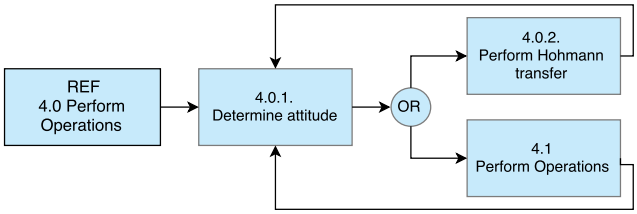

Figure 6.1: *Function flow diagram for the orbit around Mars.*

6.1 Orbit Design

Based on the requirement that a minimum of eight ground stations need to deliver data and every 50 Martian days data must be collected of the full height profile of the atmosphere, a circular orbit with an altitude of 220 km has been chosen. This way all ground stations can communicate with the orbiter every Martian day. Next to this, the instruments of the orbiter can collect data from the full atmosphere with a high resolution.

This section will describe how the orbit has been designed. Firstly, the orbit will be simulated without any disturbances. Mars will be considered as a point mass at its centre. In this case the only force acting on the orbiter will be the gravitational force, which is presented in Equation 6.1.

$$F_g = G \cdot \frac{M_{mars} \cdot m_{orbiter}}{r^2} \tag{6.1}$$

However, the orbiter will have an initial velocity in this orbit. This velocity will be calculated with the vis-viva equation shown in Equation 4.5. This is the velocity component perpendicular to the radius vector of the planet, because a circular orbit will be used. In contrary to this perpendicular velocity component the orbiter will rotate around Mars due to the gravitational force. To simulate this movement a fourth order Runge Kutta method has been used, with a stepsize of 1 second. This method has a truncation error of the fifth power.

Drag

The orbiter will not stay in a perfect, circular orbit but will decrease in altitude due to external forces. The first force considered is the drag force. The drag force experienced by the orbiter can be considered as in Equation 6.2.

$$F_d = C_D \cdot \frac{1}{2} \cdot \rho \cdot v^2 \cdot A \tag{6.2}$$

The forces will act in the opposite direction of the velocity. This will result in a decreasing altitude.

The maximum drag at an altitude of 220 km has been calculated, assuming a C_D of 1, a maximum frontal area of 19.6 m^2, and with a density as beind simulated using the Mars-GRAM[1]. The values calculated can be found in Table 6.1.

[1] Mars-GRAM: `http://spacescience.arc.nasa.gov/story/mars-global-reference-atmospheric-model-mars-gram`

Table 6.1: *Absolute maximum drag force of the orbiter around Mars.*

	Absolute value	Intensity	Direction
Drag	4.404 10^{-13} N	constant with velocity	speed

Jn,m effect

Because Mars is irregular both in shape and mass distribution, the gravitational force acting on the orbiter is not constant in orbit. To take this shape into account extra gravitational potentials need to be taken into account. This potential can be obtained by using Equation 6.3 [1], the Legendre function shown in Equation 6.4 and the Legendre Polynomial, shown in Equation 6.5 [47]. In Equation 6.3 the variable $J_{n,m}$ is a value which describes the shape of Mars, δ the latitude of Mars, and λ the longitude.

$$U_{n,m} = -\frac{\mu}{r}\left[1 - \sum_{n=2}^{\infty} J_n \left(\frac{R_{Mars}}{r}\right)^n P_n \sin\delta + \sum_{n=2}^{\infty}\sum_{m=1}^{n}\left(\frac{R_{Mars}}{r}\right)^n P_{n,m}(\sin\delta)\cos(m(\lambda-\lambda_{n,m}))\right] \tag{6.3}$$

$$P_{n,m}(x) = (1-x^2)^{m/2}\frac{d^m P_n(x)}{dx^m} \tag{6.4}$$

$$P_n(x) = \frac{1}{(-2)^n}\frac{d^n}{dx^n}(1-x^2)^n \tag{6.5}$$

To find the acceleration in the radial direction the partial derivative has to be taken in this direction.

$$a_r = -\frac{\partial U}{\partial r} \tag{6.6}$$

The Martian southern hemisphere surface lies approximately 5 km higher than its northern hemisphere [48]. The zonal harmonic difference is therefore the biggest. Because this is the biggest effect, in this study the second-order zonal harmonic (J_2) and the third-order zonal harmonic (J_3) will be taken in consideration. However for a more accurate orbit behaviour prediction, also the tesseral harmonic effect should be taken into account. This will be left for the detailed design phase. Using Equations 6.3-6.6 the equation for the radial acceleration due to the J_2 and J_3 effect can be found, shown in Equation 6.7 and 6.8.

$$a_{r,2} = 3\cdot\mu\cdot J_2\cdot R_{Mars}^2\cdot r^{-4}\left(-\frac{1}{2}+\frac{3}{2}\sin^2(\delta)\right) \tag{6.7}$$

$$a_{r,3} = -\frac{1}{2}\cdot\mu\cdot J_3\cdot R_{Mars}^3\cdot r^{-5}(82\cdot\sin(\delta) - 120\cdot\sin^3(\delta)) \tag{6.8}$$

Using these equations and values of J_2=1,960·10^{-6}, J_3=31.5·10^{-6} [48].

Table 6.2: *Forces due to J_n effect of the orbiter around Mars.*

	Force at δ=0°	Force at δ=35°	Intensity	Direction
$\mathbf{J_2}$	-8.524·10^{-3} m/s^2	1.111·10^{-4} m/s^2	Variable, always present	Radial
$\mathbf{J_3}$	0 m/s^2	7.999·10^{-4} m/s^2	Variable, always present	Radial

Third body

The orbiter will be attracted the most by Mars, however all bodies attract each other. In this section the five celestial bodies near Mars; Phobos, Deimos, Earth, Sun and Jupiter, are discussed. To check if the third body acceleration can be neglected the maximum acceleration has been calculated with Equation 6.9. The index P stands for the values of the interfering body.

$$A = 2\left(\frac{M_P}{M_{Mars}}\right)\left(\frac{R_{Mars}}{R_P}\right)^3 \tag{6.9}$$

Using Equation 6.9, Table 6.3 has been constructed. The values in this table represent a fraction of the Mars gravitational force. As can be seen Phobos produces the biggest perturbation.

Table 6.3: *Acceleration.*

	Phobos	Deimos	Earth	Sun	Jupiter
Fraction of acceleration	4.862 e-13	3.910e-15	1.066e-15	7.479e-12	2.781e-16

Solar radiation

The next disturbance considered is the solar radiation pressure. The electromagnetic radiation produced by the Sun carries momentum. By reflecting the radiation pressure an exchange of moment takes place. As a result a pressure is exerted on the orbiter. The pressure can be calculated with Equation 6.10 [49]. To calculate the maximum solar radiation pressure, the maximum solar flux ($F_\odot$) on Mars will be used as been found in Figure 4.7.

$$P_M = \frac{F_\odot}{c} \tag{6.10}$$

The perturbing effect is directly dependent on the area to mass ratio. The bigger the illuminated area the bigger the force exerted. The solar radiation force can be expressed as in Equation 6.11 [49]. In this equation the term "s", is a reflection constant between 0 and 2, in this study set to its maximum. The area used in this equation is the area pointed to the Sun, which has been set to a maximum values of $25\,m^2$. The other values used in this equation, $a_\odot$ and $r_\odot$, are the distance Sun-Mars, $2066{\cdot}10^5$ km, and Sun-Spacecraft respectively.

$$A_{SRP} = s\frac{A}{m_{orbiter}}P_M(\frac{a_\odot}{r_\odot})^2 \tag{6.11}$$

Using these values and the equation the maximum solar flux experienced during the orbit phase has been calculated, see Table 6.4.

Table 6.4: *Absolute maximum solar force of the orbiter around Mars.*

	Absolute value	**Intensity**	**Direction**
Solar Flux	$5.323{\cdot}\ 10^{-7}$ m/s	Highly variable	Away from Sun

Magnetic field

The magnetic field has been investigated by the Mars Global Surveyor. As a result the MGS found that Mars has a localised magnetic field [50]. Which makes the acceleration produced by the magnetic field very variable and therefore negligible. However in a next study more research has to be conducted to make a better magnetism profile in order to add this to the model resulting in more accuracy.

6.1.1 Orbit Overview

Now all parameters used in this study are known the orbit characteristics can be calculated. As has been explained before a circular orbit at an altitude of 220 km has been chosen. However due to the perturbations explained in the previous section the circular orbit will be disturbed. The atmospheric drag, represented in Table 6.1, creates a small force, but it is constantly exerted, which induces a significant deceleration over time. The extra gravitational potential produced by the irregular shape of Mars is variable but also always present and therefore important to take into consideration. The next perturbation treated was the perturbation due to third bodies. As has been concluded, Deimos and the Earth had the maximum perturbation. However, Earth is only this close to Mars for a short period in time and will be neglected. Deimos is always relatively close to Mars, but its accelerations are rather small. Besides, the direction of this acceleration changes constantly. This disturbance will therefore not be taken into account in this study. The last perturbation discussed is the solar flux. The solar flux is highly variable, at its closest point to the Sun the solar flux is perceptible but once the orbiter is on the other side of Mars the flux is obstructed by Mars. So in this study the solar flux will not be taken into account as well and left for the next phase. As has been discussed before in this study, the magnetic flux will not be taken into account. So taking into account drag, J_2 and J_3 the orbit characteristics have been calculated using Python. An overview can be found in Table 6.5.

Table 6.5: *Orbit characteristics.*

Initial values	
Orbit height	220 km
Mean velocity	3,445 m/s
Inclination	35 °
Period	1 hour 50 minutes
Decay rate	0.99966 day^{-1}
Eclipse time	38.83 %
Mean motion	13.5 rev/day
Designed mission duration	1,336 Sols

Using the characteristics of the orbit found, a plot (Figure 6.2[2]) has been made of the trajectory of the orbiter projected onto the Martian surface. The dots in this figure are the locations of the ten ground stations. The circles surrounding these dots illustrate the contact environment of the ground stations. This means that when the orbiter is within such a circle, the possibility exists to have contact with one of the ground stations. To construct these circles it has been assumed that the ground station can contact the orbiter if it is above an angle of 20° with respect to the surface. Such a circle has a diameter of 1,208 km at the altitude of the orbiter. Which means that the orbiter could have a maximum of 350 seconds contact time with an orbiter a time. However this value is a theoretical maximum value and will never be met.

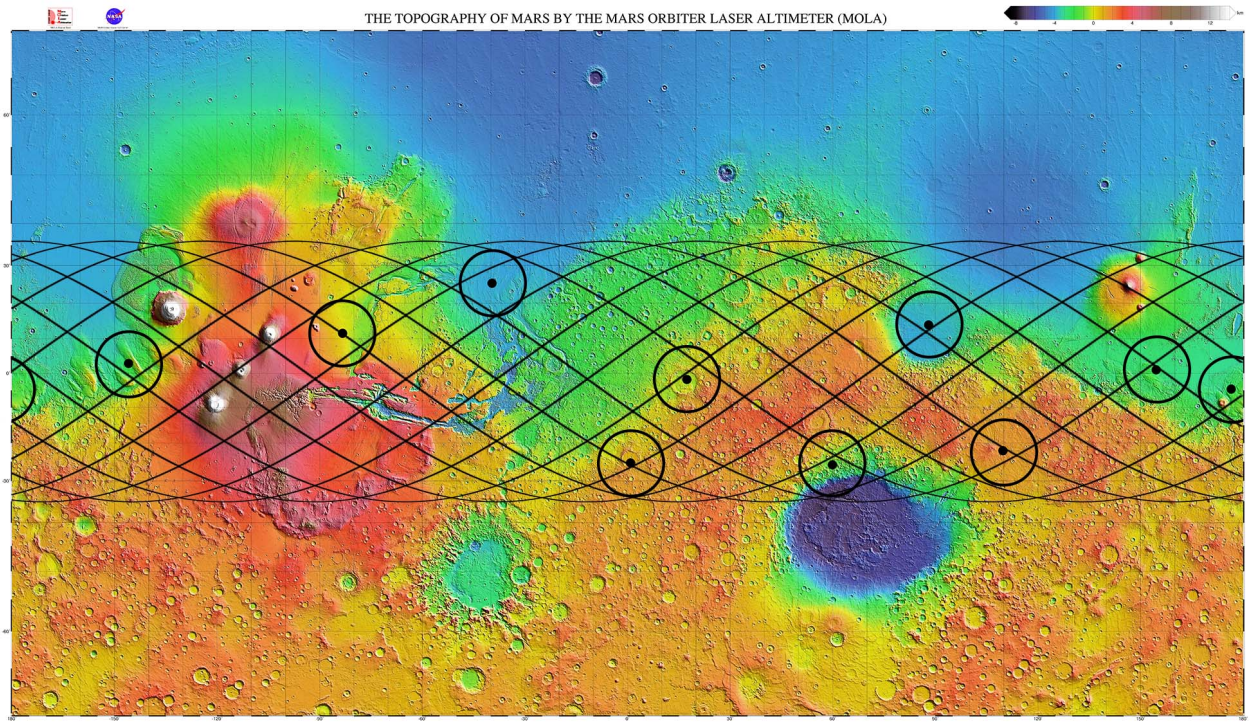

Figure 6.2: *Trajectory described during one Martian day projected on the surface of Mars, also called the ground track of the satellite.*

Using Figure 6.2 an example time schedule has been constructed, Table 6.6. Because the pattern in Figure 6.2 will shift every day, operations will differ daily. The schedule of Table 6.6 has been visualised in Figure 6.3.

Table 6.6: *Example of a day schedule.*

Round	Task	Maximum time spend
1	Communication with ground station 8	280 s
2	Communication with ground station 6	298 s
3	Communication with ground station 2	333 s
4	Communication with ground station 7	315 s
5	Communication with ground station 4	333 s
6	Communication with ground station 1	245 s
	Communication with ground station 5	245 s
7	Communication with ground station 9	315 s
8	-	-
9	Communication with Earth	1,900 s
10	Communication with ground station 3	140 s
11	Take measurements	
12	Communication with ground station 10	140 s
13	Communication with ground station 8	210 s

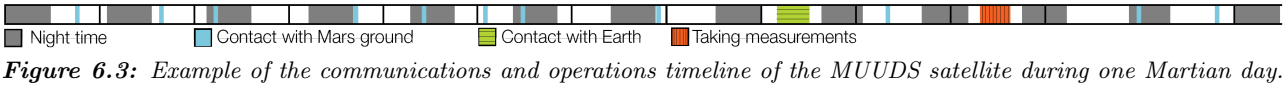

Figure 6.3: *Example of the communications and operations timeline of the MUUDS satellite during one Martian day.*

[2]MOLA: `http://mola.gsfc.nasa.gov/images.html`

6.2 Orbit Maintenance

The trajectory control system will have to correct for the spacecraft's altitude decay due to the non-uniform Martian gravity field, and due to atmospheric drag disturbances. Other disturbances are considered negligible, see Section 6.1.1. Minor adjustments to the orbit around Mars are required to compensate for these disturbances and disturbances in other directions. These minor adjustments are translated to adjustments in the magnitude and direction of the spacecraft's velocity vector. Therefore, an orbit correction is achieved by delivering a small ΔV. This ΔV will be delivered numerous times during the orbiter's life.

The orbiter will be controlled within a boundary of 1 km altitude. This means that once the orbiter has descended more than 1 km the orbiter will produce a ΔV to increase its orbit altitude. Using the orbital characteristics discussed in Section 6.1.1 the orbiter will descent in 13.93 days to an orbit altitude of 219 km. When it reached this point it will provide a ΔV to be brought in a Hohmann transfer orbit. The orbiter will provide a ΔV to go from the circular orbit to a Hohmann orbit, which has a perigee at 219 km and a apogee at 220 km. Once the orbiter is at the apogee of the Hohmann orbit it will provide another ΔV to insert in the new circular orbit. The velocity differences provided by the orbiter will be calculated with Equation 6.12, to enter the transfer orbit, and Equation 6.13 to enter the higher circular orbit. In these equations r_1 is the radius of the lowered orbit and r_2 of the required orbit.

$$\Delta V_1 = \sqrt{\frac{-2 \cdot \mu}{r_1 + r_2} + \frac{2 \cdot \mu}{r_1}} - \sqrt{\frac{\mu}{r_1}} \tag{6.12}$$

$$\Delta V_2 = \sqrt{\frac{\mu}{r_2}} - \sqrt{\frac{-2 \cdot \mu}{r_1 + r_2} + \frac{2 \cdot \mu}{r_2}} \tag{6.13}$$

Every 13.93 days a ΔV of 0.4773 m/s has to be delivered to gain altitude. In the two Martian years a total of 45.84 m/s needs to be delivered by the orbiter. However in these calculations only the altitude corrections has been taken into account. Therefore a safety factor of 10% is added. So the ADCS will be designed for a ΔV of 50.42 m/s.
Based on the total ΔV calculated to be needed during the orbiter's lifetime, the thrusters that have to deliver this ΔV can be selected and sized. In addition to that the propellant mass required for the total ΔV can be computed.

The propellant mass required to deliver the total ΔV can be computed by using the rocket Equation [1]. Equation 6.14 gives the relationship between the ΔV, the thrusters I_{sp}, and the orbiter's initial mass M_0 and propellant mass M_p.

$$\Delta V = I_{sp} \cdot g_0 \cdot ln\left(\frac{M_0}{M_0 - M_p}\right) \tag{6.14}$$

The specific impulse I_{sp} depends on the selected thruster. To select the thrusters for orbit maintenance, a comparison should be performed between different thrusters based on how much propellant they need, to achieve the ΔV required.

The propulsion systems that will be compared are cold gas, mono- and bipropellant propulsion. Electric propulsion is not considered due to its extremely high power consumption [1]. Different types of thrusters from different manufacturers are compared in Table 6.7.

Table 6.7: *Comparison between cold gas, mono- and bipropellant propulsion systems from different manufacturers [1] [33] [51] [52] [53] [54].*

	Orbit Maintenance Thrusters						
	Cold Gas		Monopropellant			Bipropellant	
Thruster	**SVT01**	**58E142A**	**MRE-0.1**	**MR-111C**	**MONARC-1**	**DST-11H**	**DST-12**
Manufacturer	AMPAC	Moog	Northrop	Aerojet	Moog	Moog	Moog
I_{sp}	70 s	57 s	216 s	229 s	227.5 s	310 s	302 s
Engine mass	0.051 kg	0.016 kg	0.5 kg	0.33 kg	0.38 kg	0.77 kg	0.64 kg
Propellant mass	15.93 kg	19.40 kg	5.29 kg	4.99 kg	5.03 kg	3.70 kg	3.80 kg

From Table 6.7 it appears that the bipropellant thruster systems are using the least propellant mass for the total ΔV that has to be delivered. However, their thruster mass is quite high compared to the cold gas and monopropellant thrusters. Once multiple thrusters are taken on board for orbit maintenance, the advantageous low propellant mass of the bipropellant systems is nullified by their increasing thruster mass. Sticking to the thruster layout as proposed in Figure 4.13, and accounting for 12 thrusters to maintain attitude and orbit control, the monopropellant systems eventually becomes lighter than the bipropellant systems when incorporating the

thruster mass in the propulsion system mass. In Table 6.8 the effect of the thruster mass on the total propulsion system mass is shown.

Table 6.8: *Comparison between cold gas, mono- and bipropellant propulsion systems from different manufacturers [1] [33] [52] [51] [53] [54].*

	Orbit Maintenance Thrusters						
	Cold Gas		Monopropellant			Bipropellant	
Thruster	**SVT01**	**58E142A**	**MRE-0.1**	**MR-111C**	**MONARC-1**	**DST-11H**	**DST-12**
Engine mass	0.051 kg	0.016 kg	0.5 kg	0.33 kg	0.38 kg	0.77 kg	0.64 kg
Number of thrusters	12	12	12	12	12	12	12
Propellant mass	15.93 kg	19.40 kg	5.29 kg	4.99 kg	5.03 kg	3.70 kg	3.80 kg
Total mass	16.54 kg	19.59 kg	11.29 kg	8.95 kg	9.59 kg	12.94 kg	11.48 kg

Based on Table 6.7 and 6.8, the decision is made to use the MR-111C thruster system developed by Aerojet. This is a convenient result, since the thrusters used for ADCS during interplanetary transfer were already determined to be the MR-111C series (Subsection 4.4.2). By using the same thrusters for attitude control during interplanetary space travel as for orbit maintenance, the cost of the propulsion systems is reduced since there is no need for an extra system. Moreover, the same propellant can be used for attitude control in transfer as for orbit maintenance (see Section 4.5). So next to cost savings and a reduced complexity by the need for only one type of thruster system for both interplanetary ADCS and orbit maintenance, the cost further reduces by the need for only one propellant type and thus only one propellant tank for interplanetary ADCS and orbit maintenance.

In summary, the total propellant mass needed for orbit maintenance is 4.99 kg when using the MR-111C thrusters which are also used for attitude control (see Subsection 4.4.2). This propellant mass will provide the orbiter with the required ΔV for orbit maintenance during its entire lifetime. The structural mass of the thruster system is 3.96 kg, as mentioned in Subsection 4.4.2, and the power consumption will accumulate to 13.64 W.

6.3 ADCS after In-Orbit Insertion around Mars

At the end of the interplanetary transfer, the spacecraft will perform a ΔV manoeuvre to achieve a circular orbit around Mars as was explained in Section 4.2. During this manoeuvre, all ADCS systems will be shut down and only the main thruster stage will deliver the ΔV necessary for in-orbit injection. The tracking system remains active, as explained in Section 6.4.

Once the spacecraft is brought in its orbit around Mars, the main thruster stage will be released and disposed off. The vehicle starts its orbiting phase around Mars, in which the orbiter segment of the spacecraft will collect atmospheric data on Mars and the landers will be released one-by-one. The ADCS during the release is discussed in Chapter 5.
However, before being able to do so, the spacecraft should be able to reposition itself after it has been brought into orbit. A coarse sun sensor will provide an initial attitude determination for the craft. This sensor will make sure that the spacecraft is able to orientate itself with respect to the Sun. After an initial attitude determination by the sun sensor, the Procyon star trackers can power up again and take over the attitude determination function in combination with the accelerometers and CIRUS (Subsection 4.4.1). The coarse sun sensor will be shut down once exact attitude determination has become possible again. It will only be powered up after the spacecraft has gone into safe mode. When the spacecraft wakes up from this mode, the spacecraft has to reorientate itself once more and needs another initial attitude determination. A coarse sun sensor can fulfil this need.

The Coarse Sun Sensor (CSS) of Moog Bradford Technology is selected to provide a means for coarse attitude determination after in-orbit injection and after safe mode. The technical specification of CSS can be found in Table 6.9. As advertised in the Moog Bradford Technology brochure, "*The Coarse Sun Sensor (CSS) delivers coarse information about the position of the sun [sic] relative to the spacecraft. This information is used for coarse maneuvering [sic] of the spacecraft and to inform the spacecraft about the position of the sun [sic] when it is in a safe mode of operation*" [55].

Table 6.9: *Coarse Sun Sensor developed by Moog Bradford Technology [55].*

Coarse Sun Sensor (CSS)	
Mass	0.215 kg
Power	0 W, passive system
Size	110 mm x 110 mm x 30 mm
Field of View	$\pm 90°$ x $\pm 90°$ hemispherical
Accuracy	$\pm 1.5°$ (3σ)
Redundancy and reliability	Self-redundant
Operational temperature	-80°C - +120°C
Radiation environment	Radiation hardened

6.4 Tracking during and after In-Orbit Insertion around Mars

Once the spacecraft is brought into orbit around Mars after the ΔV orbit injection manoeuvre, ground control on Earth should be able to assess whether the spacecraft was able to insert in and achieve its correct orbit. A profile of the spacecraft's trajectory during in-orbit insertion should be established. The position and velocity of the craft at different time instants of the in orbit insertion operation are communicated to Earth by the Small Deep Space Transponders previously mentioned in Subsection 4.3.2.

When the spacecraft has reached its circular orbit around Mars, the SDSTs start transmitting Delta-DOR signals. These signals are picked up by the Deep Space Network. The signals are processed to discover the MUUDS spacecraft's position around Mars and orbit velocity. With this information it can be validated whether the space vehicle has achieved its correct orbit, and whether the craft is able to maintain that orbit. To maintain an orbit, the spacecraft has ADCS thrusters on board for orbit maintenance. It should also be assessed by ground control on Earth whether the orbit maintenance control is executed efficiently and effectively. Again, information of the position and velocity of the spacecraft is required.

In summary, the SDSTs will provide a position and velocity profile of the spacecraft when it is in orbit around Mars. This will enable ground control on Earth to track the craft's whereabouts.

7 | In-Orbit Operations

The operations performed by the orbiter will be discussed in this chapter. First, the selected remote sensing instruments are described in Section 7.1. These instruments require a certain pointing while operating, which is discussed in Section 7.2. Finally the tracking is described in Section 7.3 during the in-orbit operations. The orbit maintenance is explained in Chapter 6 in Section 6.2.

7.1 Remote Sensing Atmospheric Measurements Orbiter

In this section the measurements performed by the orbiter are discussed. First, the selected instruments are described in Subsection 7.1.1 including their main specifications. Then an estimation is done on the amount of data produced by the instruments for each measurement in Subsection 7.1.2. From this data, in combination with orbital characteristics, specifications are made for the frequency and division of the measurements in Subsection 7.1.3. Finally an overview is given of the mass, power consumption, data volume and rate of the orbital instruments in Subsection 7.1.4.

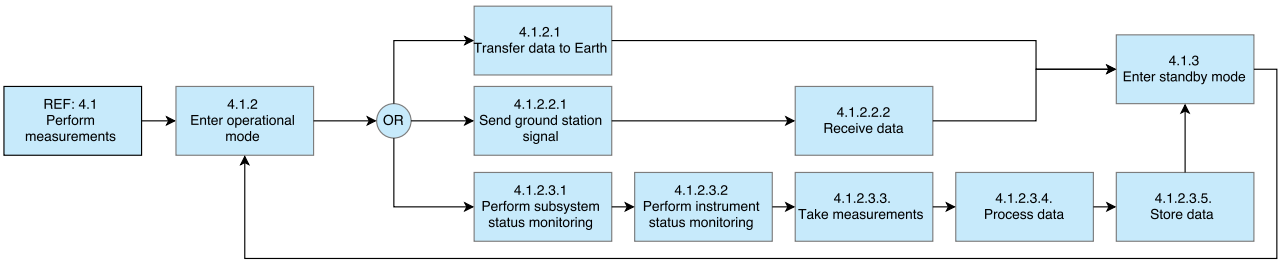

Figure 7.1: *Functional flow for the operation phase of the orbiter.*

7.1.1 Instrument Description and Specification

The orbiter will need to perform measurements of the Martian atmosphere, which includes the following data: temperature, pressure, atmospheric composition, dust and wind speed. Using remote sensing a vertical profile of the atmosphere can be created. To do this several instruments are needed, which are selected from off-the-shelf instruments, since designing the instruments would take more time than available in this project. Some of the instruments that are selected have been used in other satellites, while others are still in the development phase. Important criteria for selecting those instruments are of course mass and power consumption. As a guideline, a maximum total mass of 36 kg and a maximum total power consumption of 65 W for the instruments are taken as budgeted. Each selected instrument will now be discussed including a table of specifications. Adding up the masses and power specifications for the orbiter instruments the total mass comes down to 31.7 kg with a total power consumption of 25 W, this is excluding data storage.

UV spectrometer

This UV instrument is based on the SPICAM UV instrument block on the SPICAM Light, on board of the Mars Express Orbiter (2003) [56][57]. This UV spectrometer can measure temperature, pressure, density of O_2, O_3, CO_2 and aerosols (clouds/dust) by stellar occultation.

In stellar occultation the instrument will point towards a bright star and will measure the light spectrum. Because the satellite is in orbit, the star will slowly move behind the horizon and the line of sight of the instrument will cross the atmosphere slice by slice. The light spectra of these measurements will be compared to the 'clean' spectrum of the star and from the difference between the spectra a vertical profile of transmission spectra can be obtained. From these spectra a vertical profile of the CO_2, O_3 and O_2 density and aerosols can be calculated. The vertical profile of the CO_2 density is integrated from the top to obtain the pressure, after which the temperature is calculated applying the perfect gas law. Stellar occultation gives the best results when performed on the night side, moving away from the observed star. Some benefits of stellar occultation are: no instrument calibration needed, excellent vertical resolution (star is a point source) and the accuracy is independent of the orbiter attitude knowledge. The SPICAM instrument on the Mars Express Orbiter performed 3-5 stellar occultations per orbit and a measurement time is 1-4 minutes [57].
In Table 7.1 several specifications of this instrument are listed[1].

[1]SPICAM on Mars Express specifications: `https://pds.jpl.nasa.gov/ds-view/pds/viewInstrumentProfile.jsp?INSTRUMENT_ID=SPICAM&INSTRUMENT_HOST_ID=MEX`

Table 7.1: *Technical specifications of the SPICAM UV spectrometer for atmospheric temperature, pressure, density dust and atmospheric composition measurements [56][57].*

SPICAM Light UV spectrometer	
Measurement parameters	O_3 (vertical profile), CO_2 (atmospheric density, pressure and temperature vertical profile) Aerosols (vertical profile), O_2 (vertical profile)
Mass	4.14 kg
Dimensions	40 cm× 24 cm × 11.5 cm
Power consumption	9.5 W
Data volume	3.1 kbit per measurement
Viewing directions	limb (stellar occultation)
FOV	2°× 3.16°
Pointing accuracy	0.2°
Spectral range	118-320 nm
Spectral resolution per pixel	0.51 nm
Altitude range	O_3: 10-50 km, CO_2 : 20-160 km, Aerosols: 5-60 km, O_2 : 35-90 km
Accuracy	O_3: 2-10%, CO_2 : 2-10%, Aerosols: 10^{-3}, O_2 : 20%
Vertical resolution	O_3: <1 km, CO_2 : <1 km, Aerosols: 2-3 km, O_2 : unknown

Spectropolarimeter

A spectropolarimeter, called SPEX, will be used to obtain a vertical profile of aerosols (dust, iceclouds). Of these aerosols micro- (size, shape, composition) and macrophysical (amount) characteristics and optical thickness of the Martian atmosphere will be measured by combining the measured intensity and polarisation spectra of Mars reflected sunlight. Nine sensors will be measuring simultaneously in different directions along a line, along the track of the orbiter. Since for each location on this line measurements will be taken from nine different angles, a vertical profile of the aerosol characteristics for this location can be obtained. Because the instrument makes use of reflected sunlight, measurements can only be done when the orbiter is positioned at the day side of Mars. The SPICAM UV spectrometer (see Subsection 7.1.1) is also capable of measuring aerosols, however not as accurate and not in the same extend as SPEX, furthermore this instrument is relatively light and has a low power consumption. This instrument is still in the final stages of its development phase, nonetheless it seems to become a promising instrument with a potential place on board the Chinese Mars Orbiter, JUICE and ISS. In Table 7.2 several specifications of the SPEX instrument are shown [58][59][60][2].

Table 7.2: *Technical specifications of the SPEX spectropolarimeter for dust content measurements [58][59][60].*

SPEX spectropolarimeter	
Measurement parameters	Aerosol properties (vertical profile) Optical thickness
Mass	∼ 2 kg
Dimensions	13 cm × 13 cm × 6 cm
Power consumption	∼ 2 W
Data volume	0.5 Gbit/day (continuous measuring), 10 bits sampling
Spectral range	400-800 nm
Spectral resolution for polarisation	20 nm
Spectral resolution for intensity	2 nm
Viewing directions	9 directions: 0° (Nadir), ± 14°, ± 28°, ± 42°, ± 56°
Pointing accuracy	0.1°
FOV for each viewing direction	1°× 7° (cross-flight)
Polarisation accuracy	$2 \cdot 10^{-4}$

2-micron coherent Doppler lidar

2-micron lidar technology already exists in a ground based form on Earth and is likely to become the standard for wind measurements from space. A lidar (Laser Imaging Detection And Ranging) emits laser pulses which are partly backscattered by atmospheric particles (aerosols) that are moving with the wind. The backscattered signal experiences a shift in frequency with respect to the transmitted signal, called Doppler shift, from which the velocity of the particle can be calculated. This is done with Equation 7.1, where V is the wind velocity along the line of sight, λ is the wavelength and Δf is the Doppler frequency shift [61]. From the elapsed time the distance to the particle can be calculated. The distance and the Doppler shift together can form a 3D wind profile over the full height of the atmosphere.

$$V = \frac{\lambda}{2} \cdot \Delta f \tag{7.1}$$

[2]SPEX presentation: `http://www.lr.tudelft.nl/fileadmin/Faculteit/LR/Nieuws_en_Agenda/Nieuws/Nieuwsarchief/2009/doc/SPEX_Payload_on_FAST,_Erik_Laan,_TNO.pdf`

Current Doppler lidars for airborne applications are quite heavy (30 kg or more) and require more that 600 W power [62] [63]. The Aladin space borne lidar on the ADM-Aeolus mission from ESA is even heavier and needs 800 W power [61]. However for Martian application these lidars can become smaller and less power consuming since the requirements are less demanding for the Martian atmosphere. NASA Langley Research Center (LaRC) is currently developing a coherent 2-micron Doppler lidar together with universities and Simpson Weather Associates (SWA) [64][65]. Their current lidars are at TRL 7, with promising results for application for Earth, Mars and Venus. New laser and detector technologies from NASA ESTO (Earth Science Technology Office) and industry are lowering the power consumption of the lidar rapidly. The Laser Risk Reduction Program (LLRP) has done research on high performance 2-micron lidars as well with significant progress in accuracy and performance. The targets for readiness of space borne lidars are the 2018/2020 launches, which includes the MUUDS mission[3].

Estimated specifications of the 2-micron coherent lidar are listed in Table 7.3. These specifications are based on a proposed small Doppler wind lidar for Venus [66], however this instrument would also be suitable for measurements on Mars. For the weight a range is given between 15 and 50 kg, in order to properly size the other subsystems a value of 25 kg is assumed for the lidar.

Table 7.3: *Technical specifications of the 2-Micron Coherent Doppler Lidar for wind velocity measuring.*

2-micron coherent Doppler lidar	
Measurement parameter	3D wind profiling Backscatter (aerosols)
Mass	15-50 kg
Dimensions	unknown
Power consumption	10 W (includes cooling)
Scanning angle	20° to 40° about fixed Nadir, cross-flight
Wavelength	2 µm
Pulse energy	1 mJ
PRF (Pulse Repetition Frequency)	500 Hz
Pulse length	180 ns
Telescope diameter	0.1 m
Dwell time	10 s
Altitude range	0-90 km (and probably higher)
Accuracy	<1 m/s
Vertical resolution	1 km
Horizontal spacing between wind profiles	400 km
Maximum horizontal winds	200 m/s
Aerosol profile height	1 km
Orbit height	200-300 km

7.1.2 Measurement Data Volume

UV spectrometer

As mentioned in Subsection 7.1.1, the SPICAM UV spectrometer measures vertical profiles of spectra, which produces large amounts of data. However when processing this data with the on-board computer the amount of data can be reduced significantly. Each single UV spectrometer measurement produces 3.1 kbit of data (see Table 7.1). With a vertical resolution of approximately 1 km over a height of 155 km the total amount of data per stellar occultation comes down to 480.5 kbit. An estimation of the data volume, after processing the spectra, is shown in Table 7.4 resulting in a reduced total data volume of 2.2 kbit. The resolution of the measured parameters is based on the measurement accuracy listed in Table 7.1 on which the number of bits is chosen to represent the data. Post-processing of the data causes more processing load on the on-board computer.

Table 7.4: *Estimation of post-processed data volume of a single stellar occultation.*

Parameter	**Range**	**Resolution**	**Bit per measurement**	**Vertical range**	**Vertical resolution**	**Total data**
Temperature	90-300 K	5 K	6	20-160 km	1 km	840 bit
Pressure	0-1,100 Pa	20 Pa	6	20-160 km	1 km	840 bit
Aerosols	0-100%	1%	7	5-60 km	2.5 km	154 bit
O_2	0-100%	20%	3	35-90 km	1 km	165 bit
O_3	0-100%	2%	6	10-50 km	1 km	240 bit
Total						**2239 bit**

[3]NASA presentation at International Workshop on Planetary Instruments: `http://ssed.gsfc.nasa.gov/IPM/IPM2012/PDF/Revised_Orals/Abshire-1027.pdf`

Spectropolarimeter

The SPEX instrument has a data volume of 0.5 Gbit per day. However this is when the instrument is measuring continuously when positioned above the day side of Mars with a sampling time of 2 s and an orbital height of 300 km. From these given specifications data volume per measurement can be obtained: approximately 294 kbit per measurement. This is a large amount of data to send to Earth. However this data can be post processed as well. The two measured counter phase sinusoidal spectra are added together to obtain the flux spectrum from which a polarisation spectrum can be calculated. The degree of linear polarisation spectrum of Mars is quite smooth and does not need a large amount of data points, six points are enough to represent the spectrum accurately[4]. Of course sending the entire data set might still be interesting, however this does not need to be transmitted frequently. The data from SPEX is sampled on a signal with 10 bits [67]. Since there are nine channels, the data volume results in 540 bits per measurement. However this does mean more processing tasks for the on-board computer.

2-micron coherent doppler lidar

For the 2-micron coherent Doppler lidar no data volumes could be found in literature. The data volume is estimated in the following way: first the amount of pulses sent during one measurement is calculated by multiplying the PRF of 500 Hz with the measurement time of 10 s, resulting in 5,000 pulses per measurement. The incoming signal from the reflected laser pulses is sampled with 10 bits, resulting in 50,000 bits per measurement. The Aladin lidar on the ADM Aeolus mission uses co-adding of individual lasers signals to limit the data bandwidth and to improve the measurement performance [61]. On that lidar it reduces the amount of measurements/ data with 95.5%. This number is used to estimate the data for the MUUDS lidar, which results in 225 measurements per wind observation consisting of 2,250 bits total.

7.1.3 Measurement Schedule

A schedule is made of the measurements of the instruments on the orbiter. The data volume obtained from this is required to size the telecommunication subsystem and the C&DH subsystem. This schedule highly depends on the communication time between the orbiter and Earth and the orbiter and the ground stations because measurements and communication tasks can not be performed simultaneously. Several orbital characteristics are used as well. One day (sol) consists of approximately 88,775 s. The orbit has an eclipse time of 38.83% (34,471 s per sol), see Table 6.5. Communication time with Earth takes up 1,900 s per day (see Table 6.6) and is assumed to always take place on the day side (when the orbiter is facing the Sun). Communication time with the ground stations takes on average approximately 300 s per ground station, thus 3,000 s in total (See Table 6.6).It is assumed that the ground station communication time is equally distributed between the day and night side. Furthermore during major ADCS manoeuvres and orbit maintenance no measurements will occur. The flumes and heat from the thrusters might influence and possibly distort the measurements.

The UV spectrometer can perform 3-5 occultations per orbit with a measurement time between 1 and 4 minutes (see Subsection 7.1.1). The orbiter performs 13.5 revolutions per day (see Table 6.5) resulting in a maximum of 67 measurements per day with a maximum total measuring time of 16,080 s.

The SPEX instrument can only operate on the day side since it requires sunlight reflected by Mars. One measurement requires 2 s (See Subsection 7.1.1).

The lidar can measure on the day and night side and one measurement requires 10 s. The duty cycle is assumed to be 42%, taken the Aladin lidar on the ADM-Aeolus mission as reference [61]. This results in a interval time of 13.8 s and a total measurement time of approximately 24 s. It is assumed that the lidar and SPEX instrument can work simultaneously during the day. This fits within the power budget and within ADCS constraints, since both instruments do not require angular movement during measurements, only pointing knowledge. From a scientific perspective the combination of these instruments would result in more interesting results, since the wind velocity and dust composition data can be combined.

In Table 7.5 an overview is given of the time division between communication and measurements for one sol, using previously mentioned assumptions and estimations.

[4]Information obtained though personal communication with Dr. D.M. (Daphne) Stam, member of the SPEX Science team.

7.1.4 Overview Instruments

In Table 7.6 an overview is given of the mass, powers and data volume of the instruments on the orbiter, discussed in the previous subsections.

Table 7.5: *Time division of the communication and measurement operations of the orbiter per Martian day.*

Operation	Time per operation	Frequency	Total time
Day			54,304 s
Orbiter – Earth communication	1,900 s	1 day^{-1}	1900 s
Orbiter – ground station communication	300 s	6 day^{-1}	1,800 s
UV spectrometer	240 s	41 day^{-1}	9,840 s
SPEX	2 s	20,382 day^{-1}	40,764 s
Lidar	24 s	1,698 day^{-1}	40,752 s
Night			34,471 s
Orbiter – ground station communication	300 s	4 day^{-1}	1,200 s
UV spectrometer	240 s	26 day^{-1}	6,240 s
Lidar	24 s	1,126 day^{-1}	27,024 s
Total			**88,775 s**

Table 7.6: *Overview of the mass, power consumption and data volume of the instruments on the orbiter.*

Instrument	Mass	Power	Data volume per measurement
UV Spectrometer	4.7 kg	9.5 W	2,200 bit
SPEX	2 kg	2 W	540 bit
Lidar	25 kg	10 W	2,250 bit
Total	**31.7 kg**	**21.5 W**	**4995 bit**

7.2 ADCS Pointing of the Measurement Instruments

The satellite will have three measurement systems on board, as specified in Table 7.6. Both SPEX and Lidar have to be pointed to the Martian surface, while the UV spectrometer should be pointed to the back of the spacecraft (in counter-direction of the orbital movement).

All measurement instruments are positioned on the same surface (see Figure 7.2) [31]. The UV spectrometer is mounted in a small box, this in order to create a 90° angle with respect to the surface and to enable the spectrometer to look backwards.

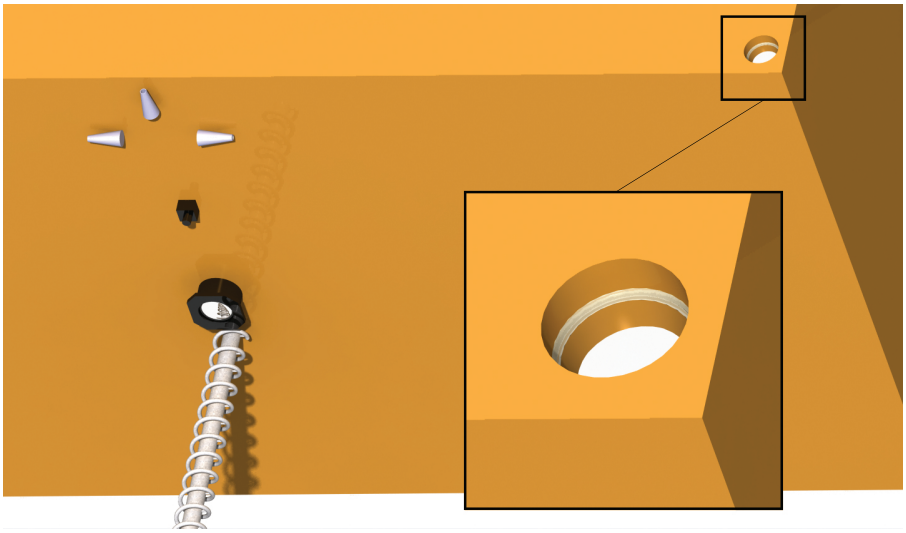

Figure 7.2: *View of nadir side of orbiter. On the left hand are visible (from top to bottom): the ADCS thrusters, the SPEX spectrometer, the doppler LIDAR and the helix antenna and the UV spectrometer on the right hand*

The instruments surface should be pointed nadir at every instance of the measurement interval described in Table 7.5. This pointing position should be established after in-orbit insertion around Mars. The ADCS

thrusters will turn the satellite's measurement surface in Mars-pointing direction, and the reaction wheel assembly will maintain this pointing position (thereby counteracting disturbances that might change the attitude of the orbiter). These manoeuvres will require propellant mass for the thruster and power for the reaction wheel assembly. However, the exact computation of these values is considered of a too detailed level for this stage of the design project.

7.3 Tracking during In-Orbit Operations

The Small Deep Space Transponders, used for Delta-DOR tracking during every other phase of the mission, will be used for tracking the whereabouts of the satellite around Mars.
These SDSTs are connected to the Low Gain Antennas, described in Subsection 10.4.3. The antennas have a large beamwidth and do not require a lot of pointing. These LGAs can therefore be used during emergency broadcasting as is explained in Subsection 10.4.3.
Connecting the SDSTs to the LGAs will therefore enable the satellite to emit Delta-DOR signals in every mode of its operational life, from operating mode to safe mode. The broad bandwidth of the LGAs will make sure that the ranging signals reach the Earth's Deep Space Network. This way, information on the orbiter's travelled path will be available to Earth ground control every time the orbiter is in view of Earth. But the path the orbiter is describing on the night side of Mars is unknown to Earth in this way.

In order to know how the satellite travels on the night side of Mars, another method can be used in combination with the Earth-orbiter Delta-DOR ranging. During nighttime, the orbiter is communicating with the ground stations on that night side by using its UHF antenna, see Subsection 10.4.3. Based on the time delay of the transmitted and received signal and its phase difference - in other words, the Doppler shift of the signal - the relative distance between the ground station and the orbiter can be determined. Knowing the begin- and endpoint of where the orbiter entered and left the night side of Mars, one can estimate the track on the night side based on this relative positioning information.
This Doppler shift ranging of the UHF antenna signal will also be used to determine the location of the ground landers after they have completed their EDL and have fully deployed for operational life. This way, the relative position of the orbiter with respect to the ground stations can be determined for each ground station.

By combining the tracking information gathered by using Delta-DOR between the Earth's DSN and the satellite's LGA, and the information gathered by using Doppler shift between the UHF antenna signals of the satellite and the ground stations, a reliable estimate of the relative positions between Earth-orbiter, orbiter-Mars, orbiter-ground stations, ground stations-Mars and ground-stations-Earth can be determined.

8 | Ground Operations

The gathering of weather data on Mars has two sides: measurements taken from the ground (for atmospheric properties as well as radiation doses) and measurements taken in orbit (for atmospheric properties). The orbit operations were discussed in Chapter 7. In this chapter, the ground station instruments are chosen and put into the perspective of the mission. The measurements shall all be processed in a similar way, which is explained in Section 8.1. In order to design the ground station, the instruments are selected and the required properties are determined (such as power supply and size) (Section 8.2). Finally, the ground station architecture in which all instruments come together is presented (Section 8.3) and the measuring set is summarised in the chapter overview (Section 8.4).

8.1 General Operations and Methods

A number of instruments are available in a wide range of types, configurations, capacities and accuracies. Because of this, estimates on their characteristics were made for these instruments according to which the exact system design has to be performed in a later stage of the project. A table was made for each instrument in which the estimated maxima of the different system properties are displayed, to make an estimate of specifications as required power and total mass.
According to the mission requirements (see Appendix B) measurements have to be performed hourly. In principle, this means that each hour one measurement has to be delivered. A sampling time of one minute is assumed for all measurements because of the required redundancy, but in the properties tables, only a single measurement is taken into account. Furthermore, exact cost analyses of the instruments are not included in this selection process: they differ a lot, but in any case take up only a small part of the total project budget. It is therefore touched upon briefly but not discussed in detail.

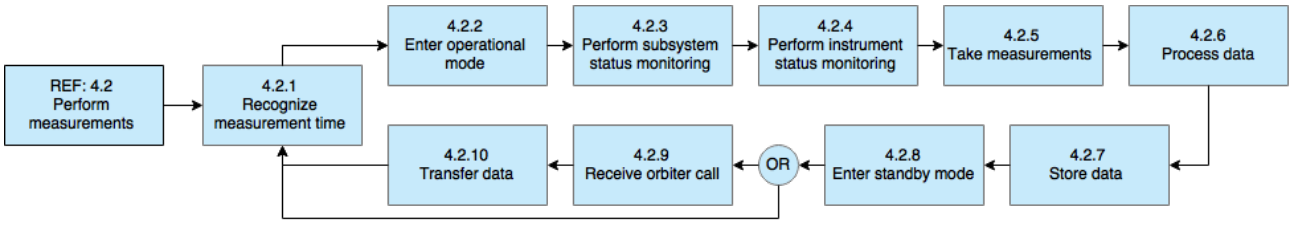

Figure 8.1: *The cyclic flow operation diagram of the ground station measurements.*

The ground station operative phase functions can be displayed in a cyclic function flow diagram (Figure 8.1), which displays the order of commands the system executes every hour. When it is time to measure data, it will leave the standby mode and perform subsystem and instrument checks. If errors are found, they will be reported and stored in a status report. After that, measurements are taken and the data is processed: this differs per instrument and is elaborated upon in their respective sections. The data centre now stores the acquired data and goes back to sleep mode. Then once per sol, data is transferred to the orbiter. Detailed analysis of the data handling system and communication processes can be found in Section 10.3 and 10.4 respectively.

8.2 Measurement Instruments Selection

Based on an analysis of the different components the ideal instruments will be selected in this section. The measured parameters on the MUUDS-mission are temperature (Subsection 8.2.1), pressure (Subsection 8.2.2), wind velocity (Subsection 8.2.3), dust content (Subsection 8.2.4), air composition (Subsection 8.2.5) and the radiation environment (Subsection 8.2.6). Since not all instruments are readily available in the desired configuration, they shall be structured according to the MUUDS-mission, but this is outside of the scope of the project.

8.2.1 Temperature Measurements

For temperature measurements there are two interesting options, namely the thermocouple (measurements based on potential difference in two wires) and the resistance thermometer device (RTD) (measurements based on the resistance of a material). Both systems are light weight, inexpensive and not complex in use. However, it appears that thermocouples are mainly suitable for high temperatures, which is not the range the mission is

expected to measure in. Since RTDs have been used before, for example in the Curiosity mission[1], a RTD system will be used as temperature measurement device. The specifications of this device in the MUUDS-mission are given in Table 8.1[2].

Table 8.1: *Technical specifications of the RTD-PT860 temperature measurement device.*

Resistance Temperature Device PT-860			
Mass	Platinum: < 0.005 kg	Measurement range	90 K - 300 K
	Subcomponents: < 0.2 kg	Measurement resolution	2 K
	Total maximum mass: 0.205 kg	Number of datapoints	107
Power consumption	< 0.5 W	Data volume	7 bits per measurement
Operational time	< 1 s	Number of instruments	3
Size	$< 5{\cdot}10^{-4}$ m^3	Total instrument costs	< €400,-

The RTD shall be installed in the tip of a small boom which extends from the side of the ground station. This is executed to ensure a measurement is taken which is not influenced by heat radiating from the station. A small current pulse is sent over the sheet of platinum, and its output voltage is measured, which is directly related to the platinum resistance through $U = IR$. The current pulse must be tiny, both in magnitude and in time-length, as resistance causes heat development which could bias the measurements. The resistance then corresponds to a certain temperature, which is determined precisely by pre-mission testing. Since RTD outputs are typically in the range of millivolts, a low-pass filter may be required to reduce high-frequency measurement noise[3]. Temperature measurements are taken in threefold, so that errors easily can be found. The embedded position of the RTD ensures that the temperature is minimally influenced by wind or direct sunlight. The system shall also contain an algorithm to eliminate significant outlying measurements. The exact details of this procedure are to be determined in a later development phase of the MUUDS project.

8.2.2 Pressure Measurements

For the pressure measurements there are two options as well: fibre optic sensing (using the behaviour of light in a fibre) and capacitive sensing (measuring capacity of two spaced plates). As the capacitive sensing is sensitive to temperature, this seems the least viable option, as the exact thermal inertia on the landing sites is unknown. The fibre optic sensor, on the other hand, is not so sensitive and can survive in harsh circumstances and is very lightweight, making it ideal for the MUUDS-mission. Therefore a fibre optic sensor is selected as pressure measurement device. The specifications are found in Table 8.2[4]. Note that a fibre optic sensor is also used for temperature measuring in some industries, however, its accurate range does not include the total temperature range of Mars. Therefore, a separate temperature measurement device was selected. The fibre optic sensor

Table 8.2: *Technical specifications of the Fibre Optic Sensor for pressure measurements.*

Fibre Optic Sensor			
Mass	Glass fibre: < 0.005 kg	Measurement range	600 K - 1,100 K
	Light source: < 0.01 kg	Measurement resolution	5 Pa
	Subcomponents: < 0.2 kg	Number of datapoints	102
	Total maximum mass: 0.215 kg	Data volume	7 bits per measurement
Power consumption	< 0.5 W	Number of instruments	2
Operational time	< 1 s	Total instrument costs	< €350,-
Size	$< 1{\cdot}10^{-3}$ m^3		

consists of a glass fibre with two lenses installed in front with an air gap in between, which is exposed to the ambient pressure p. A light source outside the outer lens emits light pulses in a variety of wavelengths. The outer lens has a thickness such that the pressure influences the size of the air gap, which again influences the behaviour of the light pulses through the glass fibre. The fibre system is highly customisable by adjusting the lens thicknesses, diameters and the initial air gap size such that an appropriate range, accuracy and maximum linearity are achieved[5]. This can again be designed and tested on ground. For redundancy and error reduction, two sensors are installed. They will be mounted facing the side of the station, omitting dust accumulation as much as possible.

[1] The REMS instruments on Curiosity: `http://msl-scicorner.jpl.nasa.gov/Instruments/REMS/`
[2] RTD product finder: `https://www.omega.com/guides/rtds.html`
[3] RTD user manual: `http://www.ni.com/tutorial/7115/en/`
[4] OPP-B Fibre Optic Sensor specifications for aerospace applications: `http://www.opsens.com/en/industries/products/pressure/opp-b/`
[5] How fibre optic sensors work `http://www.sensorland.com/HowPage072.html`

8.2.3 Wind Velocity Measurements

Wind velocity can be measured through a number of devices called anemometers. These can use laser-Doppler techniques, sonic pulses (both using the behaviour of a pulse to determine the wind velocity) or hot wire heating (using the cooling effect of the wind which varies with wind speed). It appears that all instrument types require a high level of accurate positioning for adequate measurements. They are also highly sensitive to dust accumulation. For the hot wire anemometry, however, a solution was found for the Mars Science Lab: instead of hot wires, hot films were used: very thin sheets rather than wires [68]. This makes the device much more durable to dust storms and less sensitive to dust accumulation. It is therefore deemed the best option. The specifications can be viewed in Table 8.3.

Table 8.3: *Technical specifications of the Hot Film Anemometer for wind velocity measurements.*

Hot film anemometer			
Mass	Hot film sheets: $< 0.01\,\text{kg}$	Measurement range	$0\,\text{m/s}$ - $70\,\text{m/s}$
	Subcomponents: $< 0.2\,\text{kg}$	Measurement resolution	$1\,\text{m/s}$
	Total maximum mass: $0.21\,\text{kg}$	Number of datapoints	72
Power consumption	$< 3\,\text{W}$	Data volume	7 bits per measurement
Operational time	$< 10\,\text{s}$	Number of instruments	3
Size	$< 5{\cdot}10^{-4}\,\text{m}^3$	Total instrument costs	< €500,-

The hot films are mounted on the same booms as the RTDs, which were mentioned earlier. There are two films facing either side of the boom. The films heat up to about 100 ° C above ambient temperature, and the resistivity difference between the two is a measure for the wind velocity (because of the cooling effect the wind has). The exact scale can be determined experimentally. All three booms contain a set of hot films for wind velocity measurements: this is necessary since the wind direction is variable. With three measuring points, there are two points facing the wind at all times. Two inputs are sufficient to determine both the wind speed and direction: when all three measuring points face the wind, it can be determined even more accurately and the devices are checked for errors. The mounting on the booms is beneficial for a clear measurement as well: it is positioned away from the station, and a sufficient high mounting ensures ground clearance as well.

8.2.4 Dust Content Measurements

For the sake of simplicity, optic laser measurements will be used for dust measurements: it can provide sufficient accuracy relevant for the research. It operates through a laser which illuminates a sensor. The amount of light captured by the sensor is used to determine what the dust concentration is. Lasers are chosen as they can use pulses which means that in the event of high wind speeds an accurate result can still be obtained. The device consists of a departing point (where the laser is situated) and an arriving point (where the intensity is measured). These must be spaced by about 0.5 to 1 meter (and this dimension should be included in the settings as well). The device is placed on top of the ground station, in line with the sides of the station, to cause minimum interference with other instruments and to obtain a clear measurement itself as well. The system characteristics can be found in Table 8.4.

Table 8.4: *Technical specifications of Laser Optic Dust measurements.*

Laser Optic Dust Measurement			
Mass	Laser device: $< 0.1\,\text{kg}$	Size	$< 1{\cdot}10^{-3}\,\text{m}^3$
	Optic measuring tool: $< 0.1\,\text{kg}$	Measurement range	0 % - 100 %
	Subcomponents: $< 0.1\,\text{kg}$	Measurement resolution	1 %
	Housing: $< 0.1\,\text{kg}$	Number of datapoints	101
	Total maximum mass: $0.4\,\text{kg}$	Data volume	7 bits per measurement
Power consumption	$< 0.5\,\text{W}$	Number of instruments	1
Operational time	$< 2\,\text{s}$	Total instrument costs	< €150,-

8.2.5 Atmospheric Composition Measurements

For atmospheric composition, currently two types of spectrometers are available: the emission- and the absorption spectrometer, both using the behaviour of ions to identify the elements present in a gas. Because of its wider application range, the emission spectrometer will be used.
Emission spectrometers for applications in harsh environments can be bought off-the-shelf: an example is a Residual Gas Analyzer (RGA). These are available in small[6] and lightweight configurations. One device is used which will measure the composition of the local Martian atmosphere up to 5 ppm accuracy. This causes a high

[6]RGA Microvision 2 Dimensional Drawing: `http://www.mksinst.com/docs/UR/Microvision2dim.pdf`

bit rate: however, since the bit rate is relatively small for the other instruments, this is affordable and more valuable measurements can be obtained. The specifications can be found in Table 8.5[7].

Table 8.5: *Technical specifications of the RGA Microvision 2 for atmospheric composition measurements.*

Atmospheric composition measurements			
Mass	Instrument: 1.7 kg	Size	$< 1{\cdot}10^{-3}\,\mathrm{m}^3$
	Housing: < 0.1 kg	Measurement resolution	< 5 ppm
	Subcomponents: < 0.2 kg	Data volume	40 bits per measurement
	Total maximum mass: 2 kg	Number of instruments	1
Power consumption	< 5 W	Total instrument costs	$<$ €400,-
Operational time	< 5 s		

8.2.6 Radiation Measurements

Radiation dosimetry is a complex aspect of the system design. The radiation that reaches the Martian surface is of a vast different nature than the particles that reach the Earth. Cosmic radiation and radiation coming from the Sun react with the atmosphere and the strong magnetic field around Earth, with the effect that only secondary products such as neutrons and photons reach the surface [69]. These are hardly similar to the particles originally heading for Earth. The thinner atmosphere as well as the absence of a significant magnetic field on Mars lead to a greatly different radiation environment at the surface.

When considering radiation harmful to humans, two kinds can be distinguished: chronic (low energy) radiation that is detrimental on the long term (which is mostly determined by the increased risk of getting cancer) and acute (high energy) radiation that damages the structure of vulnerable organs (such as the intestines and lungs) and which can be lethal in a matter of days or weeks[8]. The latter type of radiation originates from phenomena such as solar flares, which release waves of highly energetic protons and generally last a few (Earth) days. The degree to which the radiation is harmful is based on the total dose that is received over time: this can either be a small dose acquired over a longer time or a high dose in a short time. For space missions near Earth (but also for people working in a radiation environment), the limit radiation dose is mostly based on the long-term harmful radiation, aiming to minimise the increased chances of cancer development. However, with the goal of preparing for human exploration in mind, the most relevant type of radiation is the high-energetic particles that are lethal on the short term. For the MUUDS mission, an applicable choice would be to focus on the measurement of high-energy protons at the surface, since they will be most critical for the survival of the first humans and the operations of critical instruments. Considering radiation that is detrimental to structures, the highest threat is posed by iron nuclei: iron atoms stripped of all electrons, originating from deep space[9]. The secondary products may also harm humans inside a station.

It should be noted, however, that considering harmful radiation, more is needed than just surface measurements. Very high-energy radiation comes from greater solar events, and science has yet to figure out how to predict these. The only current solution is to have an early-warning system working with a satellite that alarms them. The amounts of radiation from the solar flares are not only harmful to humans, but most electronic devices would be damaged as well. It is thus of essential importance that the mission is protected against these threats. The data of the MUUDS mission provides a good starting point but a more extensive system is required for charting the radiation spectrum on Mars before the first humans to set foot on its surface.

Few instruments are capable of measuring proton radiation in a way where data can be measured and sent digitally: most methods require visual inspection. Also, durability is an issue: proton measurements can easily be done by measuring the impacts of particles in a material, but it is unknown if this method will even last beyond the first operational year. For the classification of protons and iron nuclei, the best option is to use a semiconductor. When protons or iron nuclei hit the material of the semiconductor, energy is released and this change of energy is measured hourly. The semiconductive material is exposed to the radiation environment at all times so that the measurement yields a time integrated result, in which peaks of radiation intensity can be seen, as well as the overall dose. Should science be able to predict solar flares more accurately by the time of the mission, it is recommended that at these times the measuring frequency is increased, such that the peaks can be measured more accurately.

[7] RGA Microvision 2 Specifications: `http://www.mksinst.com/docs/UR/Microvision2-specifications.aspx`
[8] Obtained from personal communication with ing. M. (Marcel) Schouwenburg
[9] Obtained from personal communication with ing. M. (Marcel) Schouwenburg and drs. M.J. (Mark) van Bourgondiën.

Not enough is known about specific semiconductors that might be suitable for this mission. However, it is known that protons can slip through measuring instruments quite easily when their energy is very high: it is therefore recommended that a thick semiconductor is used so that as much of the radiation as possible is captured. The instrument will "face" the sky and is mounted on the top side of the station. Since the intensity of the radiation can vary as much as by a factor 10^9 [70] [10] , the data centre should convert the radiation data to a logarithmic scale. Table 8.6 provides an indication of the maximum expected characteristics which are used in the budget analysis.

Table 8.6: *Technical specifications on radiation measurements.*

Radiation assessment			
Mass	Semiconductor: $< 9\,\text{kg}$	Measurement range	10^0 eV - 10^{10} eV
	Housing: $< 0.1\,\text{kg}$	Measurement resolution	20 points per power of 10
	Subcomponents: $< 0.2\,\text{kg}$	Number of datapoints	201
	Total maximum mass: 9.3 kg	Data volume	8 bits per measurement
Power consumption	$< 10\,\text{W}$	Number of instruments	1
Operational time	$< 10\,\text{s}$	Total instrument costs	<€400,-
Size	$< 3{\cdot}10^{-3}\,\text{m}^3$		

8.3 Ground Station Architecture

Now that all instruments have been selected, they can all be fitted in the ground station. It is shown in Figure 8.2 [31]. A hexagonal shape was chosen so that the instruments have minimum interference with each other, as well as with the solar panels. Temperature and wind speed are measured from the extended boom in the middle of the visible panel: two more of such booms are situated at the panels 120° apart from the visible one. At the top left of this panel, pressure is measured (as well as at the opposite side of the ground station). Spectrometric measurements are performed through the instrument at the low left corner of the visible panel. These are only done in one place. At the top, the measuring instrument for dust content is visible, spaced apart about 60 cm. Finally, beneath the circular hole in the top panel, the instrument for radiation measurement is positioned. The communication antenna is visible on the top panel as well.

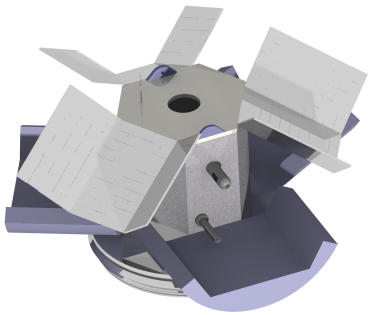

Figure 8.2: *Isometric view of the ground station during deployment.*

8.4 Instruments Overview

To conclude, a total overview of the instruments and their budgets is given in Table 8.7. In this table, the total values of the instruments selected are displayed per parameter and can be used as reference.

Table 8.7: *Overview of the ground stations' measurement instruments.*

GROUND WEATHER MEASUREMENT SYSTEM OVERVIEW					
Parameter	**Device**	**Mass**	**Power**	**Size**	**Cost**
Temperature	RTD-PT860	0.615 kg	1.5 W	$1.5 \cdot 10^{-3}\text{m}^3$	€ 400
Pressure	Fibre optic sensor	0.430 kg	1.0 W	$2.0 \cdot 10^{-3}\text{m}^3$	€ 350
Wind velocity	Hot film anemometer	0.630 kg	9.0 W	$1.5 \cdot 10^{-3}\text{m}^3$	€ 500
Dust content	Laser optic device	0.400 kg	0.5 W	$1.0 \cdot 10^{-3}\text{m}^3$	€ 150
Air composition	Emission spectrometer	1.700 kg	5.0 W	$1.0 \cdot 10^{-3}\text{m}^3$	€ 400
Radiation	Semiconductor measuring	9.300 kg	10.0 W	$3.0 \cdot 10^{-3}\text{m}^3$	€ 400
	Total	**13.075 kg**	**27.0 W**	$15.0 \cdot 10^{-3}\mathbf{m^3}$	**€ 2,400**

With this knowledge, the design process continues to orbiter measurements and the final project design.

[10] Obtained from personal communication with drs. M.J. (Mark) van Bourgondiën.

9 | End-of-life

After the launcher, orbiter and ground stations have fulfilled their allocated function they have to be discarded, as discussed in Section 9.1 till 9.3, respectively. However this needs to be done in a sustainable way. Designing an end-of-life phase is therefore paramount and will be dealt with in this chapter.

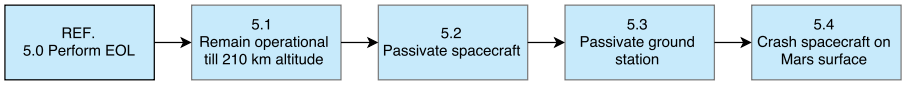

Figure 9.1: *Functional flow diagram for the end-of-life.*

9.1 Falcon Heavy Launcher

The Falcon Heavy will be used to transport the space probe to the Earth-Mars transfer orbit. This launcher has been designed to be a partially reusable launcher. Which means that once the launcher has fulfilled its purpose it will partly return to Earth. These characteristics are already elaborated upon in Chapter 3.

9.2 De-orbiting craft

The focus on active post-mission disposal of space structures has increased vastly last decades. The low-Earth orbit is heavily packed by space debris. Therefore a correct way of de-orbiting is of great importance to sustain future missions. There are three different options to undergo a de-orbit manoeuvre [71].

- Manoeuvre to an orbit where increasing drag will remove the satellite in a given time frame (uncontrolled).
- Direct retrieval and de-orbiting, also called controlled de-orbiting.
- Manoeuvre to an orbit where no harm can be done to future space missions, a graveyard orbit.

Because this mission has the intention to investigate the Martian atmosphere for future (manned) mission. Mars does not have a special graveyard orbit yet and next to it, multiple space vehicles orbit Mars with a high eccentricity which makes the third option very hard. Even for the most optimistic expectation of human civilisation on Mars, the spacecraft should not harm any human on Mars if it would de-orbit in an uncontrolled manner. Besides, the first option will also need less propellant than option two. Therefore the end-of-life phase will be designed by executing option one. Since goals were set on 2030 as being the period in which the first manned Mars missions were expected, the orbiter shall be brought to the Martian surface before 2030.

If the orbiter would not provide any ΔV manoeuvres it would slowly approach the Martian surface. In approximately 407 days the orbiter will finally crash. This value has been obtained by using the model built for the orbit design around Mars. The decay rate has been linearised for every 10 km because the used density profile varies for every 10 km. Since in this phase not all materials are known yet, a further study is recommended to investigate if the orbiter will be completely destroyed by the forces and heat generated on the craft. Once the orbiter has propellant left for only one month to execute the needed manoeuvres, the orbiter will send a signal to Earth to let the ground ops (Section 16.3) know that the end-of-life phase needs to be performed soon. Though the orbiter will remain functional, including orbit maintenance, as long as it has enough propellant. When all propellant is used up the orbiter will decelerate slowly. The orbiter will still execute its task as long as the orbiter stays above 210 km. Below this altitude the orbiter will be passivated to a level where the remaining internal stored energy is insufficient to cause breakup [72].

9.3 Passivation of Ground Stations

The EOL-solution considered for the ground stations is the passivation of the ground system controlled from Earth. Since no plutonium power source is used, no nuclear waste is created on Mars which is deemed more sustainable in the MUUDS context. If possible, the ground stations may retract its instrument to prevent excessive debris on the surface of Mars. Although an EOL-protocol is necessary for the mission, the MUUDS team strives for a mission that is extended as long as it delivers valuable data. As long as the orbiter will remain functional the ground stations will keep executing its function. Shutdown will only commence if this is the last viable option.

10 | Final Design

In this chapter the systems which are functional throughout all the different phases - and cannot be categorised in one of them specifically - are discussed. The power subsystem will be elaborated upon in Section 10.1, followed by the thermal techniques applied in the final design (Section 10.2). Afterwards both the command & data handling and the telecommunications subsystem will be discussed in Section 10.3 and 10.4, respectively. Finally, the structural layout will be presented in Section 10.5. The final design of the space probe is shown in Figure 10.1 [31].

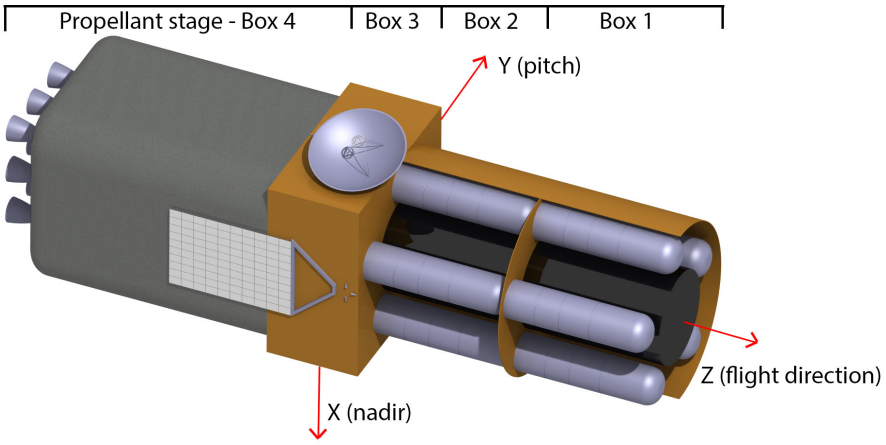

Figure 10.1: *Final space probe design.*

10.1 Power System

In this section the power system used for the mission is designed. From earlier trade-offs the decision was made to use solar panels for the power production. First of all, the electric block diagrams of the spacecraft and the ground station are presented in Subsection 10.1.1. This is followed by the explanation of the method used to size the power system in Subsection 10.1.2. In Subsection 10.1.3 an estimation of some of the remaining system properties is made, which is followed by the sizing of the battery in Section 10.1.4. After having presented the method and estimating some parameters, the power system is sized for the mission needs and this is presented in Subsection 10.1.5.

10.1.1 Electric Block Diagram

The electric block diagram shows which components are used in order to provide all the systems with power. In the diagram all components of the mission that use electric power are summarised and connected to the electric power system. Each power system consists of a solar array, which produces power. The generated power then goes to a power control unit, where it either goes to the battery or to the power distribution system. The power distribution system provides all the systems with power. More detail on the layout of the electrical power system of the spacecraft and the ground station can be seen in Figures 10.2 and 10.3 respectively.

10.1.2 Method Used for Sizing of the Power System

Solar cells are a well known source for power generation in space, what makes them very reliable for the use in a Mars mission. The key design issues for sizing the solar array are the required power, operating temperatures, radiation environment and the mission lifetime [1]. The sizing process of the solar array can be divided into two parts. The first part deals with the determination of the properties of the solar cell used and the second part deals with the sizing of the solar array.

Determination of solar cell properties

In order to size the solar array, the efficiency of the solar cell needs to be determined. The efficiency of a solar cell is defined as shown in Equation 10.1.

$$\eta = \frac{P_{\max}}{P_{in}} \tag{10.1}$$

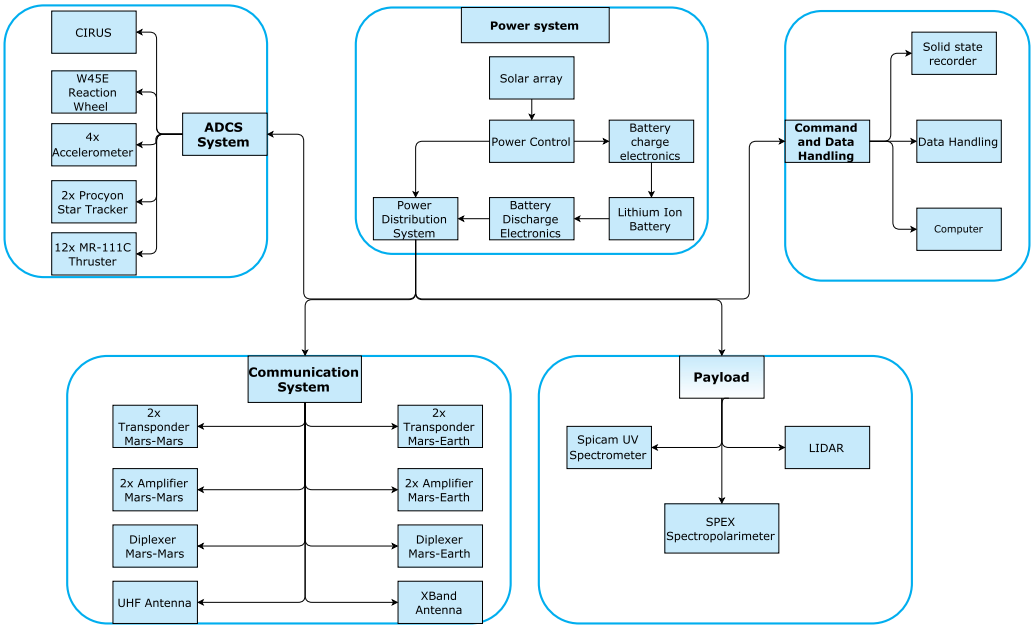

Figure 10.2: *The electric block diagram of the spacecraft.*

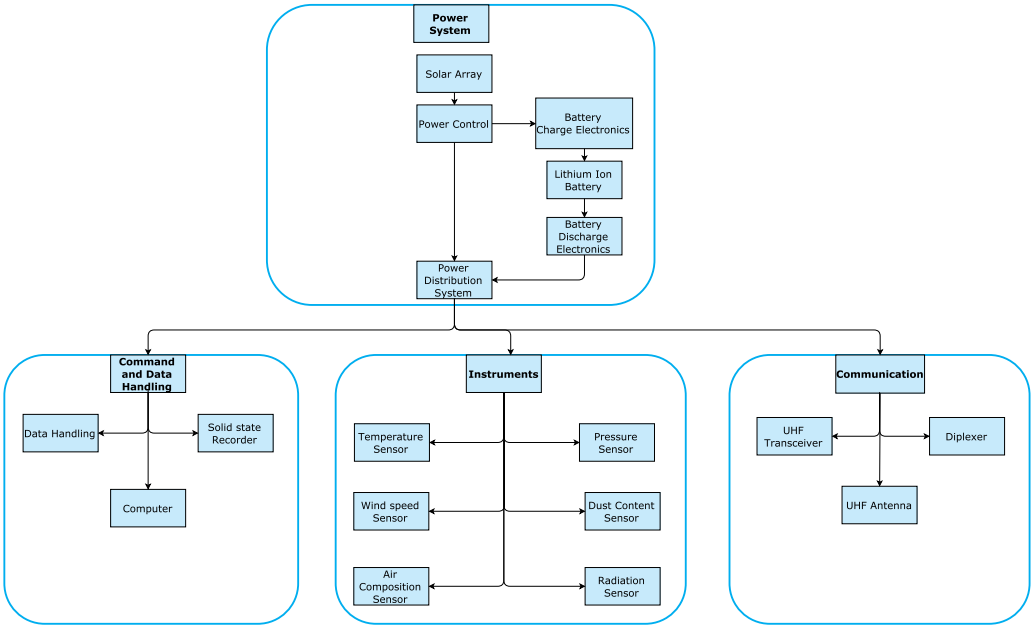

Figure 10.3: *The electric block diagram of the ground station.*

Both the powers used in Equation 10.1 can be calculated. The maximum power can be calculated using Equation 10.2 and the power that is available can be determined using Equation 10.3.

$$P_{\max} = V_{oc} \cdot I_{sc} \cdot FF \tag{10.2}$$

$$P_{in} = J \cdot A \tag{10.3}$$

In Equation 10.3 J is the radiation intensity used to test the solar panel and A is the area of one solar cell. In Equation 10.2 FF is the fill factor of the solar cell. The fill factor determines performance of the solar cell and it can be determined using Equation 10.4.

$$FF = \frac{V_{mp} I_{mp}}{V_{oc} I_{sc}} \tag{10.4}$$

The subscript mp used in Equation 10.4 indicates the voltage and current at maximum power production. In addition to that V_{oc} and I_{sc} are the open circuit voltage and short circuit current.

The performance of the solar cell is affected by the temperature of the solar cell. Due to an increase in temperature, the short circuit current slightly increases and the open circuit voltage significantly increases. The changes in voltage and current can be calculated using Equations 10.5 and 10.6.

$$V_{oc}(T) = V_{oc}(T_0) + \alpha(T - T_0) \quad (10.5) \qquad I_{sc}(T) = I_{sc}(T_0) + \beta(T - T_0) \quad (10.6)$$

The α and β used in Equations 10.5 and 10.6 are the temperature coefficients of the solar cell. The temperature T used in the equations comes from the thermal control calculations made for the spacecraft presented in Section 10.2. From a first thermal calculation, it is estimated that the equilibrium temperature of the solar panels in Martian orbit during exposure to sunlight is -40°C and for the ground station the panel temperature is estimated to be 48°C. Using both these equations, the short circuit current, open circuit voltage and the voltage/current at maximum power production can be determined at elevated temperatures. This can then be used to determine the fill factor at elevated temperatures using Equation 10.4 and the new maximum power that can be produced by the solar cell is determined using Equation 10.2 with the currents and voltages at elevated temperature. Due to an increase in temperature, the maximum power produced decreases and this leads to a decreased efficiency of the solar cell.

Sizing of the solar array

The first step in determining the required size of the solar array is to calculate the power that needs to be produced by the solar array, in order to ensure the operation of the systems. The power that needs to be generated by the solar array is given by Equation 10.7.

$$P_{sa} = \frac{\frac{P_d t_d}{\eta_d} + \frac{P_e t_e}{\eta_e}}{t_d} \quad (10.7)$$

The subscript d refers to the operations that are performed when the system is subjected to sunlight and the subscript e refers to the operations performed during the eclipse. The day and eclipse efficiencies depend on the efficiencies of the electrical components used for the system and they can be calculated using Equations 10.8 and 10.9.

$$\eta_d = \eta_{powercontrol} \cdot \eta_{powerdistribution} \quad (10.8)$$

$$\eta_e = \eta_{powercontrol} \cdot \eta_{charge\ electronics} \cdot \eta_{batterydischarge} \cdot \eta_{powerdistribution} \quad (10.9)$$

In order to be able to calculate the day and eclipse efficiencies, some estimations on the efficiencies of the more detailed electrical power system have to be made. These estimations can be found in Subsection 10.1.3.

The next step is to determine the power that can be generated by the solar cell at the beginning-of-life (BOL). In order to do so, the solar flux at the current location of the spacecraft has to be calculated using Equation 10.22. With the solar intensity and the efficiency of the solar panel at the beginning-of-life, the output performance P_0 can be determined. Having done this the power production per square meter of the solar panel at BOL can be determined using Equation 10.10.

$$P_{BOL} = P_0 \cdot I_d \cdot \cos(\theta) \quad (10.10)$$

The I_d used in Equation 10.10 is the inherent degradation of the solar array and it is composed of factors like inefficiencies of the solar array design and assembly, temperature differences and shadowing of the solar cells. The θ used is the angle of incidence between the Sun and the solar array. This determined by the orientation of the spacecraft and the accuracy of the ADCS.

After having determined the power production at the BOL, the power output at the end-of-life has be determined. Due to the radiation in space, the solar cell will degrade and lose some of its performance. The life degradation factor is given by Equation 10.11.

$$L_d = (1 - \delta)^{years} \quad (10.11)$$

Having calculated the life degradation factor using Equation 10.11, where δ is the annual degradation factor of the solar panel, the power output at EOL can be calculated using Equation 10.12.

$$P_{EOL} = L_d P_{BOL} \quad (10.12)$$

Now that the power required by the solar array P_{sa} and the power output at EOL are known, the required solar array size can be calculated. The required solar array area that is needed to power all the system is calculated using Equation 10.13.

$$A_{sa} = \frac{P_{sa}}{P_{EOL}} \quad (10.13)$$

After the calculation process that is required to size the solar array, the next step is to define some system properties of the electric power system.

10.1.3 Estimation of System Properties

In order to calculate the required size of the solar array, some details on the layout and efficiencies of other electrical units of the power system have to be determined. Designing the full electrical power system would be too detailed for this stage of the design process. So in order to size the solar arrays an estimation on the performance of the other electrical systems is made using reference literature.

A power control distribution network is needed for the power system, to deliver appropriate voltage and current to all the systems when it is required [49]. For the power control system a Switch-mode regulator is used, since they are very reliable as they are commonly used for spacecraft power control since the 1970s. In addition to that it is said that Switch-mode regulators can achieve efficiencies higher than 95% [1]. Due to this information the efficiency of the power control system is estimated to be $\eta_{powercontrol} = 0.95$. The next efficiency that is estimated, is the efficiency of the power distribution system. This system is required to distribute the power over the spacecraft (cabling), for fault protection, and it has a switching gear to turn systems on and off [1]. Looking at reference literature, an efficiency range from 95-98% can be found for the power distribution system[1]. Using this information the efficiency of the power distribution system is estimated to be $\eta_{powerdistribution} = 0.97$.

Moreover the efficiency of the battery charge electronics has to determined. Charge control is needed to maintain the lifetime of the batteries by controlling the electrical inputs to the battery [49]. In literature it can be found that the efficiency of the battery charge electronics is approximately 95%[2]. So for the design of the power system a charge efficiency of $\eta_{charge\ electronics} = 0.95$ is assumed.

The next factor that needs to be estimated is the inherent degradation factor. It summarises the effects of assembly inefficiencies, shadowing and temperature variations. During the estimation of the inherent degradation factor a distinction between the operations in space and on the surface of Mars has to be made. The first estimation is done for the inherent degradation of the solar cell used on the spacecraft. For this estimation of the inherent degradation factor, the effect of temperature variations is left out because the change in efficiency due to the temperature of the solar array is already incorporated in the calculation process as described in Subsection 10.1.2. In SMAD the range for an inefficiency due to assembly of the array is 0.77-0.9 and for the sizing process it is chosen to be be 0.85 [1]. Furthermore the factor for shadowing of the cells has a range of 0.8-1 and for the sizing it is chosen to be 0.95, as the solar array is placed on the spacecraft in such a way that shadowing is minimised. This leads to an inherent degradation factor of $I_{d,s} = 0.85 \cdot 0.95 = 0.81$. The next step is to make an estimation for the inherent degradation of the solar panels used on Mars. The inefficiency due to the assembly of the array can have the same value as for the array of the spacecraft. For the factor of shadowing however there is a difference. On Mars the solar panel it is likely for the solar panel to experience shadowing due to dust accumulation. So the shadowing factor is chosen to be 0.85. This results in an inherent degradation factor of $I_{d,g} = 0.85 \cdot 0.85 = 0.72$.

Moreover a method for the determination of the degradation factor of the solar cell has to be made. The degradation of a solar panel depends on the annual fluence of radiation per cm for particles with an energy larger than 1 MeV. So in order to determine the degradation factor due to the radiation near Mars, the radiation fluence in Martian orbit needs to be estimated. From the NEAR mission, it can be found that the annual fluence at a distance of 1.7 AU is $1.64 \cdot 10^{11}$ per cm [73]. Furthermore it can be found that the radiation environment is inversely dependent on the square of the solar distance. So knowing this the fluence near Earth at 1 AU can be calculated and with the fluence near Earth and the solar distance of Mars of 1.52 AU, an annual fluence of $2.0521 \cdot 10^{11}$ near Mars is found. Looking at data sheets of commercially available solar panels, it can be seen that the fluence environment for the degradation of the panels is higher than this value. So for the sizing of the solar array, the degradation factor at the lowest annual fluence near Earth is chosen and this leaves a sufficient safety margin to the design of the solar array.

Lastly the Sun incidence angle has to be set for the sizing of the solar array. On the orbiter around Mars a Sun-pointing system is used as further described in Section 10.1.6. During the sizing process of the solar array of the orbiter, an incidence angle of 30° is chosen in order to account for pointing inaccuracies of the pointing system. For the ground station an incidence angle of 45° is used during the sizing process.

[1] Reader: AE1222-II: Aerospace Design & Systems Engineering Elements I Part: Spacecraft (bus) design and sizing
[2] Reader: AE1222-II: Aerospace Design & Systems Engineering Elements I Part: Spacecraft (bus) design and sizing

10.1.4 Battery Choice

The use of solar panels for the electric power generation dictates the use of batteries as a back up power source. The battery supplies power to the other systems of the vehicle, when the vehicle is in an eclipse or when the solar array is not able to achieve the peak power demand of the systems. For this power system a secondary battery is required, since the mission goes over a long period and thus the battery needs to be rechargeable.

The first step in choosing a battery for the mission, is to determine the type of battery that are most commonly used. The three most common secondary battery types used for space applications are Nickel-Cadmium batteries (Ni-Cd), Nickel-Hydrogen batteries (Ni-H_2) and Lithium Ion batteries (Li-Ion). For the power system it was chosen to use Li-Ion batteries. Compared to the other two battery types it has beneficial energy density and energy efficiency characteristics [1]. So the use of a Li-Ion battery enables the use of lighter batteries and it requires a smaller solar array due to the high energy efficiency.

The battery used during the mission has to go through many charge and discharge cycles, which decrease the capacity and efficiency of the battery. In order to limit the degradation of the battery, the depth of discharge (DOD) has to be determined. A battery should never be discharged completely otherwise it will fail. So in order to increase the battery lifetime only a fraction of the capacity has to be used. The first step in determining the DOD is to calculate the amount of charge/discharge cycles. The battery that is used in the orbiter around Mars is the same for the trajectory vehicle. From the requirements it can be found that the mission runs for two Martian years, which corresponds to 687 Earth days. Furthermore it is known that one orbit around Mars takes 1,966 h and in each orbit an eclipse is present during which the battery is used. So knowing the duration of one orbit and the duration of the operation around Mars, the amount of cycles is calculated to be 8,387. In addition to this amount of cycles, a safety margin of 1,000 extra cycles is added. This safety margin accounts for the charge/discharge cycles encountered during the orbit phase around Earth and during the transfer phase and thus results in a total of 9387 design cycles for the spacecrafts battery. Knowing the amount of cycles the battery has to perform during its lifetime and knowing the type of battery used, the optimal DOD can be determined using Figure 21.16 in [1]. For the design of the satellites battery it is chosen to use a depth of discharge of 60%. The same process process has to be conducted for the sizing of the battery used in the ground station. Again the ground station has a mission duration of two Martian years, which translates to 687 Earth days. So this results in 687 charge/discharge cycles and using a safety factor of 1.5 this results in 1,030 cycles. Knowing this the DOD can be determined using Figure 21.16 in [1]. Looking at the graph for the Li-Ion batteries it can be seen that for only 1,000 cycles a high discharge percentage can be chosen. But in order to maintain the lifetime and reliability of the battery used a DOD of again 60% is chosen.

In addition to the depth of discharge, the voltage used to power all the subsystems in the vehicle has to be specified. From SMAD it can be found that the normal steady state voltage is within a range of 25 to 31 V of directional current [1]. So in order to size the battery a bus voltage of 27 V is chosen, which also is applicable for the ground station. In order to reach higher voltages with a battery, the batteries can be put in series. The voltages of each battery add up, increasing the voltage delivered while the capacity of the battery remains constant. If a high capacity is needed, batteries can also be connected parallel, which leads to a summation of the capacities while the voltage remains constant. Using this knowledge, batteries can be put together to reach the required voltage and capacity for the mission operations. Furthermore a battery efficiency has to be estimated if it is not specified by the data sheet of the chosen battery. Furthermore a very important aspect that affects the performance of the battery is the temperature of the environment in which the battery operates. Li-Ion batteries have a better performance when they are warm[3]. For batteries the efficiency typically decreases by 1% for each degree Celsius below their rated nominal temperature. For this reason during the sizing of the thermal control system, special attention is payed to the surrounding temperature of the battery.

The next step in the battery design process is to determine the required capacity of the battery. This can be done using the power that has be delivered, which then is divided by the discharge voltage. This then results in the current that is required to power all the systems. Having calculated the discharge current, the required battery capacity can be estimated using Equation 10.14.

$$C = \frac{P_e}{V_{load}} \cdot t \tag{10.14}$$

Using the required capacity, a commercially available battery can be chosen with the knowledge described in this chapter. After having determined which battery is used, parameters like the nominal capacity and nominal discharge current are known. If the battery is discharged at a higher current than the nominal discharge

[3] http://batteryuniversity.com/learn/article/discharging_at_high_and_low_temperatures

current, than the capacity of the battery decreases by the relation given by Peukert's law, which is shown in Equation 10.15.

$$C_{actual} = C\left[\frac{C}{I_{actual} \cdot t}\right]^{k-1} \tag{10.15}$$

The k used in Equation 10.15 is the Peukert constant of the battery. For Lithium Ion batteries it is known that the Peukert constant is within a range of 1.03 - 1.06[4]. Having determined the actual capacity during discharge and having determined the amount of batteries to achieve this capacity, the battery discharge efficiency $\eta_{batterydischarge}$ can be calculated using Equation 10.16.

$$\eta_{batterydischarge} = \frac{P \cdot t}{DOD \cdot V \cdot C \cdot N} \tag{10.16}$$

Now that the procedure for the estimation of the battery size is known, a commercially available battery can be chosen for the mission. The first battery that is sized, is the battery for the spacecraft. From Equation 10.19 the power usage of the satellite during the eclipse of the orbit can be found. During the eclipse, the battery has to power all the systems. Using $P_{eclipse,s} = 202$ Wh and putting it into Equation 10.14, a required capacity of C = 7.48 Ah is found. Using the required battery capacity, a commercially available battery is chosen. For the spacecraft, the Saft MP174565 Integration xtd Lithium Ion battery is chosen[5]. This battery has a nominal capacity of 4 Ah and the cell has a nominal voltage of 3.65 V and each cell has a mass of 97 g. From the nominal voltage it can be determined that eight batteries have to be put in series, in order to deliver the required bus voltage of 27 V and two of these series have to be put in parallel in order to reach the required capacity, resulting in sixteen batteries. When the battery is discharged within 0.8 h this is equal to a C-rate of 0.8 C and from this a nominal discharge current of 5 A can be determined. The actual discharge current during the operations in eclipse is equal to 12.3 A and using Equation 10.15 the actual battery capacity during discharge is calculated to be 3.39 Ah. This leads to an actual battery capacity in parallel of 6.8 Ah and this is not sufficient to provide power for all the systems during eclipse. So a further row of eight batteries has to be added, which results in three battery rows in parallel. So in total 24 batteries are used with a total mass of 2.33 kg. Using Equation 10.16 the minimum required battery efficiency in order to be able to handle the power consumption can be determined, which results in a minimum required efficiency of 0.15. However from literature it is known that Li-Ion batteries have an efficiency within a range of 80-90%[6]. So during the sizing of the solar array it is assumed that the battery has an efficiency of $\eta_{batterydischarge,s} = 0.9$.

The second battery that is determined is the battery used for the ground station. From Equation 10.20 it can be seen that the power usage during the Martian night is $P_g \cdot t = 1{,}010$ Wh, which results in a required capacity of 37.4 Ah. So for the ground station, the Saft MP176065 Integration Lithium Ion battery is chosen[7]. This battery has a nominal capacity of 6.8 Ah, a nominal voltage of 3.75 V and a mass per cell of 143 g. In order to reach the ground station voltage of 27 V, again eight batteries have to be put in series and in order to reach the required capacity, six rows of eight batteries have to be connected in parallel, which results in a total of 48 batteries. The battery is discharged within 12.33 h, which leads to a nominal discharge current of 0.55 A and the actual discharge current is equal to 12.25 A. So the actual capacity of the battery can be determined using Equation 10.15 and this leads to a capacity of 5.71 Ah. With this actual capacity, the required capacity for the power usage can not be met and that is why a further row of batteries is added in parallel, resulting in seven parallel rows of eight batteries in series. So the ground station uses 56 batteries with a total mass of 8 kg. Having determined this, the minimum operational efficiency of the battery pack can be determined using Equation 10.16 and this leads to a minimum efficiency of 0.2. The battery efficiency used for the sizing of the solar array is taken from literature as $\eta_{batterydischarge,g} = 0.9$.

10.1.5 Sizing of the Solar Array

Before being able to size the solar array, the power usage of each system of the satellite has to be known. Table 10.1 summarises the power required by each system, the run time and when the system is active.
Using Table 10.1 the required amount of Watt-hours ($P \cdot t$) during eclipse and day light of the orbit can be determined. The systems that need special attention when calculating the required amount of Watt-hours are the payload and the communication system, as they are not continuously running. The UV spectrometer only runs 4 minutes while the other instruments are off. And for the communication it has to be said that when the satellite communicates with Earth, all the measurement instruments are off during that period. It is assumed that while communicating with the Martian ground stations all instruments are active, which will

[4]Reader: AE2203: Propulsion & Power, Part: Aerospace Vehicle Electrical power systems
[5]`http://www.saftbatteries.com/battery-search/mp-small-vl`
[6]Reader: AE2203: Propulsion & Power, Part: Aerospace Vehicle Electrical power systems
[7]`http://www.saftbatteries.com/battery-search/mp-small-v`

Table 10.1: *Power usage of the orbiter.*

		Power usage	Run time
ADCS		74.2 W	Continuously running
Payload	UV Spectrometer	9.5 W	4 minutes, other instruments off, works in day light and eclipse
	SPEX	2 W	Runs all orbit except when UV is on, only works in day light
	LIDAR	10 W	Runs all orbit except when UV is on, works in day light and eclipse
Data Handling		17 W	Continuously running
Communication	Mars - Earth	75.3 W	31.66 minutes, in day light, all payload instruments off
	Mars - Mars	71 W	5 minutes, works in day light and eclipse
Thermal		150 W	Continuously during eclipse , 30% of day light

lead to a conservative design. In order to calculate the Watt-hours needed, the time for one orbital revolution is 1.96 hours, of which 60% are in daylight and 40% are in eclipse, which leads to t_{day}=1.18 h and $t_{eclipse}$=0.78 h. The required Watt-hours during daytime and eclipse can be seen in Equations 10.17, 10.18, 10.19. For the calculation of the Wh during day, a distinction between communication with Earth and with Mars is made.

$$P_{day,s_M} \cdot t = 74.157 \cdot t_{day} + 9.5 \cdot 0.066 + 12 \cdot (t_{day} - 0.06) + 17 \cdot t_{day} + 71 \cdot 0.083 + 150 \cdot 0.3 \cdot t_{day} = 181\,\text{Wh} \quad (10.17)$$

$$P_{day,s_E} \cdot t = 74.157 \cdot t_{day} + 17 \cdot t_{day} + 75.3 \cdot 0.53 + 150 \cdot 0.3 \cdot t_{day} = 201\,\text{Wh} \quad (10.18)$$

$$P_{eclipse,s} \cdot t = 74.157 \cdot t_{eclipse} + 9.5 \cdot 0.066 + 10 \cdot (t_{eclipse} - 0.066) + 17 \cdot t_{eclipse} + 71 \cdot 0.083 + 150 \cdot t_{eclipse} = 202\,\text{Wh} \quad (10.19)$$

For the sizing of the solar array the day time power usage for the communication with Earth $P_{day,s_E} \cdot t$=201 Wh is used. For the spacecraft a further power estimation has to be conducted for the trajectory phase of the mission. During this phase the power usage of the ADCS and communication system combined is determined to be 90 W, the thermal control system needs 150 W and the command and data handling subsystem has a power requirement of 5 W. This leads to a power usage during trajectory of P_{trajec}=245 W.

For the ground station a similar power usage estimation has to be made. The power required by the systems of the ground station and their run times are summarised in Table 10.2.

Table 10.2: *Power usage of the ground station.*

		Power	Run time
Instruments	Temperature	1.5 W	Runs for 1 minute every hour, during day and night
	Pressure	1 W	Runs for 1 minute every hour, during day and night
	Wind speed	9 W	Runs for 1 minute every hour, during day and night
	Dust content	0.5 W	Runs for 1 minute every hour, during day and night
	Air composition	5 W	Runs for 1 minute every hour, during day and night
	Radiation	10 W	Runs for 1 minute every hour, during day and night
Communication		43 W	5.83 minutes once per day, during day and night
Data Handling		16 W	Continuously running
Thermal		65 W	Continuously during night, off during day

Using the power data the amount of Watt-hours required to power the ground station can be calculated. A day on Mars has 24.66 h and it is divided equally in day and night time. Furthermore it can be said that the power required for the ground station is the same during day and night. The calculated Watt-hours for the day and night time is shown in Equations 10.20 and 10.21.

$$P_{day,g} \cdot t = 12.33 \cdot 0.016 \cdot (1.5 + 1 + 9 + 0.5 + 5 + 10) + 43 \cdot 0.1 + 16 \cdot 12.33 = 208\,\text{Wh} \quad (10.20)$$

$$P_{night,g} \cdot t = 12.33 \cdot 0.016 \cdot (1.5 + 1 + 9 + 0.5 + 5 + 10) + 43 \cdot 0.1 + 16 \cdot 12.33 + 65 \cdot 12.33 = 1010\,\text{Wh} \quad (10.21)$$

Next to the estimation of the power that is required by the systems of the spacecraft, some solar cell[8] [9] [10]

[8] http://www.azurspace.com/images/pdfs/HNR_0003429-01-00.pdf
[9] http://www.spectrolab.com/DataSheets/TNJCell/tnj.pdf
[10] http://solaerotech.com/wp-content/uploads/2015/03/ZTJ-Datasheet.pdf

options that can be used during the mission have to be chosen. In Table 10.3 the specific data of the solar cells considered for the mission is summarised.

Table 10.3: *Summary of the characteristics of different solar cells.*

	V_{mp}	I_{mp}	V_{oc}	I_{sc}	δ	ρ	**A**
AzurSpace Triple Junction Solar Cell	2.411 V	0.504 A	2.7 V	0.52 A	0.03	86 mg/cm^2	0.00318 m^2
Spectrolab ITJ Solar cell	2.27 V	0.496 A	2.565 V	0.523 A	0.06	84 mg/cm^2	0.0031 m^2
SolAero Technologies ZTJ Space Solar Cell	2.41 V	0.495 A	2.726 V	0.522 A	0.04	84 mg/cm^2	0.003 m^2

Now that the power usage and the characteristics of the solar cells are known, the required array size and the resulting mass of the solar array can be determined using the method presented in this section. In order to account for inaccuracies during the assumptions of the parameters used for the calculation, the final array size is multiplied with a safety margin of 1.2. The results of the calculations are summarised in Table 10.4.

Table 10.4: *Results of the solar array sizing for the MUUDS spacecraft.*

	Array size	**Cell mass**
AzurSpace Triple Junction Solar Cell	5.45 m^2	4.56 kg
Spectrolab ITJ Solar cell	6.58 m^2	5.53 kg
SolAero Technologies ZTJ Space Solar Cell	5.44 m^2	4.56 kg

Table 10.5: *Results of the solar array sizing for the MUUDS ground station.*

	Array size	**Cell mass**
AzurSpace Triple Junction Solar Cell	2.51 m^2	2.16 kg
Spectrolab ITJ Solar cell	3.1 m^2	2.6 kg
SolAero Technologies ZTJ Space Solar Cell	2.55 m^2	2.13 kg

Looking at Table 10.4 the differences in the performance of the solar cells can be seen. It can be seen that the solar cells of AzurSpace and SolAero Technologies have almost the same performance. For the use power production of the spacecraft the ZTJ Space Solar Cell produced by SolAero Technologies is used, because the total resulting area is slightly smaller. The choice for this cell is made because it can supply the required power for the spacecraft using the smallest array area of 5.44 m^2 and the small area results in a lighter design with a total cell mass of 4.56 kg, which adds to the sustainability of the mission. In order to reach the required power production, a total of 1,813 solar cells have to be used.

In addition to the spacecraft, the ground station solar array needs to be sized as well. The results of the calculations can be seen in Table 10.5. Looking at Table 10.5 again the differences in performance of the different solar cells can be seen. The performance of the AzurSpace solar cells and the SolAero Technologies cell are very similar. So for the ground station the ZTJ Space Solar Cell by SolAero Technologies is chosen because of the small mass benefit it has over the AzurSpace solar cell. So for the ground station a solar array with a total area of 2.55 m^2 and a total cell mass of 2.13 kg used. The solar array of the ground station uses 847 solar cells in order to reach the required power output.

Now that the solar arrays for the orbiter around Mars are sized, it needs to be checked whether or not the array size is sufficient to provide power during the trajectory phase. It is estimated that the power consumption is P_{trajec}=245 W and this power has to be constantly delivered. Furthermore during the trajectory phase there is no eclipse. Performing the calculations, a solar array size of 3.6 m^2 is found. This means that solar array size for the operations in the Martian orbit is sufficiently large to provide power during the trajectory phase. However the solar array needs to be deployed during the trajectory phase in order to be able to provide the required power. The deployment and control mechanism is further elaborated in Section 10.5.

When the solar arrays of the ground station and the spacecraft are assembled, the solar cells have to be connected with each other. They can be connected in series and in parallel, which increases the output voltage and capacity respectively. More details on how the cells are connected exactly in order to provide the desired voltage and capacity is elaborated upon in a further design stage. However it can already be mentioned that some safety mechanisms have to be used during the assembly of the solar cells. In order to prevent the failure of a string of solar cells (cells in series) when one cell fails, by-pass diodes have to be used. The by-pass diode can shunt the damaged cell and ensures that the string keeps working. Doing this increases the reliability of the solar array. In addition to that, it has to be noted that the mass of the solar array increases during the assembly.

The solar cells are mounted on a bottom plate and on top of the cells there is a protective layer. This protective layer is used to decrease the effects of the radiation experienced during the mission and thus decreasing the degradation and increasing the lifetime of the solar array. In order to get a first estimate of the total solar array masses, it is assumed that the back plate is made of a honeycomb structure. For the first estimation, aluminium face sheets and an aluminium honeycomb core is chosen, as this has a favourable strength to weight ratio and is a proven construction for solar arrays [74]. The thickness of the honeycomb structure for the mass estimation is assumed to be 1 cm, where the core is 0.8 cm and the face sheets have a combined thickness of 0.2 cm. Moreover for the protective layer a ceria doped micro sheet with a thickness of 1 mm is chosen. The honeycomb core has a density of 54 kg/m^3 [11] and the face sheets are made of aluminium 7075 with a density of 2810 kg/m^3 [12]. Furthermore the density of the micro sheet is taken from literature with a density of 2.6 g/m^3 [74]. Using these material properties and the results of the solar array sizing, a total solar array mass for the spacecraft is estimated to be 37.5 kg and the solar array for the ground station is estimated to have a total mass of 17.56 kg. During the further design process of the mission the power system will be worked out in more detail, as it is explained in Section 11.1.

10.1.6 ADCS Pointing of the Solar Panels

When the satellite is orbiting Mars, its position with respect to the Sun changes. The solar rays will therefore illuminate the solar arrays under a different angle in every position, which might result in a lower power generation. However, if the solar panels can turn themselves towards the incident solar rays, thereby catching the solar flux in the most optimal way, a higher power generated by those panels can be achieved.
The solar panels sized in Subsection 10.1.5 will therefore be mounted on Solar Array Drives, which can turn the panels about two axes. However, to determine the direction from which the incident solar rays are coming from, fine Sun sensors have to be used.

The Mini Fine Sun Sensors of Moog Bradford Technology will be used [75]. These sensors are positioned in every outer corner of the two solar panels, and in each corner closest to the spacecraft's surface, thus adding up to a total of eight MFSSs. These passive systems can collect data on the exact position of the Sun with respect to their position. They are thus capable of analysing under which angle the Sun is illuminating their surface.
On each panel, two sensors will be positioned on the top side of the panel (which is covered with the solar cells) and two sensors will be located on the opposite side. On the same side, they are placed diagonally with respect to each other. By this configuration, it is possible to assess whether the solar panels are illuminated on the correct side. In addition, it can be assessed whether the satellite is shading the solar panels. Based on this information, the panels can be rotated towards the Sun if they are illuminated on the wrong side (which is not covered with solar cells), or they can be elevated to get less shading. The location of the Sun sensors on the solar panels is illustrated in Figure 10.4.

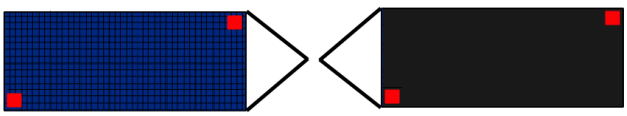

Figure 10.4: *Location of the Mini Fine Sun Sensors on the top surface of the solar panels (left) and on the bottom surface of the solar panels (right).*

The solar angle data collected by the FMSSs is forwarded to the on-board computer of the satellite. The computer processes the information, and determines the most optimal position of the solar arrays with respect to the satellite to achieve the best irradiance of the panels. A best-case-scenario is a scenario in which the solar rays are incident to the solar panels under an angle of 90°. This results in the largest power generation.
The computer sends a command to the Solar Array Drives to turn the arrays to the most optimal position determined by the computer. This position is determined as the attitude of the solar panels in which the solar incidence angle on the panels is (close to) 90°. The angle over which the solar panel has to turn is thus the starting angle of the panel with respect to the incident rays, and a 90° incidence angle.
Two SADs from Moog Bradford Technology will be used, one for each solar panel. These Type 11 Solar Array Drive Assemblies can rotate a panel over 360°, and elevate it over an angle of ±90° [76]. The drives can also make the solar panels fold completely to the surface of the satellite, which is done during entry in orbit around Mars (as is explained in Section 5.1). The Type 11 SAD is shown in Figure 10.5.

[11] http://www.honeycombpanels.eu/20/aluminium-honeycomb-
[12] http://asm.matweb.com/search/SpecificMaterial.asp?bassnum=MA7075T6

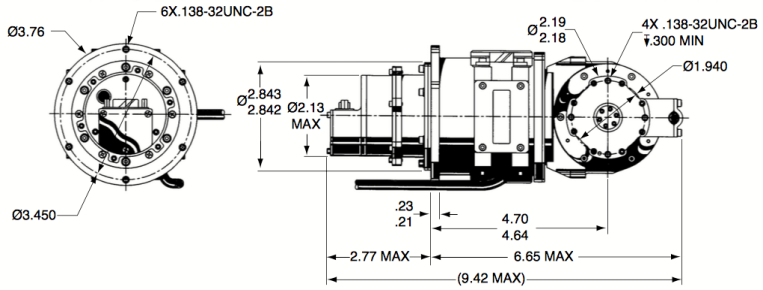

Figure 10.5: *Type 11 Solar Array Drive Assembly, used to turn the solar panels to the Sun [76].*

In summary, the Mini Fine Sun Sensors can define the angle with which the solar rays illuminate the solar panels. The on-board computer calculates a rotation angle over which the panels have to turn to achieve a 90° incidence angle of the solar rays. The rotation of the solar panels is performed by the Type 11 Solar Array Drive Assemblies. The technical specifications of the Mini Fine Sun Sensors and the Solar Array Drive Assemblies are listed in Table 10.6 and 10.7 respectively.

Table 10.6: *Mini Fine Sun Sensors developed by Moog Bradford Technology [75].*

Mini Fine Sun Sensor	
Mass	0.050 kg
Dimensions	50 mm x 46 mm x 17 mm
Field of View	± 64° x ± 64°
Accuracy	0.02° (3 σ)
Power	0 W
Temperature	-50°C - +80°C
Radiation resistance	100 krad

Table 10.7: *Type 11 Solar Array Drive Assembly developed by Moog Bradford Technology [75].*

Type 11 Solar Array Drive Assembly	
Mass	4.2 kg
Power	8 W
Operating temperature	-30°C - +61°C
Rotation angle	360°
Elevation angle	± 90°

10.2 Thermal Control System

In this section the thermal control systems used during the mission are determined and sized. The thermal control mechanisms used during the mission can be divided into two parts, the ones used on the spacecraft during the transfer phase to Mars and during the orbit phase around Mars and the ones used by the ground stations on Mars. In Subsection 10.2.1 the sizing of the thermal control subsystem of the spacecraft is described and in Subsection 10.2.2 the thermal control system of the ground stations is determined and described.

10.2.1 Thermal Control of the Spacecraft

In order to protect the spacecraft from the thermal environment in space, a thermal control system needs to be designed. There are three different modes in which heat can be transferred, which are radiation, conduction and convection. For the design of the thermal control system of the spacecraft, convection is neglected because in space there is no medium for this kind of heat transfer. A further heat transfer mechanism is conduction. There is some conduction of the heat created by the instruments of the spacecraft and between the heated surfaces of the spacecraft. In order to get a first estimate of the equilibrium temperature, it is assumed that everything of the dissipated power of the instruments is conducted to the surface of the spacecraft. For the real life design, insulation layers will be used, which results in a higher internal temperature of the satellite and in a lower outer surface temperature. In space the biggest part of the generated heat comes from radiation.

During the mission phases, the spacecraft encounters four major types of radiation, which are solar radiation, albedo radiation, planetary radiation and heat radiated by the instruments of the spacecraft. When looking at the different types of radiation a distinction between types of radiation has to be made. The Sun and the planet emit solar rays and this is indicated with the subscript s for the absorptivity, α. In addition to that long-wave infrared radiation is emitted by the Sun and by the spacecraft and this is indicated by the subscript ir for the emissivity.

The main source of radiated heat comes from the Sun. In order to calculate the amount of heat that is radiated by the Sun at each point of the mission, the solar intensity has to be calculated. This is done using Equation 10.22.

$$J_s = \frac{P}{4 \cdot \pi \cdot d^2} \tag{10.22}$$

The d used in Equation 10.22 is the distance of the spacecraft from the Sun. After calculating the solar intensity at the desired location, the amount of heat radiated by the Sun can be determined using Equation 10.23.

$$\underset{Sun}{\dot{Q}} = \alpha_s \cdot J_s \cdot A \cdot F_{i,j} \tag{10.23}$$

$F_{i,j}$ used in Equation 10.23 is the visibility factor and it indicates which surfaces of the spacecraft are exposed to any form of radiation.

Next to the solar radiation there is the albedo radiation. The albedo radiation is a form of radiation that needs to be accounted for when determining the thermal balance of the spacecraft orbiting around a planet. The albedo of the planet is the amount of solar radiation that is reflected by the surface of the planet. In order to calculate the albedo radiation, the first step is to determine the visibility factor of the spacecraft, which indicates the amount of sun rays that heat up the spacecraft's surface. For designing only the two worst cases are considered, which are when the spacecraft is on the shadow side of the planet ($F = 0$) and when the spacecraft is on the Sun-lit side of the planet[13]. The visibility factor for the Sun-lit side is calculated using Equation 10.24.

$$F = \left(\frac{r_{planet}}{r_{orbit}} \right)^2 \tag{10.24}$$

Using the visibility factor calculated in Equation 10.24, the albedo flux of the planet can be determined using Equation 10.25.

$$J_a = a \cdot J_s \cdot F \tag{10.25}$$

The radiated heat by the albedo of the planet can be calculated using Equation 10.23, but instead of using the solar flux, the albedo flux, J_a, has to be used during the calculations.

The last form of radiation that is considered in the heat balance of the spacecraft is planetary radiation. The planetary radiation is the infrared radiation emitted by the planet and it has only to be used for spacecraft orbiting around the planet and can be neglected for deep space trajectories. The first step in calculating the planetary radiation is to determine the planet flux and this is done using Equation 10.26.

$$J_{IR} = \sigma \cdot T_{IR}^4 \tag{10.26}$$

The radiated heat due to infrared radiation of the planet is calculated using Equation 10.23 only that J_{IR} is used instead of the solar flux. Furthermore a different absorptivity has to be used as this form of radiation is infrared instead of solar. By applying Kirchhoff's law $\alpha_{ir} = \varepsilon_{ir}$, the absorptivity of infrared radiation thus can be replaced by the emissivity of infrared radiation during the calculation of the heat radiated by the planetary flux.

Now that all the forms of radiation are known, the equilibrium temperature of the spacecraft can be determined by setting up a heat balance. The heat flow, from space to the spacecraft, is equal to the heat flow from the spacecraft to space. Having said this, Equations 10.27 can be set up and be further worked out to Equation 10.28.

$$\underset{in}{\dot{Q}} = \underset{out}{\dot{Q}} \tag{10.27}$$

$$\underset{absorbed}{\dot{Q}} + \sum P_{dissipated} = \underset{emitted}{\dot{Q}} \tag{10.28}$$

In Equation 10.28 the heat absorbed consists of the heat radiated by the Sun, the albedo radiation and the planetary radiation. The emitted heat is given by Equation 10.29.

$$\underset{emitted}{\dot{Q}} = \varepsilon_{ir} \cdot A \cdot F_{sat \to space} \cdot \sigma \cdot (T^4 - T_{space}^4) \tag{10.29}$$

The heat emission from the surface of the vehicle to the planet is neglected in this heat balance, since it does not affect the solution. When substituting all the equations for the radiated heats forms, the equation can be solved for the equilibrium temperature, T.

In order to calculate the equilibrium temperature of the spacecraft, the surface properties like absorptivity and emissivity have to be known. During the design process, different surface finishes are compared in order to get the optimal equilibrium temperature of the spacecraft. However one further calculation is required regarding the surface properties of the spacecraft. During the orbiting phase around Earth and during the trajectory phase, the solar panels are not deployed. During both these phases the solar panels are attached to the surface

[13] Reader: AE1222-II: Aerospace Design & Systems Engineering Elements I Part: Spacecraft (bus) design and sizing

of the spacecraft, creating a uniform surface. For this mixed surface a different absorptivity and emissivity value applies. These new surface properties can be determined by setting up Equation 10.30.

Substituting Equation 10.29 in Equation 10.30 and adjusting the subscripts for the different parameters, an expression for the absorptivity/emissivity of the mixed surface can be found. This expression is given by Equation 10.31. This equation can be used to calculate the emissivity and absorptivity for both solar and infrared radiation of the surface.

$$\dot{Q}_{mixed} = \dot{Q}_{thermal} + \dot{Q}_{panels} \tag{10.30}$$

$$\varepsilon_{mixed} = \frac{\varepsilon_{thermal} \cdot A_{thermal}}{A} + \frac{\varepsilon_{panel} \cdot A_{panel}}{A} \tag{10.31}$$

When calculating the equilibrium temperature of the spacecraft, the three different mission phases the spacecraft goes through have to be considered. For all three mission phases a hot and cold scenario is considered for the thermal balance. The first mission phase that is considered is the orbiting phase around Earth. For the calculation of the hot case it is assumed that the spacecraft is on the day side of the Earth. So it is exposed to all the mentioned forms of radiation mentioned before. For the cold case, the spacecraft is in eclipse. So there is no exposure to any form of solar radiation. So the solar radiation and the albedo radiation are equal to zero. The next phase that is considered is the trajectory phase. During the trajectory phase the spacecraft only experiences solar radiation, since there are no planets present for albedo and planetary radiation. During both the orbiting phase and the trajectory phase, the power consumption of the spacecraft is considered to be equal and constant in time. The last mission phase that is considered in the sizing of the thermal control subsystem of the spacecraft is the orbiting phase around Mars. During the hot scenario again all the radiation forms mentioned before apply, since the satellite is on the day side of Mars. Furthermore in order to calculate the solar radiation during the hot case, the minimum distance between Sun and Mars is used. For the cold scenario the spacecraft is in eclipse so the radiation depending on solar radiation are equal to zero and only the planetary radiation of Mars is considered. In addition to that the power dissipation during the hot and cold scenario around Mars is assumed to be constant.

During the calculation of the equilibrium temperatures during the Earth orbiting phase and the trajectory phase, only the part that is also used for the Mars orbiter is considered. This is done as the Mars orbiter is separated from the EDL modules and the thermal control of the EDL modules is done independently of the thermal control of the orbiter as described at the end of Section 10.2.2. The satellite dimensions that are considered for the thermal analysis of the spacecraft are a length of $l = 3\,\text{m}$, a width of $w = 1.5\,\text{m}$ and a height of $h = 1.5\,\text{m}$.

Now that all the information for the calculation of the equilibrium temperatures is gathered, some design choices for the thermal control subsystem of the spacecraft can be made. Before calculating the equilibrium temperature of the spacecraft some parameters have to be determined. The first design parameters that have to be known are the operating temperatures of the electrical systems used in the spacecraft. The known operational temperature ranges of the systems used in the spacecraft are summarised in Table 10.8.

Table 10.8: *List of the operational temperature ranges of the orbiter's on-board instruments.*

System	Operational Temperature	System	Operational Temperature
Accelerometer	-55°C - +125°C	Coarse Sun Sensor	-80°C - -120°C
Transponders	-40°C - +60°C	Fine Sun Sensor	-50°C - +80°C
Reaction Wheels	-15°C - +60°C	Battery	-40°C - +80°C
Inertial Reference Unit	-20°C - +60°C	Board Computer	-55°C - +125°C
Star Tracker	-20°C - +50°C	Solid state drive	-20°C - +50°C

Next to the desired operating temperatures, a selection of spacecraft coatings has to be made that can be used to reach the desired equilibrium temperature of the spacecraft. In order to have a high equilibrium temperature on the surface of the spacecraft, surface coatings with a high absorptivity and a low emissivity are desired. The selected coating materials that are considered for the coating of the spacecraft are shown in Table 10.9[14] [1]. In addition to that the solar absorptivity and thermal emissivity of the solar panels has to be determined. For the solar cells used the absorptivity is taken to be 0.92 and the emissivity is 0.85.

Moreover an estimation on the power dissipated by the instruments has to be made. Power dissipation occurs as a current flows through a resistor and in this case the instruments are seen as resistors. The instruments have a certain resistance to let the electrical current flow through and the current is forced through by the voltage provided by the power system. The resistance of the instruments acts as a form of friction. Due to that friction, heat is generated by the electrical current and this is called the dissipated power. Calculating the amount of power that is dissipated during the use of the instruments would be too detailed for this stage of the design.

[14] `http://www.tak2000.com/data/finish.htm`

Table 10.9: *Selected coating materials for the MUUDS spacecraft.*

	Absorptivity	**Emissivity**
MAXORB	0.9	0.1
Black Nickel	0.91	0.66
Black Anodised Aluminium	0.65	0.82
Black Copper	0.98	0.63

That is why an estimation on the power dissipated is made. For the estimation it is assumed that 100% of the power provided by the thermal control system is dissipated, as this power is used for heaters and 30% of the power provided to all the other systems is dissipated as heat. The power consumptions of the spacecrafts systems can be found in Table 10.1 in Section 10.1.5. During the trajectory phase the total power usage is 245 W, of which 150 W are for the thermal control. So this results in $P_{dissipated,t} = 179$ W during the trajectory phase. For the estimation of the power dissipation during the operations in the Martian orbit the power consumption of 333 W during the normal operations (no communication with Earth) is used. Again 150 W is used for the thermal control of the spacecraft and the total power dissipated in Martian orbit is $P_{dissipated,m} = 205$ W.

Now that all the design parameters for the thermal control of the spacecraft have been determined, the equilibrium temperatures during the mission operations can be calculated. In Table 10.10 the equilibrium temperatures in each mission phase for the different coating materials can be seen.

Table 10.10: *Equilibrium temperatures of the spacecraft during the different mission phases.*

	Earth Orbit		**Trajectory**	**Martian Orbit**	
	Hot	Cold		Hot	Cold
MAXORB	395.7 K	173.2 K	313.5 K	393.4 K	228.8 K
Black Nickel	339.7 K	193.5 K	253.8 K	251.4 K	165.3 K
Black Anodised Aluminium	318.2 K	195.6 K	237.6 K	224.6 K	161.3 K
Black Copper	344.8 K	193 K	257.6 K	258 K	166.2 K

Looking at Table 10.10 some conclusions about the thermal control and the surface of the spacecraft can be made. It can be said that none of the considered surface finishes is able to meet all the operational temperature ranges of the system as they can be found in Table 10.8. However it can be said that some coatings show a better performance for the use of the mission than others. The first surface coating that can be taken out of consideration is MAXORB. During the cold case around Mars and the trajectory phase the equilibrium temperature is acceptable but during the hot cases, the resulting temperatures are too high for all of the systems used in the spacecraft. Furthermore the black anodised aluminium is not considered as a coating for the spacecraft. In the Martian orbit both the hot and cold case equilibrium temperatures are very low compared to the equilibrium temperatures of the other surface coatings.

Now a trade-off between the black nickel coating and the black copper coating has to be made. Both these coatings perform very similar in both phases of the mission. However it can be seen that the resulting equilibrium temperatures of the black copper coating are slightly higher than the ones of black nickel. For that reason black copper is chosen as coating for the spacecraft. In the Earth orbit it can be seen that the hot case temperature is too high for most of the systems used and the cold case temperature is too cold cold for all the systems. During the trajectory, as well as during the hot case scenario in the Martian orbit, all the temperature ranges of the systems are met. However during the cold case scenario in the Martian orbit, the resulting temperature is too cold for all the systems used. Since not all temperature ranges are met during every phase of the mission, some further considerations have to be made.

The first consideration that can be made, is the use of patch heaters on the critical instruments in order to heat them up. Such a heater would be controlled by a thermostat that constantly monitors the temperature of the system and starts heating the system if the temperature drops below a certain critical temperature. For a first estimation it is assumed that thermal control systems such as patch heaters use approximately 150 W, whereas commercially available heaters use 0.8 W/m^2 [15]. However during the eclipse phase around Earth and Mars it has to be considered that more power might be required for the heating of the systems. The use of insulation layers can also be considered. These insulation layers protect the internal systems of the satellite against the large temperature differences experienced during each orbit and help to maintain a more constant internal equilibrium temperature. The steps that will be undertaken in the next design phase of the MUUDS mission are explained in Section 11.6.

[15] `http://www.nphheaters.com/quote/kapton/kapton_flexible_heaters.ht`

10.2.2 Thermal Control of the Ground Station

The ground stations used during the operative phase have to withstand a variety of thermal environments. First of all the ground stations and the landing vehicle as a whole, have to be able to withstand the space environment during the transfer phases of the mission. Moreover the thermal control system of the landing vehicle and system of the ground station have to maintain a suitable temperature range during the EDL phase. And lastly the thermal control system of the ground station has to regulate the temperature of the system during the operations on Mars. The main focus of the thermal control system sizing at this stage of the design process is on the operations phase of the mission.

In order to size the thermal control system of the ground stations, some design drivers have to be determined. The main design driver is the thermal environment on the Martian surface. Every day the temperature can fluctuate between -100°C and 20°C. In addition to that the temperature also depends on the landing site and time. This means that the time of the year, latitude, thermal inertia of the surface, dust level and elevation can change the temperature of the environment [77]. A further design driver are the optimal operational temperature limits of the instruments and systems used in the ground station. So a list of all the optimal operating temperatures has to be made and then a trade-off between them has to be made in order to select the temperature that allows all the instruments to work properly. In addition to that the different power and operation scenarios drive the design of the thermal control system as well. A distinction between maximum and minimum power usage has to be made, since this changes the amount of power that is emitted by the instruments. Moreover different temperature scenarios during day and night time have to be considered. Using these different scenarios, the thermal control system can be sized, to withstand the worst hot and cold cases during the operation phase.

In order to protect the ground stations against the thermal environment of Mars, some design considerations for the thermal structure of the station can be made. First of all a coating with a low emissivity has to be used for the outer surface of the station. This minimises the heat loss due to radiation. In addition to that insulation layers should be used to protect the instruments inside the station from the thermal swings experienced on Mars. In addition to that, a thermal insulation layer minimises the heat loss due to convection [78]. A further design option that is considered to be used in the Martian ground stations is a heat switch. A heat switch shunts the insulation layer used, in order to conduct excess heat to the outside. This excess heat is then rejected into the Martian atmosphere or soil. In order to have an efficient heat switch, the material of the switch should have high thermal conductance [78].

When calculating the equilibrium temperatures of the ground station, all the forms of heat transfer have to be considered. Unlike the calculations used for the thermal balance of the in orbit operation, conduction and convection are considered for the thermal balance of the ground station, since there is a medium present for these forms of heat transfer. The first form of heat transfer that is considered, again is radiation. In order to calculate the amount of heat that is radiated from the surface of the station to the Martian environment, Equation 10.29 has to be used. A further form of radiation that is present on the Martian surface is solar radiation. In order to calculate the solar intensity and heat radiated due to solar radiation Equations 10.22 and 10.23 have to be used.

The next type of heat transfer that is considered is conduction. On the surface of Mars there are two main forms of conduction present. The first form is the heat that is conducted from the inside of the ground station to the surface of the station. This can be determined using Equation 10.32.

$$\underset{cond,s}{\dot{Q}} = \frac{\lambda_{in} \cdot A_s}{l_{in}} (T_b - T_s) \tag{10.32}$$

The second form of conduction, is the heat that is conducted from the inside of the station into the Martian soil. This is calculated using Equation 10.33.

$$\underset{cond,g}{\dot{Q}} = \frac{\lambda_{in} \cdot A_g}{l_{in}} (T_b - T_\infty) \tag{10.33}$$

The λ_{in} used in the calculations for the heat conducted, stands for the thermal conductivity of the insulation layer and the l_{in} stands for the length of the conductive path. During the calculations the length of the conductive path is taken to be the insulation layer thickness, which is a design choice as well as the thermal conductivity of the insulation layer. Moreover the heat conducted due to the heat switch has to be determined. The equation used for the calculation of the heat conducted with the heat switch is similar to Equation 10.33, with the difference that the thermal conductivity of the heat switch material is used and that the length of the conductive path stands for the length of the heat switch. Both the length of the heat switch length and conductivity are noted with the subscript sw.

The last form of heat transfer that is considered is convection. The equation used to calculate the heat loss due to convection is Equation 10.34.

$$\underset{conv}{\dot{Q}} = h_c \cdot A_s \left(T_s - T_\infty\right) \tag{10.34}$$

The h_c used in the calculation of the heat transfer due to convection, is the convective heat transfer heat coefficient, which is defined by Equation 10.35.

$$h_c = \frac{\lambda \cdot N_{UD}}{D_h} \tag{10.35}$$

The properties used in Equation 10.35 have to be determined separately. λ is the thermal conductivity of the surrounding gas. The calculations for the thermal conductivity of Mars are done using the properties of CO_2, since this is the most dominant gas with 95% of the Martian atmosphere. So in order to calculate the thermal conductivity the method presented in Brian Burg's Thermal Control Architecture is used [78]. The D_h is hydraulic diameter of a rectangular cross section and is determined using Equation 10.36 as presented in Heat And Mass Transfer [79].

$$D_h = \frac{4 \cdot width \cdot length}{(width + length) \cdot 2} \tag{10.36}$$

The last unknown that needs to be determined is N_{DU}, which is the Nusselt number. Before calculating the Nusselt number, a distinction between two forms of convection has to be made. There exists free and forced convection. Free convection takes place if there is no wind present in the atmosphere and forced convection takes place when there is wind present. So for the thermal calculations of the ground station only forced convection is used because there is wind present in the Martian atmosphere. The Nusselt number for forced convection is calculated using Equation 10.37.

$$N_{UD} = 2 + \left(0.4 {R_e}^{0.5} + 0.06 {R_e}^{2/3}\right) {P_r}^{0.4} \left(\frac{\mu}{\mu_s}\right)^{1/4} \tag{10.37}$$

R_e is the Reynolds number on the surface of Mars and it depends on the wind speed, hydraulic diameter and kinematic viscosity. P_r is the Prandtl number, which is known for CO_2, and μ is the dynamic viscosity.

Now that the necessary equations for the analysis of the thermal calculations of the ground station are known, the equilibrium equation can be set up. But before setting up the equilibrium equation, some assumptions to the analysis have to be made in order to simplify the calculations. First of all it is assumed that the ground station has a rectangular shape. In addition to that, it is assumed that the Sun rays are perpendicular to the surfaces of the ground stations and that when being exposed to sunlight, half of the surface area of the station is exposed to the Sun rays. This assumption leads to an increase in the heat generated due to solar radiation. Furthermore it is assumed that the ground station is isothermal and homogeneous, which results in equal temperatures everywhere inside or on the surface of the station and in equal material properties everywhere. Moreover it is assumed that the temperatures used during the analysis do not change in time in order to perform a steady state analysis [78].

Now that the assumptions used during the analysis are stated, the equilibrium equations can be set up. The first equilibrium equation gives the relation between the heat conducted to the surface and the heat that is radiated and convected from the surface into the Martian atmosphere. This relation is given by Equation 10.38.

$$\underset{cond,s}{\dot{Q}} = \underset{rad}{\dot{Q}} + \underset{conv}{\dot{Q}} - \underset{Sun}{\dot{Q}} \tag{10.38}$$

The second equilibrium equation is used to describe the internal heat balance of the station. It relates the dissipated power by the instruments to the heat conducted to the surface of the station, to the ground and the heat conducted by the heat switch. This relation is given in Equation 10.39.

$$\sum P_{dissipated} = \dot{Q}_{cond,s} + \dot{Q}_{cond,g} + \dot{Q}_{cond,sw} \tag{10.39}$$

Now two equations are given that can be used to solve for the internal body temperature, T_b, and for the surface temperature, T_s, of the ground station. In order to do so a Python script has been used. When solving for the surface temperature, T_s, four solutions are computed since the surface temperature has a power of four. However only one solution for T_s is feasible as the other results are in the complex regime or below absolute zero. This result for the surface temperature can then be used to determine the body temperature.

As already mentioned before in this subsection, the thermal sizing is done using different temperature and power scenarios. In order to properly size the thermal subsystem of the ground station, the two extreme hot and cold

scenarios are considered. During the hot scenario, the ground station is on the day side of Mars, which means that it is exposed to full sunlight and thus solar radiation. In addition to that, it is considered that during this period of time the temperature is 20°C, as this is the highest measured temperature on the Martian surface[16]. The power consumption during the hot scenario is considered to be maximum, which means that all instruments in the ground station are working and thus dissipating power. In contrast to the hot scenario, there is the cold scenario. During the cold scenario the ground station is on the night side of Mars. This means that there will be no exposure to sunlight and thus the solar radiation is zero. During the night time the temperature on Mars decreases. So for the cold scenario it is assumed that the temperature is -153°C, which is the coldest temperature encountered on Mars[17]. Both the hot and cold scenario can be calculated for different heat switch configurations. The heat switch can be on or off. So when the heat switch is off, the heat conducted by the heat switch is zero. For the hot case, the day it is chosen that the heat switch is open and for the cold case in the night it is chosen that the heat switch is closed.

Now that all the information is gathered that is required to size the thermal system of the ground station, some design choices for this subsystem can be made. Similarly to the thermal control calculations performed for the sizing of the satellite, the first step for the thermal balance of the ground station is to determine the operational temperature ranges of the instruments and systems used. For the instruments that are used in the ground station, no information on the operational temperature ranges is available. So the design temperature range is determined by the battery used for the power system of the ground station. From the data sheet of the battery it can be found that the operating temperature range is between -50°C and +60°C[18].

Furthermore the dissipated power has to be determined. For the ground station a similar approach as for the spacecraft is used. The power that is used by the thermal control system is assumed to be 100% dissipated and the rest of the power used by the instruments is 30% dissipated. During the day time operations, the ground station uses 86 W and none of it is used for thermal control. So during the operation on a Martian day the dissipated power is equal to 26 W. During the night time operation, 65 W for the thermal control is added and this results in a total power usage of 151 W and so the dissipated power becomes 91 W.

Furthermore choices for the surface coating have to be made. While designing the thermal control system of the same coating options as presented in Table 10.9 are considered. Next to the coating materials listed in the table, Vaporised Deposited Gold is also considered as a coating material with an absorptivity of 0.25 and an emissivity of 0.03. In addition to that, insulation material has to be chosen. In order to protect the internal environment from the heat swings experienced by the Martian environment, an insulation layer with a low thermal conductivity is desired. For the insulation layer, it is chosen that the insulation layer has a thickness of 0.1 m. For the insulation, Silica Aerogel is chosen. Silica Aerogel has a the lowest available thermal conductivity with 20 mW/mK and also has a low density of 0.1 g/cm^3 [78]. Moreover a material for the heat switch has to be decided upon. The heat switch material should possess a high thermal conductivity in order to easily reject heat from the inside of the body to the outside environment. So for the heat switch a metal is chosen. For the sizing of the thermal control system of the ground station, it is chosen to use an aluminium heat switch with a thermal conductivity of 205 W/mK [19]. In addition to that it is chosen that the heat switch has a surface area of 0.01 m^2 and a length of 0.05 m. Now that all the required information for the sizing of the thermal control system of the Ground station is known, the resulting temperatures can be determined.

The resulting equilibrium of the surface of the ground station and the resulting internal body temperature, using the different surface coatings, can be seen in Table 10.11.

Table 10.11: *Temperature ranges experienced by the ground station.*

	Martian Day		**Martian Night**	
	Surface Temperature	Body Temperature	Surface Temperature	Body Temperature
MAXORB	351.6 K	294.7 K	135.9 K	254.6 K
Black Nickel	325.8 K	294.3 K	134.3 K	253.3 K
Black Anodised Aluminium	314.5 K	294.1 K	134.0 K	253.0 K
Black Copper	328.9 K	294.3 K	134.4 K	253.4 K
Vaporised Deposited Gold	311.8 K	294.1 K	136 K	254.8 k

[16] http://quest.nasa.gov/aero/planetary/mars.html
[17] http://quest.nasa.gov/aero/planetary/mars.html
[18] http://www.saftbatteries.com/battery-search/mp-small-v
[19] http://www.engineeringtoolbox.com/thermal-conductivity-d_429.html

When looking at the calculation results of the thermal control system of the ground station, it can be seen that the performance of the different surface coatings is very similar. During the day time operations, it is desired that the surface temperature and especially the body temperature are not too high and during the night time operations, it is desired that both the temperatures are not too low. Using this selection criterion, it can be said that the Vaporised Deposited Gold shows the best performance during both the Martian day and the Martian night and for that reason it is chosen as coating material of the ground station. With a body temperature of 294.1 K (21°C) during the day and a body temperature of 254.8 K (-18.4°C) during the night, the operational temperature range of the battery is satisfied. In the further design stages of the mission, the thermal control system of the ground station has to be analysed in further detail, as explained in Section 11.1.

Thermal Control of the EDL system

Besides the thermal control of the ground station during the operational phase, the systems of the ground station also need to be thermally controlled during the trajectory phase and the EDL phase of the mission. The thermal control sizing for the trajectory and EDL phase are only briefly described in this section, as the sizing of such a system is too detailed for the design stage of the mission.

During the trajectory phase, the ground station is packed into a landing module. All the systems used on the ground station are in a standby mode, so there is very little power consumption and power dissipation. Due to the low power dissipation and the insulation, provided by the landing module and the insulation layer of the ground station, the systems of the ground station become cold and the temperature can go beneath the operational limits.

In order to prevent damage and freezing of the systems, heating systems can be used. Options for these heating systems are fluid heating systems, which can heat up the instruments and if necessary reject excess heat from the inside of the ground station into space. Another simpler method is to use electrical heaters, which maintain the instruments of the ground station at a suitable temperature.

Furthermore the systems used during the EDL phase, like the rockets and parachute, need to be thermally controlled. These systems however can be maintained at non operational temperatures during the trajectory phase [80]. When going into the EDL phase the hardware of the ground station as well as the components used for the EDL phase have to be within their operational temperature range. Since the EDL systems can be maintained at non operational temperatures during the trajectory phase, a thermal conditioning phase before starting the entry into the Martian atmosphere is necessary [80]. During this thermal conditioning phase the systems used during the EDL are heated to their operational temperature, using electrical heaters and thermostats. The ground station is in the landing vehicle during EDL and it is thus protected from the heat, generated by the aerodynamic braking, due to the heat shield of the landing vehicle and due to the insulation layers used on the ground station and the landing vehicle. In order to safe power during the EDL phase, the hardware of the ground station is not heated or thermally controlled by other systems. Therefore the hardware relies on the insulation of both the landing vehicle and the ground station.

10.3 Command and Data Handling System

The Command and Data Handling (C&DH) Subsystem is responsible for handling all forms of commands and data involved in the system and controls all other electrical subsystems. This includes the processing, storage and preparation of data and executing received and autonomous commands. This subsystem needs to be radiation tolerant, highly reliable and safe. First an overview is given by means of a data handling block diagram. Then the total data volume that needs to be transmitted is estimated. Furthermore several components of the subsystem are discussed including their specifications.

10.3.1 Data Handling Block Diagram

A qualitative overview of the most important components of the C&DH subsystem is shown by means of a data handling block diagram in Figure 10.6. This is a general diagram, applicable for both the orbiter and the ground stations, since the architecture of data handling is basically the same. The on-board computer is displayed as a 'black box' for clarity and because investigating all the components in the subsystem, in that level of detail, is out of the scope of this project. Several of the components are selected and elaborated on in Subsection 10.3.3.

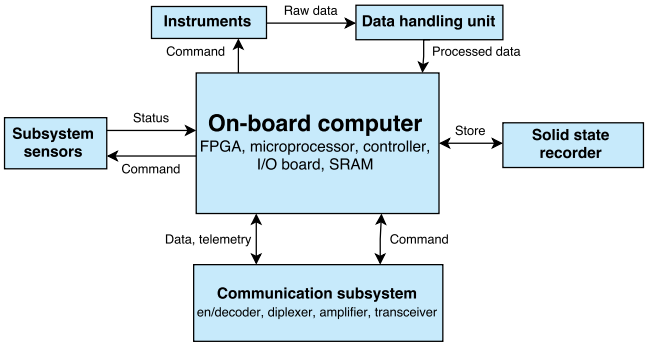

Figure 10.6: *General data handling block diagram of the C&DH subsystems.*

10.3.2 Total Data Volume

For each link an estimation is done on the data volume for an average operation day on Mars. Apart from the measurement data, data on location, time, status, etc. needs to be transmitted, called telemetry. Since an accurate number on the volume of the telemetry data is not possible in this design stage, it is estimated to be 10% of the measurement data volume[20]. For the data overhead (coding, modulation, start/stop sequences, etc.) another 10% of additional data is estimated.

Measurement data and telemetry

In Table 10.12 the total data rate for the measurements of the orbiter and ground stations for one sol is shown. This data is going to be sent daily by the orbiter to the Earth ground stations, which is discussed in Section 10.4. Data volumes and frequencies are obtained from Section 8.3, and Subsection 7.1.2 and 7.1.3.

Table 10.12: *Total data volume of the ground station and orbiter measurements for one sol.*

	Data per measurement	Measurements per sol	Data volume
Ground station			
RTD-PT860	7 bit	24	0.17 kbit
Fibre optic sensor	7 bit	24	0.17 kbit
Hot film anemometer	7 bit	24	0.17 kbit
Laser optic dust	7 bit	24	0.17 kbit
Spectrometer	40 bit	24	0.96 kbit
Radiation	8 bit	24	0.19 kbit
Additional data	52 bit	24	1.25 kbit
Subtotal ground station			1.82 kbit
Telemetry (10%)			0.18 kbit
Data overhead (10%)			0.20 kbit
x10 ground stations			**22.0 kbit**
Orbiter			
UV spectrometer	2,200 bit	67	147.4 kbit
SPEX	540 bit	20,382	11,006.3 kbit
Lidar	2,250 bit	2,824	6,354 kbit
Subtotal orbiter			17,507.7 kbit
Telemetry (10%)			1,750.8 kbit
Subtotal			19,280.5 kbit
Data overhead (10%)			1,928.1 kbit
Total			**21,208.6 kbit**

From the total data volume of the ground stations, an estimate can be made for the required data rate for the communication link with the orbiter. The minimum communication time between the ground stations and the orbiter is 140 s (see Table 6.6). This results in a data rate of approximately 16 bit/s. This is relatively low compared to the chosen data rate of 32 kbit/s for the uplink in Subsection 10.4.3. However when taking parameters into account, that were out of the scope of this analysis, an over-sized data rate is preferred. For example, possible antenna offset by elevation, signal blockage by obstacles, link establish time, etc. This conservative data rate estimation did not have a major influence on the transmitter power and SNR. Furthermore the selected components for the C&DH subsystem are fully capable of processing this data rate. If in later research it turns out more data is produced than estimated, it is anticipated by this data rate.

[20] Information obtained through personal communication with ir. Jasper Bouwmeester of Delft University of Technology.

From the total data volume that needs to be transmitted to Earth, a data rate for the communication between the orbiter and the DSN can be estimated. The contact time is estimated at 1,900 s (see Table 6.6), which results in a data rate of approximately 11.2 kbit/s, which is again quite low. The statement for the UHF link holds for this link as well and in Subsection 10.4.3 a data rate of 16 kbits/s is chosen. In this phase, the amount of data is probably underestimated, especially when comparing data with reference Mars orbiters. Thus an over-designed data rate is preferred over a tight data rate.

During the two solar conjunctions during this mission (see Subsection 4.1.3), communication will not be possible for ten days. The data produced by the measurement system in this time interval will be stored and sent after the solar conjunction has passed. This would mean an accumulated data volume of 212 Mbits, which cannot be sent during one communication link. However when dividing this data into several links, it is possible to send it over a period of seven sols.

Command

The data sent during uplink from Earth to the orbiter and from the orbiter to the ground stations on Mars is called telecommand or just command, since commands are given to the systems. The data rate of the command is of course lower than the links towards Earth, since no measurement data is sent. Since in this phase of the design it is not possible to calculate a data volume of the command data because that goes too much into detail, an estimate is taken from literature. For deep space and planetary missions a command data rate of 2,000 bit/s is common and assumed for this mission [1]. For the command link from the orbiters to the ground stations, a link of 8 bit/s is sufficient to properly operate them [81][82]. Further research into the command link has to be done in a later design stage.

10.3.3 Main Components

The main components of the C&HD subsystem are the on-board computer, the data handling unit and the solid state recorder. These components will not be designed, but selected from off-the-shelf products. Their basic characteristics, such as memory size, computing power and data rates, are listed. Of course all components are selected keeping the harsh radiative environment in mind.

On-board computer

The on-board computer (OBC) controls all processing tasks in the C&DH subsystem. It controls all the other components and other subsystems. The core element of the OBC is the microprocessor board with its violate and non-violate memories. Furthermore it regulates the power, decodes telecommunication and performs time management, storage management and subsystem status telemetry. OBCs in spacecraft are usually single-board computers. For this mission the RAD750 6U-160 CompactPCI single-board computer is chosen. BAE Systems has built proven the design of its RAD750 microprocessors in several space missions, for example on the Mars Reconnaissance Orbiter and Curiosity. The 6U-160 edition is designed for relatively long missions, with high radiation requirements. The most important and relevant specifications are listed in Table 10.13[21]. This product is radiation hardened and can withstand a substantial amount of radiation. Furthermore logical measurements are taken against radiation, for example a watchdog timer and redundant elements on system and circuit level.

The OBC will be put on every ground station and twice on the orbiter for redundancy. 260 MIPS (Million Instructions Per Second) is more than sufficient for the chosen data rates of the instruments and telecommunications. The memory size of the SRAM (Static Random Access Memory) cannot be chosen yet, since too little is known about the used software and performance of the C&DH subsystem. This memory size will determine the exact mass of the OBC. This OBC is compatible with VxWorks, the operating system of most NASA rovers. It is possible that this mission will also use VxWorks as OS, however at this moment those decisions cannot be made.

Solid State Recorder

The Solid State Recorder (SSR) is a mass memory device without movable parts, which makes it more reliable. Its stores instrument and telemetry data in between communication links. For this mission the MPC8260 Solid State Data Recorder from Surrey Satellite Technology is chosen. This is a relatively small recorder in terms of data size (2 GB) in comparison with the MRO (160 GB). However the estimated data volume of this mission is relatively small, as no high resolution data, like photographs, are stored. In Table 10.14 several specifications are stated of this SSR[22]. On each ground station, one of these SSR's will be implemented and two on the orbiter

[21] BAE Systems RAD750 6U CompactPCI datasheet: `http://www.baesystems.com/download/BAES_052280/Space-Products--RAD750-6U-cPCI`

[22] SSR Surrey Satellite Technologies:`https://www.sst-us.com/SSTL/files/21/2158d012-854d-4fa4-a567-2c0a8b530104.pdf`

for redundancy. This SSR claims to be capable of processing raw payload data, however in what extent is not known. The 2 GB data storage is sufficient for ground station and orbiter storage, which is, according to current estimates, 21 MB per sol. The available data storage is sufficient for the solar conjunction as well, since the required data volume would be 212 MB (see Subsection 10.3.2).

Table 10.13: *Technical specifications of the RAD750 6U-160 CompactPCI on-board computer.*

RAD750 6U-160 CompactPCI single-board computer	
Size	233 mm x 160 mm
Mass	1000 - 1220 g
Purchase price	$200,000
Operating voltage range	5 V and 3.3 V
Power	10 W
Operational temperature	-28°C - +70°C
Power dissipation	11 to 14 W
Total radiation dose	> 100 krad
Single event upset	$1.9 \cdot 10^{-4}$/card-day
Performance	260 MIPS @ 132 MHz
SRAM	16 MB (upgradable to 48 MB)
EEPROM	4 MB
TRL	Level 9 since 2010

Table 10.14: *Technical specifications of the MPC8260 solid state data recorder.*

MPC8260 Solid State Data Recorder	
Size	330 mm x 330 mm x 38 mm
Mass	2.2 kg
Operating voltage range	15-50 V
Power	9 W (peal), 6.5 W (typical)
Operational temperature	-20°C - +50°C
Storage volume	2 GB
Input rate	3 x 40 Mbit/s
Output rate	3 x 20 Mbit/s

Data processing unit

The data processing unit (DPU) processes the raw data from the measurement instruments and then passes the post-processed data on to the OBC. There are several options on how to assign this task. First there is the option to let each instrument have its own DPU. This way they can be customised for the assigned instrument. Another option is to have one centralised DPU, which processes all the data of the different instruments. This DPU can be a stand-alone component or integrated with the OBC or the SSR. For the orbiter the DPU has to process a maximum of 5.1 Mbit/s (see Subsection 7.1.2); for the ground stations this number is much lower. This is a data rate the SSR can handle and possibly can process as well, however the performance of the processing capabilities are unknown. Further research on this topic is needed.

If the data of the orbiter instruments would not be real-time processed, the requirements of the C&DH subsystem would significantly increase. A data storage volume of the SSR of approximately 18 GB would be needed, mainly because of the high data rate of the lidar instrument (See Section 7.1). This would mean a downlink data rate to the DSN of 74 Gbit/s, which is not within reach. A solution would be to measure with a lower frequency.

A hardware and software block diagram is intentionally not included, since they would not add any value to this report. The main hardware components of the systems are already listed in the communication flow block diagrams (Figure 10.7 and 10.8), the data handling block diagrams (Figure 10.6) and electric block diagrams (Figure 10.2 and 10.3). Since in this design stage, it does not make sense to already select detailed characteristics as the software and the operating system, the software block diagram is not made. However the functional descriptions of the main tasks required from the software are described in Figure 10.6.

10.4 Telecommunication System

In order for the orbiter and ground stations on Mars to communicate with Earth ground stations a communication system is needed. Data needs to be sent between the ground stations on Mars (from now on called 'ground stations') and the Earth ground stations. This data contains the payload, telemetry and command data of the orbiter and the ground stations. The orbiter around Mars will be used as relay station for the communication between Earth and the ground stations. For the communication between the orbiter and Earth, the Deep Space Network (DSN) will be used using the X-band frequency. The communication between the ground stations and the orbiter will use the UHF band.

First a communication flow diagram is given which illustrates the flow of the data through the systems and the interactions with their environment. Afterwards the telecommunication system is sized and selected for each communication link, including emergency telemetry and command. Before the method to make the link budgets is explained, including the equations used. Then the choices, results and link budgets for each link are stated. Finally a mass and power budget is made for the components of the telecommunications subsystem of the orbiter and ground stations.

10.4.1 Communication Flow Diagram

A qualitative overview of the components involved in the data flow through the systems is given by means of a communication flow diagram. The diagrams for the ground stations and orbiter are shown in respectively Figure 10.7 and Figure 10.8. Single arrows represent a data flow, double arrows represent a data flow combined with a command flow. The flows are not continuous, but have a certain time interval, specified in Section 10.3. The data flows also have a certain data volume and data rate, specified in Chapter 8 and Subsection 10.3.2.

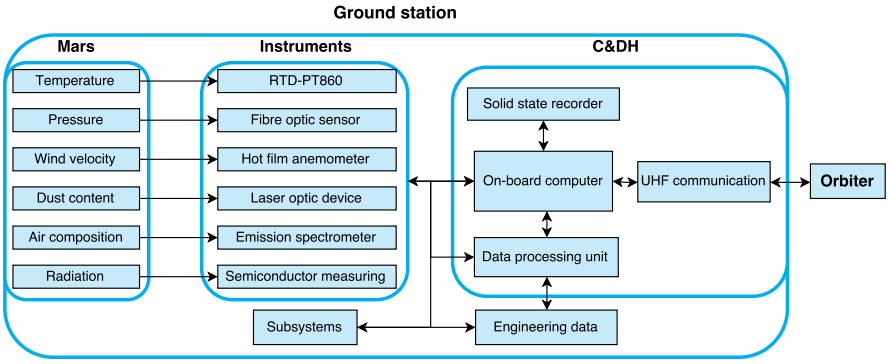

Figure 10.7: *Communication flow diagram of a ground station.*

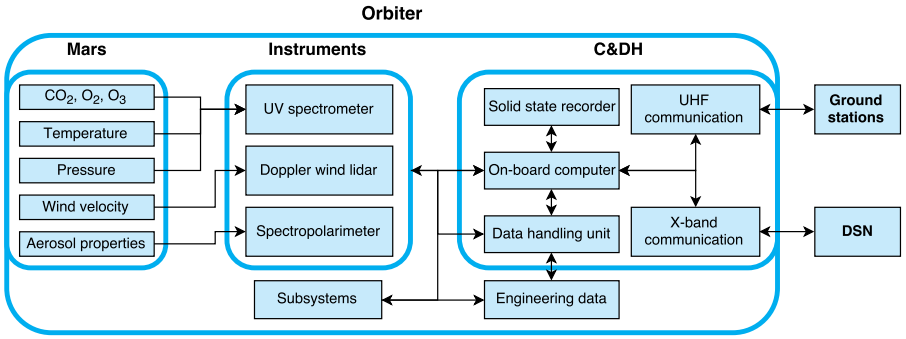

Figure 10.8: *Communication flow diagram of the orbiter.*

10.4.2 Link Budget Equations

In order to size the communication system in terms of antenna size, power and data rate a link budget is required. A link budget is a quantitative model that analyses and predicts the performance of the connection. In this budget the involved gains, losses and noises will be calculated and applied to the signal between the transmitter and the receiver. In communication technology, decibels (dB) are a widely used unit, because they give a better insight in small and large numbers, which are common in communication technology. To express a quantity in decibels Equation 10.40 is used.

$$X[dB] = 10 \cdot \log_{10}(X) \tag{10.40}$$

The required transmitting power in dB is calculated using Equation 10.41 [1]. In Table 10.15 the variables are explained and, if applicable, their equation is given. The gain and half beam-width angle of the antennas are calculated by an empirical equation for that type of antenna. For estimates on several losses, efficiencies, etc. estimates obtained from literature are used.

$$P_t = \frac{E_b}{N_0} + 10 \cdot \log_{10}(R) + 10 \cdot \log_{10}(T_s) - 228.6 - L_r - L_{pr} - L_{pt} - L_s - L_a - L_l - G_r - G_t \tag{10.41}$$

The received power in dB can be calculated with Equation 10.42 [1].

$$P_r = P_t + L_r + L_{pr} + L_{pt} + Ls + L_l + G_r + G_t \tag{10.42}$$

10.4.3 Sizing

After the link budget has been made, the actual sizing of the telecommunication systems can be performed. This is done by making use of a link budget script made in Python. The script uses the equations, as stated in Subsection 10.4.2, to calculate the SNR of the link. The inputs are the variables of the transmitter, the medium and the receiver, which can be tweaked to obtain a closing link. The script iterates over transmitter power and

antenna sizes within boundaries, in order to obtain the desired SNR and bit rate. After varying some variables, a desired configuration is found and other specifications of the link are calculated as well and reported into the link budget tables. For each link, choices are made for the antenna type, distance and bit rate, which are explained in this subsection.

Table 10.15: *Variables of the receiving power (Equation 10.42), including their equations and units.*

Symbol	Variable	Unit	Equation/description
P_t	Transmitted power	[dBW]	Output variable
E_b	Received energy per bit	[J]	$= P_r/R$
N_0	Noise spectral density	[J]	$= k \cdot T_s$
R	Data rate	[bit/s]	Input variable
T_s	System noise temperature	[K]	$= T_{ant} + T_0\left((1-L_c)/L_c\right) + T_0\left(F-1\right)$
L_r	Reception feeder loss	[dB]	From literature
L_{pr}	Receiver pointing loss	[dB]	$= -12 \cdot \left(e_r/\theta_r\right)^2$
L_{pt}	Transmitter pointing loss	[dB]	$= -12 \cdot \left(e_t/\theta_t\right)^2$
L_S	Space loss	[dB]	$= 147.55 - 20 \cdot \log_{10}\left(S\right) - 20 \cdot \log_{10}\left(f\right)$
L_a	Attenuation loss	[dB]	From literature
L_l	Line loss	[dB]	From literature
G_r	Receiver antenna gain	[dB]	From empirical equation for specific antenna
G_t	Transmitter antenna gain	[dB]	From empirical equation for specific antenna
P_r	Received power	[dBW]	Output variable
k	Boltzmann constant	[J/K]	See List of Constants
T_{ant}	Antenna noise temperature	[K]	Specified per antenna
T_0	Reference temperature	[K]	Defined as 290 K
L_c	Cable loss	[dB]	From literature
F	Noise figure	[-]	From literature
e	Off-point angle antenna	[°]	From literature
θ	Half power beam-width angle	[°]	From empirical equation or literature
f	Frequency	[Hz]	Input variable, from literature
S	Transmitter-receiver distance	[m]	Input variable
E_b/N_0	Signal-to-noise ratio (SNR)	[dB]	Output variable

For all links between the DSN and the orbiter several assumptions were made. As transmitter-receiver distance the maximum distance between Earth and Mars during the mission is taken, which is 2.64 AU, in September 2021[23]. This will occur during a solar conjunction, when the Sun is located in between Mars and Earth. During this period, which will occur twice during the mission, the communication will not be possible for 10 days (see Subsection 4.1.3 and Figure 4.8 and 4.9). The measurement data obtained during the solar conjunction will be stored until communication is possible again, for further explanation see Subsection 10.3.2. This choice will lead to a conservative design, since the communication system is sized for the maximum distance, although no communication can take place at that moment.

Orbiter - DSN: high rate telecommunications

First the high rate links are sized for the communication between the orbiter and the DSN network, when the orbiter is fully operational in its orbit around Mars. The 34 m BWG (Beam Waveguide) parabolic reflector antenna is used as receiving antenna, since these antennas have a higher availability and the number of antennas is higher than the 70 m DSN antennas. Both the down- and uplink closed with the 34 m antenna, however when a higher data rate is required to transmit more data, for example after solar conjunction, the 70 m antennas can be used as well. The specifications for DSN antennas are obtained from the Deep Space Network [83]. For the transmitting HGA (High Gain Antenna) a parabolic reflector is used. This type of antenna is mostly used in deep space communication since, apart for its high gain, it is reliable, light, simple, steerable and can easily be folded.

The gain and half power beam-width of a parabolic antenna can be calculated with respectively Equation 10.43 and 10.44, where G is the gain in dB, F the frequency in Hz, D the antenna diameter in m, η the antenna efficiency and θ the half power beam-width angle in degrees. The downlink and uplink frequency bands of the X-band are obtained from the SDST specifications [18], which will be used as transponders for the communication as well for tracking (see Section 4.3.2). Assumed is that the actual frequency of a link is the average of that band.

$$G = -159.59 + 20 \cdot \log_{10}\left(D\right) + 20 \cdot \log_{10}\left(f\right) + 10 \cdot \log_{10}\left(\eta\right) \tag{10.43}$$

$$\theta = \frac{2.1 \cdot 10^{10}}{f \cdot D} \tag{10.44}$$

[23] Obtained from Wolfram Mathematica 10.

The chosen modulation technique is QPSK (Quadrature Phase-Shift Keying), which is commonly used because of its high spectrum utilisation. The coding scheme for the downlink used is (7,1/2) convolutional Viterbi + Reed-Solomon concatenated code. This code has been proven in many prior missions and is used to cover the largest span of bit rates [82]. This modulation has a threshold SNR of 2.7 dB for a BER (Bit Error Rate) of 10^{-5} [1]. A bit rate of 16 kb/s is chosen, keeping the available communication time and data volume in mind. This bit rate is quite low relative to other relay orbiter, however the amount of data compared to other missions is low as well, of course this can increase in further research by decreasing the SNR margin. The results of the downlink budget and sizing are shown in Table 10.16.

Table 10.16: *Link budget of the high rate telecommunication between the orbiter and DSN.*

Orbiter - DSN link budget HGA				
Max. transmitter-receiver distance	2.64 AU			
Frequency	X-band DL (8.4 - 8.5 GHz)		X-band UL (7.145 -7.235 GHz)	
	Orbiter		**DSN** [83]	
Antenna type	Parabolic HGA		DSN BWG	
Antenna diameter	1.5 m		34 m	
Efficiency	0.55		-	
Half power beam-width	DL: 1.7° UL: 2.0°		0.077°	
Pointing offset	0.1° [1]		UL: 0.03°	
	Symbol	**Value**		**Unit**
Transmitter parameters [83]	**Downlink**		**Uplink**	
RF Power output	P_t	14.8	40	dBW
		30.5	10,000	W
Line loss	L_l	-0.46	-0.22	dB
Antenna gain	G_t	39.9	67.1	dBi
Antenna pointing loss	L_{pt}	-0.04	-1.82	dB
Path parameters				
Space loss	L_s	-283.1	-281.6	dB
Atmospheric attenuation [1]	L_a	-0.3	-0.3	dB
Receiver parameters [83]				
Antenna gain	G_r	68.2	38.4	dBi
Antenna pointing loss	L_{pr}	-0.1	-0.03	dB
Reception feeder loss	L_r	0.0	-0.46	dB
System noise temperature	T_s	29.2	418.8	K
Receiver power	P_r	-160.9	-138.5	dBW
		$8.1{\cdot}10^{-17}$	$1.4{\cdot}10^{-14}$	W
Data rate [1]	R	42.0	33	dB
		16,000	2,000	bit/s
Noise spectral density		$4.0{\cdot}10^{-22}$	$5.8{\cdot}10^{-21}$	dBm/Hz
SNR		11	30.9	dB
Threshold SNR		2.7	11	dB
SNR margin		8.3	19.9	dB

For the uplink of the high rate communication, mostly the same parameters are used. Only a different frequency band and a pointing offset of the DSN antenna, which is optimally pointed for downlink and because of that creating an offset for the uplink, which happens simultaneously. The power output of the DSN transmitter has a minimum operating power of 2 kW and a maximum of 20 kW [83]. For this analysis a power output of 10 kW is assumed. The uplink communication uses QPSK as well. However it does not use any error correcting code, since the amount of power is not a limiting factor for the DSN and a high SNR margin is easily obtained. Complex coding schemes would only require more computational power on the orbiter. The link budget of the uplink is shown in Table 10.16. No sizing is done since the downlink is the limiting factor for the communication between the orbiter and the DSN.

Orbiter - DSN: emergency telecommunications

When the orbiter is in an emergency situation, it will put itself into safe mode. During this mode and other events like orbit insertion, launch, etc. the orbiter will communicate with the DSN through two horn LGA's (Low Gain Antenna) [84]. These antennas require less pointing than the HGA and have a large beam-width. They are positioned on both sides of the HGA dish in order to establish a connection with the DSN when accurate pointing is not available. The horn antenna has a low gain because of its wide radiation pattern. During safe mode the orbiter will point towards the sun, called sun pointing mode, using a coarse sun sensor as described in Section 6.3. The maximum pointing offset (31°) is calculated by assuming the worst case scenario, when the Earth-Sun-Mars angle is 90° and the pointing is most off. However for the transmitter-receiver distance, still

the maximum is taken, in order to be conservative.

The gain (in dB) and half power beam width (in degrees) of the horn antennas are calculated using respectively Equation 10.45 and 10.46 [1], where λ is the wavelength of the signal in m.

$$G = 20 \cdot \log_{10}\left(\frac{\pi \cdot D}{\lambda}\right) - 2.8 \qquad (10.45)$$

$$\theta = \frac{225}{\pi \cdot \frac{D}{\lambda}} \qquad (10.46)$$

During emergency communication, simple data and commands will be transmitted in order to prevent errors and to minimise the required power of the orbiter. According to NASA, an acceptable data rate during emergency communication is 10 bit/s and a threshold SNR of 4.12 dB at a BER of 10^{-5} using standard NASA (7,1/2) convolution code [85]. The 70 m DSN antenna will be used for planned special events, such as launch, interplanetary travel and MOI. If an emergency occurs the 70 m will be used as soon as possible, otherwise (multiple) 34 m antennas can be used until it is available. The link budget is sized for the 70 m antenna. For the uplink the DSN transmitter is set to its maximum output power of 20 kW. The link budgets and results of the sizing are shown in Table 10.17.

Table 10.17: *Link budget of the emergency telecommunication between the orbiter and DSN.*

Orbiter - DSN link LGA				
Max. transmitter-receiver distance	2.64 AU			
Frequency	X-band DL (8.4 - 8.5 GHz)		X-band UL (7.145 -7.235 GHz)	
	Orbiter		**DSN** [83]	
Antenna type	Horn LGA		DSN	
Antenna diameter	0.05 m		70 m	
Efficiency	0.52		-	
Half power beam-width	DL: 52.9° UL: 62.4°		DL: 0.118° UL: 0.038°	
Pointing offset	31.0° [1]		UL: 0.003°	
	Symbol	**Value**		**Unit**
Transmitter parameters [83]	**Downlink**		**Uplink**	
RF Power output	P_t	10.6	43.0	dBW
		11.4 (x2)	20,000	W
Line loss	L_l	-0.46	-0.2	dB
Antenna gain	G_t	9.8	73.2	dBi
Antenna pointing loss	L_{pt}	-4.1	-7.5	dB
Path parameters				
Space loss	L_s	-283.1	-281.6	dB
Atmospheric attenuation [1]	L_a	-0.3	-0.3	dB
Receiver parameters [83]				
Antenna gain	G_r	74.6	8.3	dBi
Antenna pointing loss	L_{pr}	-0.1	-3.0	dB
Reception feeder loss	L_r	0.0	-0.5	dB
System noise temperature	T_s	29.2	418.9	K
Receiver power	P_r	-192.9	-168.0	dBW
		$5.1 \cdot 10^{-20}$	$1.6 \cdot 10^{-17}$	W
Data rate [1]	R	10	10	dB
		10	10	bit/s
Noise spectral density		$4.0 \cdot 10^{-22}$	$5.8 \cdot 10^{-21}$	dBm/Hz
SNR		11	24.3	dB
Threshold SNR		4.1	4.1	dB
SNR margin		6.9	20.2	dB

Ground station - orbiter telecommunications

The communication between the orbiter and the ten ground stations will need to be performed daily for each station in a relatively short time period (300 s on average). The signal uses the UHF band, frequencies estimations are based on the Elektra UHF communication of the MER [82]. The antenna used on the ground stations are quarter-wave monopole antennas[24], which will use the ground station upper deck as ground plate. The MER and Phoenix rovers use this type of 'whip' antennas as well [82][81]. These antennas are simple, light and have an omnidirectional radiation pattern in horizontal direction and a toroidal pattern in vertical direction (doughnut pattern). This means the antenna does not need steering and transmits the signal in all directions, only exactly above the antenna the gain will be relatively low. The length of the monopole is a quarter of the

[24] Information obtained through personal communication with ir. Jasper Bouwmeester.

wavelength of the signal, chosen is for the uplink wavelength since this connection is most critical. The UHF antenna on the orbiter is an axial mode helix antenna, which has low gain and a wide beam-width. Quadrifilar helix antennas were used on the Mars Odyssey and MRO [81], similar to this antenna. The gain of the monopole antenna is obtained from literature [86]. The gain (in dB) and half power beam width (in degrees) are calculated using respectively Equation 10.47 and 10.48 [1], where D is the antenna diameter in m and L the antenna length in m. The diameter of the helical antenna should lie in between 0.8-1.2 times λ divided by π.

$$G = 10 \cdot \log_{10}\left(\frac{\pi^2 \cdot D^2 \cdot L}{\lambda^3}\right) + 10.3 \qquad (10.47)$$

$$\theta = \frac{52}{\sqrt{\pi^2 \cdot D^2 \cdot \frac{L}{\lambda^3}}} \qquad (10.48)$$

Taking MER, MRO and Mars Odyssee as reference the downlink (from the orbiter to the ground stations) has an estimated data rate of 8 kbit/s since the downlink had a low data rate requirement. The downlink is uncoded and modulated with PCM/Bi-phase-L/PM. The uplink has a data rate of 32 kbit/s and is (7,1/2) convolutional coded with the same modulation [82][84][81]. This data rate, in combination with the contact time, provides adequate data transmission for the daily data volume of the ground stations (see Subsection 10.3.2). The link budgets are oversized in order to compensate for a possible elevation angle of the ground stations and possible obstacles. The link budgets and results of the sizing are shown in Table 10.18.

Table 10.18: *Link budget of the telecommunication between the orbiter and ground stations.*

Orbiter relay link				
Max. transmitter-receiver distance	317 km		(See Subsection 6.1.1)	
Frequency	UHF DL (437.1 MHz)		UHF UL (401.6 MHz)	
	Orbiter		**Ground station Mars**	
Antenna type	Axial helix		Quarter-wave monopole	
Antenna size	Length: 0.66 m, diameter: 0.22 m		Length: 0.19 m	
Efficiency	0.70		-	
Half power beam-width	DL: 53.0° UL: 59.7°		-	
Pointing offset	5.0°		-	
	Symbol	**Value**		**Unit**
Transmitter parameters [82][86]	**Downlink**		**Uplink**	
RF Power output	P_t	7.0	10.0	dBW
		5.0	10.0	W
Line loss	L_l	-1.0	-3.0	dB
Antenna gain	G_t	10.1	2.0	dBi
Antenna pointing loss	L_{pt}	-0.1	-	dB
Path parameters				
Space loss	L_s	-135.3	-134.5	dB
Atmospheric attenuation [1]	L_a	-0.1	-0.1	dB
Receiver parameters [83]				
Antenna gain	G_r	5.0	9.1	dBi
Antenna pointing loss	L_{pr}	-	-2.1	dB
Reception feeder loss	L_r	-3.0	-0.1	dB
System noise temperature	T_s	550	471.2	K
Receiver power	P_r	-114.3	-119.6	dBW
		$3.7 \cdot 10^{-12}$	$1.1 \cdot 10^{-12}$	W
Data rate	R	39	45.1	dB
		8,000	32,000	bit/s
Noise spectral density		$7.6 \cdot 10^{-21}$	$4.0 \cdot 10^{-21}$	dBm/Hz
SNR		44.8	38.2	dB
Threshold SNR		11	11	dB
SNR margin		33.8	27.2	dB

10.4.4 Overview Components

For the components of the telecommunication system of the orbiter and ground stations, an estimation is done for the mass, power and dimensions based on literature and reference missions. The estimated values are shown in Table 10.19[25]. On the orbiter, most components are double placed in order to ensure redundancy. However on the ground stations this is not the case, since there are ten ground stations, which already gives redundancy. In case of a spare component for redundancy, the total mass is listed but the power of one single component is

[25] X-band TWTA: `http://www2.l-3com.com/eti/product_lines_space_twt.htm`

taken since only one component will require power.

The SDSTs are the same devices as used for the tracking, mentioned in Section 4.3.2. As amplifier for the X-band communication of the orbiter, a TWTA (Travelling Wave Tube Amplifier) is chosen because of its high efficiency for a RF output power of higher than 15 W [1]. A diplexer is used to couple the receiver and transmitter signals together on the antenna cable. The switching network switches between the HGA and LGA antennas. In order to point the HGA towards the DSN during orbit, the HGA is attached on a two axis gimbal, including motor. The mass and power consumption is based on the MRO, by assuming a linear relation between the antenna size and gimbal characteristics [84].

The orbiter UHF system is based on the Elektra UHF transceiver system, used on multiple Mars orbiters with relay function [84][87]. The Elektra transceiver includes a SSPA (Solid-State Power Amplifier),which is an amplifier used for low RF output power, a diplexer, filter and switching unit. The ground station UHF system is based on the MER rovers consisting of a modified version of the Odyssee transceiver, and a diplexer.

All components claim to be radiation resistant with a high TRL and have been implemented on other Martian missions before.

Table 10.19: *Overview of the telecommunication instruments including mass, power and dimensions.*

Component	Quantity	Total Mass	Power	Dimensions	Comments
Orbiter – X-band					
SDST	2	6.4 kg	15.8 W	11.8 cm×16.6 cm×11.4 cm	Table 4.5
TWTA	2	2 kg	52.5 W	37 cm×7.6 cm×8.1 cm	Efficiency: 55-65%
Diplexer	2	1.2 kg	-	10 cm×22 cm×4 cm	[1]
Switching network	2	1.5 kg	-	-	[1]
LGA horn	2	1.4 kg	-	4.8 cm×4.8 cm×2.2 cm	
HGA parabolic reflector	1	6 kg	-	150 cm×150 cm×60 cm	
HGA gimbal + motor	1	22.5 kg	7 W	unknown	[84]
Orbiter – UHF					
Electra transceiver	2	10.2 kg	71 W	22 cm×22 cm×66 cm	Includes SSPA, diplexer,
UHF helix antenna	1	1.4 kg		20 cm×11.6 cm×21.7 cm	filter, switch [84]
Ground station – UHF					[82]
Transceiver	1	1.9 kg	42 W	5.1 cm×6.8 cm×3.7 cm	Includes amplifier
Diplexer	1	0.4 kg	-	2.9 cm×3.7 cm×1.3 cm	
Monopole antenna	1	0.1 kg	-	16.9 cm×1.9 cm×1.9 cm	

10.4.5 ADCS Pointing of the Communication Instruments

The telecommunications system of the orbiter knows two pointing directions, as could be derived from Subsection 10.4.3. The Earth-pointing direction of the High Gain Antenna (HGA) is requested when data has to be transmitted from the orbiter to Earth, and vice versa. That same pointing direction is desired when the satellite is in safe mode and has to point its Low Gain Antennas (LGA) in Earth direction. During communication between the ground stations and the orbiter, the satellite's UHF antenna has to point down to the surface of Mars, in Mars-pointing direction. The frequency on a daily basis with which these antennas have to point in each direction, have been listed in Table 7.5. In that same table, the duration of each communication link is given.

The ADCS system should make sure that the aforementioned pointing directions of the telecommunication system can be achieved, and that a pointing direction can be maintained over the time interval requested.

Earth-pointing direction

Two antenna types request an Earth-pointing direction during communication: the High Gain Antenna and the Low Gain Antennas.

The High Gain Antenna is mounted on a 2-axis gimbal, which can make the parabolic reflector antenna rotate over 360°, about the 0.75 m beam, on which the antenna is mounted. In addition, it can turn the antenna ±90° along that same beam, see Figure 10.9.
The HGA is located on that side of the satellite, which is under normal circumstances directed away from the Martian surface, into deep space. By being able to deflect the antenna over 360° by ± 90°, the antenna can be quite accurately pointed in the direction of Earth.

In case Earth falls outside the reach of the deflected antenna, the ADCS system can assist by slightly turning the entire orbiter. However, this manoeuvre is to be avoided, since it requires power and propellant from the reaction wheels assembly and the thrusters respectively. In any case, it should be possible to turn the orbiter to achieve communication with Earth if requested.

The relative position of Earth with respect to the satellite and Mars will determine the angle over which the gimbal has to deflect the antenna, as will this relative position determine the angle under which the HGA can not longer communicate with Earth by the limitations of the gimbal rotation. The latter will then further influence the amount of propellant and power required by the satellite to turn itself in order to regain contact. However, the calculations on the relative angles, power consumption and propellant mass for communication pointing over the course of two Martian years have proven to be too elaborate to investigate and discuss at this point.

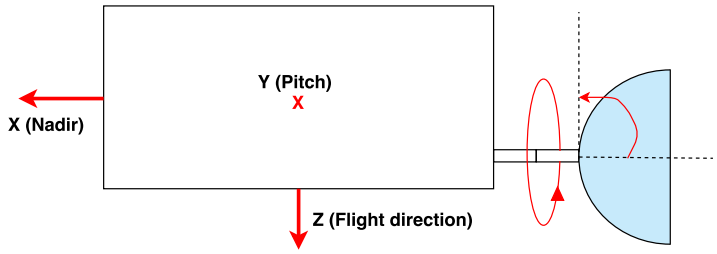

Figure 10.9: *Rotation of the High Gain Antenna about its support beam.*

When the satellite is in safe mode, the LGAs take over the communication function with Earth. These antennas do not have very strict pointing accuracies, and merely have to be directed coarsely to the Earth. The Coarse Sun Sensor[26], responsible for attitude determination when the satellite is in safe mode, transmits a signal to the on-board computer. The computer then forwards a command to the ADCS system to make the craft turn towards the Sun. When the spacecraft turns its surface - on which the LGAs and the CSS are located - to the Sun, the LGAs are capable of transmitting signals to Earth as was explained in Subsection 10.4.3.

Mars-pointing direction

To receive data from the ground station, the UHF antenna should point down towards the Martian surface. The UHF antenna is located on the same surface as the measurement instruments, of which most also have to point in nadir direction.
The ADCS system makes sure that the UHF antenna remains pointed to the Martian surface during its communication interval. The attitude of the satellite, with respect to Mars, is determined by the star trackers and CIRUS. After the on-board computer has processed the data from these sensors, the actuators will control the attitude of the spacecraft.
If the pointing of the orbiter for ground communication is off, than the ADCS reaction wheels and/or the thrusters will exert control forces on the craft to make it turn such that the antenna can point down. These correction manoeuvres will require power and propellant mass. However, these calculations are of a too detailed level for this conceptual design of the MUUDS satellite and are considered outside the scope of this report.

10.5 Structural Analysis of the MUUDS Spacecraft

The spacecraft structure's main purpose is to mechanically support the subsystems and provide the subsystems with the capability to perform their desired tasks. Important factors influencing the design of the layout of the spacecraft are, amongst other things, the mission goal and instrument requirements, size of the launcher fairing, environment, material properties, weight and safety. In the first subsection an overview of the general layout of the orbiter is given. The used launcher and the process of determining the size of the space probe are discussed. In the next subsection, the loads on the space probe are discussed and the type of material, used for the space probe, is chosen. After describing the loads on the probe, the method of determining whether the probe can withstand the loads is discussed. Next, the method for establishing a first preliminary estimate of the natural frequency of the spacecraft is covered. In Subsection 10.5.5, a selection of the materials used for the space probe is discussed. The next subsection, Subsection 10.5.6, discusses the selected materials and final mass of the different structural elements. In the last subsection, Subsection 10.5.7, the release and deployment mechanisms are explained.

[26] This sensor is located on the same surface of the orbiter as the LGAs.

10.5.1 Overview Design

The space probe consists of four boxes as shown in Figure 10.10.

- Box 1 containing 5 landers.
- Box 2 containing 5 landers.
- Box 3 consisting of the orbiter and its subsystems.
- Box 4 containing the propulsion system for the interplanetary trajectory.

The landers are covered by a cylindrical fairing to protect them against the hostile deep space environment. A general layout of the space probe is shown in Figure 10.10. The probe is designed to contain four central cylinders placed on top of each other. This design choice was made, based on the lander release system. The landers shall be released one by one and should not collide with the probe during their decoupling. By connecting the landers to a central cylinder, this requirement will be met with only a marginal risk of the landers colliding with the probe.

The load transfer between the different structural elements is best when all cylinders are placed below one another. When no inner cylinders would have been placed in box 3 and 4, panel 3 should have been very strong and stiff, which results in a higher structural mass. Furthermore, cylinders have high structural efficiency, low mass and are not complex [88].

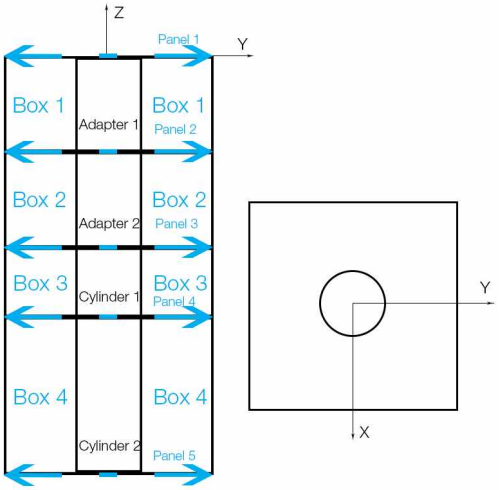

Figure 10.10: *General layout space probe.*

Launcher

The launcher, the Falcon Heavy, influences the final design of the space probe. The size and layout of the space probe is constrained by the launcher fairing size and the launcher load factors. The Falcon Heavy fairing layout is given in Figure 10.11. The maximum diameter of the space probe at the lower part of the fairing can be 4.60 m. The maximum height of the space probe is allowed to be 11.4 m. The diameter of the fairing decreases from a height of 6.6 m onwards to the top. The standard interface ring, which is used to attach the space probe to the launcher, is shown in Figure 10.12. It is possible to design a space probe adaptor/separation system instead of using the standard system, provided by SpaceX, but this is outside the scope of this project [4]. The spacecraft will be connected to the launcher through panel 5 with the engines 'hanging' in the adaptor. When the space probe is connected to the launcher using this method, the thrusters will not carry the compression loads running through the structural elements during launch.

The user manual of the Falcon 9 (see [4]) is used for the determination of the maximum loads during launch, because the user manual for the Falcon Heavy is not yet available. Therefore, higher safety factors are applied to account for the uncertainty caused by using the design load factors of the Falcon 9 instead of those of the Falcon Heavy.

Design

The probe width and height is influenced by the subsystems, most importantly by the landers and the tank volumes required for the interplanetary flight. Preferably, the diameter of the inner cylinders, in box 1 and 2, called adaptor 1 and 2, and the two inner cylinders, in boxes 3 and 4 are equal, in order to provide a good load transfer between the elements. Furthermore, the adaptors and inner cylinders are preferably located in the

middle of the probe to not create any moments. Therefore, the determination of the width and height of the space probe is an iterative process as shown in the block diagram in Figure 10.13. The maximum width of the top part of the space probe is constrained by the fairing width at the height of the space probe. In combination with the diameter of the landers and specified margins, the adaptor size can be determined. Since the adaptor size influences the inner cylinder 2, the height of box 4 can be determined. The total height of the space probe affects the maximum allowed top width of the space probe and it should be checked whether the space probe will not touch the walls of the launcher fairing.

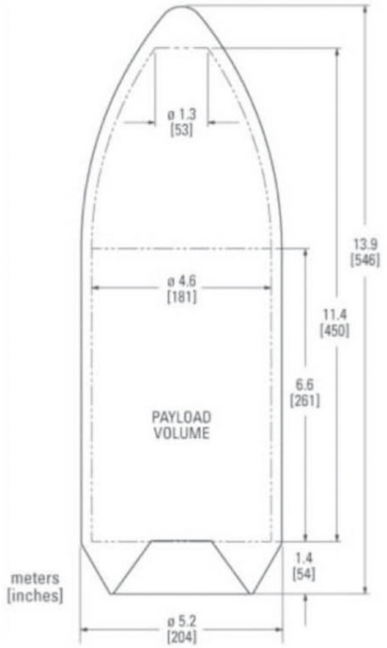

Figure 10.11: *Falcon Heavy fairing size [4].*

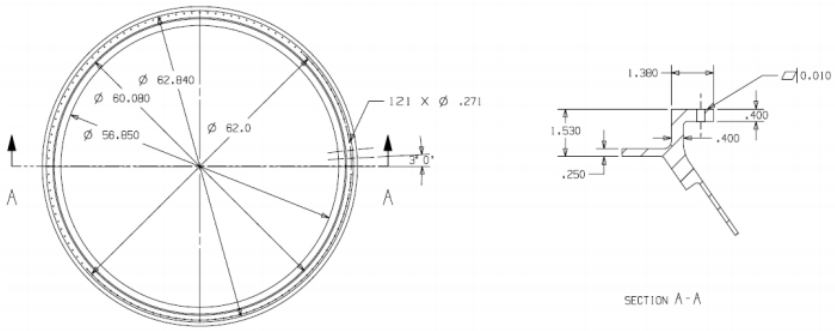

Figure 10.12: *Falcon Heavy interface ring (in inch) [4].*

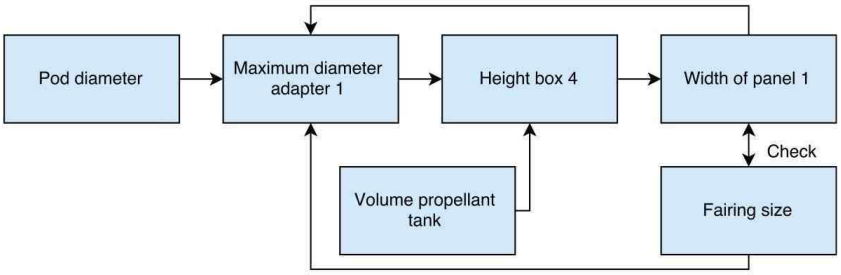

Figure 10.13: *Block diagram showing the influence of fairing size, lander diameter and propulsion volume on the final probe sizing.*

Box 1 and 2 both contain five landers. These landers should be equally positioned in a circle around the adaptor and stay within the dimensions of box 1. A margin M of 0.05 m should be used between the outer cylinder of box 1 and the circle C_0 to prevent the landers from coming into contact with the fairing panels of the probe when for example vibrations during launch occur, causing the landers to deflect from their position. The landers are attached to the central beam using a rod at the bottom of the landers consisting of explosive bolts and attached using springs between the landers and the adaptor. The length, L_{spring}, can be determined based on the available space within box 1. In Figure 10.14 a cross sectional view of box 1 is provided. The lander radius is indicated as R_L, while the radius of adaptor 1 is indicated as R_B. To fit inside the fairing, the sum of the diameter of the central beam, the diameter of two landers, the length of two spring bolts and the margin on both sides should be less than the maximum allowed width of the fairing. This sum is the diameter of the outer describing circle C_o of the landers, called D_o. D_o is calculated with Equation 10.49.

$$D_o = 2 \cdot M + 2 \cdot L_{spring} + 4 \cdot R_L + 2 \cdot R_B < 3\,\text{m} \tag{10.49}$$

Besides from having to fit within the dimensions of the box, the landers should also be equally spaced on the describing circle, C_i, that intersects with their centres. They are not allowed to touch each other. There

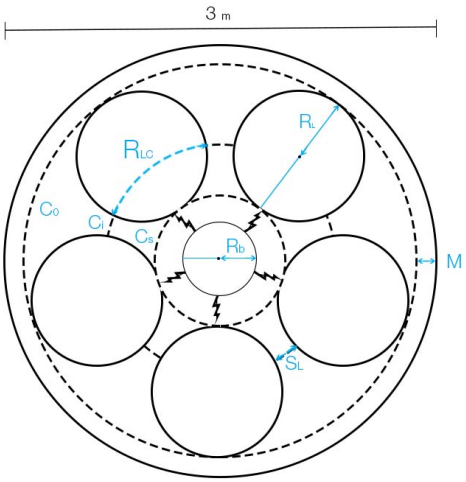

Figure 10.14: *Fitting the landers in the payload fairing of the spacecraft and spacing them on the describing circle.*

should be a minimal distance between the landers to account for any deflections of the landers from their nominal position due to vibrations or accelerations during launch. This minimal distance is indicated as S_L in Figure 10.14. The sum of these spacings, S_L, with the curved diameter of the landers, R_{LC}, should not be larger than the C_i's circumference. The circumference, CF, of circle C_i is determined using Equation 10.50.

$$CF = (R_B + L_{spring} + R_L) \cdot 2 \cdot \pi \tag{10.50}$$

To check whether the landers fit on the circle, the distance between the landers, S_L, should be larger than 0.05 m, while the total construction cannot be larger than the circumference. This is translated in a mathematical definition in Equation 10.51.

$$5 \cdot S_L + 5 \cdot R_{LC} \leq CF \tag{10.51}$$

When establishing the maximum diameter of the adaptor and setting the diameter of inner cylinder 2 of box 4 equal to the maximum diameter, the height of box 4 can be determined based on the size of the tanks. The tanks are sized to the diameter of cylinder 2, while using a margin M of 0.02 m and leaving space for the engines. The height of cylinder 2 is then determined using Equation 10.52

$$h_{cylinder2} = h_{propellanttanks} + h_{engine} + M \tag{10.52}$$

Next, the height of the space probe can be determined and the corresponding maximum top width. It should be checked whether the initial taken width fits within the launcher fairing. If this is not possible, the new maximum width can be taken to determine a new maximum diameter for adaptor 1 and the process is performed again. This process should be performed while maintaining a height of 2.3 m for box 1 and 2 and a minimum height of 1.25 m for box 3. Box 3 should preferably be as large as possible. The minimum height was established based on the positioning of the X-band antenna and the sun sensor. The X-band antenna should not cause a shadow on the sun sensor influencing the performance of the sensor. The height for box 1 and 2 was based on the length of the landers (2.1 m) and a margin on both sides of 0.1 m, which includes the height of the rod connecting the landers to the adaptor.

The found dimensions of the space probe are shown in Table 10.20. For a good load transfer between the outer cylinders and the side panels of box 3 and 4, the side panels of box 3 and 4 were also sized to be 3 m wide. The adaptor was sized to have a radius of 0.75 m, while the spring length L_{spring}, was sized to be 0.15 m, leaving a margin of 0.15 m.

With the outer dimensions of the space probe known, the subsystems can be placed in the orbiter. Each subsystem has its own requirements, concerning the location on the orbiter. For example, some orbiter measurement instruments should point towards the Martian surface, while the X-band antenna and the sun sensor should point towards the Sun. The final orbiter layout, including the location of the subsystems, is shown in Figures 10.15 and 10.16. The propulsion tanks within box four are located on top of each other within the inner cylinder, in other to decrease the shift in the mass centre of gravity of the space probe when the propellant volume in the fuel tanks decreases during the mission.

Table 10.20: Outer dimensions of space probe.

Element	Radius		Length z-direction
Outer cylinder 1	1.50 m		2.3 m
Outer cylinder 2	1.50 m		2.3 m
Adaptor 1	0.75 m		2.30 m
Adaptor 2	0.75 m		2.30 m
Cylinder 1	0.75 m		1.50 m
Cylinder 2	0.75 m		4.10 m
Element	**Length x-direction**	**Length y-direction**	**Length z-direction**
Side panels box 3	3.00 m	3.00 m	1.50 m
Side panels box 4	3.00 m	3.00 m	4.10 m

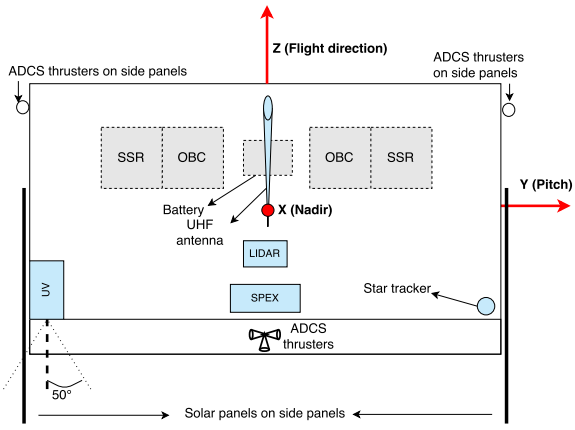

Figure 10.15: Orbiter side panel that is faced nadir.

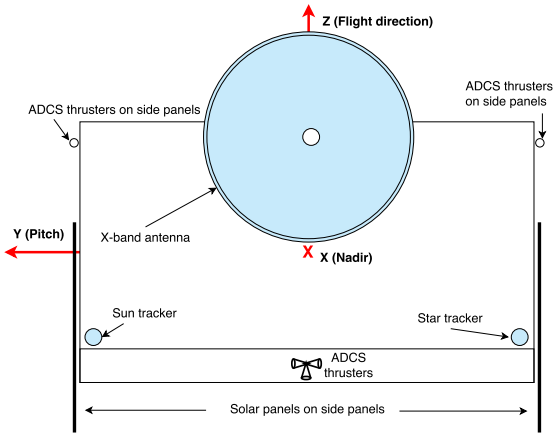

Figure 10.16: Orbiter side panel that is zenith-faced.

10.5.2 Loads

Different loads act on the space probe and its components during its lifetime. The maximum loads during the probe's lifetime are used to design the structure of the probe. These maximum forces most often occur during the launch. The probe experiences large accelerations, vibrations and shocks during the launch, which are most often the driving factor for the design of the structural elements. The probe will also experience other forces during its lifetime, such as handling and transportation loads before launch and shocks due to subsystem deployments and separations. The probe will experience thermal stresses, shock loads, 0g loads and due to possible collision with debris, impact forces in space. The landers will experience high impact loads when crashing into the Martian surface with 25 m/s, as discussed in Chapter 5.

Type of material

In order to withstand these different loads, a material for the elements should be chosen such that each structural element can withstand the loads. Sandwich panels were chosen to be used for the structural elements. The design choice for sandwich panels was made because of their low weight, resulting in lower launch mass, and high stiffness and strength [89] [90]. Furthermore, they provide a good performance at temperatures ranging from -55 °C to 170 °C. Sandwich panels consist of two face sheets and a core, which are attached using an adhesive. The stiffness and strength of the structure increases, due to the lightweight core holding the face sheets apart, and creating a uniform stiffened panel [89] [91]. A selection for the materials used for the face sheet and the core is made based on the loads and the final weight of the spacecraft and is covered in Subsection 10.5.5.

The skin and core have to withstand the tension, compression and shear forces. Furthermore, deflection should be minimised. Typical failure modes of sandwich panels are face yielding, failure due to core shear, panel buckling, intracell buckling, face wrinkling , shear crimping and local indentation. These failure modes are shown in Figure 10.17 [92]. The method used to check whether the structure will not fail under the applied forces is discussed in Subsection 10.5.5.

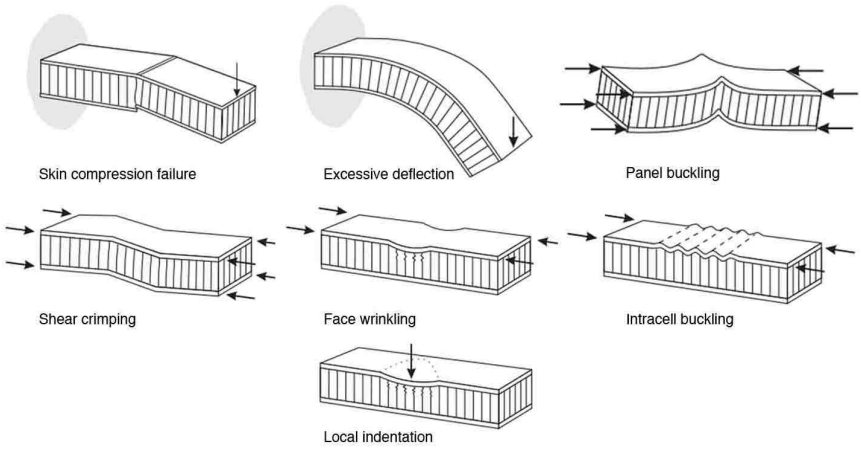

Figure 10.17: *Failure modes of sandwich panels [89].*

Loads

The spacecraft experiences the largest longitudinal and lateral accelerations during the launch. This occurs at the end of the propulsion phase of the Falcon Heavy. The longitudinal acceleration is mainly caused by the thrust profile and the drag of the launcher. The lateral accelerations are caused by wind shears, wind gusts, engine shutdowns and engine gimbal manoeuvres [4]. An envelope of the Falcon 9 design load factors is given in Figure 10.18.

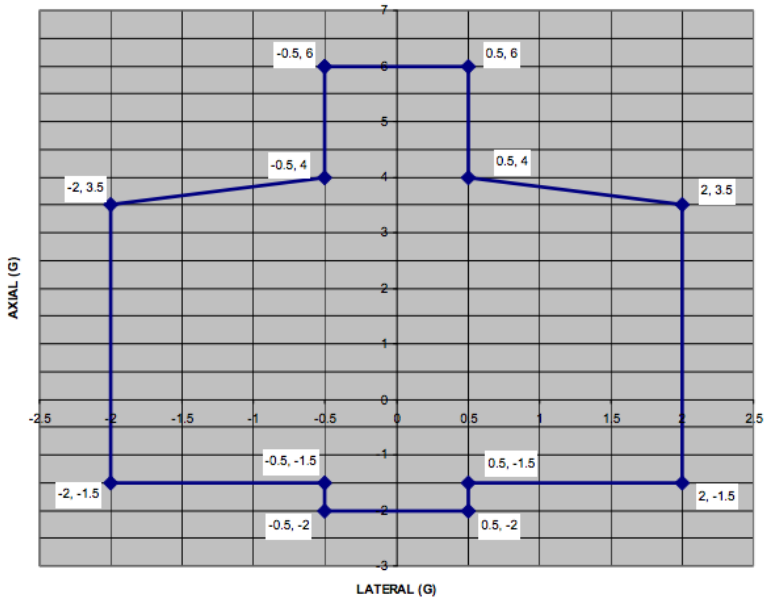

Figure 10.18: *Falcon 9 Design Load Factors [4].*

Different combinations of longitudinal and lateral accelerations are possible. The force caused by a structural element, subsystem or other object, due to the acceleration of the launcher can be determined using Newton's second law. The largest compression occurs at the lower part of the space probe where the probe is fastened to the launcher.

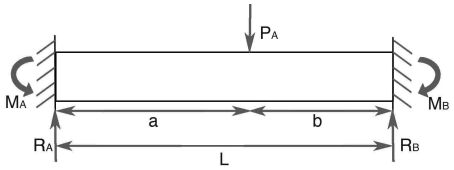

Figure 10.19: *Cantilevered beam under a load P_A.*

The space probe was analysed from top to bottom and from one side to the other. First the loads caused by each object and element were calculated. The loads were modelled as a point force through the centre of gravity of the particular object. Next, the reaction forces in the adjacent panels, to the particular panel where the object is located, were determined. To determine these reaction forces, the panels and cylinders were modelled as beams cantilevered on both sides, as shown in Figure 10.19. The reaction forces can then be determined using Equations 10.53 to 10.56.

$$R_A = \frac{P \cdot b^2}{L^3}(L + 2 \cdot a) \tag{10.53}$$

$$R_B = \frac{P \cdot a^2}{L^3}(L + 2 \cdot b) \tag{10.54}$$

$$M_A = \frac{P \cdot a \cdot b^2}{L^2} \tag{10.55}$$

$$M_B = \frac{P \cdot a^2 \cdot b}{L^2} \tag{10.56}$$

The centres of gravity of the different structural elements were determined to be in the middle of each element due to the symmetrical layout of each element. Each element has a constant sheet and core thickness and density. This results in a simplification of Equations 10.53 to 10.56 for the reaction forces, due to the elements, as distance a will be equal to distance b. An example for Equation 10.53 is shown in Equation 10.57.

$$R_A = \frac{P \cdot b^2}{L^3}(L + 2 \cdot a) = \frac{P(\frac{1}{2} \cdot L)^2}{L^3}(L + 2 \cdot \frac{1}{2} \cdot L) = \frac{P \cdot L^2}{4 \cdot L^3}(2 \cdot L) = \frac{P}{2} \tag{10.57}$$

Summing the reaction forces within a particular panel caused by different objects and elements and the mass of the own panel, the total force and moment through the panel can be determined (Equation 10.58 and 10.59). The elements, which are on the opposite side of the direction of acceleration, thus experience the highest loads, since the masses of all objects 'on top' of these elements are transferred to these panels. For example, when there is only a lateral acceleration in y-direction, the elements on the left side of the space probe structure, as seen in Figure 10.10, carry the highest loads.

$$\sum R_{panel} = \sum R_{object} + \sum R_{structuralelements} + F_{panel} \tag{10.58}$$

$$\sum M_{panel} = \sum M_{object} + \sum M_{structuralelements} + M_{panel} \tag{10.59}$$

The subsystems are not always located in the middle of a panel. The forces caused by these subsystems were assumed to act on the upper part of each structural element when determining the force acting perpendicular to the thickness of the element. It was assumed that a cylindrical element placed below another cylindrical element will carry the entire load acting in the cylindrical element located on top of it. It was assumed that the inner cylindrical elements of box 1 and 2 carry a certain percentage of the weight of the top panel, adjacent to the cylinder, panel 1 and 2 respectively. The outer cylinders carry the remaining weight. This percentage was determined by calculating the radius of the circle located exactly in the middle between the adaptor and the outer cylinder as shown in Equation 10.60.

$$R_{middle} = \frac{r_{outer} - r_{adaptor}}{2} + r_{adaptor} \tag{10.60}$$

Next, the masses of the inner part and outer parts of the panels can be determined and the total force acting on each cylinder caused by the top panels can be calculated. For the inner cylindrical structures of box 3 and 4, it was assumed that they will carry 75 % of panel 3 and 4 respectively and each side panel will carry 6.25 % of these panels. Furthermore, each side panel of box 3 will take up 25 % of the load acting through the outer cylinder of box 2.

10.5.3 Failure analysis

After all loads in each structural element have been calculated, it should be checked whether the elements do not fail under the applied load. The elements are checked for different failure modes, which were presented in Subsection 10.5.2. A safety factor, SF, of 1.5 is applied on the loads to account for uncertainties in the design load factors, imperfections in the material and the use of bolts and hinges. Where safety factors most often lie between 1.1 and 1.25 [93], the safety factor for this mission is higher due to the use of the Falcon 9 user manual. Different equations for flat panels are used than for cylindrical elements. First, the equations used to determine whether flat sandwich panels fail will be discussed. After that the equations used to determine whether cylindrical sandwich panels fail will be covered. The circular panels, panel 1 and 2, were modelled as rectangular elements with the width and length equal to two times the radius of the circular plate. The thickness of the element is determined by Equation 10.61, in which the thickness of the sheet is equal to the combined thickness of both sheet.

$$t = t_{sheet} + t_{core} \tag{10.61}$$

Flat sandwich panels

First, it is checked whether the face sheet of the panel can withstand an applied end load. The facing stress caused by a load in the skin panel is determined using Equation 10.62 [89].

$$\sigma_{facestress} = \frac{P}{2 \cdot t_{sheet} \cdot b} \tag{10.62}$$

The facing stress, due to a moment caused by a load, should not be higher than the yield strength of the face material. Thus, for the panel not to fail, statement 10.63 should be valid.

$$\sigma_{facestress} \cdot SF < \sigma_{yield,sheet} \tag{10.63}$$

Next, it should be checked whether the panel will buckle due to the applied end load. First, the bending stiffness D is determined using Equation 10.64 [89]. Using the bending stiffness D, the maximum allowed load $P_{buckling}$ can be determined for which the panel will not buckle. This maximum load is calculated using Equation 10.65 [89].

$$D = \frac{E_{sheet} \cdot t_{sheet} \cdot t^2 \cdot b}{2} \tag{10.64}$$

$$P_{buckling} = \frac{\pi^2 \cdot D}{L^2 + \frac{\pi^2 \cdot D}{G_{W,core} \cdot t \cdot b}} \tag{10.65}$$

Thus, for the panel not to fail due to buckling, statement 10.66 should be valid.

$$P_{applied} \cdot SF < P_{buckling} \tag{10.66}$$

The core can fail under an applied end load, due to the shear crimping resulting from a shear force acting through the panel. The load at which shear crimping of the core occurs can be calculated using Equation 10.67 [89].

$$P_{crimping} = t_{core} \cdot G_{core} \cdot b \tag{10.67}$$

For the panel not to fail, statement 10.68 should be valid.

$$P_{applied} \cdot SF < P_{crimping} \tag{10.68}$$

Another failure mode of the sandwich panel is wrinkling of the skin. The wrinkling of the skin occurs at a stress equal to or higher than the stress calculated using Equation 10.69 [89]. If $\sigma_{wrinkling}$ is above the allowed yield stress of the face, the skin yield stress will be more critical than skin wrinkling.

$$\sigma_{wrinkling} = 0.5 \cdot (G_{W,core} \cdot E_{core} \cdot E_{sheet})^{\frac{1}{3}} \tag{10.69}$$

For the panel not to fail, statement 10.70 should be valid.

$$\frac{P_{applied}}{A} \cdot SF < \sigma_{wrinkling} \tag{10.70}$$

Next, the panel should be checked whether the stress through the panel, due to the applied end load, is not higher than the critical stress at which intracell buckling occurs. This stress can be determined using Equation 10.71 [89]. If $\sigma_{intracellbuckling}$ is above the allowed yield stress of the face, the skin yield stress will be more critical than intracell buckling.

$$\sigma_{intracellbuckling} = 2 \cdot E_{sheet} \cdot (\frac{t_{sheet}}{cellsize})^2 \tag{10.71}$$

For the panel not to fail, statement 10.72 should be valid.

$$\frac{P_{applied}}{A} \cdot SF < \sigma_{intracellbuckling} \tag{10.72}$$

Furthermore, the sandwich panel should be checked on whether it can withstand a perpendicular applied load. The moment caused by the load can be determined using Equation 10.73 [89].

$$\sigma_{facestress} = \frac{M}{t \cdot t_{sheet} \cdot b} \tag{10.73}$$

The facing stress due to a moment caused by a load should not be higher than the yield strength of the face material. Thus, for the panel not to fail, statement 10.74 should be valid.

$$\sigma_{facestress} \cdot SF < \sigma_{yield,sheet} \tag{10.74}$$

The core of the panel should be checked whether it will not fail under a too high longitudinal applied shear force. The core stress should be below the maximum allowed shear in transverse direction. The core stress caused by the load can be determined using Equation 10.75 [89].

$$\tau_{core} = \frac{P_{applied}}{t \cdot b} \tag{10.75}$$

For the panel not to fail, statement 10.76 should be valid.

$$\tau_{core} \cdot SF < \tau_{W,core} \tag{10.76}$$

The final failure mode that should be considered for flat panels is local indentation. Subsystems put a local force on a panel over the connecting area between the subsystem and the panel. This can result in high local stresses. The local stress caused by the subsystem can be determined using Equation 10.77 [89].

$$\sigma_{localindentation} = \frac{P_{applied}}{A} \tag{10.77}$$

The local stress load should be below the maximum core compression strength. Thus, for the panel not to fail, statement 10.78 should be valid.

$$\sigma_{localindentation} \cdot SF < \sigma_{maxstrength,core} \tag{10.78}$$

If all stated equations are satisfied, the sandwich panels will not fail under the applied longitudinal loads and end loads.

Cylindrical sandwich panels

First, the bending stiffness, D_b, of the cylindrical sandwich panel can be determined using Equation 10.79 [94]. Equation 10.79 is only valid for sandwiches with faces of equal thickness.

$$D_b = \frac{E_{sheet} \cdot t_{sheet} \cdot t^2}{2 \cdot (1 - \nu^2)} \tag{10.79}$$

The transverse shear stiffness, D_q, for the core can be determined using Equation 10.80 [94]. Equation 10.80 is also only valid for sandwiches with faces of equal thickness.

$$D_q = G_{W,core} \cdot \frac{t^2}{t - t_{sheet}} \tag{10.80}$$

To determine the maximum allowed end load on the cylinder for the cylinder not to collapse or buckle due to a too high stress, Equation 10.80 [94], 10.81 [94] and Figures 10.20 and 10.21 have to be used to determine γ and $\frac{N_x}{N_0}$. Next, the maximum allowed end load can be determined using Equation 10.82 [94].

$$N_{0,axial} = \frac{2 \cdot \gamma \cdot E_{sheet}}{\sqrt{1 - \nu^2}} \cdot \frac{t}{r_{cylinder}} \cdot \sqrt{2 \cdot t_{sheet}} \tag{10.81}$$

$$N_{x,axial} = N_{0,axial} \cdot \frac{N_x}{N_0} \tag{10.82}$$

The axial load running through the cylinder should be below the maximum allowed end load, $N_{x,axial}$. Thus, for the panel not to fail, statement 10.83 should be valid.

$$P_{applied} \cdot SF < N_{x,axial} \tag{10.83}$$

In order to determine the maximum allowed perpendicular load on the cylinder, Equation 10.80 [94], 10.84 [94] and Figures 10.20 and 10.22 have to be used. Next, the maximum allowed perpendicular load can be determined using Equation 10.85 [94].

$$N_{0,bend} = \frac{2 \cdot \gamma \cdot E_{sheet}}{\sqrt{1 - \nu^2}} \cdot \frac{t}{r_{cylinder}} \cdot \sqrt{2 \cdot t_{sheet}} \tag{10.84}$$

$$N_{x,bend} = N_{0,axial} \cdot \frac{N_x}{N_0} \tag{10.85}$$

The load causing bending of the cylinder should be below the maximum allowed load $N_{x,bend}$ for bending. Thus, for the panel not to fail, statement 10.86 should be valid.

$$P_{applied} \cdot SF < N_{x,bend} \tag{10.86}$$

Besides testing the elements on failure due to axial and bending loads of the cylinder, the face of the cylindrical element should be tested. The total stress in the skin, caused by an axial end load on the cylinder, can be determined using Equation 10.87. In Equation 10.87, A_{face} is the cross sectional area of the face.

$$\sigma_{facestress} = \frac{P_{applied}}{A_{face}} \tag{10.87}$$

For the panel not to fail, statement 10.88 should be valid.

$$\sigma_{facestress} \cdot SF < \sigma_{yield,sheet} \tag{10.88}$$

The cylindrical element should also be checked for skin wrinkling. The wrinkling of the skin of a cylindrical element can be determined in the same way as the wrinkling of the skin of a flat panel. Therefore, Equation 10.69 [89] and 10.70 are valid for a cylindrical element.

Furthermore, the panel should be checked on intracell buckling. The stress at which intracell buckling starts can be determined using the reduced modulus E_R calculated using Equation 10.89 [94] and the equation for $\sigma_{dimpling}$, Equation 10.90 [94]. If $\sigma_{intracell}$ is above the allowed yield stress of the face, the skin yield stress will be more critical than intracell buckling.

$$E_R = \frac{4 \cdot E_{sheet} \cdot E_{core}}{(\sqrt{E_{sheet}} + \sqrt{E_{core}})^2} \tag{10.89}$$

$$\sigma_{dimpling} = 2.2 \cdot E_r \cdot (\frac{t}{cellsize})^2 \tag{10.90}$$

For the panel not to fail, statement 10.91 should be valid.

$$\frac{P_{applied}}{A} \cdot SF < \sigma_{dimpling} \tag{10.91}$$

The core of the cylindrical element should be checked whether it will not fail under a too high longitudinal applied shear force. Equation 10.75 [89] and statement 10.76 used for the flat panels can also be used for the cylindrical element.

The final failure mode that should be considered for cylindrical plates is local indentation. Equation 10.77 [89] and statement 10.78 can be used for the cylindrical element.

If all stated equations are satisfied, the sandwich cylinders will not fail under the applied longitudinal loads and end loads.

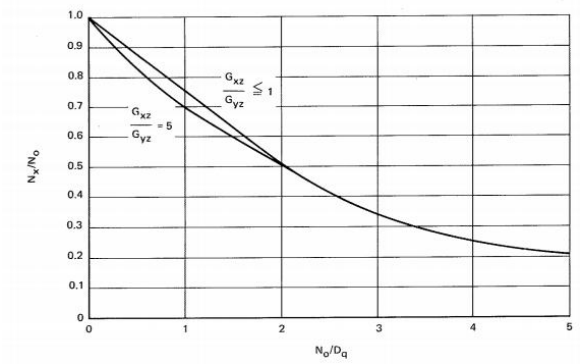

Figure 10.20: *Buckling of circular cylinders subjected to axial compression [94].*

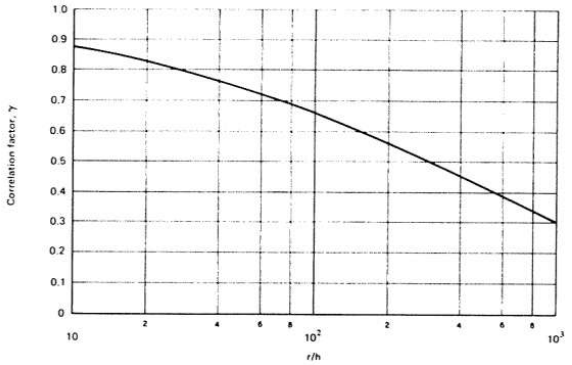

Figure 10.21: *Correlation factors for circular cylinders subjected to axial compression [94].*

10.5.4 Vibrations

The space probe will experience different vibrations during its lifetime. These vibrations can be divided into sinusoidal vibrations, random vibrations and acoustic loads [93]. SpaceX writes in the user manual of the Falcon 9 that "SpaceX recommends deriving a payload-specific sine vibration environment curve based upon a coupled loads analysis if significant flight history is not available." [4]. Using a coupled loads analysis, SpaceX produces a sine vibration input curve [4]. Therefore, it is unknown what sine vibrations the probe should be able to handle.

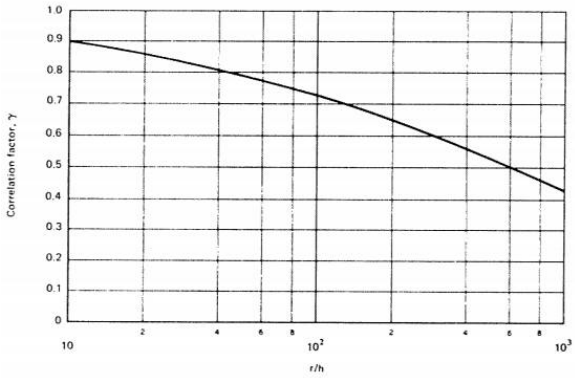

Figure 10.22: *Correlation factors for circular cylinders subjected to axial bending [94].*

For the preliminary analysis, the space probe has been modelled as a mass on top of a cantilevered beam. In order to calculate the natural frequency of the system, the location in the z-direction of the mass centre of gravity of the space probe was determined using Equation 10.92.

$$cg_{spaceprobe} = \frac{\sum z_{object} \cdot m_{object}}{\sum m_{object}} \tag{10.92}$$

The natural frequency in both longitudinal and lateral direction can then be calculated using Equations 10.93 and 10.94. The L in these equations is the distance in z-direction from the space probe-launcher adapter to the mass centre of gravity of the space probe.

$$f_{n,long} = \frac{1}{2\pi}\sqrt{\frac{3 \cdot E \cdot I}{m_{total} \cdot L^3}} \tag{10.93}$$

$$f_{n,lat} = \frac{1}{2\pi}\sqrt{\frac{E \cdot A}{m_{total} \cdot L}} \tag{10.94}$$

10.5.5 Material Selection

The structural elements of the space probe have been divided into different groups, of which the lander has also been divided into several structural groups. The possible materials are discussed in Reference [89] and [88]. The selection of the materials has been done using an optimisation process. Each material should withstand the loads on the element without failing. When a structural element of a selected material could withstand all loads, a less dense and possibly less stiff material was tried in order to find the lowest mass possible for the structure. The selected materials and final masses are discussed in Subsection 10.5.6.

10.5.6 Results

The properties of the materials selected for the space probe, landers and ground stations are shown in Tables 10.21 and 10.22 for the core materials and the face materials respectively. Using the selected materials, the mass of the entire structure can be determined. First, the mass of each structural element has been determined. The total masses of the different boxes are then calculated by summing the different elements. First, the space probe and orbiter mass will be discussed. Next, the lander and ground station mass will be discussed.

Table 10.21: *Core materials used for the space probe and landers [89].*

Product Construction		**Compression**		**Plate Shear**			
Density	**Cell Size**	**Stabilised**		**L Direction**		**W Direction**	
		Strength	**Modulus**	**Strength**	**Modulus**	**Strength**	**Modulus**
3003 Aluminium							
29 kg/m^3	19 mm	0.9 MPa	165 MPa	0.65 MPa	110 MPa	0.4 MPa	55 MPa
37 kg/m^3	9 mm	1.4 MPa	240 MPa	0.8 MPa	190 MPa	0.45 MPa	90 MPa
5056 Aluminium							
72 kg/m^3	3 mm	4.7 MPa	1275 MPa	3.0 MPa	483 MPa	1.7 MPa	193 MPa

Table 10.22: *Face materials used for the space probe and landers [89].*

Facing material	Typical strength, tension/ compression	Modulus of elasticity, tension/ compression	Poisson's ratio thickness	Typical cured ply per ply	Typical weight
Epoxy UD Carbon Tape (0°)	2,000 MPa / 1,300 MPa	130 GPa / 115 GPa	0.25	0.125 mm	0.19 kg/m^2

Space probe and orbiter

The space probe structural elements have been divided into different groups:

- **Group 1:** panel 1 and panel 2
- **Group 2:** panel 3 and panel 4
- **Group 3:** panel 5
- **Group 4:** side panels of box 3
- **Group 5:** side panels of box 4

The selected materials for these different groups and their thicknesses are shown in Table 10.23.

Table 10.23: *Material selected per group for the space probe structural elements.*

Group	Face material	Face thickness	Core material thickness	Core
Group 1	Epoxy UD Carbon Tape (0°)	0.160 mm	29-19-3003	0.0102 m
Group 2	Epoxy UD Carbon Tape (0°)	0.125 mm	29-19-3003	0.0213 m
Group 3	Epoxy UD Carbon Tape (0°)	0.125 mm	37-9-3003	0.0213 m
Group 4	Epoxy UD Carbon Tape (0°)	0.125 mm	72-3-5056	0.0059 m
Group 5	Epoxy UD Carbon Tape (0°)	0.125 mm	72-3-5056	0.0070 m
Adaptor 1 and 2	Epoxy UD Carbon Tape (0°)	0.125 mm	29-19-3003	0.0010 m
Outer Cylinder	Epoxy UD Carbon Tape (0°)	0.125 mm	29-19-3003	0.0040 m
Outer cylinder 2	Epoxy UD Carbon Tape (0°)	0.125 mm	29-19-3003	0.0045 m
Inner cylinder 1 and 2	Epoxy UD Carbon Tape (0°)	0.125 mm	29-19-3003	0.0095 m

The space probe mass is determined by summing all structural elements. The final orbiter structural mass consists of panel 3 and 4, the side panels of box 3 and the central cylinder. The results are shown in Table 10.24. The connecting element between the adaptor and lander was assumed to be 1 kg.

Table 10.24: *Mass of each structural element of the space probe.*

Structural element	Mass
Panel 1	3.70 kg
Panel 2	3.70 kg
Panel 3	7.61 kg
Panel 4	7.61 kg
Panel 5	4.57 kg
Side panel box 3	4.23 kg
Side panel box 4	4.86 kg
Adaptor 1, 2,	3.37 kg
Outer cylinder 1	8.39 kg
Outer cylinder 2	14.65 kg
Inner cylinder 1, 2	2.20 kg
Rod between adaptor and lander	1.00 kg
Structural mass space probe	**107.72 kg**
Structural mass orbiter	**34.33 kg**
Space probe mass	**5,365.09 kg**
Orbiter mass	**200.06 kg**

The maximum compression load during launch acts on panel 5 due to the longitudinal acceleration. The compression load acting on the space probe-launcher adaptor was found to be equal to 312.2 kN.

The natural frequency in the longitudinal direction of the space probe is equal to 109.84 Hz and the natural frequency in the lateral direction is equal to 30.19 Hz. These natural frequencies have been determined using Equations 10.93 and 10.94 respectively.

Lander and ground station

The selection of the material and load analysis of the lander module and the ground station will be performed using the same method as described for the space probe. The loads on the lander during impact in the Martian surface will not be analysed. The cone of the lander will take up most of the loads during impact and real-life testing will be required to determine the loads on the other elements of the lander.

The lander has been split up into five boxes as stated in Chapter 5 and shown in Figure 10.23. The structural elements have been divided, with all elements in one group having the same material size, as follows:

- **Group 1:** Cylindrical elements except for the cylinder around the ground station. Panels 1 to 5, except for panel 3.
- **Group 2:** Cylindrical element around the ground station.
- **Group 3:** Panel 3
- **Group 4:** Ground station structure

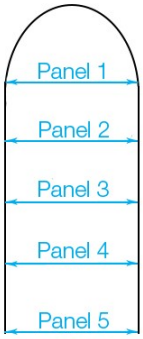

Figure 10.23: *General layout lander.*

An optimisation process was performed to select the materials and the found materials for the defined lander groups are shown in Table 10.25. The properties of the used materials can be found in Tables 10.21 and 10.22. The cylindrical panels of group 2 are the side panels protecting the ground station. The given core thickness of group 2 in Table 10.25 is the average thickness, which was determined using the volume of one of the side panels (equal to $0.12\,m^3$). The calculation is shown in Equations 10.95 and 10.96.

$$r_{inner} = \frac{-V + \pi \cdot r \cdot 0.5^2.}{\pi \cdot 0.5^2} \tag{10.95}$$

$$t_{core} = \frac{r_{inner}}{2} - t_{sheet} \tag{10.96}$$

With the material selected, the structural masses can be determined. The masses of the different elements and final mass of each lander and ground station are shown in Table 10.26.

Table 10.25: *Material selected per group for the lander and ground station.*

Group	Face material	face thickness	Core material	Core thickness
Group 1	Epoxy UD Carbon Tape (0°)	0.125 mm	29-19-3003	0.031 m
Group 2	Epoxy UD Carbon Tape (0°)	0.125 mm	29-19-3003	≈0.148 m
Group 3	Epoxy UD Carbon Tape (0°)	0.500 mm	29-19-3003	0.0311 m
Group 4	Epoxy UD Carbon Tape (0°)	0.125 mm	29-19-3003	0.010 m

Table 10.26: *Mass of each structural element of the lander and ground station.*

Structural element	Mass
Panel 1 and 2	0.693 kg
Panel 3	1.060 kg
Panel 4 and 5	0.693 kg
Group 1	6.260 kg
Group 2	5.220 kg
Group 3	0.694 kg
Structural mass lander	**15.31 kg**
Structural mass ground station	**0.694 kg**
Lander	**89.36 kg**
Ground station	**43.65 kg**

The maximum compressive load on the lander during launch acts on the lowest panel 5 due to the longitudinal acceleration. The compressive load acting is equal to 5,260 N. The natural frequencies of the lander can be determined using Equations 10.93 and 10.94 and are equal to 1,425 Hz and 1,087 Hz respectively.

The maximum compressive load on the ground station during launch acts on the lower panel due to the longitudinal acceleration. The compressive load acting is equal to 2569 N. The natural frequencies of the ground station can be determined using Equations 10.93 and 10.94 and are equal to 2178 Hz and 1204 Hz respectively.

10.5.7 Release and Deployment Mechanisms

During the mission the landers have to be separated, the propulsion system has to be jettisoned and some subsystems have to be deployed. For the release mechanism of box 4, explosive bolts will be used and for the deployment mechanisms, preloaded hinges will be used. A combination of explosive bolts and separation springs will be used for the separation of the landers. An example of an explosive bolt is shown in Figure 10.24 and an example of a separation spring is shown in Figure 10.25. The mechanism behind explosive bolts, separation springs and preloaded hinges will be described. Furthermore, the different separations and deployments during the MUUDS mission will be discussed.

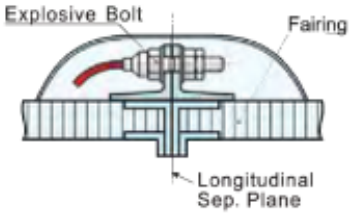

Figure 10.24: *Explosive bolt [95].*

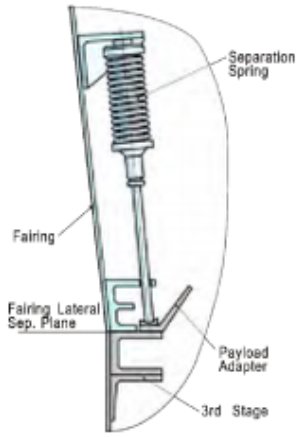

Figure 10.25: *Separation spring [95].*

Explosive bolts, also called pyrotechnic fasteners, are used to fasten objects together which have to be remotely separated at one point during the mission. For example, explosive bolts are used to fasten the space probe to the launcher adaptor [95]. The explosive bolts contain an explosive charge, which can be activated and will break the bolt, thereby releasing the fastened objects.

Separation springs are used to push an object away from another object [96]. The springs are preloaded, creating a pushing force as soon as the springs have the freedom to extend. Separation springs are used at the fairing adaptor to push the lander away from the launcher [96].

Preloaded hinges will be used for the deployment of the X-band antenna and the UHF antenna. The hinges contain preloaded torsion springs, which provide the energy required to open the hinge for deployment of the subsystem. The UHF antenna will be directly connected to the orbiter using a preloaded spring. The X-band antenna is connected to the orbiter using a 0.6 m long rod, which is divided in two equal parts. A preloaded hinge is used to connect the orbiter and the rod and another hinge is used to connect the two parts of the rod. After insertion into an orbit around Mars, the X-band antenna and UHF antenna will be deployed.

Immediately after the Martian orbit insertion of the space probe, the propellant tanks used during the interplanetary trajectory have to be separated from the space probe due to their high mass. Explosive bolts will be placed between the side panels of box 4 and panel 4 and between cylinder 2 and panel 4. Furthermore, separation springs will be used to push box 4 away from panel 4. These springs will be placed within the structure to not affect the thermal control. During separation, the explosive bolts will first unfasten the objects after which the springs push away the propulsion box. The probe around Mars then only consists of the upper three boxes. Before the propulsion system can be released, the solar panels should be fully deployed in order to not damage them during the separation.

Before the landers can be released, the fairing used to protect the landers during the trajectory should be separated from the probe. First, the upper panel, panel 1, will be released. Panel 1 will be fastened to the adaptor and the panels of the outer cylinder 1, using explosive bolts. Panel 1 is then pushed away from the probe by the preloaded spring. Next, the outer cylinder should be released. The outer cylinders will be split into two parts during the release. The two parts are fastened together using explosive bolts and lateral separation springs are placed between them. Furthermore, explosive bolts and springs are placed between the outer cylinder of box 1 and panel 2. In addition, two springs will be placed between the top part of adaptor 1 and the panels of the outer cylinder 1. The springs were placed at this position in order to guarantee no turning of the side panels. When only a pushing force is applied at the bottom, a moment might be created and thereby the possibility that the panels will collide with the spacecraft. This is prevented by placing a separation spring between the adaptor and the side panel.

After the fairing is released, the landers will be released one by one. The landers are fastened to the adaptor using a rod containing explosive bolts. Furthermore, on the side of the landers, between the lander its side surface and the adaptor, separation springs are located. The explosive bolts will be activated and the preloaded springs will give the landers an initial velocity away from the spacecraft, making sure the landers will not collide with the probe during their release.

When the first five landers in box 1 are separated, panel 2 shall be jettisoned. Panel 2 will be jettisoned using the same method as was used for the separation of panel 1. However, not only panel 2, but also adaptor 1 will be separated from the space probe when panel 2 is released from the side panels of box 2. Next, the panels of the fairing of box 2 shall be released. This will again be executed using the same method as described before. It should be noted that during the release of the fairing of box 2, the X-band antenna should be positioned downwards, towards the lower part of the probe, in order to prevent a possible collision of the side panels and the X-band antenna. The separation line of the fairing of box 2 is located above the panels carrying the solar panels in order to minimise the risk of the panels hitting the solar panels. After the separation of the fairing of box 2, the five remaining landers will be separated in the same manner as described for the landers in box 1. The last action of the separation process consists of separating adaptor 2 from box 3. This will again be done using explosive bolts and separation springs.

11 | Verification and Validation

The focus of this chapter will lie on the methods and techniques used to prove that the right solution is solved (validation), while solving it with the right methods (verification). Throughout the report numerical and analytical design steps have been executed, for which the verification and validation methods are applied first, followed by the remaining issues, which were simply not possible to perform due to time constraints and the scope of this project. In the following section these methods are elaborated upon.

11.1 Interplanetary Trajectory and Launch

The model on which the interplanetary trajectory results rely is an approximation of reality by using simplifications and assumptions. Those were discussed, as well as their effect on the outcome, in Chapter 4 and will not be elaborated upon in this paragraph. Due to the scope of this mission, verification methods are applied continuously throughout the different phases of the report. Mentioning all the different unit and systems tests for both Mars and Earth would result in an elaborate, but too extensive discussion which is not the focus of this report. It can be concluded that the offset between hand and model calculations did not approach the order of magnitude in which results were required.

Validating this model against high-precision databases is time-extensive and should definitely be considered when a high accuracy is actually required. For this first-order approximation the values in the figures below will be compared to the values listed in the list of constants.
In Figure 11.1 till 11.4 the heliocentric orbit of Mars and Earth as well as their velocity profiles are presented, of which the values at perihelion (θ= 0° and t = 0 + period) and aphelion (θ= 180° and t = period / 2 + period) can be compared the most efficiently with reference values. Keeping the first-order approximation in mind, it can be concluded that the difference in the calculated values and reference values is negligible since the accuracy required in this context is not affected by the range of this error.

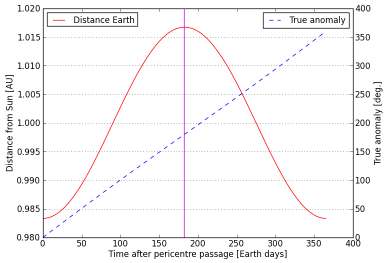

Figure 11.1: *Position profile heliocentric orbit Earth.*

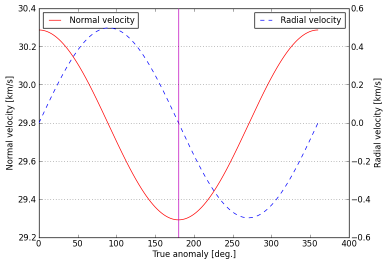

Figure 11.2: *Velocity profile heliocentric orbit Earth.*

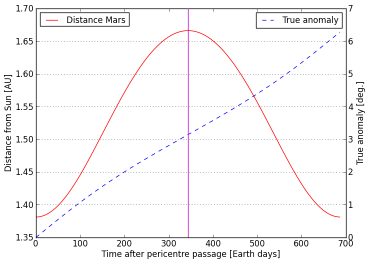

Figure 11.3: *Position profile heliocentric orbit Mars.*

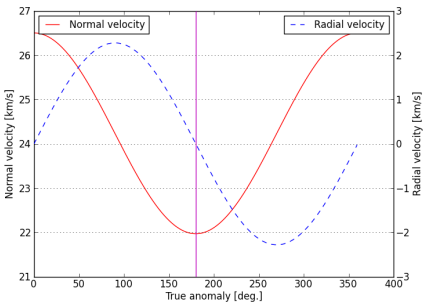

Figure 11.4: *Velocity profile of heliocentric orbit Mars.*

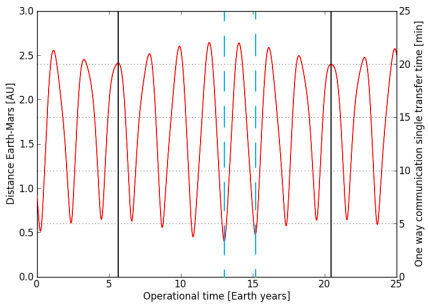

Figure 11.5: *Synodic and total repeat period Mars-Earth.*

In Figure 11.5 the two heliocentric models of Mars and Earth are combined and plotted. The distance of Earth-Mars is presented here in which the synodic period of 2.14 Earth years and an absolute repetition period of around 15 Earth years can be found and tracked [6]. Considering the launch window and date, a small offset can be considered although still within acceptable limits. A comparison is made between hand calculations

(assuming coplanar, circular orbit), the future launch opportunities predicted by NASA in Reference [97] and model calculations. As a conclusion the current launch date of 24 August 2020 seems feasible in the context of this project.

Table 11.1: *Comparison of launch dates.*

Parameter	Hand calculations	Model	Difference	NASA Prediction
Launch date	19 June 2020	24 August 2020	67 days	July 2020 - Sept 2020

Remaining issues

Throughout Chapters 3 and 4 a simplified model of the heliocentric orbits of both Mars and Earth is developed. By using the heliocentric position of the planets at the J2000 epoch and iterating in time using this simplified model, results will show an increasing offset in time compared with the correct value. It is recommended that a 3D planetary ephemerides is used when accurate, up-to-date data of solar-system bodies are desired. A reliable and high precision database which has been examined, but not considered feasible in the scope of this project, is the JPL's HORIZONS system[1].

Based on this database calculations can now be performed with more certitude in both time and position. In order to pick a more accurate launch window, resulting in much more efficient fuel usage, Lambert targeting methods should be scrutinised. This method allows to determine the connecting orbit when an initial and final position are given together when a certain time of flight such that specific scenario's could be compared in terms of ΔV and time duration. Multiple off-the-shelf programs are already available, but building a personal one is always recommended, as one can be more aware of possible assumptions and simplifications. When using a reliable Lambert method solver[2] for the specific launch data of the MUUDS mission a plot of the transfer orbit can be found in Figure 11.6.

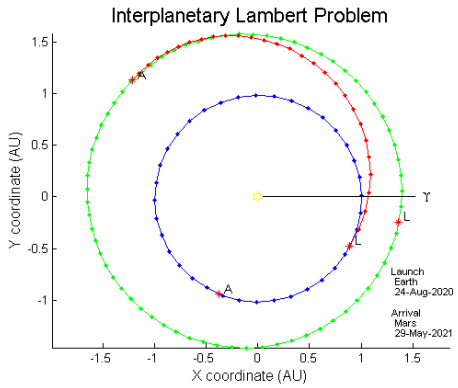

Figure 11.6: *Lambert targeting method for MUUDS planned launch date and transfer time.*

The best way to pick an optimal launch date is by making a porkchop plot, which interrelates all the above mentioned parameters and shows those in a clear plot.
If the requirements would turn out to be more flexible, transfers such as low-thrust chemical transfers could be considered, if operational time would not be a driving constraint. Opting for a Hohmann transfer results in a very efficient ΔV delivery, an efficiency which not seems sensible when comparing this to reality, where disturbances and 3D correctional manoeuvres need to be dealt with frequently.

11.2 Interplanetary Propulsion System

The model used for the sizing of the MUUDS thruster and storage system was verified by performing a unit test on the 12 different sections of code. For each unit test, two different data sets were used as input to show an acceptable limit of reliability. A unit test is shown in Table 11.2 to get a grasp of the procedures. For clarity and efficiency, not all unit tests are shown.
The system verification and validation has been executed using an example calculation found in literature [40]. The masses of the different type of fuel tanks are displayed, since for this all the other calculated values need

[1]NASA JPL: http://ssd.jpl.nasa.gov/?ephemerides
[2]Lambert method: http://www.mathworks.com/matlabcentral/fileexchange/39530-lambert-s-problem/

Table 11.2: *Example of an unit test used to verify the propulsion system model.*

	Case	Hand	Code	Difference	% Difference
Radius pressure tank	case 1	0.3093644 m	0.3094 m	-0.0000356 m	-0.01151
	case 2	0.26659 m	0.26660 m	-0.00001 m	-0.00375
Height pressure tank	case 1	2.38127 m	2.381200 m	0.00007 m	0.00294
	case 2	5.46682 m	5.4668 m	0,00002 m	0.00037

to be correct as well. If the example found in literature matches the results of the model, the system is verified. The outcome of the system test can be found below in Table 11.3. A possible explanation for the error margins are due to iteration and round-off errors. Therefore, it can be assumed the model is verified an validated.

Table 11.3: *Result of the system test used to verify the propulsion system model.*

	Example	Code	Difference	% Difference
Mass fuel tank	163 kg	163.2793 kg	0.2793 kg	0.0017
Mass oxidizer tank	271 kg	271.1173 kg	0.1173 kg	0.0433
Mass pressurant tank	368 kg	367.6127 kg	0.3873 kg	0.0011

Remaining issues

During the design process of the propulsion system, different assumptions and simplifications have been made. First, the propellant management system should be sized, since sloshing fuel on the inside of the tanks can causes shifts in centre of gravity location. Secondly, the feed system and its components could be chosen to get a more accurate weight estimate of the system. Finally, the impact of the flume on the spacecrafts solar panels and instruments must be investigated thoroughly in the future since plumes can disturb the functioning of measurement instruments, communication and solar panels.

11.3 Orbit around Mars

The first model that was built during this project was based on the Euler method. Since this turned out to be too inaccurate, a new model has been built using the Runge Kutta method. To verify if the Runge Kutta model is a more accurate predicting tool, the fluctuations in velocity, height and energy were compared with the Euler method and its analytic value. In this comparison only the gravitational force has been taken into account. For all cases a more accurate outcome for the Runge Kutta method has been achieved in comparison to the Euler method.

In this report, only the comparison of the energy will be worked out. The energy is the sum of the potential energy and the kinetic energy, which means that the velocity and height differences are compared in the plots below. The energy found for one rotation around Mars computed with the Euler method can be found in Figure 11.7 and the energy, found with the Runge Kutta, can be found in Figure 11.8. The analytical value of the energy should be constant, because both the height and velocity should stay the same. The error induced by the Runge Kutta method is negligibly small. An analytical value of -11867868 Joule has been found, which means that the energy calculated using the Euler method fluctuates around an error of 0.048%. Although an error of 0.048% seems small it will result in a height difference of the orbiter of more than 1.7 km with respect to the real value obtained, which is not acceptable. Therefore the Runge Kutta method has been chosen to model the orbit around Mars, the entry phase of the ground stations and the end-of-life of the orbiter. The other model

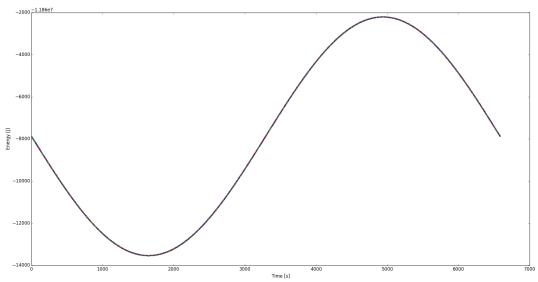

Figure 11.7: *Energy profile using the Euler method.*

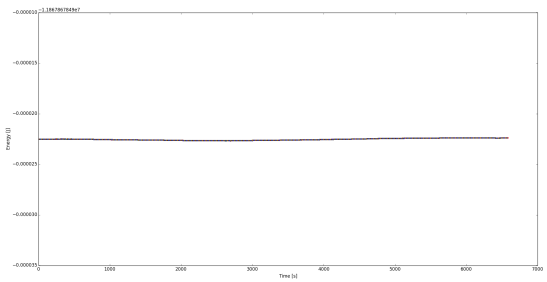

Figure 11.8: *Energy profile using the Runge Kutta method.*

that needs to be verified and validated is the model which calculates the ΔV required for a Hohmann transfer orbit around Mars. The programme has been compared with the values calculated for an interplanetary transfer using reference data [1]. Although this reference data shows values for interplanetary transfer, by changing the parameters the reference data deemed sensible for these calculations. Because both values are calculated with an analytic approach and equal input, the answers are exactly the same.

Remaining issues

As has been discussed in Chapter 6 the orbit around Mars has been designed by only using some disturbances, based on their relevance. However to make a more accurate prediction of the orbit, more parameters are needed. For example, more values of J_n could be accounted for, as well as the effect of the solar radiation and magnetic disturbances. Next to this, the disturbances in directions other than the radial direction need to be investigated. Thus, in this study only a selection of disturbances in radial direction were taken into account.

11.4 Entry, Descent and Landing

In this section the verification and validation methods are stated for several subsystems of the EDL phase. For each one of these sections, the remaining issues are discussed as well.

11.4.1 Heat shield analysis

For the sizing of the heat shield, the thickness of the isolation layer was driving. The higher heat flux on Mars was the reason for the larger isolation layer. It makes sense to see if the ratio between the percentage increase in heat flux divided by the percentage increase in heat shield mass equals approximately 1. If this is not equal to 1, there are several possible explanations. As an example, the entire heat shield does not completely consist out of isolation layer, or the various safety factors that have been applied. However, the ratio should be somewhere between 0.9 and 1.1. A value lower than 1 resembles a more conservative design in this context, as the percentage weight increase is higher. The ratio is shown in Equation 11.1.

$$\frac{Heatfluxincrease}{Massincrease} = \frac{1.25}{\frac{8.2 \cdot \frac{83.6}{50}}{10.6}} \approx 0.97 \tag{11.1}$$

Remaining issues

The HIAD analysis was executed using Monte Carlo simulations to estimate the isolation layer thickness. This was done making use of probabilistic parameters, inherent to the material of the heat shield. As these method has proven to be accurate, while being less conservative than older methods, it should be properly validated using realistic simulation tests.
Some final remarks have to be made on the simulation process. The sample size of 2000 is not large enough to draw definitive conclusions on the behaviour of the system, however, it gives a valuable indication for the initial sizing of the heat shield. Furthermore, it should be noted that a safety margin of 25 % may be reduced as the simulation is improved in the future. Lastly, tests for verification purposes should be executed to assess the actual behaviour of the TPS.

11.4.2 Parachute analysis

Two ways are presented to verify and validate the model. Firstly, the model is compared to a numerical example[3] using the same input variables. The results should be similar. Secondly, the resulting peak load (opening force) per m^2 is compared between the MSL project and the MUUDS project. The margins can be somewhat more different, as the actual MSL sizing may have been done in a slightly different way, and safety factors may be different. The results of both methods are described in Table 11.4.

Table 11.4: *Verification and validation of the parachute sizing results.*

	Value MUUDS model	**Value reference model**	**Unit**	**% Difference**
Fx	17,892	17,973	N	0.45
Fx/S	1,035	1,100	N/m	6.28

[3] University of St. Louis: `http://www.mrc.uidaho.edu/~atkinson/IPPW/IPPW-3/Parachute`

Remaining issues

The results from the parachute analyses have been verified and validated, however there is an uncertainty enclosed in the values. There are multiple reasons for this. Firstly, the behaviour of a canopy is of a stochastic fashion. The weather is also of a stochastic behaviour and lastly at this phase of the project, no tests have been executed on the parachute. In further phases therefore, more advanced modelling and testing is required. As of the probabilistic behaviour of certain factors, a Monte Carlo simulation would be a good approach to continue. Lastly, an analysis on the relation between the angle of attack and the required surface and peak load is required. Currently only vertical flight, without side wind, is considered.

11.4.3 Other remaining issues

Thruster analysis

The sizing of EDL propulsion system is performed with a similar model as used in sizing process of the trajectory propulsion system. The same methods are used to verify and validate this script. These methods are explained in section 11.2

CFD analyses

The SolidWorks CFD analyses are not perfect for various reasons. Firstly, it is a process in which a continuous system is modelled as a mesh, which results in minor errors. Furthermore, and more importantly, the effects that occur due to the hypersonic flow, such as shear and warping are neglected. The topic of analysing hypersonic flows has been of great interest for many decades. The transition from laminar to turbulent layers plays a paramount role in that story. The brief explanation for the occurrence of transitions and their locations is that physical effects such as shear and warping, create small perturbations in the flow. In certain ways, the vorticity is proportional with the shear of a flow. The classical approach to tackle these phenomena was developed in the 1950s in Delft by prof. van Ingen [98]. His e^n approach, provided a practical solution to capture the grow rate of the earlier mentioned transitions. The gain, e^n, can be determined by integration of the Orr-Somersfeld equation. This equation results from the Navier-Stokes equation. It is an eigenvalue equation that describes disturbances of a viscous parallel flow. The input of this equation, for practical applications, requires an enormously accurate flow field, a Direct Numerical Simulation (DNS). SolidWorks is not capable of taking into account these physics, so the results should be questioned. However, the statement that a higher vorticity strongly relates to the location where perturbations (Tollmien-Schlichting waves) occur, is very probable. [99] On the basis of that statement, it can be said that the intensity of the vorticity can be linked directly to the turbulence and thus the effectiveness of the fins.

In further stages of the design, more advanced CFD analyses should be executed. Besides, a model of the EDL penetrator should be evaluated in a wind tunnel, for various Mach numbers. For now the qualitative analysis of the control surfaces is justified to make the design choices that have thus far been made.

Inclination analysis

The analysis that has been executed for the inclination with which the projectiles hit the ground, was done using very rough estimated probabilistic distributions. Further phases in the project should decrease the uncertainty in these estimations and these parameters should be evaluated by tests and more extensive modelling.

Impactors

The crushable impactors have now been roughly sized. A COTS product of this application does not exist at this point and will be developed as the project matures, as specified in the production plan. Extensive testing is needed on the impact handling and the safety of the payload.

11.5 Power Subsystem

In order to verify and validate the code for the sizing of the solar arrays used during the design process, some measures are taken. First of all the code is verified by performing a calculation by hand and using the script and the outcomes of those calculations are compared. The outcome of the verification can be found in Table 11.5.
Comparing the calculated values from the Python model and the hand calculations it can be seen that the differences are below 1% and thus small. This difference can be explained by rounding errors introduced in the

Table 11.5: *Verification of the power system model.*

	Python model	Hand calculations	% Difference
Cell efficiency at BOL	0.2616	0.2615	0.038
Array size	11.412 m^2	11.424 m^2	0.1

calculations performed by hand. Due to the small difference between the analytical hand calculations and the numerical Python calculations it can be said that the model is verified.

Remaining issues

First of all, the power estimations used for the sizing of the battery and solar array has to be worked out in further detail by elaborating more on the exact power usage and time of usage for each subsystem. Additionally a power budget for the EDL vehicle has to be made to size the battery for the power supply during the EDL phase. Extra knowledge needs to be gathered concerning the ability of the battery for the orbiter to provide power during the launch phase. Moreover, the structure of the solar array has to be sized in more detail. The solar array has to be sized in such a way that it is able to withstand the maximal loads and vibrations encountered during the mission. The use of composite materials would enable a lighter design of the solar arrays used for the spacecraft and ground station, which complies with the sustainability requirements of the mission.

11.6 Thermal Control Subsystem

For the thermal control system, two scripts need to be verified. In order to verify both models, the calculations performed by the script are done by hand using the same values as used in the script. The first script that is verified is the thermal control script used for the calculation of the equilibrium temperature of the spacecraft. The script calculates the temperatures for the orbiting phase around the Earth, trajectory phase and the orbiting phase around Mars. For the verification process, both the hot and cold scenarios encountered in the orbit around Mars are compared of which the result of this first verification can be found in Table 11.6.

Table 11.6: *Verification of the thermal model of the spacecraft.*

	Python model	Hand calculations	% Difference
$T_{hot_{Mars}}$	234.57 K	235.34 K	0.327
$T_{cold_{Mars}}$	154.5 K	150.5 K	2.66

Looking at the differences between the numerical and analytical solution, those are within an acceptable margin. It can be explained by the inaccuracy introduced to the result of the analytical solution due to rounding errors. Considering the inaccuracy due to rounding the result of the analytical solution it can be said that the Python script for the thermal calculations of the spacecraft is verified and thus can be used for sizing the thermal system.
In order to verify the Python script for calculating the surface and body temperature of the ground station, the calculation result of the Python model is compared to the results of calculations by hand. The results of the numerical and analytical solution can be found in Table 11.7.

Table 11.7: *Verification of the thermal model of the ground station.*

	Python model	Hand calculations	% Difference
T_s	312.2 K	316.46 K	1.34
T_b	303 K	395.33 K	23.35

The difference for the surface temperature is 1.34%, which is within an acceptable range considering the inaccuracies introduced during the analytical solution. Due to these inaccuracies the difference of 23.35% for the body temperature arises. The body temperature depends on the surface temperature with the power of four. Due to this large exponent, the initially small inaccuracy increases rapidly. As a conclusion, it can be said that the Python model is verified and can be used for the sizing of the thermal control system of the ground station.

Remaining issues

In order to properly size the thermal control system of the satellite further investigation on heater and insulation systems has to be made. In addition to that, a transient model of the heat transfers of the satellite and the ground station have to be made in order to get a more accurate representation of the equilibrium temperatures. Moreover some research on the operational temperature ranges of the instruments used in the ground station has to be conducted. With these temperature ranges it can be further investigated whether or not the thermal control measures taken for the ground station are sufficient. These steps will be undertaken in the next design phases of the MUUDS mission.

11.7 Telecommunications Link Budget

The link budget is calculated in decibels, this way an overview is kept when encountering large and small numbers. As verification of the used link budget calculations, as shown in Subsection 10.4.2, the link budget is calculated by hand without using decibels. This method would reveal any errors in both the Python code as the decibel link budget method. As example, the SNR for the high data downlink between the orbiter and DSN is taken. In Equation 11.2 the SNR equation is shown in "normal" form, opposed to the decibel form shown in Subsection 10.4.2.

$$SNR = \frac{E_b}{N_0} = \frac{P_t \cdot L_l \cdot G_t \cdot L_a \cdot G_r \cdot L_s \cdot L_{pr} \cdot L_{pt} \cdot L_r}{R \cdot k \cdot T_s} \tag{11.2}$$

The result of the decibel calculating performed by the Python script gives 11.00353 dB as result and the normal by hand calculation, converted back to decibels, 11.00184 dB. The difference between the outcomes is 0.015%, which is an acceptable deviation and probably introduced by round-off errors. Furthermore unit tests were performed for antenna gain, half power beam width, losses and other parameters by comparing those outcomes with typical values obtained from literature. Since this is a conceptual design the values were not exactly the same, however they were all in the same ballpark. Since the same calculations are performed for all calculated link budgets, it can be said that all these calculations have been verified.

The link budget analysis is still a model and values deviate from reality. In order to validate the model, measurements should be done in terms of antenna gain, efficiency, radiation pattern, system noise etc. to compare with.

Remaining issues

The overall data rates and volumes produced by the instruments, handled by C&DH subsystem and transmitted by the telecommunication are relatively low. The chosen components of those subsystems are clearly capable of delivering more science data back to Earth, which is preferred. However not post-processing the data is not feasible, as stated in Subsection 10.3.3. An idea for further research on this mission and design might be to determine the level of on-board processing of instrument data at which handling and transmitting of that data is still feasible.

11.8 Structural Analysis

For the structural analysis part, three scripts have to be verified. For verification of the models, the result calculations were redone by hand and compared with the results, which were determined using the model. The three scripts that have to be verified are the script determining the loads on the launch vehicle, the script determining the loads on the lander and the script determining the loads on the ground station. The maximum compression, experienced by each structure, was determined using the Python model. The same calculation was executed by hand, summing the forces of all objects which are located on top of the location where maximum compression occurs, as shown in Equation 11.3.

$$F = m \cdot a_z = \sum m_{objects} \cdot a_z = 5,305.2 \cdot 6 \cdot 9.81 = 312.3 \text{ kN} \tag{11.3}$$

The same equation can be used to determine the maximum compression load on the lander during launch as shown in Equation 11.4.

$$F = m \cdot a_z = \sum m_{objects} \cdot a_z = 89.15 \cdot 6 \cdot 9.81 = 5,247.4 \text{ N} \tag{11.4}$$

The same is done for the maximum compression load on the ground station during launch (Equation 11.5).

$$F = m \cdot a_z = \sum m_{objects} \cdot a_z = 43.6 \cdot 9.81 \cdot 6 = 2,566.3 \text{ N} \tag{11.5}$$

Table 11.8: *Verification of the structural analysis of the launch vehicle, lander and ground station.*

	Python model	**Hand calculations**	**% Difference**
Maximum compression launch vehicle	312.3 kN	312.2 kN	0.025
Maximum compression lander	5,259.9 N	5,247.4 N	0.24
Maximum compression ground station	2,569.2 N	2,566.3 N	0.11

The results of the calculations are shown in Table 11.8. The last column shows the difference between the two methods of calculation. It can be seen that there are only small differences between the calculations of 0.025 %, 0.24 % and 0.11 % for respectively the maximum compression load on the launch vehicle, the lander and the ground station. These differences are within an acceptable margin. The differences occur due to rounding errors in the analytical solution when determining for example the mass of a structural element. Since the error is within an acceptable margin, the model is verified and can be used to determine the structural mass and loads.

Remaining issues

Only a preliminary analysis has been performed for the vibrations. The spacecraft-launcher system can be modelled as a single-degree of freedom system (SDOF) with a spring and a damper and a base excitation. Using stiffness matrices, the final vibrational frequencies of the entire spacecraft can be determined, but also the vibrations experienced by the different subsystems on the space probe.
An analysis should also be done on the structure, what the effect of acoustic loads are and what the effect of different shock loads are, during e.g. transportation on Earth or separation of modules in space. Furthermore, the effect of pressure changes and possible impacts of small debris can be determined.

To expand the analyses, a finite element analysis (FEM) analysis should be performed, using e.g. programs such as Abaqus[4]. FEM models are used to do analyses on strength/stiffness, thermo-elastics, dynamics, coupled loads analysis and vibroacoustics [93].

Bolts should be taken into account in a further design, since these might lead to higher stresses in the material. Furthermore, higher stresses might occur at locations where the subsystems are mounted to the structure. Furthermore, the effect of the use of explosive bolts should be investigated. The springs used to push the landers and panels away, should be designed. The forces and moments on the spacecraft can then be determined and the required ADCS thrusting can also be calculated.

Using these expanded analyses, the thickness and material for each structural element can be determined, instead of grouping several elements and sizing these at once. Furthermore, a research can be conducted into the use of other materials than those investigated during this design phase. In a further design stage, the final design stage, test models can be made and tests on the structure can be performed, e.g. static test, modal surveys, shaker vibration sine and random tests, shock tests and acoustic tests [93]. These test are performed in order to qualify and verify the design.

Besides the structural design of the space probe, the spacecraft-launcher adapter can be designed when this is required (if for example the sizing of the standard adapter provided by SpaceX does not comply with the MUUDS design).

[4] `http://www.3ds.com/products-services/simulia/products/abaqus/`

12 | Market Analysis

The purpose of this section is to present a market analysis, related to the industry of the project. The market analysis is divided in several categories like market size, market growth rate and market trends. This division was made my the renowned marketing expert D. A. Aaker [100]. In this study, of main focus will be the most dominant space agencies in the world, NASA and ESA. Furthermore, growing space agencies, particularly in Asia will be discussed. Lastly, the commercialisation of space will be discussed.

12.1 The Space Market

In this section the space market is elaborated upon. This is done by assessing the size of the market, the market growth in the coming years and the market trends.

12.1.1 Market Size

A first indication of the size of the market is to view the budgeting for governmental space agencies. Table 12.1 displays the budgeting of both ESA and NASA for the fiscal years 2009 to 2015.

Table 12.1: *ESA and NASA budgeting for the fiscal years 2009 to 2015.*

Fiscal year	**2009**	**2010**	**2011**	**2012**	**2013**	**2014**	**2015**
ESA budget (mln €)	2,819	2,778.6	2,975	2,900	3,109.5	4,102	4,433
NASA budget (mln $)	17,782	18,724	18,448	17,770	16,865	17,647	18,010

The size of the two largest space agencies cannot only be determined by the annual budgeting, but also by the number of employees. NASA has as of today approximately 18,000 employees. Furthermore, NASA has thousands of external parties with which NASA has contracts. The number of external persons involved in NASA project is a lot more than the actual NASA employees. The number of ESA employees exceeds 2000.

Lastly, there are the budgets of the Asian space agencies. It is estimated that the China National Space Administration, CNSA, has a budget of $ US 500 million. The Indian Space Research Organisation has approximately $ US 1.1 billion budget annually.

12.1.2 Market Growth

It is of interest to assess what the expectations are for the growth of the major parties in the coming years. For NASA, the budgeting prognoses are available up to the fiscal year 2019, it is displayed in Table 12.2.

Table 12.2: *Prognosis of the NASA budget for the fiscal years 2015-2019.*

Fiscal year	**2016**	**2017**	**2018**	**2019**
Prognose NASA budget (mln $)	17,635	17,812	17,990	18,170

This is a more or less constant budget, when considering inflation for the coming years. As the US economy is expected to grow, this might even resemble a relative decline in the NASA spending. On the other hand there is ESA. When considering the last years, a recent trend of larger budgets can be seen, where they were more or less constant beforehand. Explanations for the recent increase in ESA spending lie in the end of the global economic crisis and the participation of more and more countries to the ESA project. The recent trend in ESA budgeting can be seen in Figure 12.1.

12.1.3 Market Trends

The aerospace industry is an industry that can be seen as an industry of trends. The perspective has shifted from the moon and reconnaissance missions to further planets and the search for exo-planets. This can be seen in the percentages of the large space agencies' budgets that are allocated to these type of missions. A manned mission to Mars is also the topic of discussion in many places. This is in line with the MUUDS project. The focus of the commercial space companies is more difficult to link to the MUUDS project, however the growing market, a more competitive, commercial market, is beneficial for large missions. These missions require a lot of external companies. Also, the launch of higher and higher masses has drawn the attention of companies like SpaceX.

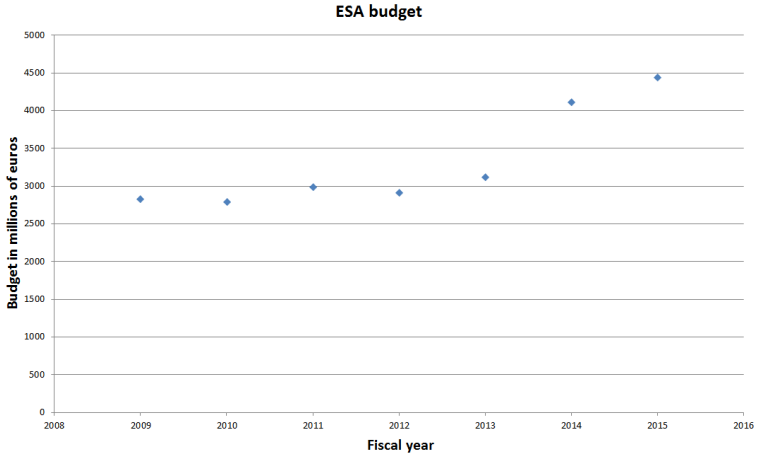

Figure 12.1: *ESA budgeting from the fiscal years 2009-2015.*

12.2 Stakeholders

Many stakeholders are involved in the MUUDS project, these will be described in this section.

Scientific community: Exploration of Mars is of main interest for various scientific disciplines. Fields related to meteorology, geology, seismology etc. would value the MUUDS data. Moreover, for other (Mars) missions, and especially manned (Mars) missions, the technologies demonstrated can be of great importance. For example, the use of a HIAD aeroshell may show some great advantages, but might carry a slightly lower reliability, making it undesirable for manned missions.

Governments: The Aerospace and Defense industry was an over US$ 300 billion industry last year, making it extremely interesting for governments to participate in. Besides, tells the level of participation in aerospace something about the state of the country. The government is a major stakeholder, as the budget allocated for the project is determined by that party.

Environmentalists: Involved in any space mission is an extremely polluting launch, which raises doubts with environmentalists. Also, space (and Earth) debris are ecologically unfriendly results from most space missions.

Employees: Employees are a major stakeholder for the company executing the mission. The success of the mission depends to a large extent on the quality and the motivation of the employees.

Authorities: As a space mission, and in particular the launch, can be quite dangerous, the company has to comply with a lot of regulations, managed by the proper authorities. It is important that there is a good relationship between these two parties and that regulations are met.

External companies for producing components: A single company cannot produce an entire space mission. A lot of external parties are used for specialised products. This is beneficial for all parties, as know-how is increased, however it can results in difficulties to hold to the time schedule, as more parties are involved.

13 | Risk and Contingency Management

In the following sections the importance of implementing risk management throughout the different phases of the MUUDS mission will be elaborated upon. Section 13.1 will deal with the tool used during the technical risk management. The contingency method used in this project is discussed in Section 13.2. Both methods will be put into practice in the last section, Section 13.3.

13.1 Technical Risk Management

It is paramount that risk factors are assessed as detailed as possible, as major design flaws in any space project can turn out catastrophically due to the lack of possibility for any modifications. Risk consists out of two components and forms a measure of the inability to achieve the mission requirements and objectives, as can be seen in the equation below.

$$Risk = Severity \cdot Likelihood$$

These two components are: 1) severity which represents the consequences when not being able to achieve a certain outcome and 2) the likelihood/probability of not being able to achieve this outcome [101].

The iterative steps taken throughout the different phases of the MUUDS mission design are itemised below. The outcome of this process is detailed in the consecutive subsections.

1. The technical risks were firstly identified per category (as will be clarified in Subsection 13.1.1) and are all summed up in Appendix A.
2. Technical risk assessment is conducted which resulted in a score for the severity and likelihood of the risk. These are represented in Appendix A.
3. The focus in this phase of the project design is to transfer unacceptable risks to more acceptable risks. In order to prevent the risks from becoming reality, risk mitigation techniques will therefore be designed and can be found in Section 13.3.
4. In order to monitor the status of each risk and to discover new risks, a weekly meeting was organised in which each group member was encouraged to re-evaluate the risks corresponding to its domain of expertise.
5. When risks would occur the implementation of the technical risk mitigation by means of a contingency plan will be triggered. Contingency management will be discussed in Section 13.2 and states the techniques necessary to prevent a risk from increasing its impact.
6. At the end the whole process is repeated periodically.

13.1.1 Risk Management Tool

The tool used in this project is a risk map, which allows the allocation of both severity and likelihood to a specific risk factor in a structured and clear manner. The advantages are the ability to track the status and the effect of a specific risk and the benefits of communicating the risk status properly. The successful character of this risk map relies on its simplicity and clarity.

A risk map has limitations as well though. Interactions cannot be represented since only individual risks will be implemented in the matrix. Also the combined risks such as total risk are hard to implement. By putting risks in boxes they become "fixed" and are more difficult to place in the context of a certain program. It can form difficulties to categorise a certain risk since the likelihood and consequence should be known [101].

Since working in a team demands a certain methodology in order to avoid cluttered communication and confusion a risk item evaluation key is developed. This key offers the ability to perform equal, ranking resulting in consistency and is discussed in the following paragraphs.

The likelihood or probability of occurrence is divided in five components, in increasing order of likelihood, which are: rare, unlikely, moderate, likely, and expected. These can be expressed in more intuitive nomenclature: proven flight design, extrapolated from existing flight engineering, extrapolated from non-flight engineering, working laboratory model, and feasible in theory, respectively.
The severity or consequence of risk is divided in five component as well, ranging from insignificant to catastrophic. Insignificant stands for a negligible or no impact on the mission objectives. Minor is understood as a risk which will have a low impact to the full mission success criteria. Moderate stands for impact on the full mission success with success in a specific margin. Major can be explained as the achievement of the minimum mission success

criteria. Finally, catastrophic represents a risk due to which mission success is not possible anymore.

Each risk will now be categorised and itemised. Firstly the risk factors are categorised in specific groups, namely: Power & Propulsion (P), Communication (C), Measurements (M), Launch & Landing (L) and Operations (O). Each risk will have its own identifier and risk map location ([Severity, Likelihood]). All the risks are listed in Appendix A. The second categorisation is based on how critical it is and is subdivided into three categories, each with its own colour mark (as can be seen in Table 13.1).

- Low risk (green): Has almost no effect on the performance of the mission. Keeping the risks in this domain can be done by regularly keeping track of the risks and their status.
- Moderate risk (orange): May cause degradation of performance which requires special actions to avoid propagation of the risk to more serious levels.
- High risk (red): Most likely to harm the performance of the MUUDS mission. Immediate action is required to handle the risk.

Table 13.1: *Colour indicators used in the risk matrix.*

Low	Moderate	High

Reality is that not all the risks can be distinguished. The MUUDS mission will need to be able to deal with unidentified risks as well. These risks will be encountered when operating in unfamiliar areas, but can't be dealt with in the scope of this project.

13.2 Contingency Management

First, the concept of contingency management will be placed in the context of designing the MUUDS mission, followed by its specific implementation in this project. While risk management will focus more on the deployment and development of plans to mitigate the risks, contingency management will deal with the impact reduction of an already occurred risk.

Concept

Implementing contingency management will provide the means to bring a system in its current state, subjected to requirements and constraints, to a next desired state. This next desired state should be achieved with minimal cost and the highest probability of success [102].

The benefit of contingency management results from the fact that in the early process of setting up, the requirements and objectives need to be balanced against the possible, future conditions of the system. Using this approach, cost effectiveness is achieved because solving problems is more favourable than changing design plans in later phases of the project.

The goals of contingency management are a more safe and reliable spacecraft system, achieved with the optimal cost effectiveness and mission success. It helps to track down possible risks in the early phases of the process and avoids the growth from small failures to project-threatening catastrophes. It will develop alternative plans to respond to the occurrence of a risk.

Implementation

This strategy is strongly related to the existing risks. The contingency management is implemented by making sure that the status of the spacecraft is constantly updated in order to iterate over occurring faults until all the errors are solved or mitigated.

Contingency plans are developed in Subsection 13.3 for the highest, unacceptable risks. The benefit is that now contingencies can be tracked against the background of risk planning. Secondly, design margins or contingencies are implemented during the design of the MUUDS spacecraft. This is primarily discussed throughout the different design chapters. The first method is the usage of safety factors throughout the design and sizing of the subsystems.

13.3 Implemented Risk Strategies

Now the two technical risk management approaches have been discussed, all the tools are now available to start assessing the high category risks, specific to the MUUDS mission. One can find these risks placed into the risk matrix presented in Figure 13.2 and the corresponding strategy below.

Table 13.2: *Risk map with the least acceptable risk factors.*

Likelihood	1. Insignificant	2. Minor	3. Moderate	4. Major	5. Catastrophic
5. Expected			P7,L15,L19	O15	L2
4. Likely				C11,L12	
3. Possible					P11,P19,C7 M2,M3,M5
2. Unlikely					
1. Rare					
	Severity				

P = Power & Propulsion

- Identifier: P7 Risk location = [3,5]
  Risk: Dust accumulation on power systems.
  Mitigation: Placement of solar system as far as possible from the Martian surface.
  Contingengy management: If power control system allows, move solar panels to remove excess dust.
- Identifier: P11 Risk location = [5,3]
  Risk: Main thruster failure during Martian orbit insertion.
  Mitigation: Simulation and testing such that reliability of the thruster can be ensured.
  Contingengy management: If event occurs, no alternative plan can be implied and spacecraft will not be capture by the gravity field of Mars.
- Identifier: P19 Risk location = [5,3]
  Risk: Failure of thruster control during descent.
  Mitigation: Simulation and testing of stability of ground pod under aforementioned circumstances.
  Contingengy management: Sizing of ground pods for larger impact velocities and inclination angles than the nominal path assumes.

C = Communications

- Identifier: C7 Risk location = [5,3]
  Risk: Failure of antenna gimbal.
  Mitigation: Opt for gimbal which has already proven its feasibility in past missions.
  Contingengy management: Use orbiter pointing in when situation allows it to point antenna.
- Identifier: C11 Risk location = [4,4]
  Risk: Uplink unable to establish due to too little contact time.
  Mitigation: Design Martian orbit such that contact time is optimised.
  Contingengy management: Provide orbital manoeuvring of spacecraft such that contact time can be increased.

M = Measurements

- Identifier: M2 Risk location = [5,3]
  Risk: Failure of an orbital instrument.
  Mitigation: Design instruments such that the probability of failure is considerably small.
  Contingengy management: Use the functioning instruments on the ground and in orbit to keep the mission running.
- Identifier: M3 Risk location = [5,3]
  Risk: Failure of ground instruments due to too high temperature ranges during EDL.
  Mitigation: Provide thermal control during EDL and size the heat shield such that the payload is minimally

affected.
Contingengy management: If occurs, mission needs to be executed with the instruments still available.

- Identifier: M5 Risk location = [4,5]
  Risk: Significant dust accumulation on instruments.
  Mitigation: Provide coverage of most sensitive instruments and provide protection against dust entering the ground station.
  Contingengy management: Use deployment mechanisms in order to attempt shaking of the excess dust.

L = Launch & Landing

- Identifier: L2 Risk location = [5,5]
  Risk: Failure of ground station due to high impact velocity.
  Mitigation: Testing and simulation are a necessity to size for this manoeuvre.
  Contingengy management: Safety factors margins needs to be applied such that the structures will not fail under normal launch conditions.
- Identifier: L12 Risk location = [4,4]
  Risk: Hinges to unfold ground stations are situated below the surface.
  Mitigation: Simulation of opening force of shell of ground pod.
  Contingengy management: Add a margin by placing the hinges higher than required such that deployment will still be possible.
- Identifier: L15 Risk location = [5,3]
  Risk: Failure of separation of ground station from orbiter.
  Mitigation: Redundancy of ten ground stations.
  Contingengy management: Develop the deployment mechanisms such that it does not obstruct the remaining pods from executing the EDL phase.
- Identifier: L19 Risk location = [5,3]
  Risk: Contamination of Mars during impact.
  Mitigation: Iterate on all possible design failures in order to prevent this situation.
  Contingengy management: Fulfil at least the minimum COSPAR requirements.

O = Operations

- Identifier: O13 Risk location = [5,3]
  Risk: On-board computer fails due to short circuit
  Mitigation: Implement a second on-board computer as redundancy.
  Contingengy management: Switch to second on-board computer.

14 | Budgeting and Sensitivity Analysis

Based on the building blocks of the final design, an overview can be given for the flow of resources in terms of mass, power, link budget and cost. The estimated budgets will be discussed in Section 14.1, followed by the sensitivity analysis discussed in Section 14.2.

14.1 Resources Allocation

In this section, a quantitative summary will be presented for the final design of the MUUDS mission. It includes the allocated resources for the mass, power, link budget and cost of this design.

14.1.1 Mass Budget

The mass of the launch vehicle will be discussed in this subsection. The different subsystems are grouped and the mass of each group is shown in Table 14.1. The total launch vehicle mass is equal to 5,365 kg which consists out of the four boxes: two boxes containing the ground stations, one box containing the orbiter and one box consisting of the propulsion system required for the travel to Mars. The orbiter mass is approximately equal to 200 kg, the lander mass equals 89 kg and the ground station mass is equal to 44 kg.

Table 14.1: *Mass budget of the launch vehicle.*

Component group	**Subcomponent group**	**Mass**
Interplanetary Vehicle		5,365.09 kg
	Structure and thermal	107.72 kg
	Propulsion system	4,198.0 kg
	Landers	893.64 kg
	Orbiter without structures	165.73 kg
Orbiter		200.06 kg
	Structure and thermal	34.33 kg
	Power	39.05 kg
	Instruments	31.14 kg
	ADCS	36.8 kg
	Communication	47.9 kg
	Command and data handling	10.84 kg
Lander		89.36 kg
	Structures	15.31 kg
	Crushables	2 kg
	HIAD	8.2 kg
	Ground station	43.65 kg
	Thrust	12.2 kg
	Parachute	8.0 kg
Ground Station		43.65 kg
	Structure and thermal	5.69 kg
	Power	17.98 kg
	Instruments	13.16 kg
	ADCS	0 kg
	Communication	2.4 kg
	Command and data handling	4.42 kg

14.1.2 Power Budget

In this subsection the power usages of the subsystems used on the spacecraft and ground stations of the mission are summarised. The power consumptions can be found in Table 14.2.
Looking at Table 14.2, it can be seen that the spacecraft has a total power consumption of 409 W and the ground station has a power consumption of 151 W. A more detailed breakdown of the power consumptions of both systems can be found in Section 10.1.5 in Tables 10.1 and 10.2.

Table 14.2: *Power budget of the spacecraft and the ground station.*

Subsystem	**Power consumption**	
	Spacecraft	Ground Station
ADCS	74.2 W	0 W
Instruments	21.5 W	27 W
Command andData Handling	17 W	16 W
Communication	146.3 W	43 W
Thermal Control	150 W	65 W
Total	**409 W**	**151 W**

14.1.3 Link Budget

The link budget of the communication links of the mission are summarised in Table 14.3. For a communication link between the orbiter and Earth (with the DSN) the characteristics of the normal (with the HGA) and emergency communication (with the LGA's) are listed. For the communication between the ground stations on Mars and the orbiter, the downlink is the command link towards the ground stations and the uplink is the data link towards the orbiter. The most important parameters of these lists are listed in dB (data rate in bit/s). The full link budgets are shown in Subsection 10.4.3.

Table 14.3: *Link budget summary of the communication links.*

	Value					
	Orbiter – DSN				Mars – Orbiter	
	HGA		LGA			
Parameter	Downlink	Uplink	Downlink	Uplink	Downlink	Uplink
Data rate (bit/s)	16,000 dB	2,000 dB	10 dB	10 dB	8,000 dB	32,000 dB
Transmitted power	15 dB	40 dB	10 dB	43 dB	7 dB	10 dB
Gain	108 dB	106 dB	84 dB	82 dB	15 dB	11 dB
Loss	-284 dB	-284 dB	-287 dB	-293 dB	-137 dB	-140 dB
Received power	-161 dB	-138 dB	-193 dB	-168 dB	-115 dB	-119 dB
SNR margin	8.3 dB	19.9 dB	6.9 dB	20.2 dB	33.8 dB	27.2 dB

14.1.4 Cost Budget

In this subsection, the expected costs of the mission are discussed. The statistical data of reference space missions was leading for determining the costs [1]. The relations were inserted in a Python script that has calculated the costs as described in Table 14.4. There has been corrected for the expected inflation in the coming years [1]. For the calculations, it has been assumed that the cashflow will be proportional during the mission lifetime. This is a conservative assumption, as in reality the majority of costs will be made in the first phase of the project, when the currency is expected to have more value due to the positive inflation. The total costs of the mission are now estimated to be $1.643 million.

Table 14.4: *Cost breakdown of the MUUDS project, divided in recurring and non-recurring costs.*

Component group	**Subcomponent group**	**Recurring costs (MLN $)**	**Non-recurring costs (MLN $)**
1. Spacecraft Bus			
	1.1 Structure & Thermal	26.6	87.3
	1.2 ADCS	8.3	14.5
	1.3 EPS	12.0	23.7
	1.4 Propulsion	2.5	100.7
	1.5 TT&C	7.9	67.3
2. Payload		19.3	63.0
3. Spacecraft Integration, Assembly and Test		23.7	173.8
4. Program level		58.6	275.7
5. Flight Support		196.9	-
6. Aerospace Ground Equipment (AGE)		-	25.2
7. Operations		93.9	-
8. Facilities		77.6	-
Total Cost		**527.3**	**831.2**
Total Cost with Inflation Correction		**637.5**	**1,005.4**

14.2 Sensitivity Analysis

The sensitivity analysis is used to identify the strengths and weaknesses of the mission design. This is done by checking the influence of some possible uncertainties during the progress of the mission on performance of the design. In order to check whether or not the design is able to handle the possible uncertainties some design parameters are changed. This is then followed by a check if the design is still able to perform the mission in a successful way or not. To check the sensitivity of the design of the MUUDS mission, the following three different scenarios are considered. The first scenario is that the final mass of the complete system after production is higher than the estimated mass during the design phase. This scenario is further explained in Subsection 14.2.1. The next scenario deals with the possibility that the requirement on the measurement data changes. So it might be required that additional parameters need to be measured or more data has to be gathered, which is described in more detail in Subsection 14.2.2. The last scenario, considered for the sensitivity analysis, is a change in the schedule of the mission as will be explained further in Subsection 14.2.3.

14.2.1 Scenario 1: Higher Final Mass

The probability of the final mass being higher than the mass used during the design phase always exists. An explanation could be the assumptions and simplifications made during the design process, resulting in an offset from the final value. Furthermore it occurs that during the production process of the components additional mass is added (e.g. bolts or connections). This additional mass has an influence on the following subsystems of the spacecraft: ADCS, propulsion system and the structure of the spacecraft. In addition to that, additional mass influences the EDL concept of the mission. First of all a distinction in the amount of mass added needs to be made.

Firstly, the effects of a small mass increase are investigated. In order to account for this scenario the systems are sized using safety margins of about 10% on average. An analogous approach can be applied for the EDL concept. The ADCS is the only subsystem that is sensitive to a small increase in mass. Since, in order to save mass, there is no safety margin on the propellant used for attitude control and the ADCS thrusters are exactly sized to a certain mass. So even a slight increase in mass is critical for the ADCS system.

Secondly, the scenario of a larger increase in mass needs to be investigated. If the increase is too high, it might happen that the safety margins are not effective anymore and the complete design of the spacecraft needs to be reevaluated. The first system that is investigated is the ADCS. If the total mass of the spacecraft exceeds 7,000 kg there are no reaction wheels available to control the attitude of the spacecraft. Furthermore it has to be noted that a large mass increase can disable proper functioning of the inertial reference system. This means that the attitude determination of the spacecraft does not work accurately enough anymore. In addition to that there is an increase in the power consumption of the ADCS systems. This power has to be delivered by the electrical power system, which is already sized with a safety margin of 20%.
Closely related to the ADCS is the propulsion system of the spacecraft. A large increase in mass requires the propulsion system to deliver a larger ΔV to get into transfer and operational Martian orbit. This larger ΔV means that more propellant is required and thus larger thrusters and propellant tanks are required.
Furthermore a large increase of the total spacecraft mass has an effect on the structure of the spacecraft. Due to the mass increase, the probability of buckling failure during launch increases. In addition to that it needs to be noted that loads acting on the structure during the manoeuvres of the spacecraft increase, which might lead to failure of the structure. However the increase in mass results in a lower natural frequency of the spacecraft, which is beneficial for the vibrational response of the spacecraft during the launch phase.

As a conclusion it can be said that a large increase in mass should be avoided, since this cannot be handled by the current design. A large increase in the spacecraft mass results in a snowball effect on all the system as they need to be re-sized in order to perform the mission.
In addition to this, the effect of a large mass increase on the EDL module needs to be investigated. A first effect is that the descent velocity increases which leads to less time for the EDL systems to decelerate the vehicle. Furthermore the parachute used during the EDL has the risk of failure when subjected to higher velocities. So, in order to account for an increase in mass the parachute used during EDL needs to be re-sized to be able to handle the forces experienced.

14.2.2 Scenario 2: Additional Measurements

This scenario can be further divided in two sub-scenarios. The first sub-scenario considers the case when the requirement on the type of data that needs to be gathered would change. Since additional measurement instruments need to be taken to Mars then, an increase in mass of the spacecraft would be a consequence of which the influences can be found in Subsection 14.2.1. Moreover additional data is generated by additional measurement instruments, which leads to the second sub-scenario, which considers that the requirement on the measurement time intervals has changed. A change in the time interval would result in more measurement data as well. Additional measurement data has an impact on the design of the following subsystems, of both the spacecraft and the ground stations: communication subsystem, command and data handling and the electrical power subsystem.

An increase in the data volume can be handled by the command and data handling system. The current mission is estimated to have a low data generation, so the C&DH has a lot of capacity left over to handle additional measurement data, generated by the instruments. In addition to that, the communication system is able to handle an increase in data volume as well. For the current design the signal-to-noise ratio for the uplink from Mars to the orbiter is 38.2 and the downlink from the orbiter to Earth is 11. The data for the Mars - Earth communication is still readable with a SNR of 11 and since the Deep Space Network is used as a receiver on Earth, the minimum allowable SNR is 2.7. So there are sufficiently large margins for the transmission of more data which means that the power consumption does not have to increase in order to keep sending readable data. A downside of having more data volume that needs to be transmitted, is the need of more communication time. In order to be able to send more data in the same time, more power is required. The power system can account for more power required, as it is sized with a safety margin of 20%. But depending on the amount of data increase, the power system might not be able to handle the required communication power. So in case of a very large increase in data volume the communication time and the desired signal to noise ratio have to be reevaluated.
All in all it can be said that an increase of the total data volume which needs to be transmitted is not significant for the mission of which the affected systems are able to handle the increase in data.

14.2.3 Scenario 3: Schedule Changes

In this scenario the possibility of a delay in the mission schedule is evaluated. Such a delay would result in a later launch date for the mission. This sensitivity analysis inspects the effects on the design if the requirement on the availability of the scientific data by the year 2025 still has to be met.
The launch of the mission currently is scheduled to be on the 24^{th} of August in 2020. A 30-day launch window is chosen as it enables the most propellant efficient transfer to Mars. The propellant mass is sized with margins that account for this possible 30 day variation in the launch date. If this launch window is missed, the next possible window would be 2.15 years later.
In order to still meet the requirement of providing the data by 2025, a less efficient trajectory to Mars has to be used, which means that a larger ΔV is required. The current design is not able to deliver such a ΔV. This means that if the spacecraft is sent into space outside of the launch window, the mission will not be successful with the current spacecraft design. So in order to meet the requirement, the whole spacecraft concept needs to be redesigned. Redesigning the spacecraft concept would require a possible focus on different facets of the mission such as Technology Readiness Levels, available funding or more flexible top-level requirements. But this would result in a less sustainable mission design and that is why it is not recommended to launch outside the determined launch window.

15 | Sustainability Approach

Sustainability is an important aspect of modern day engineering. Since the Martian Weather Data System project wants to contribute to the development of humanity, without compromising the needs of future generations, sustainability plays a big part in every aspect of the mission. The purpose of this chapter is to get an overview of the approach regarding sustainability. All the actions that are executed have been described per mission phase. Important to mention is that throughout the design and development of the MUUDS concept this sustainability approach is continuously interwoven in the trade-off processes, technical calculations and mission descriptions of this report.

Sustainability has to be taken into account from the beginning of the project. This means that focus on sustainability is apparent during the design phase. When designing the mission, the goal is to make the total spacecraft as lightweight as possible. This is due to the fact that a reduction in weight leads to a reduction in fuel which reduces the environmental footprint on both Earth and Mars. When the design is finished, components and (sub)assemblies need to be tested to ensure mission success. The amount of tests shall be reduced to a minimum, so less resources, material and fuel are used. Besides, all tests shall be executed in a safe and suitable environment. This means that the used test facilities are capable of providing safety measures to ensure a safe work environment for the employees and that the surrounding environment and researchers stay unharmed in case of test failure.

After the tests have been completed successfully, the spacecraft can be produced. One of the biggest concerns regarding sustainability during the production, is that every component of the spacecraft obeys the COSPAR regulations []. This means that the spacecraft is free of any Earth-based bacteria or other possible contamination, which may cause an imbalance of the Martian environment. Next, the used materials should not be harmful to employees when assembling the spacecraft. If it is inevitable to use a harmful material, appropriate measures should be taken to ensure the health of the employees and safety of the environment. Materials which are produced or mined without harming people and the environment are preferred. When looking at the production site, the safety of the employees is an important factor as well. Besides, the location of the production facility should be as close as possible to the launch site in order to minimise the emissions and costs of transportation of the sub assemblies. Another requirement is that the energy used during the production process is generated from renewable energy sources in order to promote the change from fossil fuels to renewable energy.

Once the production of the spacecraft is finished, the launch phase of the mission starts. The launch date was selected with the sustainability of the mission in mind. The date is chosen in a way that the spacecraft can complete the most fuel efficient trajectory towards Mars. Sustainability plays a big part in the launcher selection process. The Falcon heavy was the best option, as it actively de-orbits its first stage and booster rockets, which minimises the generation of space debris around Earth. The first stage and booster rockets can land in a controlled way, so they can be used for multiple missions, reducing the use of materials and cuts the launch costs.

During the operational phase of the mission there are some sustainability considerations made as well. Furthermore the COSPAR regulations apply to the ground stations and orbiter of the mission. So in case of a failure of a system during operational phase or end-of-life phase, the waste material that accumulates shall not destroy the Martian environment in any way.

In a general sense there are some further sustainability considerations that can be associated with the MUUDS mission to Mars. First of all the data gathered by the MUUDS missions is useful for the scientific community in order to expand the knowledge about Mars and phenomena encountered on Earth as well since there are similarities between the two planets[1]. Besides, missions like MUUDS enable support of the technological and economical growth of the society. Furthermore, it is known that NASA wants to land on Mars in the near future. By providing crucial information on the weather and other environmental parameters of Mars, the MUUDS mission contributes to the exploration of the solar system.

[1] http://www.nasa.gov/pdf/657307main_Exploration%20Report_508_6-4-12.pdf

16 | Development of Final Design

After the conceptual design analysis (Phase A), followed by a preliminary design phase (Phase B) it is required to start elaborating more deeply on the more detailed and technical design options, dealt with in Phase C, the detailed design phase. After this design phase the production phase, Phase D, will commence. These phases have been visualised in a Gantt Chart, Figure 16.1 and will become reality during the operations, discussed in Section 16.3 . A limited margin is available in terms of succession of events in time due to the constraining requirement that all data has to be available before 2025.

ID	Task Name	Duration	Start	Finish
1	**Detailed design phase**	**793 days**	**Mon 6-7-15**	**Wed 6-9-17**
2	Detailed design phase	793 days	Mon 6-7-15	Wed 6-9-17
3	**Production phase**	**1081,67 day**	**Wed 6-9-17**	**Sun 23-8-20**
4	Documentation production	993 days	Wed 6-9-17	Tue 26-5-20
5	Manufactering sub-assembly, subsystem	200 days	Wed 6-9-17	Sun 25-3-18
6	Testing sub-assembly, subsystem	150 days	Sat 6-1-18	Tue 5-6-18
7	Manufactering prototype of elements	250 days	Tue 5-6-18	Sun 10-2-19
8	Receiving off-the-shelve products	21 days	Mon 1-10-18	Mon 22-10-18
9	Quality assurance of the off-the-shelve products	60 days	Mon 22-10-18	Fri 21-12-18
10	Testing prototype of elements	50 days	Tue 1-1-19	Wed 20-2-19
11	Integrate to segments	250 days	Wed 20-2-19	Mon 28-10-19
12	Integrate whole system	150 days	Mon 28-10-19	Thu 26-3-20
13	Contigency time	92 days	Thu 26-3-20	Fri 26-6-20
14	Clean system to COSPAR regulations	14 days	Fri 26-6-20	Fri 10-7-20
15	Prepare for transport	14 days	Fri 10-7-20	Fri 24-7-20
16	Transport to South Texas Launch Pad	2 days	Fri 24-7-20	Sun 26-7-20
17	Integrate in launcher	7 days	Sun 26-7-20	Sun 2-8-20
18	Prepare for launch	21 days	Sun 2-8-20	Sun 23-8-20
19	**Transport**	**283 days**	**Mon 24-8-20**	**Thu 3-6-21**
20	Launch	1 day	Mon 24-8-20	Tue 25-8-20
21	Hohmann transfer orbit	278 days	Tue 25-8-20	Sun 30-5-21
22	Brought in Mars orbit	1 day	Sun 30-5-21	Mon 31-5-21
23	EDL ground station	2 days	Mon 31-5-21	Wed 2-6-21
24	Check	1 day	Wed 2-6-21	Thu 3-6-21
25	**Operation phase**	**1973 days**	**Tue 26-5-20**	**Mon 20-10-25**
26	Start operation phase	1374 days	Thu 3-6-21	Sat 8-3-25
27	Receiving data	1374 days	Thu 3-6-21	Sat 8-3-25
28	Process data	1600 days	Thu 3-6-21	Mon 20-10-25
29	Documentation life	1973 days	Tue 26-5-20	Mon 20-10-25
30	**End-of-life**	**500 days?**	**Sat 8-3-25**	**Tue 21-7-26**
31	End-of-life	500 days?	Sat 8-3-25	Tue 21-7-26

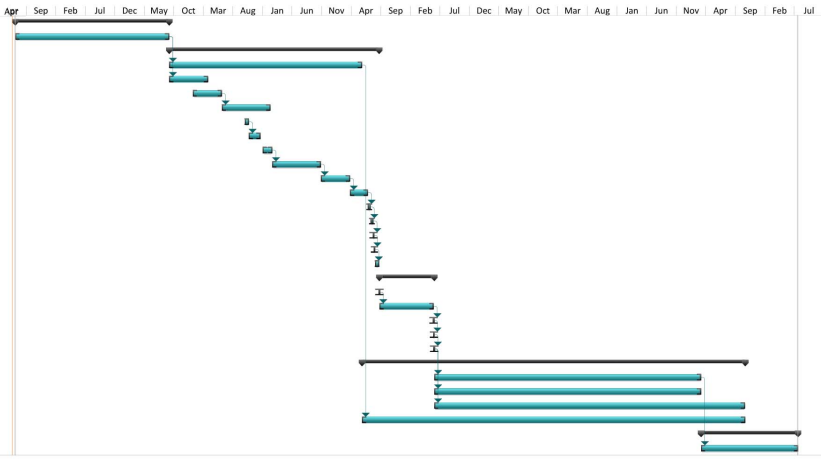

Figure 16.1: *Gantt chart on the development of the MUUDS spacecraft design.*

The more practical steps which need to be undertaken throughout the mission timeline are presented in chronological block diagram in Figure 16.2.

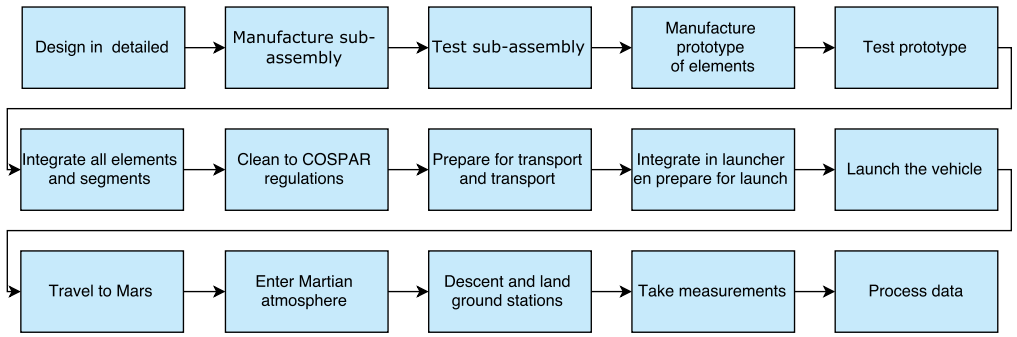

Figure 16.2: *Project design & development logic.*

16.1 Phase C: Detailed Design Phase

In this phase, the chosen mission concept will be designed in more detail, while the quality assurance of the project will be implemented parallel to this detailed design. The launch environment, accelerations and vibrations, acoustic noise, shocks and rapid depressurisation will be simulated and when possible tested as well. Once all loads are known, all parts, including every drill hole and connection mechanism, that has not been designed yet in the preliminary design will be elaborated upon. As a supplement to the design, a production plan will be made and regulations will be set. Although some material analysis already has been conducted, not all materials have been selected yet. Therefore further extensive research has to be executed concerning the material selection. Since the designed products consist out of a space probe including ground stations, not only the strength of the material is of great importance. Following properties need to be tested for a space mission as well:

- Temperature and thermal cycles
- Vacuum
- Offgassing and toxicity
- Flammibility
- Radiation
- Electrical charge/discharge
- Corrosion
- Fluid compatibility

16.2 Phase D: Production and Qualification

Once the mission is totally designed, the production phase will start. In this phase the raw material will be fabricated to sub-assemblies, which will be checked individually on their quality. The qualified sub-assembly will then be assembled to the final product, which will also be checked on its quality. Next to the production also the qualification is a part of this phase.

Location

As discussed in Chapter 3, the Falcon Heavy will be used as launcher to bring the space probe into interplanetary trajectory. The Falcon Heavy is a launcher designed, manufactured and supported by SpaceX. The production of this launcher is in-house executed in Texas by SpaceX itself. Having similar launch and production locations turns out to be convenient since this means that the launcher does not need to be transported over large distances, which is now possible by truck.

Because the launch will take place in South Texas it would be best if the assembly of the orbiter and ground pods will be centred in Texas as well. However in the preliminary study most products have been chosen. Which means that also the manufacturer of these products has been chosen indirectly. For example, sun and star sensor are produced in the Netherlands and need to be transported to Texas. However some parts (such as the crushable nose cone structure and the inflatable aeroshell) will be manufactured in their own technical centres. Placing those technical centres in Texas is not only convenient for the distance to the launch platform but also because a lot of space companies are situated here, which could provide support if deemed necessary. In this technical centre the final assembly of the product will take place.

Regulations

Detailed design regulations will be set for the production of all components. The most important regulations will make sure that no harm shall be done to the environment. In other words no harm will be done to the Mars environment by complying to the COSPAR regulations as minimum requirement [103]. But also the waste produced during production will be minimised, recycled there where possible and discarded in a clean way if necessary. But besides these regulations aiming for a sustainable production also regulations will be set in terms of documentation and traceability of all parts. In this way mistakes and errors will be minimised and it will be possible to trace back faults more efficiently.

Transportation

Some parts will be produced in-house while others will be off-the-shelf products. These off-the-shelf products have to be transported from their own facilities. Most instruments produced overseas are very small and can be send easily. For large distances this will be done by airmail. For relatively small distances the subsystems will be transported by road. In all cases the vibrations and loads during transport need to be investigated before transporting.

Quality assurance

As has been stated before the quality assurance starts in the detailed design phase. However, to ensure the quality of the final product testing, simulation and modelling of the product is of utmost importance.

Testing

The spacecraft should be subjected to several tests. Two versions of the design will be built, which are tested to check whether the design can withstand the different environments it will be subjected to during its lifetime. Mechanical tests, e.g. a static test, shaker vibrations sine test, shock tests and acoustic tests, should be performed on the sub-assemblies and systems and the entire design [1], [93]. Furthermore, environmental testing, e.g. thermal vacuum tests and humidity tests, shall be conducted [1], [104]. Besides these tests, the elements and subsystems will for example be tested on radiation and electrical tests [1]. Testing can be used to verify and validate the designed models and qualify the design [1], [93]. Tests are carried out following the test plan, which contains how and in which order each test should be carried out. This plan contains the objectives of the test, a measurement plan, predictions and the requested outputs [93].

16.3 Phase E: Operations Concept Definition

Figure 16.3 will discuss the operations concept definition. It includes the support and the use of the system and shows the relation between the operational ground segment and the space segment. It is an iterative process which needs to be repeated throughout the two Martian years wherein the satellite is operational. It consist out of different steps which are briefly discussed below.

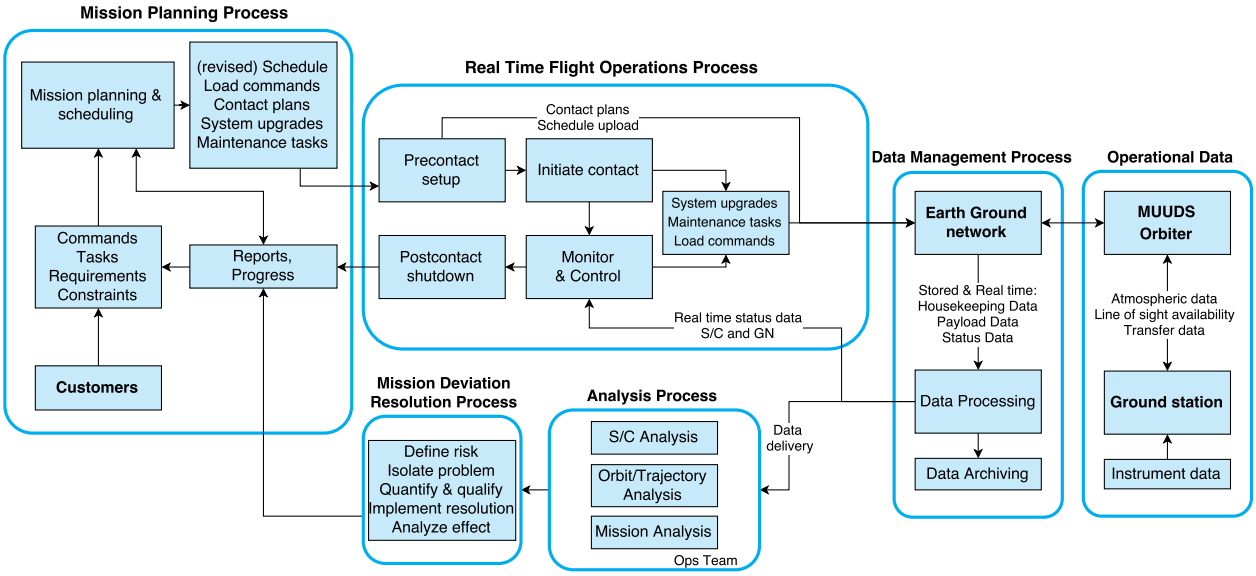

Figure 16.3: *Operational flow diagram.*

- **Mission planning process**:
  This first phase is a very important facet of the ground operations since in this phase the input of the customer and the requirements and constraints will be combined. The outcome for this phase are the different tasks the spacecraft design will need to perform throughout the missions operational life.

- **Real time flight operations process**:
  This phase includes the steps which need to be undertaken in order to transfer the outcome from the mission planning process to the actual space operations. The steps can be found in Figure 16.3.

- **Data management process**:
  Finally the different tasks are sent to all the different segments of the mission. Since one needs to be able to constantly monitor the effect and the status of some tasks it is required to send back this data for further monitoring and analysis.

- **Operational data**:
  Having received the tasks it needs to perform, both the orbiter and the ground station will execute those tasks. More information of the different steps undertaken to transmit and gather the measurement data are already discussed in the previous chapters of the report.

- **Analysis & Resolution process**:
  Having received the measured and provided data, the analysis of this data can now take place in order to determine possible deviations from the nominal state. If any would occur, mitigation methods will need to be implied to restore this state.

It is important to state that all the results and steps undertaken will need to be reported in such a way that new tasks and schedules can be made. This is an important aspect that needs to be included in the further design and will affect the telemetry and command subsystem as well as the command and data handling subsystem.

17 | Conclusion

The last big step in the manned exploration of celestial bodies was the moon landing in 1969. The next leap in manned space exploration will be the landing of humans on Mars by mid-2030. Before being able to achieve this goal a lot of work has to be done and more extensive research on the Martian environment has to conducted. The MUUDS mission fits right into the current trend of space exploration. The aim of the mission is to help humanity to achieve this next big step in the exploration in the universe by providing extensive data on the environmental conditions encountered on Mars.

The Martian weather data system is designed to provide in atmospheric measurements on ten different landing sites on Mars. These measurements include data on the temperature, pressure, wind speed, dust content, air composition and radiation assessment. In addition to the measurements performed on the Martian surface, there will be data of the in-atmospheric conditions. This data includes a temperature-; pressure-; wind velocity and air composition profiles over the full height of the Martian atmosphere.

In order to achieve these measurements by the year 2025 the MUUDS team came up with a detailed mission concept. The MUUDS mission scheduled to launch on the 24^{th} of August 2020 using the Falcon Heavy, which brings the spacecraft, which consists of ten landing vehicles and a Mars orbiter, into a trans-Martian orbit. The initial launch mass of the spacecraft will be 5,365.09 kg. The journey to Mars will take 278 days until arrival. Here a ΔV of 1.885 km/s is needed in order to bring the spacecraft into a circular orbit around Mars with an altitude of 220 km.
When in the Martian orbit the landing vehicles are separated from the orbiter, they will enter the Martian atmosphere with a ballistic trajectory. To decelerate during this descending phase an inflatable aeroshell is used right after the entry of the atmosphere. This is followed by the deployment of parachutes and in the last part of the descent, deceleration rockets will be used. Close to the surface the landing vehicle is released and lands on the surface using crushable cone. Each landing vehicle has an initial mass of 89.36 kg, which brings the ground station with a mass of 43.65 kg to the surface. Each ground station is equipped with a solar array with a size of 2.55 m^2 to provide power for the measurement instruments, the communication system and required subsystems.
The data produced by the ground station is communicated to the orbiter. For the communication between the orbiter and Earth, the Deep Space Network is used a receiver of the gathered data. This orbiter has a total mass of 200.06 kg and next to being used as a relay for the communication between the ground stations and Earth, it also performs the in atmospheric measurements using a LIDAR system, a spectropolarimeter and a UV spectrometer. Similar to the ground station, the orbiter is powered using a solar array with a size of 5.44 m^2.

The next step in the MUUDS mission is to further work out the current spacecraft and ground station design in more detail in order to ensure the optimal performance during the mission. After this, the first components have to be prototyped and tested for their functionality during the mission.

Bibliography

[1] Everett D. F. Puschell J. J. Wertz, J. R. *Space Mission Engineering: The New SMAD*. Space Technology Library. Microcosm Press and Springer, Hawthorne, California, 2011.

[2] Ho K. Schreiner S. S. Owens A. C. de Weck O. L Do, S. "An Independent Assessment of the Technical Feasiblity of the Mars One Mission Plan". *65^{th} International Astronautical Congress*, IAC 14, A5.2.7., Toronto, Canada, Sep - Oct 2014.

[3] Goverment of the United States of America. "National Space Policy of the United States of America", June 28, 2010. Technical report.

[4] "Falcon 9 Launch Vehicle Payload User's Guide". User's Guide SCM 2008 - 010 Rev. 1, Space Exploration Technologies Corporation, Hawthorne, California, 2009.

[5] Office of Commercial Space Transportation. Exective Summary and Chapters 1 – 14. In *"Final Environmental Impact Statement SpaceX Texas Launch Site"*, volume 1.

[6] S. Kemble. *Interplanetary Mission Analyis and Design*. Springer, 2006.

[7] Range Safety Group. "Global Positioning and Inertial Measurements Range Safety Tracking Systems' Commonality Standard". Standard 324-01, Range Commanders Council, New Mexico, US, 2001.

[8] Carr M. Friesen H. D. Moore, T. C. Launch Vehicle Mission Capability Enhancement through Global Positioning System Metric Tracking. *IEEE*, March 2011. doi: 10.1109/AERO.2011.5747486.

[9] "Falcon 9 Launch Vehicle Payload User's Guide". User's Guide SCM 2008 - 010 Rev. 1, Space Exploration Technologies Corporation, Hawthorne, California, 2009. p. 29.

[10] Range Safety Group. "Flight Termination Systems Commonality Standard". Standard 319-10, Range Commanders Council, New Mexico, US, 2010.

[11] K.F. Wakker. *Astrodynamics-I*. Course AE4874. Delft University of Technology, 2010.

[12] K.F. Wakker. *Astrodynamics-II*. Course AE4874. Delft University of Technology, 2010.

[13] R.W. Zurek and Smrekar S.E. An overview of the Mars Reconnaissance Orbiter (mro) Science Mission. *Journal of Geophysical Research*, May 2007. doi:10.1029/2006JE002701.

[14] Neufeld M.J. "Spacecraft Accelerometer Auto-Alignment". United States Patent 4,749,157, Hughes Aircraft Company, Los Angeles, California (USA), 1986.

[15] "ADXL377". Data Sheet D10765-0-9/12(0), Analog Devices Inc., Norwood, Massachusetts (USA), 2012.

[16] Michel P. Morgan-Owenl R. Winton A., Gerner J.-L. "The Transponder - A Key Element in ESA Spacecraft TTC Systems". *ESA Bulletin*, (86), May 1996.

[17] Halsell A. Highsmith D. Long S. Bhat R. Demcak S. Higa E. Mottinger N. Jah M. You T.-H., Graat E. "Mars Reconnaissance Orbiter Interplanetary Cruise Navigation". *20^{th} International Symposium on Space Flight Dynamics*, 2007.

[18] "Small Deep-Space Transponder (SDST): Reliable X-Band and Ka-Band Deep Space Transmission". Technical Specifications Sheet DS5-813-12, General Dynamics, Fairfax, Virginia (USA).

[19] Michel P. Morgan-Owenl R. Winton A., Gerner J.-L. "Delta-DOR - A New Technique for ESA's Deep Space Navigation". *ESA Bulletin*, (128), November 2006.

[20] Recommendation for Space Data System Practices - Delta-Differential One Way Ranging (Delta-DOR) Operations. *The Consultative Committee for Space Data Systems*, (CCSDS 506.0-M-1), April 2011. p. 2-2.

[21] Puschell J.J. Starin S.R.-Eterno J. Wertz J.R., Everett D.F. *Space Mission Engineering: The New SMAD - Control Systems*. Space Technology Library. Microcosm Press and Springer, Hawthorne, California, 2011. p. 565 - 600.

[22] "CIRUS & CIRUS EX — Compact Inertial Reference Units for Space". Technical Specifications Sheet, L-3 Space & Navigation, Budd Lake, New Jersey (USA), August 2014.

[23] "CT-602 Star Tracker". Technical Specifications Sheet 1-09 D0540, Ball Aerospace & Technologies Corp., Boulder, Colorado (USA), 2015.

[24] "Rigel-L Star Tracker". Technical Specifications Sheet 0134009 V004, Surrey Satellite Technology Ltd., Surrey (UK), 2014.

[25] "Procyon Star Tracker". Technical Specifications Sheet 0176394 V005, Surrey Satellite Technology Ltd., Surrey (UK), 2015.

[26] "Star Tracker HE-5AS". Technical Specifications Sheet, Terma Space, Lystrup, Denmark, 2012.

[27] "Reaction Wheel Unit". Technical Specifications Sheet 500-816 1114, Bradford Engineering, Heerle, The Netherlands, 2014.

[28] "High Motor Torque Momentum and Reaction Wheels (HT-RSI)". Technical Specifications Sheet, Rockwell Collins, 2015.

[29] "RDR 68 Momentum and Reaction Wheels (RDR)". Technical Specifications Sheet, Rockwell Collins, 2015.

[30] Reyhanoglu M. Krishnan H., McClamroch N.H. Attitude Stabilization of a Rigid Spacecraft using Two Momentum Wheel Actuators. *Journal of Guidance, Control, and Dynamics*, 18(2), April 1995. doi: 10.2514/3.21378, p. 256-263.

[31] Dassault Systemes. *CATIA*, version 5 edition.

[32] "Monopropellant Thrusters - MONARC-5". Technical Specifications Sheet 500-934 0613, Bradford Technology, Niagara Falls, New York (USA), 2013.

[33] "MR-111C 4N (1.0-lbf) Rocket Engine Assembly". Technical Specifications Sheet, Aerojet, Redmond, Washington (USA), April 2006.

[34] "MRE-1.0 Monopropellant Thruster". Technical Specifications Sheet, Northrop Grumman Space Technology, Redondo Beach, California (USA), 2015.

[35] "Space Propulsion Chemical Bi-Propellant Thruster Family 4N, 10N, 22N, 200N, 400N". Technical Specifications Sheet, EADS Astrium, Taufkirchen, Germany, 2013.

[36] G.P. Sutton and O. Biblarz. *Rocket Propulsion Elements*. John Wiley & Sons Inc., 1955.

[37] "R-42Dm 890N (200-lbf) Dual Mode High Performance Rocket Engine". Technical Specifications Sheet, Aerojet, Redmond, Washington (USA), May 2006.

[38] "R-40B 4,000N (900-lbf) Bipropellant Rocket Engine". Technical Specifications Sheet, Aerojet, Redmond, Washington (USA), May 2006.

[39] "Aestus Upper Stage Engine". Technical Report, Astrium [EADS], Munich, Germany.

[40] Humble R.W. Henry G.N. Larson W.J. *Space Propulsion Analysis And Design:*. McGraw-Hill Companies Inc. Primis Custom Publishing, 2001.

[41] Powell R.W. Chen A. Steltzner A.D.-San Martin A.M. Burkhart P.D. Way, D.W. and G.F. Mendeck. "Mars Science Laboratory: Entry, Descent, and Landing System Performance". 2006.

[42] S.A. Tobin and J.A. Dec. "A Probabilistic Sizing Demonstration of a Flexible Thermal Protection System for a Hypersonic Inflatable Aerodynamic Decelerator". 2015.

[43] Dyakonov A.A. Wright M.J. Edquist, K.T. and C.Y. Tang. "Aerothermodynamic Design of the Mars Science Laboratory Heatshield". 2009.

[44] A. Witkowski and M. Kandis. "Reefing the Mars Science Laboratory Parachute". 2010.

[45] Reese J.M. Greenshields, G.J. "Rarefied hypersonic flow simulations using the Navier-Stokes equations with non-equilibrium boundary conditions.". *Progress in Aerospace Sciences*.

[46] Burnage S.T. Cottard H. Doengi, F. and R. Roumeas. "Lander Shock Allevation Techniques". *ESA bulletin*, 93, February 1998.

[47] DiPrima R.C. Boyce W.E. *Elementary Differential Equations*. John Wiley & Sons. Inc., 2009.

[48] Lissauer J.J. de Pater I. *Planetary Sciences*. Cambridge University Press, 2001.

[49] Swinerd G. Stark J. Fortescue, P. *Spacecraft Systems Engineering*. Wiley, 4th edition, 2011.

[50] M.H. Acuña N.F. Ness G. Kletetschka-D.L. Mitchell R.P. Lin Connerney, J.E.P. and H. Rème. "Tectonic implications of Mars crustal magnetism". *Proceedings of the National Academy of Sciences*, 102(42), October 2005. pp. 14970-14975.

[51] "MRE-0.1 Monopropellant Thruster". Technical Specifications Sheet, Northrop Grumman Space Technology, Redondo Beach, California (USA), 2015.

[52] "Monopropellant Thrusters - MONARC-1". Technical Specifications Sheet 500-934 0613, Bradford Technology, Niagara Falls, New York (USA), 2013.

[53] "Bipropellant Attitude Control System (ACS) Thrusters - DST-11H". Technical Specifications Sheet 500-939 0914, Bradford Technology, Niagara Falls, New York (USA), 2014.

[54] "Bipropellant Attitude Control System (ACS) Thrusters - DST-12". Technical Specifications Sheet 500-939 0914, Bradford Technology, Niagara Falls, New York (USA), 2014.

[55] "Coarse Sun Sensor". Technical Specifications Sheet 500-814 0213, Bradford Technology, Heerle, The Netherlands, 2014.

[56] J.L. Bertaux, D. Fonteyn, O. Korablev, E. Chassefière, E. Dimarellis, J.P. Dubois, A. Hauchecorne, M. Cabane, P. Rannou, A.C. Levasseur-Regourd, et al. "The study of the Martian atmosphere from top to bottom with SPICAM light on Mars Express". *Planetary and Space Science*, 48(12):1303–1320, 2000.

[57] J.L. Bertaux, O. Korablev, S. Perrier, E. Quemerais, F. Montmessin, F. Leblanc, S. Lebonnois, P. Rannou, F. Lefèvre, F. Forget, et al. "SPICAM on Mars Express: Observing modes and overview of UV spectrometer data and scientific results". *Journal of Geophysical Research: Planets (1991–2012)*, 111(E10), 2006.

[58] J.H.H. Rietjens, F. Snik, D.M. Stam, J.M. Smit, G. van Harten, C.U. Keller, A.L. Verlaan, E.C. Laan, R. ter Horst, R. Navarro, et al. "SPEX: The spectropolarimeter for planetary exploration". In *International Conference on Space Optics*, volume 4, page 8, 2010.

[59] G. van Harten, F. Snik, J.H.H. Rietjens, J.M. Smit, J. de Boer, R. Diamantopoulou, O.P. Hasekamp, D.M. Stam, C.U. Keller, E.C. Laan, et al. "Prototyping for the Spectropolarimeter for Planetary EXploration (SPEX): calibration and sky measurements". In *SPIE Optical Engineering+ Applications*, pages 81600Z–81600Z. International Society for Optics and Photonics, 2011.

[60] D.M. Stam, E. Laan, F. Snik, T. Karalidi, C. Keller, R. Ter Horst, R. Navarro, C. Aas, J. de Vries, G. Oomen, et al. "Polarimetry of Mars with SPEX, an Innovative Spectropolarimeter". *LPI Contributions*, 1447:9078, 2008.

[61] P. Clissold. "ADM-AEOLUS: science report". In *ESA Special Publication*, volume 1311, 2008.

[62] J. Yu, B.C. Trieu, M. Petros, Y. Bai, P.J. Petzar, G.J. Koch, U.N. Singh, and M.J. Kavaya. "Advanced 2-µm solid-state laser for wind and CO2 lidar applications". In *Proc. of SPIE Vol*, volume 6409, pages 64091C–1.

[63] U.N. Singh, J. Yu, M. Petros, S. Chen, M.J. Kavaya, B. Trieu, Y. Bai, P. Petzar, E.A. Modlin, G. Koch, et al. "Advances in high-energy solid-state 2-micron laser transmitter development for ground and airborne wind and CO2 measurements". In *Remote Sensing*, pages 783202–783202. International Society for Optics and Photonics, 2010.

[64] U.N. Singh, G.D. Emmitt, J.S. Levine, W.C. Engelund, J. Yu, G.J. Koch, and M.J. Kavaya. "A Mars-orbiting 2-micron LIDAR system to monitor the density, winds and dust of the atmosphere of Mars". In *The fourth international workshop on the Mars atmosphere: modeling and observation*, 2011.

[65] U.N. Singh, G. Koch, J. Yu, M. Petros, J. Beyon, M.J. Kavaya, B. Trieu, S. Chen, Y. Bai, E.A. Modlin, et al. "Compact, high energy 2-micron coherent Doppler wind lidar development for NASA's future 3-D winds measurement from space". 2010.

[66] U.N. Singh, G.D. Emmitt, J. Yu, and M.J. Kavaya. "Doppler Lidar for Wind Measurements on Venus". 2010.

[67] F. Snik, T. Karalidi, C. Keller, E. Laan, R. ter Horst, R. Navarro, D. Stam, C. Aas, J. de Vries, G. Oomen, et al. "SPEX: an in-orbit spectropolarimeter for planetary exploration". In *SPIE Astronomical Telescopes+ Instrumentation*, pages 701015–701015. International Society for Optics and Photonics, 2008.

[68] J Gómez-Elvira, C Armiens, L Castañer, M Domínguez, M Genzer, Francisco Gómez, R Haberle, A-M Harri, V Jiménez, H Kahanpää, et al. REMS: The Environmental Sensor Suite for the Mars Science Laboratory Rover, August 2012. [Online; posted 04-August-2012].

[69] *Annals of the ICRP - Assessment of Radiation Exposure of Astronauts in Space*, volume 42. International Commission on Radiological Protection, 2013.

[70] Myung-Hee Y. Kim, John W. Wilson, Francis A. Cucinotta, Lisa C. Simonsen, William Atwell, Francis F. Badavi, and Jack Miller. Contribution of high charge and energy (HZE) ions during solar-particle event of september 29, 1989, May 1999. [Online].

[71] Lübberstedt H. Romberg O. Janovsky R., Kassebom M. End-of-life de-orbiting strategies for satellites. *Deutscher Luft- und Raumfahrtkongress 2002*, (DGLR-JT2002-028).

[72] NASA. *Process for Limiting Orbital Debris*. NASA Technical Standard, NASA, Washington, DC 20546, 2011. Changes approved in 2012.

[73] Michael H. Butler Jason E. Jenkins, George Dakermanji and P. Uno Carlsson.

[74] Vincent L. Pisacane. *Fundamentals of Space Systems*. Oxford University Press, 2005.

[75] "Mini Fine Sun Sensor". Technical Specifications Sheet 500-812 0714, Bradford Technology, Heerle, The Netherlands, 2014.

[76] "Spacecraft Mechanisms Product Catalog - Type 11 Solar Array Drive Assembly". Technical Specifications Sheet SAD114/99, Moog Bradford Technology, Schaeffer Magnetics Division, Chatsworth, California (USA).

[77] E. Tunstel. "Validation of autonomous rover functionality for planetary environments". In *Automation Congress, 2004. Proceedings. World*, volume 15, pages 447–452. IEEE, 2004.

[78] B. Burg. *"Thermal control architecture for planetary and lunar (sub-) surface exploration robots"*. PhD thesis, Diploma thesis, ETH Zürich, 2006, 2006.

[79] K. Mayilsamy R. Rudramoorthy. *Heat and Mass Transfer*. Pearson, 2nd edition, 2011.

[80] Keith S. Novak Gary M. Kinsella Charles J. Phillips Glenn T. Tsuyuki, Eric T. Sunada. Mars exploration rover entry, descent, & landing: A thermal perspective. Technical report, Jet Propulsion Laboratory, California Institute of Technology, Pasadena, California, USA.

[81] Edwards Jr. C.D., Erickson J.K. Bruvold, K.N., Guinn J.R. Ilott P.A. Benhan J. Johnston M.D. Kornfeld R.P. Martin-Mur T.J. Gladden, R.E., et al. "Telecommunications Relay Support of the Mars Phoenix Lander Mission". In *Aerospace Conference, 2010 IEEE*, pages 1–13. IEEE, 2010.

[82] Makovsky A. Barbieri A. Tung R. Estabrook P. Thomas A.G. Taylor, J. "Mars Exploration Rover Telecommunications. *Deep Space Communications and Navigation Systems. Jet Propulsion Laboratory*, 2005.

[83] Yuen J.H. *Deep Space Communications*. Deep Space Communications and Navigation Series. Jet Propulsion Laboratory, California Institute of Technology, Pasadena, California, October 2014. p. 17-19.

[84] Lee D.K. Shambayati S. Taylor, J. "Mars Reconnaissance Orbiter Telecommunications". *DESCANSO Design and Performance Summary Series*, 12, 2006.

[85] Lee C.H. Morabito D.D. Cesarone R.J. Abraham D.S. Shambayati, S. "Emergency Communications for NASA's Deep Space Missions". In *Aerospace Conference, 2011 IEEE*, pages 1–13. IEEE, 2011.

[86] Simu E. Kohlenberg J. Prathaban, M. "An Antenna Selection Algorithm for Mars Exploration Rover to Increase Data Return with Minimum Delay". In *Aerospace conference, 2009 IEEE*, pages 1–10. IEEE, 2009.

[87] Ilott P. Makovsky, A. and J. Taylor. "Mars Science Laboratory Telecommunications System Design". *Descanso Design and Performance Summary Series, Article*, 14, 2009.

[88] ESA. "Structural Materials Handbook: Vol. 2 New Advanced Materials". Handbook, European Space Agency.

[89] "HexWebTM Honeycomb Sandwich Design Technology". Technical Specifications Sheet AGU 075b, Hexcel Composites, Duxford, United Kingdom, 2000.

[90] Swinerd G. *How Spacecraft Fly*. Copernicus, 2009. p. 206-208.

[91] "HexWebTM Sandwich Panel Fabrication Technology". Technical Specifications Sheet LTU 018, Hexcel Composites, Duxford, United Kingdom, 2002.

[92] Petras A. "Design of Sandwich Structures". Technical report, Robinson College, Cambridge.

[93] Wijker J.J. *Spacecraft Structures*. Springer-Verlag Berlin Heidelberg, 2008. p. 24, 27-69.

[94] V.I. Weingarten, P. Seide, and J.P. Peterson. "Buckling of Thin-walled Circular Cylinders. *NASA SP-8007*, 1968.

[95] "LM-3A Series Launch Vehicle User's Manual". User's guide, China Great Wall Industry Corporation, Beijing, China, 2011.

[96] "Rockot User's Guide". User's Guide EHB0003 - Issue 5 Rev. 0, address = Bremen, Germany, year = 2011 month = August, EUROCKOT Launch Services GmbH.

[97] D.J. McCleese. *Robotic Mars Exploration and Srategy*. National Aeronautics and Space Administration, 2006.

[98] J.L. van Ingen. "The e^n method for transition prediction. Historical review of work at TU Delft". 2008.

[99] M.E. Goldstein. "Scattering of acoustic waves into Tollmien-Schlichting waves by small streamwise variations in surface geometry". 1985.

[100] McLoughlin D. Aaker, D.A. *Strategic Market Management: European Edition*. John Wiley and Sons, Ltd, 2007.

[101] National Aeronautics and Space Administration. *NASA Systems Engineering Handbook*. Pearson, first edition, 2007.

[102] Orchard M.E. Zhang B. Vachtsevanos G. Tang L. Lee Youngjin Saxena, S. and Y. Wardi. *Automated Contingency Management for Propulsion Systems*. European Control Conference, 2007.

[103] COSPAR/IAU Workshop on Planetary Protection. *COSPAR Planetary Protection Policy*. Committee on Space Research, 2002. Amended 2005.

[104] Gilmore D. G. *Spacecraft Thermal Control Handbook*. The Aerospace Press, 2nd edition, 2002.

A | Risk Factors

Below one can find the risk map used during the risk management procedures discussed in Chapter 13.

Table A.1: *Risk map.*

Likelihood						
	5. Expected					
	4. Likely					
	3. Possible					
	2. Unlikely					
	1. Rare					
		1. Insignificant	2. Minor	3. Moderate	4. Major	5. Catastrophic
		Severity				

Below one can find the full set of risk factors considered and taken into account throughout the analysis and design of the MUUDS mission. The location of the risk factor is given in coordinates of the risk map in the format as described below. Only the risk factor is mentioned while the consequence is left out.

$$[Severity, Likelihood]$$

Table A.2: *Full set of risk factors for the power and propulsion subsystems.*

P = POWER & PROPULSION		
Identifier	**Location**	**Description**
P1	[4,2]	Failure of solar cells due to unexpected events
P2	[3,2]	Malfunction of deployment mechanism of solar array
P3	[3,1]	Failure of battery system
P4	[3,1]	Malfunction of cabling infrastructure
P5	[5,1]	Failure of power distribution system
P6	[5,1]	Failure of power control system
P7	[3,5]	Dust accumulation on power systems
P8	[2,1]	Significant drop in solar power flux for a short period in time
P9	[2,1]	Increased degradation of power systems due to hostile space environment
P10	[4,2]	Leakage of toxic propellant to outer space
P11	[5,3]	Main thruster failure during Martian insertion orbit
P12	[3,3]	Thruster misalignment resulting in wrong attitude control manoeuvres
P13	[3,4]	Propellant feeding system malfunction
P14	[4,3]	Occurrence of impurities in propellant feed system
P15	[4,2]	Propellant plume pollution and damaging off other subsystems (eg. solar cells, communications means)
P16	[3,3]	Occurrence of frozen propellant
P17	[5,1]	Propellant shortage due to unexpected manoeuvring
P18	[4,2]	Failure of thrust delivery during descent phase
P19	[5,3]	Failure of thruster control during descent

Table A.3: *Full set of risk factors for the communication subsystem.*

C = COMMUNICATION		
Identifier	**Location**	**Description**
C1	[1,2]	Unplanned orbital manoeuvres of orbiter around Mars
C2	[5,1]	Failure of antenna(s) service
C3	[3,1]	Insufficient power delivery to antenna systems
C4	[3,2]	Insufficient data rate
C5	[4,1]	Too low signal-to-noise ratio
C6	[3,4]	Antenna offset
C7	[5,3]	Failure of antenna gimbal
C8	[5,1]	Unavailability of Deep Space Network
C9	[4,3]	Undesired antenna interference
C10	[5,1]	Antenna breaks off during ΔV delivery
C11	[4,4]	Uplink unable to establish due to too short contact time
C12	[4,2]	Failure of transponders causing malfunction of telecommand, telemetry and navigation

Table A.4: *Full set of risk factors for the measurement subsystem.*

M = MEASUREMENTS		
Identifier	**Location**	**Description**
M1	[3,3]	Lower TRL (=Technology Readiness Level) than predicted
M2	[5,3]	Failure of an orbital instruments
M3	[5,2]	Failure of ground instruments due to too high loads during EDL
M3	[5,3]	Failure of ground instruments due to too high temperature ranges during EDL
M4	[3,2]	Wrong calibration of ground instrument providing wrong experimental data
M5	[4,5]	Significant dust accumulation on instruments
M6	[3,4]	Extreme operational ranges in Martian environment
M7	[2,2]	Insufficient power supply to instruments
M8	[3,2]	Inability to communicate payload data
M9	[3,4]	Unexpected high radiation levels of Martian environment
M10	[3,3]	Orbital instrument fails in taking measurements at lower altitudes due to dust in atmosphere
M11	[2,3]	Instrumental decay due to hostile space environment

Table A.5: *Full set of risk factors for the launch and landing phases.*

L = LAUNCH & LANDING		
Identifier	**Location**	**Description**
L1	[4,3]	Payload cannot deal with launch loads
L2	[5,3]	Failure of ground station due to high impact velocity
L3	[2,3]	To high heat generation during EDL phase
L4	[3,2]	Wrong calibration of ADCS due to launch loads
L5	[4,2]	Unable to open the heat shield
L6	[5,2]	Malfunction of parachute during descent
L7	[4,3]	Parachutes chords snap under too high snatch force
L8	[3,3]	Failure of thruster release mechanism
L9	[3,3]	Temperature generation exceeds bordline temperature of 400 °C
L10	[4,3]	Failure of impactors
L11	[2,3]	Reentry is executed with a too large inclination
L12	[4,4]	Hinges to unfold ground station are situated below the surface
L13	[1,1]	Failure of one of the control surfaces of the ground pod
L14	[3,4]	Landing on unfavourable terrain
L15	[5,3]	Failure of separation of ground station from orbiter
L16	[2,1]	Not able to launch in the available launch window
L17	[5,2]	Failure of launching vehicle
L18	[4,1]	SpaceX cannot provide the agreed service
L19	[5,3]	Contamination of Mars during impact
L20	[5,1]	Launch cannot be performed due to political reasons

Table A.6: *Full set of risk factors for the operational phase of the orbiter.*

O = OPERATIONS		
Identifier	**Location**	**Description**
O1	[3,3]	Material imperfections causing structural failure
O2	[3,2]	Imperfections created in production phase
O3	[4,2]	Collision of space vehicle with space debris
O4	[5,2]	In space collision between two or more functional spacecraft
O5	[3,2]	Failure of heaters causing instrument errors
O6	[4,2]	Overheating of instruments
O7	[3,4]	Misalignment momentum wheels
O8	[4,2]	Failure of momentum wheels causing potential loss attitude control
O9	[4,2]	Failure accelerometer causing potential loss attitude determination
O10	[5,2]	Failure of thruster causing inability to de-spin transgress storage of momentum wheels
O11	[5,1]	Failure of the Deep Space Network causing the lose of tracking, telemetry and telecommand
O12	[5,2]	Spacecraft fails in capturing the Martian gravity field
O13	[5,3]	On-board computer fails due to short circuit
O14	[5,2]	On-board computer fails due to unexpected radiation levels
O15	[2,2]	On-board computer fails in recognising biased data

B | Requirements Compliance Matrix

The list of requirements is checked whether each requirement was achieved (A), partially achieved (P/A) and not achieved (N/A). The most important requirements are listed in Table B.1 and B.2.

B.1 Perform Mission Technically

Table B.1: *Requirements to perform the mission technically.*

Requirement	A	P/A	N/A	Reason
Mission Control Requirements				
MUUDS-Tech-Mission Control.01 The mission shall be unmanned	✓			
MUUDS-Tech-Mission Control-ADCS.01 The ADCS shall provide attitude control during operation.		✓		Not for ground operations.
MUUDS - Tech - Mission Control - Power.01 The spacecraft shall have an Electrical Power System (EPS).	✓			
MUUDS - Tech - Mission Control - Power - Operation - Performance - Ground station.03 The EPS shall be able to hold its functionality during two yearly global dust storms of <tbd> hours.		✓		During the sizing of the EPS safety margins where used. So the EPS should be able to provide power during dust storms.
MUUDS - Tech - Mission Control - Power - Operation - Performance - Ground station.04 The EPS shall not cause interference with measurement instruments.			✓	This is not investigated during the current design process and has to be done in the future.
MUUDS - Tech - Mission Control - Propulsion - Trajectory.01 The spacecraft shall have a propulsion system for propulsion after launch.	✓			
MUUDS - Tech - Mission Control - Thermal.03 Exposed components shall be protected against extreme environment changes encountered in short time intervals.	✓			
MUUDS - Tech - Mission Control - Thermal.04 The thermal control system shall maintain all the spacecraft components within the allowable temperature limits for all operating modes of the vehicle.		✓		Further investigation on the thermal control system has to be done, to be sure that the spacecraft can handle all temperatures ranges during the mission.
Data Retrieval Requirements				
MUUDS - Tech - Data Handling - Communication.01 The communication system shall support all mission phases including launch, in orbit, operations execution and end-of-life.	✓			
MUUDS - Tech - Data Handling - Communication - Performance.06 The design of the space link shall take account of continuous background noise (natural or man-made) sources as well as burst sources such as those due to solar events or structural interference.		✓		Solar events not included in the analysis.
MUUDS - Tech - Data Handling - Communication - Performance.08 During operation the orbiter shall have a downlink with the Earth ground station for 2.4 hours per day.			✓	32 minutes per day.
MUUDS - Tech - Data Handling - Data Retrieval.01 Data at ground level shall be collected at a minimum of eight measurement sites.	✓			
MUUDS - Tech - Data Handling - Data Retrieval.02 Data at ground level shall be collected at a minimum of once a per hour.	✓			
MUUDS - Tech - Data Handling - Data Retrieval.03 Atmospheric data shall be collected at a minimum of once a per 50 days.	✓			
MUUDS - Tech - Data Handling - Data Retrieval - TM.01 Temperature data shall be collected at ground level.	✓			
MUUDS - Tech - Data Handling - Data Retrieval - TM.02 The temperature sensors shall collect temperature data through the full height of the Martian atmosphere for non-ground measurements.		✓		Temperature profile for 20-160 km height.
MUUDS - Tech - Data Handling - Data Retrieval - PS.01 Pressure data shall be collected at ground level.	✓			
MUUDS - Tech - Data Handling - Data Retrieval - PS.02 The pressure sensors shall collect pressure data through the full height of the Martian atmosphere for non-ground measurements.		✓		Pressure profile for 20-160 km height.
MUUDS - Tech - Data Handling - Data Retrieval - RS.01 The radiation sensors shall collect radiation data at ground level.	✓			
MUUDS - Tech - Data Handling - Data Retrieval - DMD - Dust.01 Data on the dust content shall be collected at ground level.	✓			

Requirement	A	P/A	N/A	Reason
MUUDS - Tech - Data Handling - Data Retrieval - DMD - Dust.02 The spectrometer shall collect dust content data through the full height of the Martian atmosphere for non-ground measurements.	✓			
MUUDS - Tech - Data Handling - Data Retrieval - WS.01 Wind velocity data shall be collected at ground level.	✓			
MUUDS - Tech - Data Handling - Data Retrieval - WS.02 The wind velocity sensors shall collect wind velocity data through the full height of the Martian atmosphere for non-ground measurements.		✓		Wind velocity profile for 0-90 km height.
MUUDS - Tech - Data Handling - Data Retrieval - Spectrometer.02 Data on the atmospheric composition shall be collected at ground level.	✓			
MUUDS - Tech - Data Handling - Data Retrieval - Spectrometer.03 The spectrometer shall collect atmospheric composition data through the full height of the Martian atmosphere for non-ground measurements.		✓		O_3: 10-50 km, CO_2 : 20-160 km, O_2 : 35-90 km.
General Technical Constraints Requirements				
MUUDS - Tech - Constraints - Payload.01 The payload dimensions shall not exceed the maximum allowed payload dimensions of the launcher.	✓			
MUUDS - Tech - Constraints - Payload.02 The payload mass shall not exceed 13 tons.	✓			
MUUDS - Tech - Constraints - Structures.01 Structural assemblies and components shall be designed to withstand applied loads due to the mechanical environments to which they are exposed during the service-life.	✓			
MUUDS - Tech - Constraints - Materials.01 The material strength shall be established for the most critical combination of mechanical and thermal effects expected during its lifetime.	✓			
MUUDS - Tech - Constraints - Materials.02 For all components subject to alternating stresses, it shall be demonstrated that the degradation of material properties over the complete mission remains within the specified limits.		✓		The demonstrations have to be performed in later design stages.

B.2 Perform Mission within Non-Technical Constraints

Table B.2: *Requirements to perform the mission within non-technical constraints.*

Cost and Sustainability Requirements				
Requirement	**A**	**P/A**	**N/A**	**Reason**
MUUDS - Constraints - Cost.01 The total cost of the mission, including launch and excluding Earth-based operations after launch, shall not exceed 2 billion euro (PV 2015).	✓			
MUUDS - Constraints - Sus - EOL.01 The mission shall last at least 2 Martian years.	✓			
MUUDS - Constraints - Sus - EOL.02 Minimal harm shall be done to the Martian environment by debris during EOL.	✓			
MUUDS - Constraints - Sus - EOL.03 Debris in Earth orbit shall be properly disposed to not cause additional debris.	✓			
MUUDS - Constraints - Sus - EOL.05 EOL shall result in immediate propulsion and power system passivisation.		✓		Except when the mission is able to run longer than 2 Martian years.
RAMS Requirements				
MUUDS - Constraints - RAMS - Rel.01 *"All single points of failure shall be eliminated by redundant components."*		✓		Not all systems are redundant due to mass constraints.
MUUDS - Constraints - RAMS - Rel.02 The subsystems shall have a reliability of <tbd> %.		✓		The reliability has to be determined in a later design stage.
MUUDS - Constraints - RAMS - Avail.01 All data shall be collected for two full, consecutive Martian years.	✓			
MUUDS - Constraints - RAMS - Avail.02 A minimum of two Martian years of data shall be available for analysis by 2025.		✓		Unlikely for the mission to be fully developed in time for the launch date.
MUUDS - Constraints - Schedule.01 The launch shall take place between April 2018 and May 2018 or between July and September 2020.		✓		Unlikely for the mission to be fully developed in time for the launch date.